Magnetic field effects in the reoxidation of avian cryptochrome: a computational exploration

Submitted by Jean Deviers, to the University of Exeter as a thesis for the degree of Doctor of Philosophy in Physics, April 2023.

This PhD project is a part of the UK-French PhD programme, supported and funded jointly by the Defence Science and Technology Laboratory (DSTL) and the Agence de l'Innovation de Défense (AID). In the spirit of this collaboration, it was carried out both in the UK, in the Living Systems Institute (LSI) at the University of Exeter, where I worked under the supervision of Dr. Daniel Kattnig; and in France, in the Institut de Chimie Physique at the Université Paris-Saclay, where I worked with Dr. Aurélien de la Lande and Dr. Fabien Cailliez.

Abstract

Biological magnetoreception, a sensory modality most notably exhibited by migratory birds, is one of the most intriguing yet still poorly understood phenomena of the emerging field of quantum biology. Thought to arise from the quantum spin dynamics of a photo-initiated radical pair or triad in the ocular Cryptochrome protein, magnetoreception still has no definitive mechanism, identity or number of reactant radicals.

Motivated by the recent formulation of a theoretically more sensitive mechanism, implicating 3 radicals instead of the commonly postulated flavin/tryptophan pair, as well as by experimental results suggesting the involvement of radical species formed later in the flavin photocycle, we report in this thesis an investigation into the magnetosensitivity of a $FADH^{\bullet}/O_2^{\bullet -}/Y^{\bullet}$ triad, formed in the so-called "dark reoxidation" of cryptochrome 4, within the context of the scavenging mechanism, whereby the spin dynamics of a primary radical pair are affected by a third, "scavenger" radical.

Spin dynamics simulations were employed to identify, within an avian cryptochrome protein structure (*Columba livia* cryptochrome 4, or *cl*Cry4), a tyrosine residue, Y319, realistically able to function as a scavenger in a $FADH^{\bullet}/O_2^{\bullet -}/Y^{\bullet}$ radical triad with fast-relaxing superoxide. In an effort to parametrise our spin dynamics model, we computed hyperfine coupling (HFC) tensors for $FADH^{\bullet}$ and $FAD^{\bullet -}$ using Density Functional Theory (DFT). Dynamical effects were incorporated using long Molecular Dynamics (MD) simulations and a cluster model of the flavin chemical environment. It was found that the flavin electronic structure was significantly perturbed by structural fluctuations, and was well-insulated from electronic polarisation.

Superoxide electrostatic trapping at the protein surface was uncovered with the use of MD simulations. 5 chemically relevant binding sites, able to be populated either from the bulk or from a putative formation site inside the crypt, were identified. Binding times, rotational correlation times, and spin relaxation times for a bound $O_2^{\bullet -}$ were computed. It was found that 10^2 ns spin relaxation times were possible for 3 of these sites, possibly contributing non-averaged electron-electron dipolar (EED) to the radical triad's spin dynamics for a significant portion of its lifetime.

Using a spin dynamics simulation model thus parametrised, we verified the ability of Y319 to elicit magnetosensitivity in a more realistic environment. Particularly promising is its ability to deliver significant MFEs across a broad ranges of conditions, with or without superoxide relaxing; this robustness could play a role in delivering a strong, consistent compass reading from an inhomogeneous ensemble of cryptochrome proteins.

Dedication and acknowledgements

I express my heartfelt gratitude to my supervisors, Daniel Kattnig, Aurélien de la Lande, and Fabien Cailliez, for their constant guidance and encouragement. This thesis could never have been completed had it not been for their seemingly endless patience and availability, whether to troubleshoot a problem or simply to discuss. I also greatly appreciate all the opportunities they gave me to communicate my work, whether in the lab or at conferences. It has been a privilege to work with such dedicated researchers. These thanks also extend to my second tutor at Exeter, Pr. Gyaneshwar Srivastava, for his time monitoring and guiding the advance of the thesis, and his wise advice on redaction.

I would like to thank my jury assessors, Pr. Ilia Solov'yov and Pr. Frank Vollmer, for accepting to take the time to read and evaluate the work done in these three years, which I look forward to discussing with them.

I acknowledge the support and resources provided by the DSTL which made this research possible. I am thankful for the opportunities and facilities provided by the institution that helped me conduct my research and complete this thesis.

I'm obviously heavily indebted to all my colleagues, both in France and in the UK, without whose professional and personal help this thesis would not have gone on, or would at least have been much duller. In no particular order, a warm "thank you" to: Baptiste, Feven – spero di non averti fatto odiare la poesia francese; I'll admit that was not all Duolingo –, Valeriu, Julia, Joachim, David, Lea, Damien, Duda, Evaristo, Carine, Nathan, Rika, Lou, Jess (UK), Jess (FR, although that's a grey zone... pick your side, but keep in mind: 10-53), Raphaël, Dominik, Chris, Audrey, Tom... and probably others I'm forgetting and whose names will pop up as soon as this manuscript is sent. The coffees, lunches at the office and outside, beers and discussions will remain memories I'll cherish. Also, a special thank you to Karwan for being the loveliest office-mate one could dream of.

I also want to thank Chloé, whose unwavering support and acceptable chess skills were what it took to get through months of COVID lockdowns, multiple house moves and life in general.
Last but not least, I want to thank my family from the bottom of my heart; thank you for always being there despite the distance, and for always believing in me.

ACRONYMS

ACF Auto-Correlation Function

ADFT Auxiliary Density Functional Theory

APBS Advanced Poisson-Boltzmann Solver

Asc Ascorbic Acid

AtCry *Arabidopsis thaliana* Cryptochrome

BE Binding Event

BET Back Electron Transfer

BLUF Blue-Light Utilizing Flavin adenine dinucleotide

BSSE Basis Set Superposition Error

clCry4 *Columba livia* cryptochrome 4

COM Center Of Mass

Cry Cryptochrome

C-SUP Cavity-SUPeroxide

CTT C-Terminal Tail

DFT Density Functional Theory

DmCry *Drosophila melanogaster* cryptochrome

DNA DeoxyriboNucleic Acid

EED Electron-Electron Dipolar coupling

ENDOR Electron-Nuclear Double Resonance spectroscopy

EPR Electron Paramagnetic Resonance

ErCry4 *Erithacus rubecula* cryptochrome 4

E-SUP Escaping SUPeroxide

ET Electron Transfer

ETF Electron Transfer Flavoprotein

FAD Flavin Adenine Dinucleotide

FADH Flavin Adenine Dinucleotide, semiquinone

FC Fermi Contact

FD-CL Free-Diffusing Cl^- (chlorine)

FD-SUP Free-Diffusing SUPeroxide

FF Force-Field

GAFF2 General All-Atom Force Field 2

GGA Generalised Gradient Approximation

GPU Graphics Processing Unit

GPX Glutathione PeroXidase

HFC HyperFine Coupling

HFCC HyperFine Coupling Constant

KS Kohn-Sham

LDA Local Density Approximation

LFE Low-Field Effect

LJ Lennard-Jones

LOV Light, Oxygen, Voltage

MD Molecular Dynamics

MFE Magnetic Field Effect

mGGA meta-Generalised Gradient Approximation

MHz MegaHertz

MM Molecular Mechanics

NADPH reduced Nicotinamide Adenine Dinucleotide Phosphate

NVE Microcanonical thermodynamical ensemble

NVT Canonical thermodynamical ensemble

NpT Isothermal-Isobaric thermodynamical ensemble

PBC Periodic Boundary Conditions

PBL Phosphate-Binding Loop

PCM Polarisable Continuum Model

PDB Protein DataBank

PME Particle Mesh Ewald

QM Quantum Mechanics

QM/MM Quantum Mechanics / Molecular Mechanics

RDF Radial Distribution Function

RESP Restricted ElectroStatic Potential

RF Radio-Frequency

RMSD Root-Mean-Square Deviation of atomic positions

RMSF Root-Mean-Square Fluctuation of atomic positions

RNA RiboNucleic Acid

ROS Reactive Oxygen Species

RP Radical Pair

RPM Radical Pair Mechanism

SCF Self-Consistent Field

SD Spin-Dipole

SI Supplementary Information

SIE Self-Interaction Error

SOC Spin-Orbit Coupling

SOD SuperOxide Dismutase

SRI Spin-Rotational Interaction

SUP Superoxide

Trp Tryptophan

T-SUP Trapped SUPeroxide

Tyr Tyrosine

vdW van der Waals

W Tryptophan

XC Exchange-Correlation

XRD X-Ray Diffraction

Y Tyrosine

TABLE OF CONTENTS

LIST OF TABLES

List of Figures

CHAPTER 1

GENERAL INTRODUCTION

This thesis addresses the mechanism underpinning the ability of cryptochrome to function as magnetic field transducer in weak magnetic fields. Motivated by recent suggestions of magnetosensitivity associated with the re-oxidation of cryptochrome in a dark state reaction, an emphasis is put on the flavin semiquinone/superoxide radical pair. I derive pertinent spin Hamiltonian parameters taking the environment and thermal fluctuation into account, discuss the magnetosensitivity of the re-oxidation in radical pair and novel radical triad models, and investigate the interaction of superoxide with cryptochrome. The main conclusion is that radical triad models can in principle deliver a sensitivity enhancement beyond comparable radical pairs, but the electron-electron dipolar interaction is detrimental and appears to not be well compensated assuming that the third radical in triad models is a cryptochrome-bound tyrosine. Superoxide binding can reduce the rotational correlation time sufficiently to permit a magnetic field sensitivity in weak magnetic fields. My findings pave the way to a understanding of dark-state magnetosensitivity in cryptochrome. However, additional studies of more complex model systems will be required to understand if this processes could deliver the required sensitivity to underpin the avian compass sense.

The remarkable ability of some birds to migrate over very long distances to a specific location – consider the Pacific Golden Plover,[4] that travels 2000 miles over the Pacific ocean to the Hawaiian Islands – is not yet a completely understood phenomenon. It is believed that avian navigation actually relies on distinct map and compass senses; the former consisting of a magnetic map,[1,5] of the ability to recognise landmarks,[1] and to use the sun and stars for navigation;[6,7] and the latter of a magnetic inclination compass.[8] This summary focuses on the

mechanisms underpinning directional magnetosensitivity in migratory birds, and therefore shall concern itself mainly with the magnetic compass sense.

The difficulty is to formulate a biologically credible mechanism, which accounts for the high angular precision[9] of the avian magnetic compass; for its sensitivity to magnetic fields as weak as the Earth's; and for its ability to function, for some species such as night-migratory songbirds, even under dim light.[10] It should also satisfy the requirement of being only sensitive to the inclination of the Earth's magnetic field, and not to its polarity;[8] and also that the magnetosensitive reaction step appears to happen in the dark,[11,12] but still relies on photo-initiation of some sort. Other intriguing features of the avian compass include its considerable tunability,[13] and its sensitivity to weak radio-frequency (RF) fields.[14,15] On a more technical note, this reaction is thought to rely on the sustenance of quantum state superposition of two electron spins for extended periods of time, which is difficult to achieve in a "warm, wet and noisy" biological environment.[1,16]
Many years of study suggest that the sense relies on a flavoprotein called cryptochrome,[1,17,18] located in birds' eyes.[17] Variants of this protein can also be found in a variety of non-migratory animals, and even in some plants.[19–22] Bird cryptochromes shall be preferably investigated throughout this project; unlike plant cryptochromes, avian cryptochromes have been under evolutionary pressure to develop a performant, directional magnetic compass. The difficulty however arises that the available protein structures, resolved using X-ray Diffraction (XRD) on *in vitro* cryptochromes without their native chemical environment, might differ conformationally from the *in vivo* structure.[23] This point also limits the possibility to investigate early-stage signal transduction pathways, which is hypothesized to be initiated by a conformational change in the C-Terminal Tail (CTT) of the cryptochrome. In any case, the generation of a neural signal carrying directional information likely relies on separate amplification pathways, whose investigation pertains to the domain of biology rather than computational chemistry and physics. The multiscale nature of the phenomenon requires a multidisciplinary approach to fully describe it. In this thesis, we restrict our research to the microscopic scale, on a single protein.

In particular, two mechanisms have been proposed to give rise to magnetosensitivity in the cryptochrome: the more dominant one, the Radical Pair Mechanism (RPM), relies on the coherent spin dynamics of a pair of radicals being affected by the orientation of the geomagnetic field. This dependence is then inherited by the spin-selective reactivity of the radicals, making the final concentrations of reaction products – the signaling state – also dependent on the orientation of the Earth's magnetic field. The spin-selective reaction is hypothesized to correspond to the recombination of the radicals' unpaired electron *via* electron transfer, reforming a diamagnetic pair. For the yield of spin-selective recombination reaction to be depen-

dent on the spin dynamics of the radical pair, recombination must compete with a spin-independent reaction, yielding a distinct chemical or conformational product identified with the signaling state.

In the RPM scheme, the most commonly considered radical pair is the $FAD^{\bullet -}/W^{\bullet +}$, born of the photo-activated reduction of a Flavin Adenine Dinucleotide (FAD) by a chain of tryptophan. The popularity of the $FAD^{\bullet -}/W^{\bullet +}$ radical pair is owed to a number of mutation studies, performed on multiple (avian, insect and plant) cryptochrome, which report a strong decline or even complete extinction of Magnetic Field Effects (MFEs) after mutation of one or several tryptophan(s) in the chain.[24] Due to the weakness of the Earth's magnetic field, its ability to significantly impact the spin dynamics of a radical pair system relies on the near-degeneracy of singlet and triplet spin states, *i.e.* the fact that singlet and triplet spin configurations are energetically very close, and are crucially of the same order of magnitude as the strength of the Zeeman coupling, *i.e.* the interaction of a radical electron with the geomagnetic field. Spin states' energetic separation is mainly determined by the radicals' respective hyperfine structure (i.e. the magnetic interaction between an unpaired electron and neighbouring N and H nuclei) and by their distance from one another, which modulates the strength of EED coupling between them.[1] This delicate state is however extremely sensitive to electron-electron dipolar (EED) coupling, an interaction modality between radical electron spins that can strongly separate spin states, especially at short distances.[25] Although often neglected in earlier spin dynamics simulations, this interaction was found to significantly hamper singlet/triplet interconversion in a realistic (*i.e.* with biologically consistent relative orientation, separation distance and hyperfine structure) $FAD^{\bullet -}/W^{\bullet +}$ pair, thereby strongly reducing predicted MFEs.

On the other hand, the massive decline in Magnetic Field Effects (MFEs) upon inclusion of EED couplings into the simulation model can be mitigated with the addition of a third radical. By breaking the symmetry of a 2-radical system, where EED couplings are reciprocal and tend to settle the pair into a stabilised spin state, the presence of a third radical can drive singlet/triplet interconversion, even in the absence of hyperfine interactions.[26] The inclusion of both EED and hyperfine interactions, as is expected from a flavin-containing radical system, gives rise to spin dynamics governed by a complex interplay of hyperfine and EED coupling, which nonetheless proves powerfully magnetosensitive for certain geometries.[27] Furthermore, beyond its electronic contribution, we have to consider the reactivity of the third radical: much like the radicals in a radical pair recombine in a spin-selective manner, "scavenging" by the third radical is achieved *via* spin-selective electron transfer.

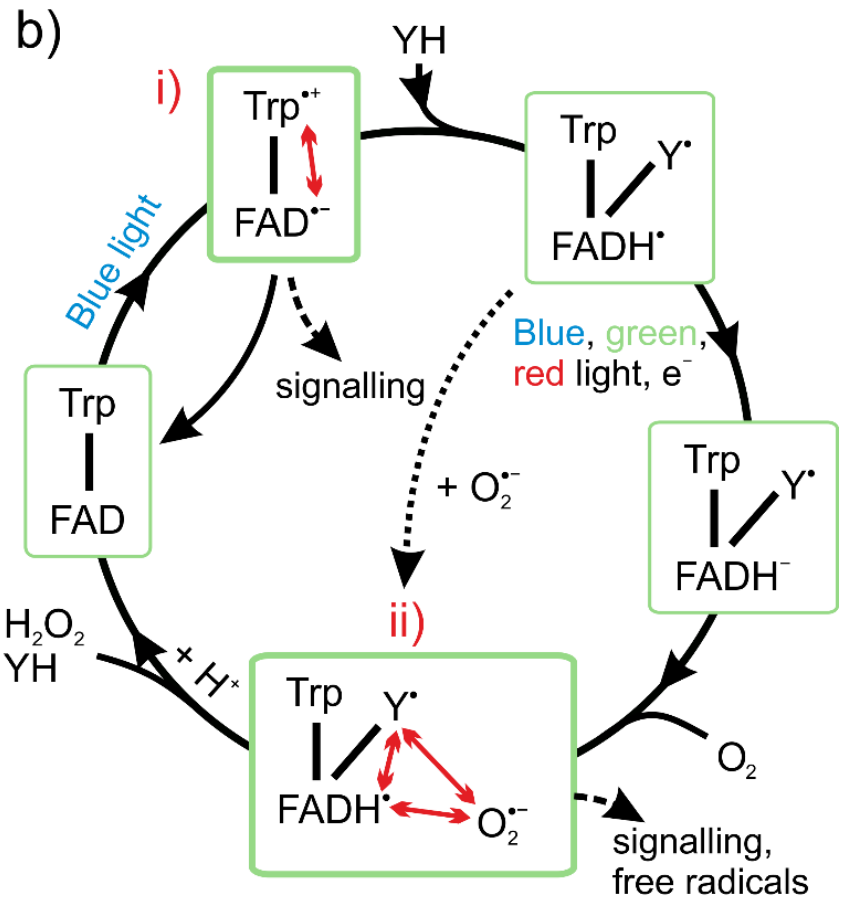

Figure 1.1: Photocycle of the cryptochrome undergoing a two-step photoreduction and reoxidation.

As mentioned earlier, recent experimental results found that the magnetosensitive step, while still requiring photo-initiation, is able to proceed in the dark, after a delay past which any $FAD^{\bullet-}/W^{\bullet+}$ radical pairs are expected to have decayed or recombined.[11] This apparent incompatibility in lifetimes led to the formulation of an alternative radical system, involving species downstream in the flavin photocycle. Specifically, we focus throughout this thesis on the $FADH^{\bullet}/O_2^{\bullet-}/Y^{\bullet}$ radical triad, arising from the (dark-state) reoxidation of a fully reduced flavin $FADH^{-}$ by triplet molecular oxygen $^3O_2$.[28] The reoxidation step yields a correlated $FADH^{\bullet}/O_2^{\bullet-}$ radical pair, while the radical electron of $W^{\bullet+}$ is transferred to a nearby tyrosine, yielding a $Y^{\bullet}$ radical able to act as a scavenger to the primary radical pair.[29] The choice of tyrosine as a reducing agent for $W^{\bullet+}$, leading to the formation of a long-lived $Y^{\bullet}$, was informed by the detection of a radical tyrosine in pigeon cryptochrome, found to be necessary to complete the photoreduction step.[30]

The flavin photocycle is presented in greater detail in Figure 2.1 (b), which is reproduced here (Figure 1.1) for convenience. The redox-cycle involves two potentially magnetosensitive radical pairs, $FAD^{\bullet-}/Trp^{\bullet+}$ in the first photo-reduction (labelled *i*)

and the $FADH^{\bullet}/O_2^{\bullet -}$ radical pair resulting from the oxidation of the fully reduced $FADH^-$ by oxygen (at step ii). The first photo-reduction occurs by absorption of UV and blue light up to about 500 nm by the fully oxidised flavin (FAD),[11] promoting FAD to an excited state and triggering a cascading electron transfer down a chain of 4 (for avian, *e.g.* pigeon, cryptochromes) tryptophan residues. The resulting $FAD^{\bullet -}/Trp^{\bullet +}$ radical pair, which is largely researched as a strong candidate for being the actual magnetosensitive radical pair, is expected to have a lifetime between 1 and 10 μs in order to acquire appreciable magnetosensitivity.[1] The present thesis is however focused on the investigation of another model of magnetoreception, involving 3 radicals, and in particular with the possible involvement of a superoxide radical. We also take as clues for the identity of the radicals involved the results presented in Ref. 11, suggesting the sustenance of magnetosensation past 100 ms – although the limitations of this study shall be discussed later. For this reason, we suggest the transfer of the radical electron on the terminal tryptophan to a nearby tyrosine YH, able to form extremely long-lived radicals.[31–33] $FAD^{\bullet -}$ gets protonated to its semiquinone form $FADH^{\bullet}$ in the process, although the identity of the donor remains unclear; it is here assumed to be the protonated tyrosine YH, although it could also be a protonated tryptophan residue. In a second time, $FADH^{\bullet}$ gets converted to the fully reduced $FADH^-$ by absorption of light in the UV to about 570 nm green. We finally consider the interaction with a free-diffusing molecular oxygen O_2 molecule, coming into close contact with $FADH^-$ to reoxidate it to $FADH^{\bullet}$, thereby forming a correlated $FADH^{\bullet}/O_2^{\bullet -}$ radical pair with a $Y^{\bullet}$ radical in the vicinity. This radical triad, labelled ii, is the main focus of the exploratory work reported in this thesis. The practicalities of the reoxidation step, such as for instance the location and duration of O_2 immobilisation for completing the electron transfer, are examined in Ref. 2, although on a different cryptochrome than the one considered here. While these are important considerations, we focus throughout this thesis, and in particular in Chapter 4, on events occurring after $FADH^-$ oxidation and $O_2^{\bullet -}$ formation; we assume that the correlated $FADH^{\bullet}/O_2^{\bullet -}$ pair has been formed, and then assess the potential for magnetosensitivity in such a system. Finally, electron recombination with either $O_2^{\bullet -}$ or $Y^{\bullet}$ (scavenging), coupled with a proton transfer to either of these species, regenerates the fully oxidised flavin FAD with which the photocycle began. This process is associated with the reformation of protonated tyrosine YH or with the liberation of H_2O_2. A more complete description of the flavin photochemistry can be found in Ref. 28.

In this thesis, the scavenging model of magnetoreception based on a scavenged $FADH^{\bullet}/O_2^{\bullet -}/Y^{\bullet}$ radical triad is examined in more details. In particular, we aim to identify a suitable $Y^{\bullet}$ radical in the structure of an avian cryptochrome 4. We are working with a model of a pigeon (*Columba livia*) cryptochrome 4, *cl*Cry4, resolved

using XRD, apart from a reconstructed loop for which the structure is validated in Ref. 34. The assessment of tyrosine radicals' ability to function as a strongly magnetosensitive scavenger is notably achieved by refining the current simulation model, *i.e.* by parametrising the spin Hamiltonian and other simulation terms presented later in Chapter 1. Specifically, we focus on obtaining an accurate description of the hyperfine structure of the flavin in both of its potentially magnetosensitive states, $FAD^{\bullet -}$ and $FADH^{\bullet}$. The particular symmetry of the flavin hyperfine structure is what confers the magnetic compass directional sensitivity, and we investigate here the impact of molecular motion and electronic polarisation on its nuclei-borne hyperfine coupling tensors. Another avenue for achieving more realistic modeling of the radical pair or triad is the discovery of $O_2^{\bullet -}$ binding locations and the computation of spin relaxation rates. These quantities inform the strength and the lifetime of non-averaged, coherent EED coupling with other radicals. These two effects, hyperfine and electron-electron dipolar couplings, determine the baseline spin dynamics of the pair or triad which the geomagnetic field can then perturb. Using a simulation thus parametrised, we finally strengthen the results obtained in Chapter 2 and propose a specific $Y^{\bullet}$ to scavenge a $FADH^{\bullet}/O_2^{\bullet -}$ system, as well as $O_2^{\bullet -}$ binding sites and coherence lifetimes. A more detailed breakdown of the works presented in this thesis is provided below.

The benefits of elucidating the mechanism responsible for a biological magnetosensitivity of such precision are several: first, it would provide insight into the potential effects of very weak electromagnetic fields on biological systems, which applies to humans as well.[35] Even if just for curiosity, as no obvious applications for such a principle could realistically be developed in the near future, uncovering one of nature's most intriguing phenomenona is still a way to complete our general understanding of the world. In the longer run, we can tentatively suggest some practical applications for biological quantum magnetoreception, should it follow the principles explored in this thesis: for instance, discovering Nature's way of delaying the onset of decoherence could help design longer-lived qubits for quantum computing and sensing.[36] Lastly, understanding the mechanism could guide the development of novel, robust and purely organic sensors; eventually, one could even imagine developing a biologically integrated magnetic compass.

Chapter 1 is an exposition of the theoretical background for this thesis. In a first time, the various mechanisms advanced to explain the phenomenon of magnetoreception are explained, and the current state of knowledge on their respective merits and limitations is detailed. A second part focuses on the various methods employed throughout this thesis, offering both a theoretical introduction and some practical details relating to their use. Additionally, some properties of interest which are computed with each method are presented and detailed. In particular, the theory

underpinning rotational correlation times and hyperfine couplings, both linked to the parametrisation of the spin dynamics simulation method used in this thesis, are presented in this chapter.

Chapter 2 reports the results of an investigation into the ability of a tyrosine radical $Y^\bullet$ to function as a scavenger in a realistic [$FADH^\bullet$-$O_2^{\bullet-}$-$Y^\bullet$] radical triad, using spin dynamics simulations parametrised with radicals positions and relative orientations taken from a pigeon (*Columba livia*) cryptochrome protein structure, *cl*Cry4. Importantly, $O_2^{\bullet-}$ spin relaxation and electron-electron dipolar (EED) coupling between radicals were included in the simulations. A [$FADH^\bullet$-$O_2^{\bullet-}$] radical pair was found not to function due to its fast spin relaxation. On the other hand, for a [$FADH^\bullet$-$O_2^{\bullet-}$-$Y^\bullet$] system, sizable MFEs exceeding those achieved by a [$FAD^{\bullet-}$-$W^{\bullet+}$] RP could be achieved in the case of rather fast scavenging. Relative singlet yield anisotropy Γ_S values are reported for each of the 18 tyrosine present in *cl*Cry4, all potentially able to function as a scavenger in the *cl*Cry4 protein. In all cases, a strong quenching of MFEs by EED coupling was uncovered. The control of EED strength by distance left most tyrosines with sufficient surviving MFEs realistically unable to achieve sufficiently fast scavenging rate. Y319 was however identified as a promising candidate, with the potential ability to realise its optimal scavenging rate. Further mechanistic justifications were cited for this tyrosine. Finally, strong magnetic sensitivity was reported for a [$FADH^\bullet$-$O_2^{\bullet-}$-$Asc^{\bullet-}$] system. This research resulted in a publication in the Journal of Chemical Physics (DOI: 10.1039/d1cp05804e).[37]

Chapter 3 presents a comprehensive computational study of the hyperfine coupling (HFC) tensors describing the magnetic structure of the cryptochrome-bound flavin in a partially XRD-resolved *cl*Cry4 structure. Two important dynamical effects, the structural fluctuations due to thermal energy and the electronic polarisation by its immediate chemical environment, are accounted for *via* the use of long (800 ns) MD simulations. The respective impact of both these effects is decorrelated, and we find that both $FADH^\bullet$ and $FAD^{\bullet-}$ are surprisingly well insulated from their environment, but are quite sensitive to geometrical distortions. Specific changes to large and anisotropic tensors, with implications to the performance of a magnetic compass, are outlined and linked to the effect of polarisation, or a particular geometrical feature. The main contributions of this chapter are an updated set of average hyperfine coupling tensors, taking into account the aforementioned dynamical effects; the distribution of each tensor component, potentially useful to model the dynamics of HFC tensors or inhomogeneous ensembles; and the delineation of a cluster of polarising residues surrounding the flavin, for calculations of electronic structure properties susceptible to polarisation. This work resulted in a publication in the PCCP journal (DOI: 10.1063/5.0078115).[38]

Chapter 4 concerns itself with an investigation of the ability of a *cl*Cry4 protein to bind and immobilise, through nonbonded interactions, a $O_2^{\bullet -}$ radical. The aim of the research reported therein is to estimate the magnetosensitivity of a $FADH^{\bullet}/O_2^{\bullet -}/Y^{\bullet}$ radical triad inside the *cl*Cry4, parametrising spin dynamics simulations with radicals locations (*i.e.* $O_2^{\bullet -}$ binding sites) for a correct estimation of the EED coupling, and with radicals relaxation times (computed for $O_2^{\bullet -}$from rotational correlation times and g-tensor values) for a correct description of the spin dynamics via the Lindbladian operator. Geometrical data from a number of Molecular Dynamics simulations are reported, both for $O_2^{\bullet -}$ and for the biologically available Cl^- ion. Due to the latter ion's negative charge, presupposing an affinity with similar partners as $O_2^{\bullet -}$, and its abundance in the intracellular medium, we considered the possibility of Cl^- and $O_2^{\bullet -}$ competing for the same binding sites. This case appears unlikely, with Cl^- exhibiting both rarer, shorter and less localised binding patterns compared to $O_2^{\bullet -}$. The binding capabilities of a proposed $O_2^{\bullet -}$ formation site were investigated, for which remarkably long binding and spin relaxation times were computed. Its accessibility in a *cl*Cry4 structure was however not guaranteed. We then investigated another putative formation site, and monitored $O_2^{\bullet -}$ diffusion and trapping by the protein; in particular, trapping by 5 binding sites of chemical significance. Binding times of the order of 10^2 ns were routinely achieved within these sites. Rotational correlation times τ_2, proportional to spin relaxation times for $O_2^{\bullet -}$, as long as 10^5 times its value in solution are reported; besides this extreme result, factors of 10^4 were routinely achieved by several of these sites. Spin relaxation times of up to almost $1\,\mu$s, but often of the order of 10^2 ns, were estimated for the binding events achieving the largest τ_2. Finally, the set of $Y^{\bullet}$ radicals investigated in Chapter 2 were re-tested with an updated spin Hamiltonian and $O_2^{\bullet -}$ located in the binding sites, in the limit of slow spin relaxation. Y319 was found to be quite insensitive to $O_2^{\bullet -}$ status, whether tumbling in solution or bound with non-averaged, short-range EED coupling.

Chapter 5 comes as a recap of the most salient conclusions from each chapter and lists the future avenues of research that could build on that presented in this thesis.

1.1 Proposed mechanisms of magnetoreception

1.1.1 The magnetite hypothesis

One of the theories for rationalising avian magnetoreception involves magnetite (Fe_3O_4) particles, endowed with permanent magnetic moments, whose reorientation, triggered by the application of an external magnetic field, could act upon mechanosensors and/or open ion channels, thus generating an electrical signal de-

pendent on the direction of a magnetic field. Although such particles might exist in the upper beak of migratory birds,[5,39] where they appear to feed into the bird's nervous system through the ophthalmic branch of the trigeminal nerve,[1] experimental evidence disproves its involvement in the avian compass sense. Indeed, it has been shown that anaesthetisation of the beak and severance of the aforementioned nerve does not disorient birds, and that exposure to a strong electromagnetic pulse, which re-magnetises an iron-based system, does not prevent birds from using their magnetic sense.[14,40] There is however some evidence suggesting its participation in a magnetic map sense, which provides positional rather than directional information: notably, ablating the V1 nerve prevents migratory reed warblers to compensate for a 1000 km displacement.[41] Still, this effect is outside the scope of the present summary, which focuses on the compass sense; therefore, the thesis of magnetite-based magnetoreception in this context shall not be developed further.

1.1.2 The Radical Pair Mechanism

In 2000 Ritz *et al.* suggested, based on previous work by Schulten,[42] that the primary magnetic sensor is located in the eyes of birds,[17] following an observation dating back to 1993 by Wiltschko *et al.* that the process of magnetoreception is light-activated.[43] This claim is substantiated by the observation that Cluster N, a forebrain locus which is especially active when the bird is orienting using its compass[44] – and which forbids magnetic orienting when damaged[45] –, is part of the visual system (linked to the eyes through the thalamofugal pathway) and cannot function in the absence of light.[46]

To this day, the most credible candidate for light-activated magnetoreception is the cryptochrome[1] class of flavoproteins, notably located in the retina of birds, but also in plants, cockroaches, newts, and even humans. Cryptochromes belong to the same family as photolyases, with which they share a homology region around the flavin adenine dinucleotide (FAD cofactor), a riboflavin derivative capable of absorbing blue light. Whether in plants, where it regulates growth, or in animals, where it entrains the circadian rhythms, Cryptochrome activation is always mediated by light irradiation in the FAD absorption window – in various redox states. Most interestingly, even species which do not require a magnetic compass sense for survival exhibit some magnetosensitivity: for instance, in *Drosophila melanogaster* (a fruit fly), removal and overexpression of cryptochromes, respectively, suppressed and increased magnetic field sensitivity of their circadian period by exposure to blue light.[22] Birds on the other hand, for whom successful wintering and homing migrations – sometimes across oceans – are vital, require a precise navigation sense.

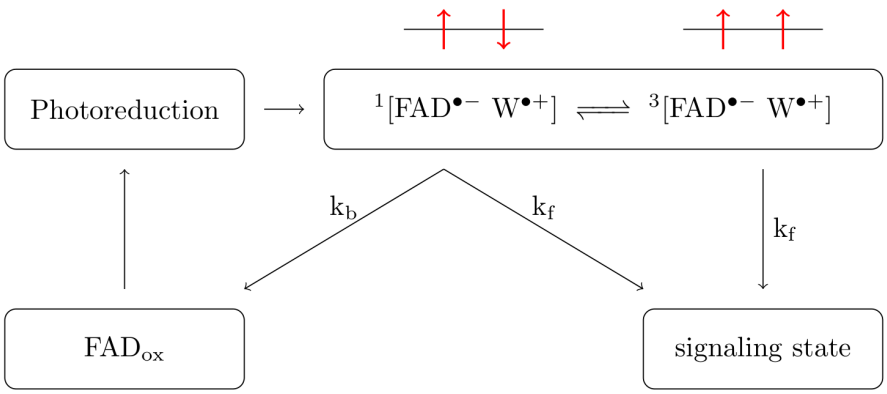

Figure 1.2: Schematic representation of the RPM. Red arrows denote radical spin states, with an upward arrow corresponding to spin-up and a downward arrow to spin-down. The antiparallel configuration therefore symbolises a singlet configuration of the radical pair, and the parallel a triplet.

Mechanism: The mechanism proposed for explaining magnetosensitivity in cryptochromes is the radical pair mechanism (RPM), schematised in Figure 1.2. A radical is a molecule with an unpaired electron, which by virtue of its uncompensated spin angular momentum possesses a magnetic moment. The fully oxidised FAD, initially a closed-shell molecule (even number of electrons, all paired) absorbs light at a wavelength below 500 nm, which promotes a valence electron to a higher, virtual orbital. The rapid timescale of the electronic motion prevents spin-flip from occurring, which results in the excited FAD to remain in the initial spin state – *i.e.* singlet.[18]

An adjacent residue, here taken to be a tryptophan (Trp), subsequently donates an electron to the FAD, thereby leaving one electron with uncompensated spin on the FAD and one on the tryptophan, thereby forming a correlated radical pair.

Both radicals have different chemical environments, in particular with respect to nearby ^{1}H and ^{14}N atoms, which have a non-zero nuclear angular momentum, conferring them a magnetic dipole moment able to interact with that of the radical electrons. The radicals spins precess in the local magnetic field resulting from the coupled nuclei and the external magnetic field. The oscillation frequency is dictated by the energy differences of the spin Hamiltonian, $\omega_{\mathrm{mn}} = \frac{\Delta E_{\mathrm{mn}}}{\hbar}$.
As a consequence, the overall spin state of the radical pair, of spin $\hat{\mathrm{S}} = (\hat{\mathrm{S}}_A \oplus \hat{\mathrm{S}}_B)$ (where A, B refer to the radicals), interconverts coherently between a singlet (total spin angular momentum S = 0) and 3 triplet (S = 1) states, as shown in Figure 1.3. Singlet and triplet states can be represented as particular spin configurations of the radical pair, where the unpaired electrons on radical A and B can be in a "spin-up" (represented ↑, with spin angular momentum $\mathrm{S}_A = 0.5$) or "spin-down" (↓,

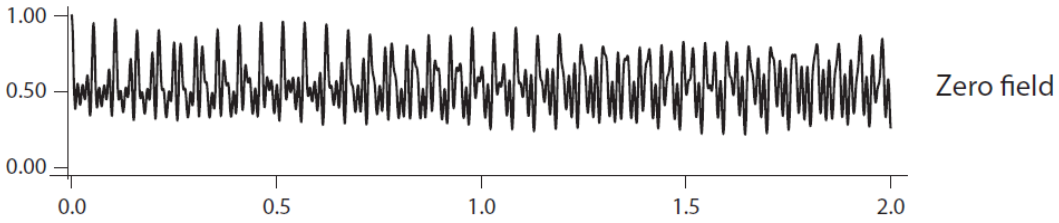

Figure 1.3: Variation of the singlet fraction of a simplified $FAD^{\bullet -}/W^{\bullet +}$ radical pair, in which one electron couples to two nuclear spin of $I = 1$ by an anisotropic hyperfine interaction resembling the dominant hyperfine interactions in FAD, while the other does not. The x-axis is time t, expressed in μs, and the y-axis is the singlet fraction. No external magnetic field is applied to the system. This figure was taken from Hore and Mouritsen's 2016 review.[1]

$S_A = -0.5$) state. The spin state of the radical pair is determined by the total spin angular momentum (quantum number l) and its z component m; and a singlet state is defined as $l = 0$, while a triplet state has $l = 1$. With 2 unpaired electrons, the 4 states accessible to the radical pairs are:

$$|l = 0, m = 0\rangle = \frac{(|\uparrow\downarrow\rangle - |\downarrow\uparrow\rangle)}{\sqrt{2}} \tag{1.1}$$

$$|l = 1, m = 0\rangle = \frac{(|\uparrow\downarrow\rangle + |\downarrow\uparrow\rangle)}{\sqrt{2}} \tag{1.2}$$

$$|1, 1\rangle = |\uparrow\uparrow\rangle \tag{1.3}$$

$$|1, -1\rangle = |\downarrow\downarrow\rangle \tag{1.4}$$

where $\sqrt{2}$ is a normalisation factor for the mixed states involving a quantum superposition.

Spin-state interconversion between the singlet and triplet states, illustrated in Figure 1.3, arise as a consequence of interactions of the unpaired electron spin with their magnetic environment or with the other radical electron. In the former case, 2 main coupling modalities are considered: hyperfine coupling (presented in further details in Section 1.2.2.3), *i.e.* the coupling of an unpaired electron's magnetic moment to neighbouring nuclei with non-zero nuclear magnetic moments (^{1}H and ^{14}N; ^{13}C is neglected due to its very low abundance); and the Zeeman coupling, *i.e.* the interaction between the magnetic moment of an unpaired electron with an applied magnetic field, such as that of the Earth. In the latter case, inter-electron couplings can take the form of electron-electron dipolar (EED) coupling and of the exchange interaction. EED coupling corresponds to the interaction between the magnetic moments of the unpaired electrons, dependent on their respective orientation and on the distance separating them; while the exchange coupling has a more quantum origin and arises from the Pauli exclusion principle, which forbids 2 electrons located in the same orbital to have the same spin and therefore imposes an energy penalty

on $|\uparrow\uparrow\rangle$ and $|\downarrow\downarrow\rangle$ configurations, again as a function of distance. The regularity, or periodicity, of singlet-triplet interconversion can be perturbed by the modulation of these interactions, *e.g.* via molecular motions that modulate the strength of hyperfine and inter-electron couplings.

Recombination of both radical electrons to reform the initial, fully-oxidised FAD is possible but conserves the spin angular momentum; as a consequence, only the singlet state is able to regenerate FAD, as the exchange penalty for crossing spins from a triplet state would be too high. The other, competing reaction, which proceeds at a similar rate constant k_f, is the formation of the signaling state. This reaction involves no recombination of radicals, and can therefore occur indiscriminately from the singlet or triplet pair. For this reason, k_f^{-1} is often referred to as the **lifetime** of the radical pair. This signalling state is a compound necessary to the generation and transmission of magnetic information to the bird's brain. Its yield increases with the fraction of triplet-state RP, since radical recombination can only proceed from the singlet population, as discussed above.

Simulating the operation of a RPM-based compass, using numerical abstractions of the chemical species listed in Figure 1.2, requires providing values for the k_b and k_f rate constants. While these values would ideally be tailored to the exact chemical system under consideration, estimating an electron transfer rate is extremely tricky and standard values are often used. Results from spin dynamics simulations, quantifying the degree of magnetosensitivity of a given arrangement of a given set of radicals, will be reported at various points throughout the thesis; and the rate constants used in the simulation will be provided should the reader wished to reproduce the results.

k_f^{-1}, the radical lifetime, is thought to lie between 1 and 10 μs. Spin dynamics simulations are usually run with these two values in order to obtain a best- and worst-case estimate of the magnetosensitivity of a given system. The lower bound of $k_f^{-1} = 1\,\mu$s is based on the theoretical consideration that a radical pair needs to survive for at least the length of one Larmor precession period, *i.e.* $\simeq 700$ ns, for a radical electron to have its spin dynamics significantly affected by the geomagnetic field.[1] The higher-bound estimate of $k_f^{-1} = 1\,\mu$s, on the other hand, corresponds to the estimated lifetime of spin coherence for the flavin; beyond 10 μs, spin relaxation in the flavin is expected to massively decrease the magnetosensitivity of the radical pair or triad.[47] In some cases, particularly in Chapter 4, a lifetime of $k_f^{-1} = 3\,\mu$s is used, consistent with experimental findings on migratory songbirds.[48]

The back-electron transfer (BET), or electron recombination, is the spin-selective step which can only proceed from a singlet configuration and which reforms the diamagnetic ground-state, with a fully oxidised flavin FAD_{ox} and a neutral tryptophan W. A common assumption for its rate is $k_b = k_f$.

The Low-Field Effect: The low-field effect (LFE)[49] is the increased population of a triplet product in a coherently interconverting radical pair in the presence of weak magnetic fields, compared to that in zero field; it is distinctively different from the magnetic field effects that occur in "strong" applied magnetic fields (by which is meant: much stronger than the split between hyperfine energy levels), which split the triplet sublevels by the Zeeman interaction to the extent that the triplet states become, in part, energetically inaccessible, thereby impeding the generation of triplet products. Weak fields, on the other hand, split previously degenerate hyperfine states, providing new oscillation frequencies through which the triplet and singlet state coherently interconvert.

$$\begin{aligned}\Phi_S &= k\int_0^\infty \langle \hat{P}^S\rangle(t)e^{-kt}\mathrm{d}t \\ &= \frac{1}{\mathrm{M}}\sum_{\mathrm{m}=1}^{4\mathrm{M}}\sum_{\mathrm{n}=1}^{4\mathrm{M}}\left|P^S_{\mathrm{mn}}\right|^2 f(\omega_{\mathrm{mn}}) \\ &= \frac{1}{\mathrm{M}}\sum_{\mathrm{m}=1}^{4\mathrm{M}}\sum_{\mathrm{n}=1}^{4\mathrm{M}}\left|P^S_{\mathrm{mn}}\right|^2 \frac{k^2}{k^2+\omega^2_{\mathrm{mn}}}\end{aligned} \tag{1.5}$$

For a simple model (that neglects decoherence processes and assumes that the singlet and triplet state are depopulated at the same rate, k), the singlet yield is given by Eq. 1.5,[18] which is derived in more details in Timmel's 1998 paper.[49] The singlet yield Φ_S, which is the fraction of radical pairs that have reacted via the singlet recombination channel for $t \to \infty$, is reduced by the emergence of new oscillation frequencies ω_{mn}, where $|m\rangle$, $|n\rangle$ are spin eigenstates of the Hamiltonian $\hat{H}$. $\hat{P}^S$ is the singlet projection operator, which here is also proportional to the initial ($t = 0$) density operator by a factor of 1/M, where M is the number of nuclear spin configurations. The matrix elements of the singlet projector in the eigenbasis of H are denoted $P^S_{\mathrm{mn}} = \langle m|\hat{P}^S|n\rangle$, and k is the rate of product formation, taken to be identical for both the singlet and triplet states. Although this model neglects spin relaxation, the anisotropy of hyperfine interactions and the possibility for a spin-selective radical recombination reaction, it provides insight into the emergence of the LFE.

Another way of visualising the Low-Field Effect[49] is by considering that the Zeeman precession of radical electron spins induced by the application of an external magnetic field adds another axis of rotation for the electron spin angular momentum, making it explore a larger section of spin space in its oscillations. Since only one configuration yields a singlet spin state, but three correspond to the triplet, the population of the latter state is expected to register a stronger increase.

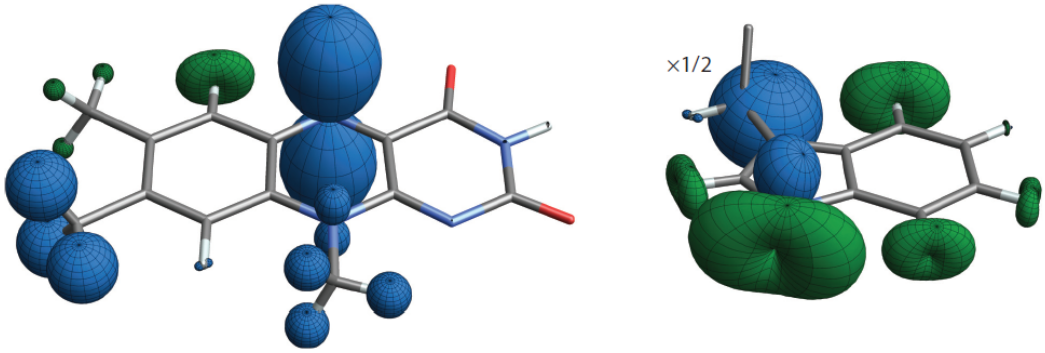

Figure 1.4: Representation of the hyperfine interactions between a radical electron and, respectively, a truncated $FAD^{\bullet -}$ (left) and a $Trp^{\bullet +}$ (right). The distance between the centre and the surface is proportional to the strength of the hyperfine interaction in that direction. The interaction takes positive values for a blue surface, and negative values for a green surface. These tensors were calculated in Gaussian 03 using DFT. This figure was taken from Hore and Mouritsen's 2016 review.[1]

Because of the anisotropy of hyperfine interactions[1,18] (shown in Figure 1.4), the extent and number of spin states degeneracy lifting depends on the direction of the applied magnetic field. This could thus form the basis of a magnetic compass; however, some requirements must be satisfied.

Constraints on the operation of the compass: Radical spin recombination and product formation reactions should be in competition: the back electron transfer (BET) reaction should occur on a timescale comparable to the formation of the signaling state. Otherwise, without a spin-selective step, the singlet fraction could not be depleted and the concentration of the signaling state could therefore not depend on the external magnetic field. This requirement of competition imposes a distance constraint: for recombination to be sufficiently fast, radicals should be separated by about 1.5 nm.[50] This estimation of the distance is computed using Marcus theory, *i.e.* assuming a direct electron transfer, for a radical pair lifetime of 1 μs.

Although the inter-radical distance constraint of 1.5 nm is satisfied for FAD-Trp RPs in *A. thaliana* cryptochromes, it is not the case for avian cryptochromes, which exhibit a tetrad, instead of a triad, of tryptophan residues.[51,52] The end-to-end distance of the electron transfer chain for a pigeon cryptochrome is of 1.96 nm, therefore slowing down the back electron transfer. Additionally, the increasing solvent exposure of Trp residues as one goes along the chain energetically disfavours the back reaction, because of the associated increase in solvent reorganisation energy. On the other hand, a recent study emitted the possibility of fast and reversible electron transfer between the third and fourth (terminal) Trp residue in an avian cryptochrome, which could allow to keep recombination efficient.[53] Besides, the rate

constant is also dependent on the mechanism of electron transfer; while a "hopping" mechanism has traditionally been proposed to evaluate ET rates, Cailliez and colleagues also proposed that a "flickering resonance" mechanism could be involved,[52] whereby an electron tunnels through multiple energetically degenerate Trp.[54]

Another key requirement is that spin-spin interactions should be minimised so that the radical spins states are largely dictated by the hyperfine structure, which would in turn allow the Zeeman splitting from the geomagnetic fields to make a significant impact on the spin states. Hyperfine coupling being the main predictors of RP spin states energetic separation implies that the dipolar and exchange interactions should have largely decayed at their separation distance, which suggests the inter-radical separation should be as large as possible. It was suggested that a compensation of exchange and dipolar interactions could ease this constraint at shorter distances of $1.5-2.0\,\mathrm{nm}$,[55] but recent research find the possibility of exchange-EED cancellation unlikely:[25] indeed, a systematic modulation of the inter-radical exchange coupling over a wide (-50 to $+50\,\mathrm{MHz}$) range of intensities, including those prescribed in Ref 55 to cancel out EED coupling, fails to compensate the quenching effect of EED on MFEs. This same conclusion was reached for multiple radical pairs identities and configurations. Besides, experimentally determined exchange coupling values[56] are too small to reach the cancellation conditions.

A crucial condition is that the radical pair lifetime must be long enough for the external magnetic field to affect its spin dynamics; considering an Earth-strength magnetic field $\vec{B}_0$ of strength $50\,\mu\mathrm{T}$ inducing a Zeeman spin precession of the electron spins of $1.4\,\mathrm{MHz}$ in radical electrons, a full period takes $700\,\mathrm{ns}$ to complete.[1] This unique value of $B_0 = 50\,\mu\mathrm{T}$, roughly corresponding to the geomagnetic field strength over most of North America and Europe, is used – throughout this thesis and in most of the literature – for convenience; over the globe, B_0 can range from 0.22 to $0.67\,\mu\mathrm{T}$, thereby modulating the Larmor precession period between 0.616 and $1.876\,\mathrm{MHz}$. In the simplistic picture introduced before, this additional motion of the radical electron spins, around the axis of the incident magnetic field, make them adopt formerly unexplored orientations, which in turn gives rise to new spin pair configurations, and therefore affects the interconversion pattern shown in Figure 1.5. However, for this change to have a significant effect on the signaling state yield, it should ideally persist for a full Larmor precession period. This implies that spin correlation, the coherent interconversion between a singlet and a triplet spin pair state, should be maintained for at least such a length of time.

Spin relaxation,[16,57] the randomisation of individual spin motion to the extent that all periodicity in the oscillation of the overall spin pair state is lost, is typically brought about by the modulation of hyperfine interactions felt by the radical elec-

tron, because of the thermal motions of the molecule hosting it. For decoherence not to occur quickly, these motions should ideally be fast ($10^9\,s^{-1}$) and of low amplitude.[50] Spin entanglement, which introduces a correlation of purely quantum origin in the motion of both radical electron spins formed in the singlet state, has been suggested to enhance the compass sense if it is sustained long enough. This possibility was however found to be unlikely to enhance the compass because even in an idealised system of 2 electron spins, where one is coupled to a single nuclear spin, entanglement decays fairly rapidly;[58,59] and this decay is accelerated with every nuclear spin added to the system, *i.e.* is expected to be fast for realistic radicals. Besides, MFEs have been reported, both experimentally[60] and computationally,[61] for radical pairs or triads formed in an initially uncorrelated state, thereby precluding any involvement of entanglement.

Limits of the flavin-tryptophan radical pair mechanism: While the Radical Pair Mechanism is magnetosensitive in principle, the question remains whether it can still provide sufficient directional sensitivity, in the form of sizable singlet yield anisotropy, in the "warm, wet, and noisy" conditions of a biological medium. One major factor to take into account is the onset of spin relaxation, *i.e.* the extinction of spin coherences *via*, for instance, librational averaging of the hyperfine interactions. Since it is precisely the anisotropic nature of these hyperfine couplings which imparts a dependence of the spin state of each radical on the orientation of the external magnetic field, a shift towards a more isotropic hyperfine structure via the action of thermal motions would result in a much less directionally sensitive system. A molecular dynamics (MD) study on atCry1,[47] a plant (*Arabidopsis thaliana*) cryptochrome, found that taking into account thermal librations have a quenching effect on the singlet yield of a [$FAD^{\bullet -}$ $Trp^{\bullet +}$], rendering the spin dynamics of this radical pair realistically quite insensitive to an Earth-strength magnetic field. These observations are however made on a plant cryptochrome for which a magnetic compass of high angular precision provides no survival or fertility advantage, and therefore has likely never been under evolutionary pressure. On the other hand, bird cryptochromes – and perhaps even only *migratory* birds cryptochromes –[53] may have evolved a more rigid chemical environment for the magnetosensitive radicals, better able to preserve coherence.

Another difficulty for the [$FAD^{\bullet -}$ $Trp^{\bullet +}$] radical pair model is its large number of hyperfine interactions without common symmetry, which tend to quench MFEs as more nuclei are included.[62] Although realised on a Drosophila cryptochrome, this study found the Trp radical anion to be unable to realise simultaneously a sensitive and a precise compass;[63] the two properties were anti-correlated in the range of orientations available to this particular protein. On the other hand, the

tyrosine radical was found to allow for a simultaneous optimisation of sensitivity and precision, and the more favourable symmetry of its hyperfine structure made it outperform the tryptophan radical for most orientations. We should still keep in mind the caveat that the flavin-tryptophan and flavin-tyrosine relative orientations sampled in this study are taken from a Drosophila cryptochrome, which differs structurally from a bird cryptochrome such as *cl*Cry4, and possibly even more so from a migratory bird cryptochrome such as *er*Cry4.

Additionally, behavioural studies[11,64,65] suggest the magnetosensitive step might actually be the reoxidation of $FADH^-$ to $FADH^\bullet$. Particularly relevant to the case of avian magnetoreception is the experiment in Ref. 11, where birds pre-exposed to white light were able to orient under green light (560 nm), despite the fact that FAD cannot be excited (to eventually form $FAD^{\bullet-}$) above 500 nm. This result points to a magnetosensitive radical pair of the form $[FADH^\bullet\ B^\bullet]$, where B could be $O_2^{\bullet-}$, $Asc^{\bullet+}$, or a yet unknown radical species generated along the reaction. Other behavioural experiments, while also pointing to the dark-state cryptochrome reoxidation as the magnetosensitive step, are performed on plant (*Arabidopsis thaliana*) cryptochromes and with magnetic field intensities exceeding the Earth's by a factor of 10,[64,65] thereby revealing the magnetosensitivity of dark-state cryptochrome, but making any comparison with the bird cryptochrome within geomagnetic field strengths unclear. A common point to all these studies is that they implicate cryptochrome 1A (Cry1A) as the locus for the magnetosensitive reaction, instead of the more commonly considered Cry4. Cry1A involvement is supported by immunohistochemical studies suggesting the formation of dark-state reactants in chicken retinae,[66,67] although a later study could not reproduce these results.[68] The relevance of Cry1A for magnetoreception is also put into doubt by the fact that vertebrate Cry1A proteins do not strongly bind FAD *in vitro*.[69,70]

An important feature of the avian compass is its remarkable angular precision, which is better than 5°. Hiscock *et al*.[3] remarked that extraordinarily long coherence times, of the order of 100 μs, led to the emergence of a spike in the directional dependence of the signaling state yield; such a feature, arising from avoided crossings of spin states of different singlet character, could deliver very precise directional information. Interestingly, the spike vanishes if the non-axial elements of the hyperfine tensor are zero. Since only one anisotropic hyperfine interaction in each radical is sufficient for the emergence of the spike – after long coherence times –, then one might argue that only ascorbic acid could be considered as an alternative radical pair, as superoxide has no nuclear magnetic dipole moment and therefore can have no hyperfine interactions with electrons – at least if the spike is considered crucial. Unfortunately, it is unclear how such long spin coherence times could be achieved, especially in a biological environment.

A significant signal-to-noise ratio should also be achieved for the magnetic information to be detected; this requires the magnetosensitive molecules to be somewhat ordered and immobilised so the signal is not rotationally averaged. Polarisation of incident light, as it can occur in the atmosphere, could be relevant in breaking rotational symmetry as well.[71]
The predicted singlet yield anisotropy of a realistic [$FAD^{\bullet -}$ $Trp^{\bullet +}$] radical pair is small, even if disregarding detrimental effects such as spin relaxation and electron-electron dipolar coupling: about 0.1%.[47,72] A [$FAD^{\bullet -}$ $O_2{}^{\bullet -}$] radical pair, on the other hand, is expected to yield a more promising 14.6% singlet yield anisotropy – if it was not undergoing very fast spin relaxation (the rapid rotation of superoxides couples with its spin and relaxes it in the order of 1 ns).[1] The [$FADH^{\bullet}$ $O_2{}^{\bullet -}$] RP, formed from the dark reoxidation of $FADH^-$, registers a slightly decreased anisotropy of 11.6%. However, all these values are calculated in the absence of spin relaxation and of inter-radical interactions. Without knowledge of the amplification mechanism, it is difficult to estimate what value of singlet yield anisotropy would be sufficient to overcome the noise created by a biological environment. Longer acquisition times could be envisaged as a way to clean up the signal,[73] as well as heading direction averaging over all members of a migrating flock.[74]

Another issue is the photon flux, which ought to be sufficient even at night to activate the magnetosensors despite the competition for absorption with vision-related proteins, such as opsins. There is experimental evidence that night-migratory songbirds are able to navigate on moonless nights, provided the stars are visible.[75] An Information Theory approach[76] to determining the minimum amount of photons necessary to achieve a sub-5° angular precision, even making generous assumptions with respect to the efficiency of the transduction pathway and the late onset of decoherence, found the $FAD^{\bullet -}/Trp^{\bullet +}$ radical pair to be, at equal lifetimes, less sensitive than $FAD^{\bullet -}/O_2^{\bullet -}$ or $FAD^{\bullet -}/Asc^{\bullet -}$ radical pairs, due to the numerous large and nearly isotropic hyperfine couplings present on $Trp^{\bullet +}$. Crucially, this paper finds the current incarnation of the flavin-tryptophan radical pair model of magnetoreception unlikely to permit navigation on moonless nights, and estimates an increase in sensitivity of about 10^3 to be necessary for it to function. Further amplifications pathways, either as those suggested at the end of the previous paragraph or relying on the addition of a third radical, are suggested. A detailed exposition of the approach, which relies on evaluating the uncertainty on the singlet yield as a function of the number of independent cryptochrome reaction cycles, *i.e.* of the number of reaction-initiating incident photons, can be found in Ref 76.

Although proof-of-principle for the radical pair mechanism was achieved by

Maeda *et al.*[77] for a porphyrin-carotenoid-fullerene system, for which a singlet yield anisotropy of about 1.5% was recorded by varying the direction of an incident, Earth-strength static magnetic field, this success does not carry over to the avian compass, as these experiments require low temperatures and no chemical environment to resist spin relaxation.

Building on the notion that the current model of $FAD^{\bullet -}/Trp^{\bullet +}$-based magnetoreception does not seem to provide sufficient singlet yield anisotropy for night-migration, we dedicate our work throughout this thesis to exploring the feasibility of a system which, all other things being equal, shows in theory an inherent enhanced sensitivity to the Earth's magnetic field: the scavenging mechanism, with a $FADH^{\bullet}/O_2^{\bullet -}/Y^{\bullet}$ radical triad. There are, naturally, a number of caveats to be considered with the scavenging mechanism as outlined in Figures 1.1 and 1.5, and we are not presenting it as a silver bullet to solve all of the inadequacies of the current $FAD^{\bullet -}/Trp^{\bullet +}$ RP model. At the moment, this performance advantage comes at the cost of increased complexity, increased resource needs (2 photons instead of 1), and a largely speculative scheme for generating its reactants: we are not certain that a sufficiently stable radical tyrosine could be formed in the cryptochrome, nor do we know whether molecular oxygen could be suitably trapped to oxidise $FADH^{-}$, and finally, the proposed radical triad has not been observed *in vitro*. These are questions which will need to be answered for the scavenging hypothesis to gain credibility; in the meantime, this thesis seeks to evaluate its viability assuming that the reactants can be formed.

Besides, there exist a surprising number of magnetosensitive biological processes which could realistically involve a $FADH^{\bullet}/O_2^{\bullet -}$ radical pair, as the review in Ref. 78 shows, and research done within the context of avian magnetoreception (particularly regarding superoxide trapping and delaying spin relaxation) could be transferable to these other areas.

Finally, we do acknowledge that the current theoretical model of $FAD^{\bullet -}/Trp^{\bullet +}$ RP, or of any other cryptochrome-bound radical pairs or triads, is not perfectly representative of migratory cryptochrome, as the current best, XRD-resolved cryptochrome structure is a pigeon cryptochrome 4, *i.e.* a non-migratory species. *In vitro* results indicate this could be significant, and that migratory cryptochrome could be much more sensitive,[53] presumably due to evolutionary pressure; however, these results do not yet exist for Earth-strength magnetic field.

1.1.3 The scavenging mechanism

Consider the addition of a third, paramagnetic radical, which reoxidates a fragment of the radical pair according to the reaction scheme outlined in Figure 1.5.

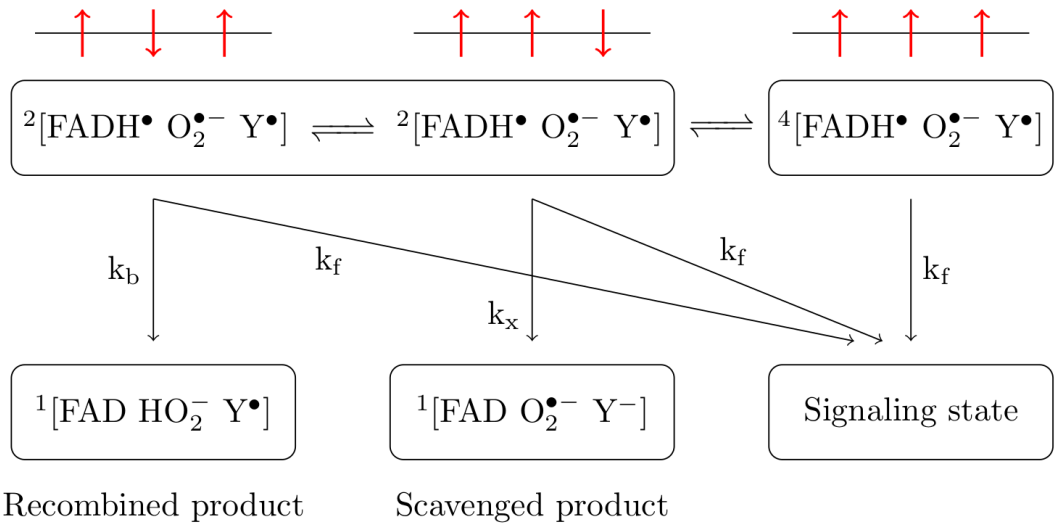

Figure 1.5: Schematic representation of a scavenged RPM involving FADH$^\bullet$, a triplet oxygen reduced to $O_2^{\bullet-}$, and a tyrosine scavenger Y$^\bullet$. Again, red arrows represent the spin state of the corresponding radical.

Here, the signalling state is assumed to proceed from a conserved [A$^\bullet$ - B$^\bullet$ - C$^\bullet$] radical triad. While the precise identity of each radical is not known, a typical triad considered throughout this work is [FADH$^\bullet$ - $O_2^{\bullet-}$ - Tyr$^{\bullet+}$], where the flavin and superoxide ($O_2^{\bullet-}$) constitute the primary radical pair, scavenged by a radical tyrosine. The scavenger C, which reacts with radicals in a spin-selective manner, affects the singlet/triplet (S/T) interconversion dynamics in the following manner:

- If C is a singlet ($S = 0$), there are no spin restrictions on the reaction, all radicals react with C and there are no radical pairs left at $t \to \infty$.

- If C is a doublet ($S = 1/2$), then at $t \to \infty$, 3/4 of the [A$^\bullet$ - B$^\bullet$] pairs survives, and 3/4 of these are singlets.

- If C is a triplet ($S = 1$), then at $t \to \infty$, 2/3 of the [A$^\bullet$ - B$^\bullet$] pairs survives, and 2/3 of these are singlets.

The derivation of these results is presented in detail by Kattnig *et al.* in Ref. 29.

For a realistic [FAD$^{\bullet-}$ Trp$^{\bullet+}$] radical pair, scavenged by a $S = 1/2$ molecule without hyperfine interactions: assuming a scavenging rate constant of $k_c = 24\,\mu s^{-1}$(*i.e.* the optimal electron transfer rate, giving rise to the maximal achievable relative anisotropy Γ_S for this specific system), the relative anisotropy is of 431% when

radical recombination in the primary pair is impossible and 338 % when recombination is twice as fast as product formation. Additionally, the very high anisotropies calculated for scavenging reactions are fairly independent of the number of hyperfine interactions on the radicals.

The scavenging mechanism also provides resistance to spin relaxation for one of the radicals,[29] which makes credible the [$FADH^{\bullet}$ $O_2{}^{\bullet -}$] RP. For this specific triad, scavenging must be carried out by a compound with a relaxation time equal or superior to that of the $FADH^{\bullet}$; this condition forbids superoxide as a scavenger radical, but tryptophan[79] or tyrosine could perfectly work. There is precisely in pigeon cryptochrome a tyrosine residue, located close to the Trp tetrad, which could serve the role of a scavenger. The fact that very long lifetimes have been reported for tyrosine radicals[32,80,81] make it especially suited for such a role.

Another interesting feature of the scavenged $FADH^{\bullet}/O_2^{\bullet -}$system is that, in the case where recombination is non-zero, relaxation of one of the radicals would actually enhance the signalling product yield anisotropy.[82] Since, when the magnetic field is oriented parallel to the symmetry axis of the N-based hyperfine interaction (taken to be the z axis in a FAD-centred basis), $S \leftrightarrow T_{\pm}$ is forbidden by symmetry, but the scavenging reaction creates RPs in these T states, which can't revert back to S and therefore can only generate the signalling state. $S \leftrightarrow T_0$ is however still possible. On the other hand, if $B^{\bullet +}$, the counter-radical to FAD, is able to relax, then $T_{\pm}$ states get populated by the random motion of the relaxed spin, increasing total triplet population and therefore the signalling state concentration.

And finally, scavenging reactions have the added benefit of presenting sharp anisotropy spikes when coherence is sustained for a long time, much stronger than those achieved in the conventional RPM,[3] which could explain the precision of the avian compass.

The scavenging mechanism hypothesis presents the advantage of increasing the sensitivity of the radical pair to an external magnetic field, thereby reducing the number of reaction cycles necessary for magnetic information to be detected; of extending the model to accommodate fast decoherence in one radical without loss of sensitivity; of freeing the system of a distance constraint by abolishing the need for recombination as the spin-selective step, allowing radicals to be located far enough from one another for dipolar interactions to become negligible; and of delivering sufficiently accurate directional information to account for the high angular precision of the avian compass. Although very promising, this mechanism has not been located in the protein, and molecular dynamics simulations to evaluate the

position and motions of the $O_2^{\bullet -}$ radical with respect to the flavin could be useful. The identity of the scavenger molecule remains also to be elucidated. There is a number of tryptophan and tyrosine residues suitably located in the vicinity of the FAD which could serve this purpose.

1.1.4 Dipolarly coupled three-spin systems

An alternative pathway for the emergence of magnetic field effects is through dipolar coupling of three-spin systems.[26]
Consider again Eq. 1.5 for the singlet product yield given earlier: the spin states of the full system (of the form $\left|S^{(1,2)}\pm\right\rangle$), where the $\pm$ is the spin of the 3$^{\text{rd}}$ radical) are not eigenstates of the spin Hamiltonian. Because the dipolar interactions are no longer symmetrical for 3 spins, then similarly to the hyperfine-driven case, the application of an external magnetic field stabilises some states and destabilise others, which in turn impacts coupling matrix elements P^S_{mn} and ω_{mn}, giving rise to MFEs.

Non-linear spin triads, which are geometries relevant to a biological system subject to thermally-induced stochastic structural fluctuations, exhibit singlet yield anisotropies as high as 21.5% for geometries where radicals are up to 4 nm apart, which suggests the emergence of magnetic field effects is not dependent on the unlikely event of 3-spin encounter; reducing the inter-radical distance to 0.75 nm can even generate anisotropies superior to 100%. Most importantly, directional sensitivity to Earth-strength – and lower – magnetic fields is possible. The applied field here can give rise to spikes in the MFE profile, the position and width of which can be tuned by the exchange interaction to even give rise to MFEs at magnetic fields smaller than the Earth's. These spikes remain significant even for microsecond lifetimes, which makes them applicable to a biological compass.

The concept of EED-induced MFE are generalisable to a N-spin system, provided the SU(2) symmetry between dipolar interaction remains broken. Research is currently being done on the feasibility of such a compass in a bird cryptochrome.[26,83]

1.2 Methods

While some mechanistic inference can be made from behavioural studies on live birds, this method has limitations; indeed, the inner workings of the previously proposed radical compass, as it is activated in a bird's retina during an orientation event, cannot currently be probed experimentally. The inscrutability of a complex

biological system forces us to resort to theoretical methods, and the scale of the problem requires us to select inherently approximate methods; approximate in the fact that some uncertainty is introduced both in the modeling of the system under investigation, and in the representation of the physical forces and processes acting on it. Furthermore, due to the multiscale nature of the investigation reported in this thesis – we propose to reproduce the structural evolution of a protein over microsecond timescales, the electronic structure of a molecule, and the evolution of a 2- or 3-spin system over microseconds – we needed to use and combine multiple simulation methods.

1.2.1 Molecular Dynamics

1.2.1.1 Theory

Molecular Dynamics, or MD, is a classical simulation method based on solving Newton's equations of motion. The evolution of a system as obtained using MD is represented as a *trajectory*, as each step of the simulation – each *microstate* – is generated as a result of the propagation in time of the system from an initial state. In thermodynamical terms, a microstate is a specific system configuration accessible within a *macrostate*, defined by thermodynamical quantities such as temperature (T), pressure (p), internal energy (U), etc... A thermodynamical *ensemble* is defined by which of these quantities are held constant; for instance, in the canonical ensemble, or NVT ensemble, the number N of particles, the system volume V and its temperature T are left fixed, while their conjugate variables μ (chemical potential), p (pressure) and S (entropy) are allowed to fluctuate. A macrostate within the NVT thermodynamical ensemble is defined by a specific set of N, V, and T values – *e.g.* $N = 10^3$ atoms, $V = 10^4\,\text{Å}^3$ and $T = 298\,\text{K}$ – ; and any realisation of the molecular system which satisfies these constraints is a microstate.
All "production" MD simulations reported in this thesis, *i.e.* all trajectories of a solvated cryptochrome within a biologically plausible salt concentration, are carried out in the NVT ensemble. This is standard practice for simulations mimicking *in vivo* conditions.

For each microstate, the temperature T and pressure p are computed in the following way:

$$\langle \frac{1}{2} m v^2 \rangle = \frac{1}{2} M_f k_b T \tag{1.6}$$

$$pV = N k_b T + \frac{1}{3} \langle \sum_{A \neq B}^{N} r_{AB} \cdot F_{AB} \rangle, \tag{1.7}$$

where M_f is the number of degrees of freedom of a system containing N particles (of mass m and velocity v), and F_{AB} the force exerted by particle A on particle B. This force F_{AB} is calculated as follows:

$$\mathbf{F}(\mathbf{R}_A) = -\vec{\nabla} V(\mathbf{R}_A), \tag{1.8}$$

where $V(\mathbf{R}_A)$ is the *potential* felt by A. This potential, which in this formalism is subdivided in various bonded and nonbonded contributions, can be computed using a **force field**, or **FF**.

Propagation: From the potential energy, the acceleration of each particle can then be computed using Newton's second law:

$$-\vec{\nabla} V(\mathbf{R}_A) = \mathbf{F}(\mathbf{R}_A) = m_A \mathbf{a}_A, \tag{1.9}$$

where $\mathbf{a}_A$ is the acceleration of particle A and m_A its mass. The position and velocity of particles at time $t + \Delta t$ are then computed using the velocity Verlet algorithm, which relies on solving the following 2 equations:

$$\begin{aligned} \mathbf{R}_A(t+\Delta t) &= \mathbf{R}_A(t) + \mathbf{v}_A(t)\Delta t + \frac{\mathbf{a}_A(t)}{2}\Delta t^2 \\ \mathbf{v}_A(t+\Delta t) &= \mathbf{v}_A(t) + \frac{\mathbf{a}_A(t+\Delta t) + \mathbf{a}_A(t)}{2}\Delta t \end{aligned} \tag{1.10}$$

Every Δt, a new configuration of the system is generated. Δt is referred to as the *timestep* of the simulation, and must be set short enough to capture the fastest atomic motion of the system. Here, this corresponds to the water hydrogen vibration, which typically occurs with a period of $\sim 10^{-13}$ s; for this reason, a timestep of 2.0×10^{-15} s (2.0 fs) was employed for all MD simulations throughout the thesis.

The methodology outlined above (Velocity Verlet-propagation of particles interacting via a Force Field) is sufficient to correctly describe the evolution of a system within the microcanonical, or NVE, ensemble; however, imposing a constraint on temperature, as is done within the NVT ensemble, requires the use of a thermostat. Temperature control can be achieved through the use of Langevin dynamics, a stochastic alternative to the Newtonian dynamics described above, which allows, through coupling with a phenomenological heat bath, to maintain the target T and to allow for minor fluctuations. In the Langevin formalism, a damping term is added to equation 1.8, which becomes for time t:

$$m_A \mathbf{a}(t) = -\vec{\nabla} V(\mathbf{R}(t)) - \gamma M \mathbf{F}(\mathbf{R}(t)) + \mathbf{G}(t), \tag{1.11}$$

where γ is a damping constant called the collision parameter, and $\mathbf{G}(t)$ a random-force vector statistically governed by:

$$\begin{cases} \langle \mathbf{G}(t) \rangle = 0 \\ \langle \mathbf{G}(t)\mathbf{G}(t')^T \rangle = 2\gamma k_b T M \delta(t-t') \end{cases} \tag{1.12}$$

where δ is the Dirac delta.

The AMBER force field: A force field is a model used to compute the total energy of a given system via a set of potential energy terms, each describing a modality of interatomic interaction, using fitted parameters to better reproduce the respective properties (*e.g.* VdW radius, charge, typical bond length with an *e.g.* hydrogen atom) of each atom in the system. Throughout this thesis, we use one of the most popular and widely validated force fields, the AMBER FF.[84] Other force fields, characterised by different definitions of the energy terms and consequently different associated parameters, exist, such as the popular CHARMM force field.[85] The basic approximations, consistent across popular non-polarisable force-fields, are (a) that electrostatic interactions between atoms are mediated by point charges, and (b) that chemical bonds are approximated as springs, modeling stretching, bending and torsion with harmonic potentials parametrised with a force constant and an equilibrium value. The form of the force field energy terms used here, *i.e.* following the AMBER conventions, is given below:

$$V_{\text{bonds}} = \sum_{\text{bonds}} K_b (b - b_0)^2 \tag{1.13a}$$

$$V_{\text{angles}} = \sum_{\text{angles}} K_\theta (\theta - \theta_0)^2 \tag{1.13b}$$

$$V_{\text{dihedrals}} = \sum_{\text{dihedrals}} K_\varphi (1 + cos(n\phi - \delta)) \tag{1.13c}$$

$$V_{\text{impropers}} = \sum_{\text{impropers}} K_\omega (\omega - \omega_0)^2 \tag{1.13d}$$

$$V_{\text{LJ}} = \sum_{\text{nonbonded}} \varepsilon_{ij} \left[\left(\frac{r_{ij}^{min}}{r_{ij}} \right)^{12} - 2 \left(\frac{r_{ij}^{min}}{r_{ij}} \right)^{6} \right] \tag{1.13e}$$

$$V_{\text{Coulomb}} = \sum_{\text{nonbonded}} \frac{q_i q_j}{4\pi\epsilon_0 r_{ij}}, \tag{1.13f}$$

where K_b, K_θ, and K_ω are harmonic force constants, K_φ an amplitude, n a multiplicity, ϕ a dihedral angle and δ a phase; b, θ and ω are the bond length, angle and improper angle variables, with b_0, θ_0 and ω_0 their equilibrium value. The last two potential energy terms, V_{LJ} and V_{Coulomb}, correspond respectively to the Lennard-Jones term (describing Van der Waals interactions) and to the Coulomb

term (describing electrostatic interactions). These nonbonded interactions terms are also parametrised: r_{ij}^{min} refers to the equilibrium distance between atoms i and j, and ε_{ij} to the potential well depth. q_i refers to the atomic charge of atom i, and $epsilon_0$ is the vacuum permittivity.

Practical details of the MD implementation: In order to reduce computational costs associated with evaluating nonbonded interaction contributions between all possible particle pairs, and given the rapidly decaying nature of these interactions, a "cutoff" distance r_{cut} can be introduced, such that for a pair of particles i and j, $V_{\text{LJ}} = V_{\text{Coulomb}} = 0$ if $r_{ij} \geq r_{\text{cut}}$.

In order to eliminate boundary effects, *i.e.* the nonphysical absence of interactions felt by a particle located close to the edge of the simulation box, *Periodic Boundary Conditions* (PBC) are implemented in all MD simulations carried out in this thesis. PBC conceptually consists in surrounding the simulation box with fictitious identical systems, in all N spatial dimensions where it is defined. Thus, a real molecule right by the edge of the real simulation box interacts with particles in the next, fictitious box, which corresponds to the opposite side of the real simulation box. This method allows to simulate infinite systems, free from the artifacts introduced by boundary effects.

Another advantage is the possibility to use Ewald summation – the method of choice for computing electrostatic interactions in a periodic system –, in which the electrostatic energy term is split into 2 contributions: a short-distance and a long-distance term. The short-distance term is computed over charge pairs in real space, whereas the long-distance contribution is calculated in reciprocal space, where it converges quickly. While the use of Ewald summation, with the constraint of involving a fast Fourier transform, imposes some constraints on the system dimensions and total charge, it also provides a tremendous speedup in the computation of electrostatic interactions.

1.2.1.2 Properties computed from MD simulations

RMSD and RMSF The Root-Mean-Square Deviation of atomic positions, or RMSD, is a tool often used to measure the flexibility of a molecule or protein along a dynamic. It is calculated as

$$\text{RMSD} = \sqrt{\frac{1}{N}\sum_{i=1}^{N}(\vec{r}_i - \vec{r}_i^{\,0})^2}\,, \tag{1.14}$$

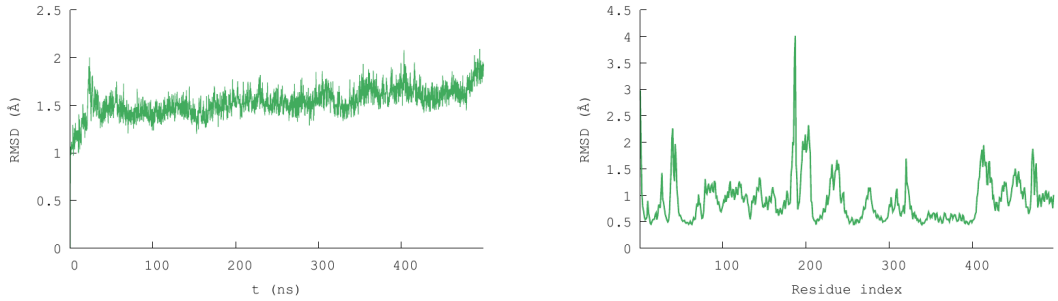

(a) RMSD (b) RMSF

Figure 1.6: (a) RMSD and (b) RMSF of a 497-residue, pigeon cryptochrome 4 (*cl*Cry4) protein along a 500-ns MD simulation.

where N is the total number of atoms and $\hat{r}_i$ the position of atom i, while $\vec{r}_i^{\,0}$ is the *reference* position of atom i. The reference structure of the molecule or protein under investigation is typically its structure at time $t = 0$, *i.e.* its initial conformation; or it can be a preferential conformation, identified through a clustering analysis. Conceptually, the RMSD is a measure of the average distance an atom or group of atoms has moved from its initial position. A stable RMSD denotes a stable dynamic, whereas jumps correspond to large conformational changes in the protein, such as the release of a loop, or the unfolding of an helix or a sheet. The latter class of events, the degradation of the secondary structure, is a process called denaturation which may cause loss of protein functions. Naturally, any insight gained from analysis of a denatured protein is difficult to transfer to the case of an *in-vivo*, active protein. On the other hand, such a process could also be functional.

When considering *e.g.* a molecular dynamics simulation, the RMSD can be plotted as a function of time to (a) estimate the flexibility of the entire structure, and (b) pinpoint in time the instant of a large-scale structural change, which appears as a sudden increase in the RMSD. Consider Figure 1.6 (a): while the protein maintains a fairly stable overall structure throughout most of the dynamics, indicated by a nearly constant RMSD, we note a sudden jump around $t = 25\,\text{ns}$ which denotes a large conformation change, such as the uncoiling of an α-helix.

A complementary information can be provided by the RMSF, or Root-Mean-Square Fluctuations of atomic positions. The RMSF, calculated for atom i as $\sigma_i = \sqrt{\langle(\vec{r}_i - \langle\vec{r}_i\rangle)^2\rangle}$, is typically used to gauge the flexibility or mobility of a substructure across the dynamics. In Figure 1.6 (b), the RMSF for each residue in the protein, averaged over the entire length of the 500-ns simulation, are reported. An elevated RMSF allows to identify which residues ranges in the protein are particularly flexible. Here, a particularly flexible chain of residues can be identified for indices 184 through 187.

Rotational correlation times Spin relaxation, *i.e.* the loss of coherence in the spin dynamics of a radical, is a process to which the $O_2^{\bullet -}$ radical is particularly sensitive. For this small, symmetric diatomic molecule, spin relaxation arises through the Spin-Rotational Interaction, or SRI, whereby the magnetic moment of the spin couples with the rotation axis of the molecule. Since a $O_2^{\bullet -}$ in solution tumbles very quickly, this coupling triggers a very fast randomisation of the spin.

The timescale at which SRI causes spin relaxation can be computed from[86]

$$\frac{1}{\tau_s} = \frac{\overline{\delta g^2}}{9}\frac{1}{\tau_c}, \tag{1.15}$$

where

$$\overline{\delta g^2} = \left(g_\parallel - g_e\right)^2 + 2(g_\perp - g_e)^2 = \sum_{i=1}^{3}(g_{ii} - g_e)^2 \tag{1.16}$$

In this last equation, g is the g-tensor for the radical and $g_e = 2.00232$ is the g-factor for a free electron. While $g_\parallel$ and $g_\perp$ are experimentally determined quantities, we can use g_{ii} with $i \in \{1,2,3\}$ which are eigenvalues of the g-tensor computed *e.g.* using DFT.

τ_c is the rotational correlation time applying to second-order tensorial quantities. It can be computed by integrating the time-correlation function of molecular orientation ("ACF" in Figure 1.7), which essentially tracks how fast memory of the initial orientation of the molecule is lost. This "ACF" (for "auto-correlation") or $C_2(t)$ function is defined as[87]

$$C_2(t) = \langle P_2\left[\vec{u}(0)\cdot\vec{u}(t)\right]\rangle, \tag{1.17}$$

where $P_2(t) = \frac{1}{2}\left(3t^2 - 1\right)$ is the second-order Legendre polynomial and $\vec{u}(t)$ is the molecular orientation at time t. In our investigations of the rotational correlation time of the $O_2^{\bullet -}$ radical, we defined $\vec{u}$ as the O1-O2 interatomic vector. The $C_2(t)$ function quantifies the correlation between $O_2^{\bullet -}$ orientations at different points in time, decaying exponentially to 0 as $O_2^{\bullet -}$ rotates away from its initial orientation.

Integrating $C_2(t)$ yields the characteristic reorientation time τ_2, which is the same as τ_c in Eq. 1.15. Instead of integrating the raw $C_2(t)$ function, we first fit a double exponential function of the form $f(t) = A_0 e^{A_1 \times t} + A_2 e^{A_3 \times t}$. Figure 1.7 shows the decaying $C_2(t)$ (points) and its biexponential fitting (line) for two $O_2^{\bullet -}$ radicals modeled in MD. Note that the two graphs in Figure 1.7 do not share the same units for time: **(a)** is in ps, and **(b)** in 10^2 ps. The reported τ_2 values at the top of the graph, however, are both in ps. The graphs in Figure 1.7 are generated from $O_2^{\bullet -}$ trajectories presented in further details in Chapter 4, and are provided here only to illustrate the behaviour of the $C_2(t)$ function (or "ACF", as named in Figure 1.7) and the fidelity of

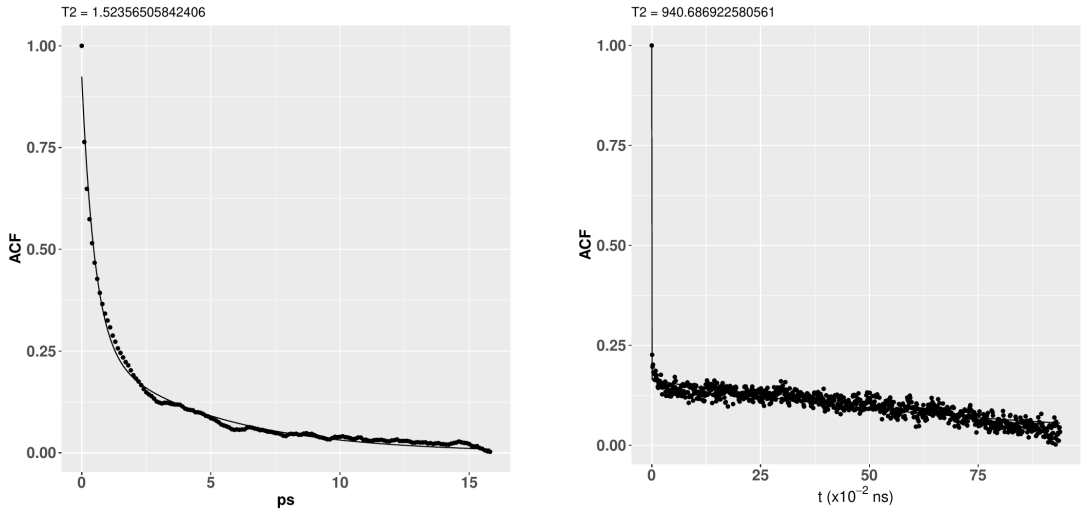

(a) Free $O_2^{\bullet -}$: $\tau_2 = 1.52$ ps (b) $O_2^{\bullet -}$ in site 2: $\tau_2 = 940.69$ ps

Figure 1.7: $C_2(t)$ of **(a)** a free $O_2^{\bullet -}$ in solution and **(b)** a $O_2^{\bullet -}$ radical trapped in a binding site at the surface of *cl*Cry4. Solid lines materialise the biexponential fitting of this data.

biexponential fitting.

1.2.2 QM methods

1.2.2.1 The Schrödinger equation

The Schrödinger equation, formulated in 1924 by Erwin Schrödinger, is the cornerstone of quantum chemistry. While its exact solution is fundamentally out-of-reach for systems containing more than 2 electrons, physicists and computational chemists use it to determine the energy and wavefunction of a system, from which numerous electronic and nuclear properties can be extracted. In its nonrelativistic and time-independent form, the Schrödinger equation reads:

$$\hat{H}\Psi = E\Psi \tag{1.18}$$

where Ψ is the wavefunction containing all the information about the system of interest, and where $\hat{H}$ is the Hamiltonian operator, which allows to extract the total energy of the system. A typical Hamiltonian for a molecular system, given here in atomic units, can take the form:

$$\hat{H} = -\frac{1}{2}\sum_{i}^{N}\nabla_i^2 - \frac{1}{2}\sum_{A}^{M}\frac{\nabla_A^2}{m_A} - \sum_{i,A}^{N,M}\frac{Z_A}{|\mathbf{r}_i - \mathbf{R}_A|} + \sum_{j<i}^{N,N}\frac{1}{|\mathbf{r}_i - \mathbf{r}_j|} + \sum_{B<A}^{M,M}\frac{Z_A Z_B}{|\mathbf{R}_A - \mathbf{R}_B|} \tag{1.19}$$

where i, j refer to the N electrons, A and B the M nuclei, $\nabla^2 = \Delta$ the Laplacian operator (the operator taking the sum of the second partial derivatives with respect

to space variables), m and Z the mass and atomic number of nuclei, and $\mathbf{r}$ and $\mathbf{R}$ the positions of electrons and nuclei, respectively.

Eq. 1.19 can be simplified by taking the Born-Oppenheimer approximation, *i.e.* considering that since nuclei are heavier than electrons, their motions are slower; we can therefore make the approximation that there is no nuclear motions at all on the timescales relevant for electronic processes. This assumption allows to remove all purely nuclear terms in the Hamiltonian, simplifying it to an electronic Hamiltonian of the following form:

$$\hat{H} = -\frac{1}{2}\sum_{i}^{N}\nabla_i^2 - \sum_{i,A}^{N,M}\frac{Z_A}{|\mathbf{r}_i - \mathbf{R}_A|} + \sum_{j<i}^{N,N}\frac{1}{|\mathbf{r}_i - \mathbf{r}_j|} \tag{1.20}$$

Still, for the case of a system containing more than 2 electrons, there is no general analytical solution. We therefore need to resort to approximations.

1.2.2.2 Density Functional Theory (DFT)

Density Functional Theory (DFT) is an alternative method for solving the Schrödinger equation (Eq. 1.18); the electrons in the system are described with an electronic density function $\rho(\mathbf{r})$, which is refined in an iterative manner. Note that DFT is formally exact; however, all its current implementations include one approximated term, for which the general form remains unknown. The basis for DFT is found in the Hohenberg-Kohn theorems:

- **"The ground state density ρ determines the external potential energy V to within a trivial additive constant."**, which implies the electronic energy of the system can be exactly computed from the electronic density ρ.
- **"The ground state density $\rho(\mathbf{r})$ can be determined from the ground state energy functional $E[\rho(\mathbf{r})]$ via the variational principle by variation only of the density."**, by which we know that the procedure to find the electronic density which best describes the ground-state of our system obeys the **variational principle**, *i.e.* the lowest-energy density is the best one.

The computational implementation of DFT used throughout this thesis is based on the Kohn-Sham method – the most common approach to conduct DFT calculations –, in which the real system of interacting electrons is replaced by a fictitious system of independent electrons, which however reproduces the real density. The electronic density is thus described by a set of monoelectronic orbitals:

$$\rho(\mathbf{r}) = \sum_{i}^{\text{occ}} |\,\psi_i(\mathbf{r})\,|^2, \tag{1.21}$$

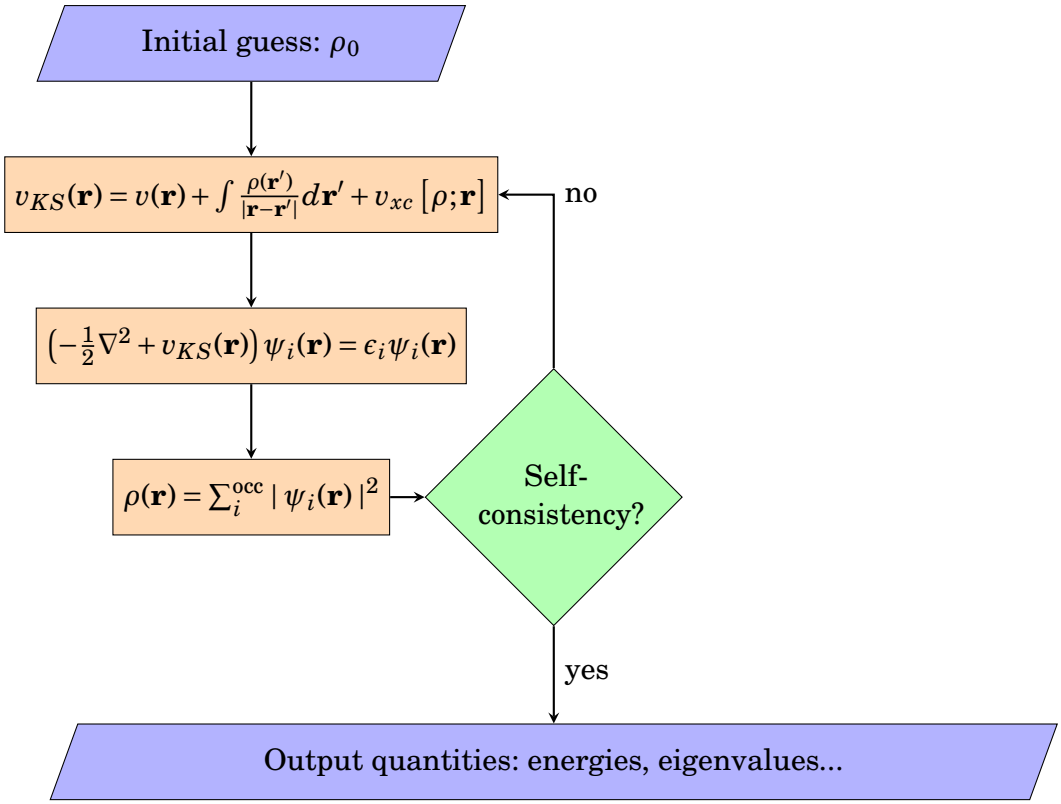

Figure 1.8: Flow diagram of a typical SCF procedure.

where ψ is a Slater determinant formed of the orthonormal Kohn-Sham spin-orbitals ψ_i, which can contain only one electron, according to the Pauli exclusion principle. In this fictitious system, the potential felt by electrons is approximated by an effective potential – the Kohn-Sham potential v_{KS} – which notably includes a correction for the exchange-correlation energy, for which the general analytical expression is unknown.

The energy associated with this set of KS orbitals is then computed using equation 1.22

$$\left(-\frac{1}{2}\nabla^2 + v_{KS}(\mathbf{r})\right)\psi_i(\mathbf{r}) = \epsilon_i \psi_i(\mathbf{r}), \tag{1.22}$$

and the effective potential is computed as follows:

$$v_{KS}(\mathbf{r}) = v(\mathbf{r}) + \int \frac{\rho(\mathbf{r}')}{|\,\mathbf{r}-\mathbf{r}'\,|} d\mathbf{r}' + v_{xc}[\rho;\mathbf{r}], \tag{1.23}$$

where v_{xc} is the exchange-correlation potential. In any case, this quantity depends on the electronic density $\rho(\mathbf{r})$, which itself depends on the orbitals composing $\psi(\mathbf{r})$ through Eq. 1.21, and which in turn depends on v_{KS}. It is therefore necessary to provide an initial guess of the electronic density, which will then be iteratively refined, via the modulation of the Kohn-Sham orbitals coefficients, by cycling through these steps in what is called a Self-Consistent Field, or SCF, cycle (see Fig. 1.8).

Following the second Hohenberg-Kohn theorem, the SCF procedure seeks to *converge* to an electronic density of the lowest energy possible, expected to correspond

to that of the ground-state. Another constraint applied along the SCF procedure is the preservation of the orthonormality of KS orbitals.
This is the general theory behind Kohn-Sham DFT. Its computational implementation, as well as its application to chemical problems such as the determination of the electronic structure – and most importantly, properties – of molecules, requires the reformulation of certain terms. In particular, in the codes used throughout this thesis, Kohn-Sham orbitals are expanded into a set of of nuclei-bound, *i.e. atomic* orbitals $\mu(\mathbf{r})$, such that:

$$\psi_i(\mathbf{r}) = \sum_{\mu} c_{\mu i}\mu(\mathbf{r}) \tag{1.24}$$

These atomic orbitals are themselves built from a linear combination of Gaussian primitive functions $\mu(\mathbf{r})$, and can be tailored to reproduce the various symmetries of orbitals s, p, d, etc... commonly used in physical chemistry. The Kohn-Sham orbital ψ_i containing electron i, being a linear combination of atom-centred *atomic* orbitals μ, can be thought of as a Kohn-Sham *molecular* orbital.

It follows from this expansion that Eq. 1.21 can be rewritten in the following manner:

$$\rho(\mathbf{r}) = \sum_{i}^{N} \left|\psi_i(\mathbf{r})\right|^2 = \sum_{\mu,\nu}\left(2\sum_{i}^{\text{occ}} c_{\mu i}c_{\nu i}\right)\mu(\mathbf{r})\nu(\mathbf{r}) = \sum_{\mu,\nu} P_{\mu,\nu}\mu(\mathbf{r})\nu(\mathbf{r}) \tag{1.25}$$

where μ,ν are atomic orbitals and P is the density matrix, computed from the products of coefficients of each basis function in the Kohn-Sham orbitals, and N is the number of occupied Kohn-Sham orbitals.

The set of atomic orbitals from which Kohn-Sham orbitals are formed is called a **basis set**, and we can already intuitively guess that the richer this basis set, the better the electron density can reproduce reality. A larger and more symmetrically diverse basis set however also implies that the mathematical form of these molecular orbitals becomes heavier, thereby incurring an additional computational cost on every operation performed onto them. The choice of the basis set for a DFT calculation therefore typically results from a trade-off between the desired accuracy and the available computational resources.

The expression for the total energy as a function of the electronic density can be rewritten, in the density matrix formalism, as follows:

$$E = \sum_{\mu,\nu} P_{\mu\nu}H_{\mu\nu} + \frac{1}{2}\sum_{\mu,\nu}\sum_{\sigma,\tau} P_{\mu\nu}P_{\sigma\tau}\langle\mu\nu\|\sigma\tau\rangle + E_{\text{xc}}\left[\rho\right] \tag{1.26}$$

where:

$$H_{\mu\nu} = \langle\mu| - \frac{1}{2}\nabla^2|\nu\rangle - \sum_{C}^{\text{Atoms}} \langle\mu|\frac{Z_C}{|\,\mathbf{r}-\mathbf{C}\,|}|\nu\rangle, \text{ and}$$
$$\langle\mu\nu\|\sigma\tau\rangle \equiv \int\int \frac{\mu(\mathbf{r})\nu(\mathbf{r})\sigma(\mathbf{r}')\tau(\mathbf{r}')}{|\mathbf{r}-\mathbf{r}'|} d\mathbf{r}d\mathbf{r}' \tag{1.27}$$

in which H refers to the one-electron Hamiltonian matrix, built from the kinetic and nuclear-attraction energy terms of the electrons. The second term in Eq. 1.26 contains the electron-electron Coulomb interaction, and scales as N^4, where N is the number of basis functions in the system.

The third term, E_{xc}, is the exchange-correlation energy. This term introduces the energetic contributions of exchange, which is an energy penalty to putting same-spin electrons in interaction and as such, an enforcement of Pauli's exclusion principle; and the correlation energy, which exists as a correction for the approximation made in the Kohn-Sham framework that electrons are non-interacting. Its explicit form is not known, and various strategies have been put in place to evaluate E_{xc}.

Exchange-Correlation functionals: Listed below are the classes of exchange-correlation functionals, sorted in ascending order of sophistication (the Jacob's ladder hierarchy), and therefore, as a rule of thumb, of accuracy.

- **Local Density Approximation (LDA):**[88] E_{XC} is computed by applying a "uniform electron gas" model on infinitesimal volumes. This approach results in a spurious uniform electronic density, which leads to an underestimation of the exchange energy and an overestimation of the correlation energy. The LDA class of functionals tends to overestimate bond energies and, during geometry optimisations, to underestimate equilibrium bond lengths.

- **Generalised Gradient Approximation (GGA):**[89] a dependence of E_{XC} on the gradient of the electronic density, $\nabla\rho(\mathbf{r})$ is introduced to describe the inhomogeneity of the electron density. The analytical form of the exchange and correlation terms can be adjusted to fit empirical data. These modifications notably improve the energies, geometries, and vibrational frequencies computed using this class of functionals.

- **meta-GGA (mGGA):**[90] a dependence on the Laplacian (the second derivative) is further added, as well as on the kinetic energy density. These refinements allow a better description of atomic energies, dissociation energies, and lattice

parameters in solids. Popular mGGA functional include TPSS, or the Minnesota family, *e.g.* the M06 functional.

- **Hybrids:**[91] A parametrisable proportion of Fock exchange, or exact exchange, is introduced to mitigate the self-interaction error, a nonphysical phenomenon whereby an electron with a density probability within multiple orbitals interacts with itself. Popular hybrid functionals include B3LYP and PBE0.

- **"Range-separated" hybrids:**[92,93] The proportion of Fock exchange is modulated by the length of the interaction. Since electronic correlation is crucial at short distances, as it arises from repulsive electron-electron electrostatic interactions decaying as r^{-2}, and since Fock exchange presents a correct asymptotic (long-range) behaviour, a function is introduced to progressively include more exchange as the interaction length increases. Popular RS-hybrid functionals include CAM-B3LYP and ωB97X-D.

1.2.2.3 Properties computed from DFT calculations

Hyperfine Coupling (HFC) Hyperfine coupling, or HFC, is the name given to the interaction between an unpaired electron spin and the uncompensated nuclear spins of neighbouring nuclei; when in close proximity with each other, the coupling of their magnetic moments further splits spin states, creating new coherences. This lifting of degeneracy can be observed experimentally, for instance in Electron Paramagnetic Resonance (EPR) experiments, by the presence of additional transitions in the absorption spectra of radical molecules.

Computationally, a hyperfine interaction between an unpaired electron and a given nucleus is represented by a hyperfine coupling **tensor** of rank 2, defined within a three-dimensional Cartesian frame, and centred on the nucleus whose magnetic interactions it describes. The hyperfine structure of a radical molecule is therefore the collection of hyperfine tensors associated with each of its magnetic nuclei.

In this thesis, the main radical system under investigation is the flavin, in its radical anion and radical semiquinone forms. An investigation into the hyperfine structure of the flavin, especially its isoalloxazine moiety from which the ribityl tail was truncated, is presented in Chapter 3. Due to this, the only magnetically active nuclei, *i.e.* nuclei with a nonzero magnetic moment, are ^{1}H ($S = \frac{1}{2}$) and ^{14}N ($S = 1$).

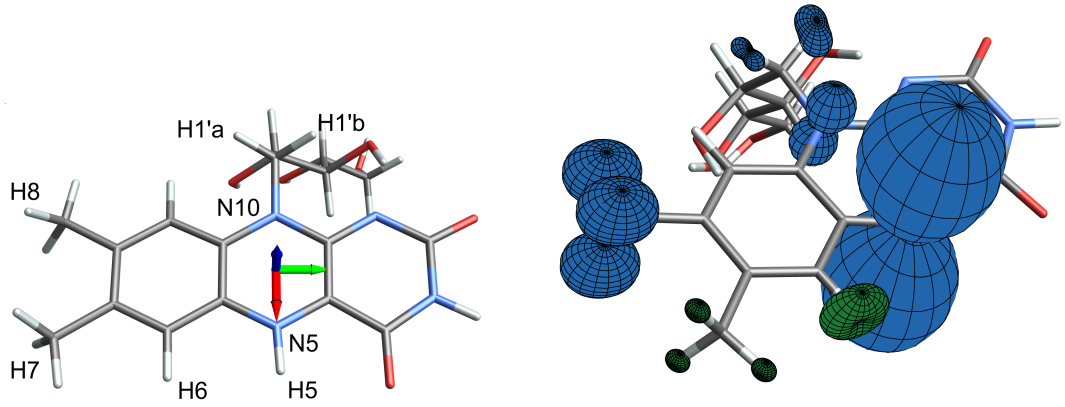

(a) FADH• atom names (b) FADH• HFC couplings

Figure 1.9: (a)FADH• atom names use throughout this thesis. (b) Visual representation of the averaged hyperfine structure of a FAD•− isoalloxazine + truncated ribityl chain, computed using aDFT at the B3LYP/EPR-III/GEN-A2* level on 400 MD-generated flavin structures. Blue lobes denote a positive value of the hyperfine interaction, green a negative value. This figure is a result and is analysed in greater details later in the thesis, in Chapter 3.

Figure 1.9 (a) represents the atom names of the flavin, used throughout the manuscript. Hydrogen N5 is the one that is not present in FAD•−. Figure 1.9 (b) is a representation of the hyperfine structure of a flavin isoalloxazine, computed using ADFT at the B3LYP/EPR-III/GEN-A2* level of theory. The details of the calculations and of the post-treatment of hyperfine tensors are given in Chapter 3. In this representation, the Cartesian frame is set up such that the z axis is normal to the plane of the isoalloxazine, while the x and y axes are within the plane.

Each hyperfine coupling tensor is represented by a surface which, for direction $\mathbf{r}$, is at a distance from the nucleus N proportional to $\mathbf{r}^{\mathbf{T}}\mathbf{A}_N\mathbf{r}$, where $\mathbf{A}_N$ is the HFC tensor centred on N; in other words, the further the surface from the nucleus, the stronger the hyperfine coupling in this direction. The largest HFC tensors are those of the nitrogen atoms, N5 and N10, whose strongly anisotropic shapes are an interesting feature. Additionally, their large magnitude and nearly colinear arrangement strongly biases the overall hyperfine structure, giving it a large A_{zz} component. More details on the importance of a strongly anisotropic hyperfine structure for the operation of a magnetic compass will be given later.

As stated earlier, a HFC tensor takes the form:

$$A = \begin{pmatrix} A_{xx} & A_{xy} & A_{xz} \\ A_{yx} & A_{yy} & A_{yz} \\ A_{zx} & A_{zy} & A_{zz} \end{pmatrix} ; A_{\mathrm{N5}}^{\mathrm{fr88}} = \begin{pmatrix} -2.546 & 0.204 & -1.455 \\ 0.210 & -1.685 & -5.387 \\ -1.454 & -5.388 & 46.935 \end{pmatrix} \text{(MHz)} \qquad (1.28)$$

In the coordinate frame where the calculation was run. An example HFC tensor

$A^{\mathrm{fr88}}_{\mathrm{N5}}$, calculated for the N5 atom on one of the geometries (index 88, hence the superscript) of the $\mathrm{FAD}^{\bullet-}$ considered in the study in Chapter 3, is also provided.

$A^{\mathrm{fr88}}_{\mathrm{N5}}$ is composed of two main contributions: the Fermi Contact (FC), which is the isotropic component of the tensor, and the Spin-Dipole (SD) part, the anisotropic remainder. Taking into account relativistic effects, which can be sizable for heavy nuclei such as transition metals, a second-order contribution from the Spin-Orbit Coupling (SOC) is also added. This contribution is included in the example tensor reported here, but is very small (0.1% of $\mathrm{a_{iso}}$).

The FC and SD contributions can be separated by diagonalising A, *i.e.* rotating and scaling the $\{x,y,z\}$ frame in such a way that the HFC tensor, expressed in the new (*eigen*)frame $\left\{x^{'},y^{'},z^{'}\right\}$, only has elements on its diagonal:

$$A^{'} = A^{'}_{\mathrm{FC}} + A^{'}_{\mathrm{SD}}; i.e \begin{pmatrix} A^{'}_{xx} & 0 & 0 \\ 0 & A^{'}_{yy} & 0 \\ 0 & 0 & A^{'}_{zz} \end{pmatrix} = \begin{pmatrix} a_{\mathrm{iso}} & 0 & 0 \\ 0 & a_{\mathrm{iso}} & 0 \\ 0 & 0 & a_{\mathrm{iso}} \end{pmatrix} + \begin{pmatrix} T_{11} & 0 & 0 \\ 0 & T_{22} & 0 \\ 0 & 0 & T_{33} \end{pmatrix} \quad (1.29)$$

Here, $A^{'}_{ii}$ are the eigenvalues of the HFC tensor $A^{'}$. a_{iso}, or the hyperfine coupling constant (HFCC), is computed as $a_{\mathrm{iso}} = \frac{1}{3}\sum_i^3 A^{'}_{ii}$. The first tensor in the decomposition of $A^{'}$ shown above is therefore fully isotropic, and predominantly corresponds to the Fermi-Contact contribution $A^{'}_{\mathrm{FC}}$.

a_{iso} corresponds to the magnitude of the rotationally averaged hyperfine coupling, and can be measured in EPR experiments where the radicals are tumbling in solution or arranged with a high degree of static disorder. This is however not the case for the system under investigation in Chapter 3, in which the flavin is prevented from tumbling by the cryptochrome binding it.

For this reason, the anisotropic contribution to the hyperfine structure of the flavin is also important in our study. This term is given by $A^{'}_{\mathrm{SD}}$, a *traceless* tensor (*i.e.* which satisfies $\sum_i^N T_{ii} = 0$) containing the Spin-Dipole contribution to the HFC. For tensors with sufficiently high symmetry (at least a threefold principal symmetry axis), the eigenvalues of $A^{'}_{\mathrm{SD}}$ satisfy $(T_{11}, T_{22}, T_{33}) = \left(-a_{\mathrm{dip}}, -a_{\mathrm{dip}}, 2a_{\mathrm{dip}}\right)$.

Applying the same decomposition to the diagonalised example tensor $A^{'\mathrm{,fr88}}_{\mathrm{N5}}$:

$$A^{'\mathrm{,fr88}}_{\mathrm{N5}} = \begin{pmatrix} 14.257 & 0.000 & 0.000 \\ 0.000 & 14.257 & 0.000 \\ 0.000 & 0.000 & 14.257 \end{pmatrix} + \begin{pmatrix} -16.797 & 0.000 & 0.000 \\ 0.000 & -16.517 & 0.000 \\ 0.000 & 0.000 & 33.313 \end{pmatrix} (\mathrm{MHz}), \quad (1.30)$$

we obtain $a_{\mathrm{iso}} = 14.257\,\mathrm{MHz}$ and $a_{\mathrm{dip}} \simeq 16.6\,\mathrm{MHz}$. The reason why a_{dip} is not exactly known is because of the slight departure of the $A^{\mathrm{fr88}}_{\mathrm{N5}}$ tensor from its ideal $D_{\infty h}$

symmetry.

The actual implementation of the EPR module in deMon2k shall be the topic of an article to be published by its creator Bernardo Gutiérrez, and therefore will not be discussed here, but we can still gain some insight from examining the way the various contributions to the HFC tensor are computed in ORCA, another quantum chemistry software.

The FC contribution is computed as follows:

$$a_{\text{iso}}(N) = \left(\frac{4}{3}\pi\langle S_Z^{-1}\rangle\right) g_e g_N \beta_e \beta_N \rho^{(\alpha-\beta)}\left(\vec{R}_N\right) \tag{1.31}$$

where g_e, g_N are the electron and nuclear g-factors, and β_e, β_N the electron and nuclear magnetons. These quantities parametrise the magnitude of the response of a nuclear + electronic system to a magnetic field and are therefore grouped into $D_N = g_e g_N \beta_e \beta_N$ in the further terms. $\langle S_Z\rangle$ is the expectation value of the z-component of the total (*i.e.* nuclear + electronic) spin, and $\rho^{(\alpha-\beta)}\left(\vec{R}_N\right)$ is the converged *spin density* of the radical **at the nucleus** N.

The spin density $\rho^{(\alpha-\beta)}$ is obtained by introducing an additional spin variable in the Kohn-Sham equations, allowing the electrons to be distributed in ψ^α ("spin-up") or ψ^β ("spin-down") orbitals, and converging with a very similar SCF procedure to a total electron density $\rho(\mathbf{r}) = \sum_i^{N_\alpha} |\psi_i^\alpha(\mathbf{r})|^2 + \sum_i^{N_\beta} |\psi_i^\beta(\mathbf{r})|^2 = \rho^\alpha(\mathbf{r}) + \rho^\beta(\mathbf{r})$. The spin density $\rho^{(\alpha-\beta)}$ is readily evaluated as $\rho^{(\alpha-\beta)} = \rho^\alpha - \rho^\beta$.

The SD contribution is calculated in the following manner:

$$A_{\mu\nu}^{\text{SD}}(N) = D_N \sum_{k,l} \rho_{kl}^{(\alpha-\beta)} \langle \phi_k | r_N^{-5} \left(3\vec{r}_{N\mu}\vec{r}_{N\nu} - \delta_{\mu\nu} r_N^2\right) | \phi_l \rangle \tag{1.32}$$

where $\vec{r}_N$ is a vector pointing from the nucleus N to the electron.

Both contributions (FC and SD) crucially depend on the distribution of spin density over the radical, a quantity computed from the total electron density $\rho(\mathbf{r})$ and which therefore, as we've seen, requires an appropriate choice of functional and basis set to be accurate. In particular, the FC contribution is computed from the spin density at the nucleus, a property very susceptible to Self-Interaction Error (SIE), a common pitfall of KS-DFT which can be mitigated by the inclusion of Fock exchange in the exchange-correlation functional. This is a feature of hybrid and range-separated hybrid functionals. Another requirement for the correct description of electronic density at the nucleus is on the basis set employed, which should include additional tight, s-type functions to accommodate electron density near the core,

instead of over-delocalising into valence orbitals.

The SD term, on the other hand, is computed from the distribution of spin density over the whole molecule. Again, this is achieved through an accurate description of the total electronic density, which especially for anionic radical – characterised by a more diffuse electronic density than their neutral counterparts – requires the use of "diffuse" functions in the basis set, *i.e.* larger basis functions that allow placing electron density further away from nuclei.

These constraints guided our choice to use the B3LYP hybrid functional with the EPR-III basis set, especially fitted to compute magnetic properties: this combo was the standard level of theory for computing flavin HFC tensors for use in spin dynamics calculations.[94,95]

The crucial role of the anisotropy of hyperfine couplings in the operation of a compass sensitive to magnetic-field inclination is not easily intuitively grasped. In fact, it is the anisotropy of the hyperfine structure of the flavin, dominated by its N5 and N10 tensors, which imparts a directional sensitivity to the spin dynamics of a radical – and by extension, of a radical pair or triad.

As mentioned earlier, each radical-bound unpaired electron oscillates coherently in its own local magnetic field (its hyperfine structure), even in the absence of an external magnetic field or of another unpaired electron spin. That is, the unpaired electron explores accessible spin states, symbolised by nonzero coherences in the spin density matrix, and interconverts at a rate proportional to the energy difference between states. It should be noted that for such systems, the ground-state, or state of lowest energy, is not significantly more populated than low excited states, due to the extremely small energy difference – of the order of $10^{-6}\, k_b T$ – separating them.

Recall the one-electron spin Hamiltonian, describing the spin states accessible to a single radical, with a single unpaired electron, within a hyperfine structure. The application of the external magnetic field, modeled by the Zeeman term, lifts the degeneracy of the spin states of the unpaired electron (spin "up" or "down"), by stabilising the antiparallel configuration and destabilising the parallel. Adding in a second time the energetic contribution of the interaction of this electron spin with magnetic nuclei around, the electron + nuclear spin states are further split.

The energy difference between two given spin states m and n determines the frequency ω_{mn} at which the system interconverts between m and n; *i.e.*, the spin dynamics of the system. A very large splitting can have an effect similar to a very large applied field and effectively confine the dynamics to groups of states. To il-

lustrate this phenomenon within the context of the singlet-triplet spin dynamics of our 2- or 3-radical mechanisms, a large splitting can makes a certain spin state nearly inaccessible to the system, and if this state participates to an *e.g.* triplet configuration with another radical electron, then the overall proportion of triplet states accessible to this radical pair decreases. As we've seen from Fig. 1.2, this in turn impacts the concentration of signaling state produced, and therefore the visual stimulus received by the bird which is finally interpreted as an orientational cue.

Critically, the anisotropy of the hyperfine structure modulates the magnitude of the hyperfine-induced split; this means that any rotation induces a change in the spin state coherences, affecting the singlet/triplet ratio of the electronic radical pair and in turn the visual navigation cues.

Formally speaking, in our case of a pair of radicals separated by a distance of the order of 10^0 nm, there is additional splitting from the interaction between the unpaired electron on radical A and the hyperfine tensors of radical B, by virtue of a nonzero A^{dip} contribution; however, the fast decay with distance and the fact that the magnetic moment of the electron is 658 times that of the proton mean that such inter-radical hyperfine coupling should be both negligibly small and overshadowed by the electron-electron dipolar coupling.

1.2.3 Spin dynamics

In this section, the theoretical framework within which the spin dynamics of a radical triad were simulated is presented. In particular, the spin Hamiltonian used throughout the thesis is detailed. The equations of motions used to propagate the spin state of a radical triad system, including the treatment of chemical reactions and spin relaxation, are also presented. Finally, we describe the computation of observables of interest, in particular performance indicators of the compass. This section is largely inspired by the introduction of Ref.[37]

We present here the methodology applied to simulate the spin dynamics of a radical triad of the form [$A^\bullet$ - $B^\bullet$ - $C^\bullet$], where [$A^\bullet$ - $B^\bullet$] constitutes the primary radical pair scavenged by radical $C^\bullet$. Again, while the identity of each radical is not fully known, we consider a [$FADH^\bullet$ - $O_2^{\bullet -}$ - $Tyr^{\bullet +}$] radical triad, in which the AB pair (*i.e.* [$FADH^\bullet$ - $O_2^{\bullet -}$]) is formed in a triplet state from the reduction of triplet O_2 by $FADH^-$. C ($Tyr^{\bullet +}$), on the other hand, is initially uncorrelated to the AB pair.

Equation of motion: The spin state of this radical triad is described by its population-weighted spin density operator $\hat{\rho}$, formed in the combined Hilbert space of the three radicals. $\hat{\rho}(t,\Omega)$ is then propagated in time with the following equation of motion:

$$\frac{d}{dt}\hat{\rho}(t,\Omega) = -i\left[\hat{\hat{H}}(\Omega),\hat{\rho}(t,\Omega)\right] + \hat{\hat{K}}\hat{\rho}(t,\Omega) + \hat{\hat{R}}\hat{\rho}(t,\Omega), \tag{1.33}$$

which can be separated into three parts. The first term is a commutator (*i.e.* $\left[\hat{A},\hat{B}\right] = \hat{A}\hat{B} - \hat{B}\hat{A}$) and describes the coherent evolution of the system under the spin Hamiltonian $\hat{H}$. The last 2 terms, on the other hand, are non-conservative – they do not preserve the trace of $\hat{\rho}$, *i.e.* its total populations – and respectively account for chemical reactions between radicals, and spin relaxation. Ω represents the angle of the applied external magnetic field, here taken to be the geomagnetic field of strength $\mathbf{B}_0 = 50\,\mu\text{T}$.

The spin Hamiltonian: Coming back to the first term: the spin Hamiltonian $\hat{H}(\Omega)$ takes the following form:

$$\hat{\hat{H}}(\Omega) = \sum_{K\in\{A,B,C\}} \hat{\hat{H}}_K(\Omega) + \sum_{K\neq L\in\{A,B,C\}} \hat{\hat{H}}_{K,L}, \tag{1.34}$$

and can be separated into a monoelectronic Hamiltonian, describing physical effects acting on individual radicals; and a bielectronic Hamiltonian to evaluate, in a pairwise manner, the energetic contributions of inter-radical interactions. Both are given below in angular frequency units.

The monoelectronic Hamiltonian takes the following form:

$$\hat{\hat{H}}_K(\Omega) = g\mu_B\hbar^{-1}\mathbf{B}_0\cdot\hat{\mathbf{S}}_K + \sum_j^{N_K}\hat{\mathbf{S}}_K\cdot\mathbf{A}_{Kj}\cdot\hat{\mathbf{I}}_{Kj}, \tag{1.35}$$

where the first term describes the Zeeman coupling with the external field $\mathbf{B}_0$, and the second term the hyperfine coupling with the N_K neighbouring magnetic nuclei, described by their hyperfine tensors A_{Kj}. Here, $\hat{S}_K$ and $\hat{\mathbf{I}}_{Kj}$ are the vector operators of, respectively, the electron spin $K \in \{A,B,C\}$ and of the nuclear spin j in radical K. For spin-$\frac{1}{2}$ particles in their respective sub-Hilbert spaces, the spin operators are constructed as $\hat{S}_{K,j,a} = \frac{1}{2}\hat{\sigma}_a$, where σ_a is the Pauli operator and $a \in \{x,y,z\}$.

The bielectronic Hamiltonian takes the following form:

$$\hat{\hat{H}}_{K,L} = -J_{KL}\left(\frac{\hat{1}}{2} + 2\hat{\mathbf{S}}_K\cdot\hat{\mathbf{S}}_L\right) + \frac{\mu_0 g^2\mu_B^2}{4\pi r_{KL}^3\hbar}\left(\hat{\mathbf{S}}_K\cdot\hat{\mathbf{S}}_L - 3\left(\hat{\mathbf{S}}_K\cdot\mathbf{n}_{KL}\right)\left(\hat{\mathbf{S}}_L\cdot\mathbf{n}_{KL}\right)\right), \tag{1.36}$$

including the exchange interaction and the electron-electron dipolar coupling, or EED, in the point-dipole approximation. In the first term, $2J_{KL}$ is the exchange-induced singlet/triplet energy difference. In the second term, which described the strength of inter-electron interactions as a function of distance and relative orientation, r_{KL} is the distance separating the centers of spin density in radicals K and L, measured along $\mathbf{n}_{KL}$, the unit inter-radical vector.

Chemical reactions: The chemical evolution of the radical triad, following the reaction pathways outlined in Figure 1.5, are modeled by the second term of Eq. 1.33. $\hat{\hat{K}}$ is a superoperator formulated following the Haberkorn approach, and its action on $\hat{\rho}$ can be written as:

$$\hat{\hat{K}}\hat{\rho}(t,\Omega) = -\frac{1}{2}k_X\left[\hat{\hat{P}}^{(S)}_{AC},\hat{\rho}(t,\Omega)\right]_+ - \frac{1}{2}k_S\left[\hat{\hat{P}}^{(S)}_{AB},\hat{\rho}(t,\Omega)\right]_+ - \frac{1}{2}k_T\left[\hat{\hat{P}}^{(T)}_{AB},\hat{\rho}(t,\Omega)\right]_+ - k_f\hat{\rho}(t,\Omega), \tag{1.37}$$

where k values are rate constants. Precisely, k_X, k_S and k_T are electron transfer rates for, respectively, the scavenging reaction (in the [A$^\bullet$ - C$^\bullet$] pair), the singlet recombination and the triplet recombination in the primary pair ([A$^\bullet$ - B$^\bullet$]). We take this last process to be effectively impossible, due to spin-flip being a slower process than electron transfer; for this reason, we set $k_T = 0$. k_f, on the other hand, corresponds to the lifetime of the radical pair $\hat{\hat{P}}^{(S)}_{AC}$ and $\hat{\hat{P}}^{(T)}_{AB}$ are the singlet and triplet projectors operators to act on the subspace of the electron spins of radicals AC and AB, respectively.

Spin relaxation: The process of spin relaxation, *i.e.* the randomisation of radicals' spin states, is introduced in the third term which takes the form of a Lindbladian operator:

$$\hat{\hat{R}}_K\hat{\rho}(t,\Omega) = \gamma_K\left(\sum_{i\in\{x,y,z\}} S_{K,i}\hat{\rho}(t,\Omega)S_{K,i} - \frac{3}{4}\hat{\rho}(t,\Omega)\right), \tag{1.38}$$

where γ_K is the dephasing rate of radical K. The relaxation model used here is a random-field one.

Observables: After all radicals have been allowed to either react or relax, the quantum yield of signaling state is evaluated like so:

$$Y_S(\Omega) = k_f\int_0^\infty \mathrm{Tr}\left[\hat{\rho}\right]dt = k_f\mathrm{Tr}\left[\hat{\bar{\rho}}(\Omega)\right], \tag{1.39}$$

in which $\hat{\bar{\rho}}(\Omega)$ is the accumulated spin density operator, defined as $\hat{\bar{\rho}}(\Omega) = \int_0^\infty \hat{\rho}(t,\Omega)\,dt$. The performance of a magnetic compass operated by a given pair or triad or radical

can then be measured by computing the anisotropy of the yield of the signaling state, which is a measure of the directional dependence of Y_S. Both the absolute (Δ_S) and relative (Γ_S) anisotropies can be computed:

$$\Delta_S = \max_{\Omega}[Y_S(\Omega)] - \min_{\Omega}[Y_S(\Omega)] \text{ and } \Gamma_S = \frac{\Delta_S}{\langle Y_S \rangle}, \tag{1.40}$$

where

$$\langle Y_S \rangle = \frac{1}{4\pi} \int Y_S(\Omega) d\Omega. \tag{1.41}$$

CHAPTER 2

REALISTIC 3-RADICAL SPIN DYNAMICS MODELING: IDENTIFYING A SUITABLE TYROSINE SCAVENGER

2.1 Chapter introduction

The following Chapter is an investigation into the scavenging abilities of tyrosine residues within an actual avian Cryptochrome 4 structure. Given the recent experimental evidence suggesting magnetic orienting being possible in the dark,[11] and therefore pointing to cryptochrome reoxidation rather than photoreduction as the step creating the magnetosensitive radicals, we focus here fully on the [$FADH^{\bullet}$-$O_2^{\bullet -}$] as the primary radical pair. While a radical pair model is briefly considered, the main point of focus here is the [$FADH^{\bullet}$-$O_2^{\bullet -}$-$Y^{\bullet}$] radical triad, formed by reoxidation of a dark-state $FADH^-$ by triplet molecular O_2 and by an electron transfer from the terminal tryptophan W_D to a tyrosine scavenger. This 3-radical system, which has already garnered attention in previous studies due to its potential for large singlet yield anisotropy Γ_S,[29,82] a measure of magnetosensitivity, is here investigated in both a more realistic and concrete manner. Realistic because we include in our spin Hamiltonian the contribution of electron-electron dipolar (EED) coupling, an often neglected effect which can have a dramatic impact on the spin dynamics; and concrete because the simulations reported in this article are parametrised with radical positions and orientations taken from an avian cryptochrome. This latter point allows an accurate estimation of the EED coupling strength, which is dependent not only on the distance separating radicals but also on their relative orientations.

In this Chapter, we identify in particular one $Y^{\bullet}$ radical which could operate an efficient 3-radical compass, exceeding the Γ_S values expected of a *e.g.* [$FAD^{\bullet -}$-W_D] radical pair. Encouragingly, this particular tyrosine, Y319 in *cl*Cry4, has an

equivalent in *er*Cry4, a potentially more sensitive avian cryptochrome.[53]

Finally, we also explore the possibility of a free-diffusing $Asc^{\bullet-}$ scavenger radical, which could allow to sidestep the EED issue. While extremely strong magnetosensitivity is predicted for the [$FADH^{\bullet}$-$O_2^{\bullet-}$-$Asc^{\bullet-}$], these results remain very preliminary.

This is a reproduction of the article entitled "Anisotropic magnetic field effects in the re-oxidation of cryptochrome in the presence of scavenger radicals" published in the Journal of Physical Chemistry and available at https://doi.org/10.1063/5.0078115. Supporting Information are provided in Appendix A.

This work is the result of a collaboration, and was carried out both at the University of Exeter and at Université Paris-Saclay. In terms of contributions: the spin dynamics Matlab code and initial cryptochrome structures were provided by Daniel Kattnig. Spin dynamics simulation of Y319 analogues and of the Ascorbyl-containing triad, estimation of electron transfer rate for *cl*Cry4 Y319 scavenging, creation of most figures and writing of the bulk of the text were also carried out by Daniel Kattnig. Spin dynamics calculation of [$FADH^{\bullet}/O_2^{\bullet-}/Y^{\bullet}$] triads in *cl*Cry4 and *Dm*Cry, with and without EED, andthe creation of corresponding figures were carried out by Jean Deviers. This project was carried out in close collaboration with both universities, and frequent discussions with Aurélien De la Lande and Fabien Cailliez, who also participated in the redaction of the article, were essential to complete this work.

2.2 Abstract

The avian compass and many other of nature's magnetoreceptive traits are widely ascribed to the protein cryptochrome. There, magnetosensitivity is thought to emerge as the spin dynamics of radicals in the applied magnetic field enters in competition with their recombination. The first and dominant model makes use of a radical pair. However, recent studies have suggested that magnetosensitivity could be markedly enhanced for a radical triad, the primary radical pair of which undergoes a spin-selective recombination reaction with a third radical. Here, we test the practicality of this supposition for the reoxidation reaction of the reduced FAD cofactor in cryptochrome, which has been implicated with light-independent magnetoreception but appears irreconcilable with the classical radical pair mechanism (RPM). Based on the available realistic cryptochrome structures, we predict the magnetosensitivity of radical triad systems comprising the flavin semiquinone, the superoxide, and a tyrosine or ascorbyl scavenger radical. We consider many hyperfine-coupled nuclear spins, the relative orientation and placement of the radicals, their coupling by the electron-electron dipolar interaction, and spin relaxation in the superoxide radical in the limit of instantaneous decoherence, which have not been comprehensively considered before. We demonstrate that these systems can provide superior

magnetosensitivity under realistic conditions, with implications for dark-state cryptochrome magnetoreception and other biological magneto- and isotope-sensitive radical recombination reactions.

2.3 Introduction

Magnetoreception presents itself as a mysterious sensor modality. Despite having been documented in a wide and diverse array of animals and even bacteria, the sensory mechanism has remained opaque.[40] The two main mechanisms discussed attribute the phenomenon either to ferrimagnetic or superparamagnetic particles[96] or magnetic field dependent spin dynamics in radical pairs (RP), presumably in the flavo-protein cryptochrome.[1] The latter hypothesis has nurtured interest beyond sensory biology because it serves as an example for a putative quantum-processes underpinning biology in a non-trivial manner, *i.e.*, a subject of the emerging field of quantum biology.[97,98]

The idea of magnetoreception underpinned by quantum mechanics is mostly developed and researched in the context of the avian magnetoreception, where it is widely attributed to a light-dependent inclination compass that is susceptible to interference from weak radio frequency magnetic fields.[1]

The quantum hypothesis of magnetoreception, as conceptually suggested in 1978 by Schulten and co-workers[42] and sophisticated to its current form by Ritz et al.,[17] builds on the magnetosensitivity of a radical pair recombination reaction in the protein cryptochrome.[1] Such magnetosensitive radicals are, for example, generated in cryptochromes in the photo-reduction of the non-covalently bound flavin cofactor.[53,73,99] In this system, a succession of intra-protein electron transfer processes generates an electron spin-correlated pair of radicals, comprising the flavin anion radical and tryptophan radical cation.[52] The pair's electronic singlet and triplet states coherently interconvert due to magnetic interactions in the radicals and with the geomagnetic field, thus rendering the reaction outcome—either charge recombination or structural rearrangement—sensitive to the applied magnetic fields. This mechanism has been clearly demonstrated for various cryptochromes *in vitro*, albeit in magnetic fields typically exceeding the geomagnetic fields by orders of magnitude.[53,73,99]

Besides the photo-reduction, the reoxidation has been implicated with magnetosensitivity. A transient flavin semiquinone/superoxide radical pair has been suggested[100,101] and amply discussed.[82,102] Such a radical pair is, *e.g.*, expected to result from the oxidation of the fully reduced flavin cofactor in cryptochrome by

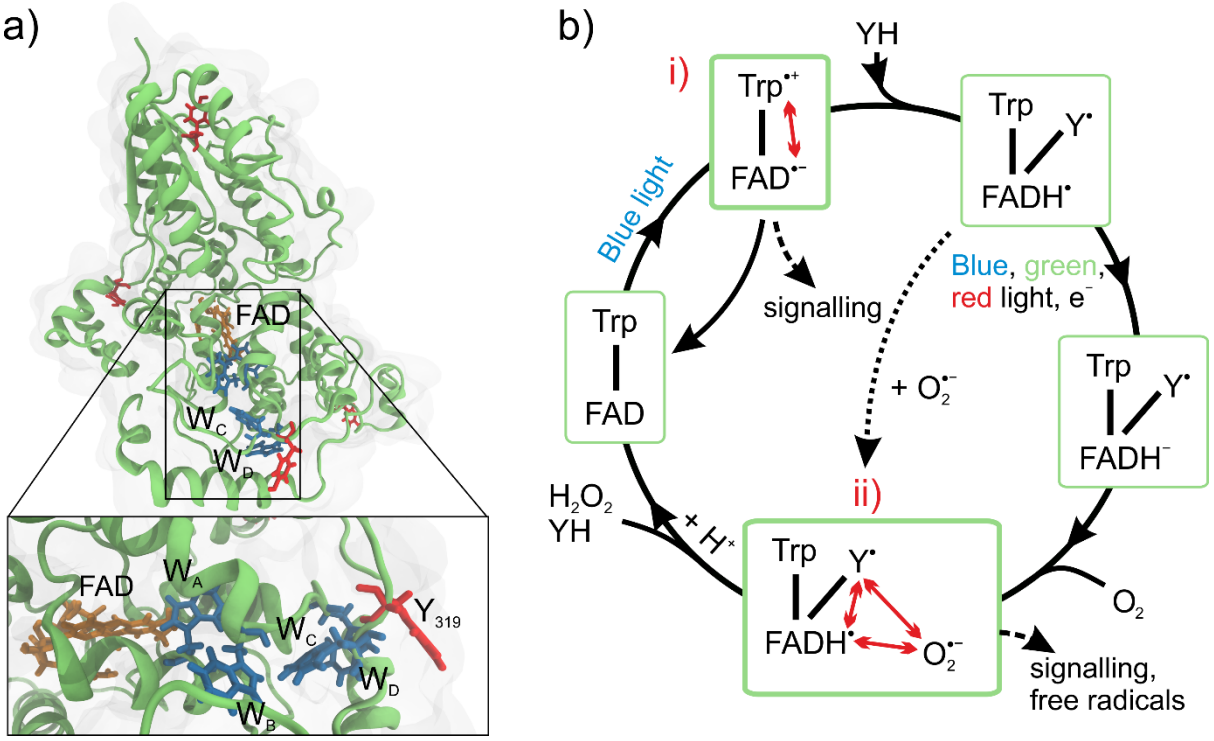

Figure 2.1: (a) Schematic representation of pigeon cryptochrome 4, *Cl*Cry4. The insert highlights the FAD (orange), the tryptophan tetrad (blue) and the surface exposed tyrosine residue, Y319, extending the latter. Selected tyrosine residues are shown in red: Y319, Y32, Y441, Y134. These sites can give rise to large magnetosensitivity in the $FADH^{\bullet}/O_2^{\bullet-}/Y^{\bullet}$ radical triad system with fast relaxing $O_2^{\bullet-}$, provided that the scavenging reaction is sufficiently rapid (see Discussion). (b) Photo-cycle of cryptochrome undergoing a two-step photoreduction and reoxidation. The photo-reduction is assumed to lead to the formation of the persistent radical $Y^{\bullet}$, which acts as a scavenger to $FADH^{\bullet}$ in the subsequent re-oxidation with molecular oxygen. The redox-cycle involves two potentially magnetosensitive radical pairs, $FAD^{\bullet-}/Trp^{\bullet+}$ in the first photo-reduction (labelled *i*) and the $FADH^{\bullet}/O_2^{\bullet-}$ radical pair resulting from the oxidation of the fully reduced $FADH^{-}$ by oxygen. The identity of the proton donor for the protonation of $FAD^{\bullet-}$ into $FADH^{\bullet}$ is here assumed to be a tyrosine YH, although it could also be a protonated tryptophan WH. A mobile $O_2^{\bullet-}$ will not be magnetosensitive in the geomagnetic field due to swift spin relaxation. Engaging a scavenging reaction in $FADH^{\bullet}/Y^{\bullet}$ resurrects the magnetosensitivity. $Y^{\bullet}$ could be a long-lived tyrosine radical or a radical derived from a radical scavenger, such as ascorbic acid. Cryptochromes that cannot be fully photo-reduced (*e.g.* *Dm*Cry) could form flavin/$O_2^{\bullet-}/Y^{\bullet}$ radical triad systems by correlating with a pre-formed $O_2^{\bullet-}$ in a random encounter (dashed arrow).

molecular oxygen.[28] Although a demonstration of a clear-cut magnetic field effect (MFE) of this radical pair has so far not been delivered *in vitro*, the hypothesis has gained new impetus through a series of *in vivo* experiments demonstrating magnetoreception in (intermittent) darkness, *i.e.*, under conditions for which the photo-reduction has been ruled out.[11,64,65] From the conceptual point of view, a superoxide/semiquinone radical pair offers potential advantages but also raises fundamental questions. As such a radical pair is of the so-called reference-probe coupling topology, *i.e.*, lacks significant hyperfine interactions in one of the radicals, much larger magnetic field effects are predicted by models employing the radical pair mechanism (RPM) than is the case for flavin/tryptophan pairs.[72,103] On the other hand, superoxide is known to be subject to fast spin-rotational relaxation, which would abolish the magnetic field sensitivity of the reaction if the anion was freely tumbling in solution.[69,102]

A previous work has suggested that the issue posed by fast spin relaxation could be overcome in an extended model relying on a radical triad instead of a radical pair.[73,82] Specifically, it has been shown that a scavenging reaction of a radical pair by a third radical can markedly boost the magneto-sensitivity of the recombination reaction (observed for the primary pair) both for flavin/tryptophan and flavin/superoxide reactions and even if the primary pair does not recombine (on the relevant time scale).[73] The enhancement process is robust to fast spin relaxation in one member of the primary pair, which, at least conceptually, allows for the inclusion of superoxide and other reactive oxygen species (ROS) beleaguered by fast spin relaxation.[82] In addition, a recent study demonstrated that the effect remains effective in the presence of the unavoidable but oft-neglected electron-electron dipolar (EED) interactions.[25] While these previous studies are promising, the models used had been simplified in many respects, thus elucidating the principal idea rather than their practicality for magnetoreception.

While the scavenged three-radical processes offers many virtues, its obvious downside is the increased complexity resulting from the need to recruit a scavenging radical to interact with the primary radical pair. Reference 82 suggests that this could be realized through a reaction scheme, where the scavenger radical is generated in the photo-reduction and conserved in the form of a persistent radical until demanded in the three-radical reoxidation. In the avian cryptochromes, such reoxidation processes could be induced by molecular oxygen from the fully reduced cryptochrome (see Fig. 2.1).[30] In cryptochromes that do not undergo complete photoreduction, such as the cryptochrome from *D. melanogaster* (*Dm*Cry),[104] the radical triad could result in an encounter processes with a pre-formed superoxide. Many persistent radicals are known in nature; in the context of cryptochromes, long-lived

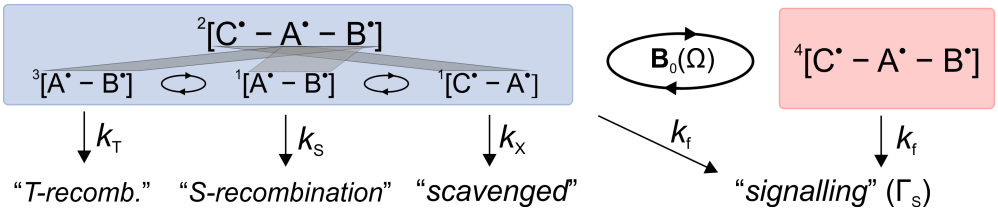

Figure 2.2: Scheme 1: Reaction scheme underpinning the theoretical model. The sub-states shown for the doublet manifold (underlaid in blue) only show the reacting pair of radicals and are not mutually exclusive, *i.e.*, orthogonal.

tyrosine radicals are well-documented.[31,32] With this motivation in mind, we here are set to elucidate the directional magnetic field effects (MFEs) that the model from Ref. 82 predicts for a tyrosine radical-scavenged flavin semiquinone superoxide radical pair if the electron-electron dipolar coupling and the scavenger radical identity (and thus its orientation) are taken into account. Specifically, we ask the question if one of the tyrosine residues, as present in prototypical cryptochromes, could function as a radical scavenger to boost the magnetosensitivity of the reoxidation of cryptochrome. We base our analysis on the recently resolved crystal structure of the pigeon cryptochrome 4 (*Cl*Cry4), close in sequence to the European Robin Cryptochrome 4 (*Er*Cry4) and, for comparison, *Dm*Cry.[30,105] The latter has been used widely as a model cryptochrome system to study magnetoreception.[3,63] This includes the original studies proposing the three-radical model.[29,82] *Cl*Cry4 is the only bird cryptochrome for which the crystal structure has been resolved so far.[30] It shares broad sequence homology with cryptochromes from migratory birds, for which a compass sense has been extensively studied (85.6% sequence identity with *Er*Cry4). Using a variety of template structures, our study thus reveals the range of magnetic sensitivities realizable in realistic, *i.e.*, existing, structures. While it is understood that the sensor *in vivo* will most likely deviate from these established structures,[53] they provide a well-defined frame of reference and target for systematic exploration. We present data for reasonably complex radical systems as a function of the scavenging rate constant and discuss the effects of spin relaxation in the superoxide and the electron-electron dipolar coupling of radicals. A comprehensive evaluation of the effect for the various tyrosine sites allows predicting the most apt residue. The majority of the analysis has been carried out in the limit of infinitely fast spin relaxation within the superoxide anion, thereby highlighting the design principles that allow realizing large magnetosensitivity in reactions involving swiftly relaxing species.

2.4 Theory

We consider systems of three radicals, henceforth denoted $A^\bullet$, $B^\bullet$, and $C^\bullet$. Radicals $A^\bullet$ and $B^\bullet$ are thought to form the primary radical pair (RP), while $C^\bullet$ assumes the role of the scavenger (Scheme 2.2). The latter reacts with $A^\bullet$ in a spin-selective reaction forming a diamagnetic product distinct from the signaling state. For the majority of this paper, $A^\bullet$, $B^\bullet$, and $C^\bullet$ are thought to be realized by $FADH^\bullet$, $O_2^{\bullet -}$, and $Y^\bullet$ in cryptochrome (cf. Fig. 2.1). In the "Discussion", we will also consider the ascorbyl radical in place of $C^\bullet$. The spin dynamics and magnetic field effects of this system are described in terms of the population weighted spin density operator in the combined Hilbert space of the three radicals, $\hat{\rho}(t,\Omega)$. Its equation of motion is of the form:

$$\frac{d}{dt}\hat{\rho}(t,\Omega) = -i\left[\hat{\hat{H}}(\Omega),\hat{\rho}(t,\Omega)\right] + \hat{\hat{K}}\hat{\rho}(t,\Omega) + \hat{\hat{R}}\hat{\rho}(t,\Omega), \tag{2.1}$$

and comprises a conservative part describing the coherent evolution of the spin system under the spin Hamiltonian $\hat{H}(\Omega)$ and a non-conservative part that accounts (phenomenologically) for the two important consequences of the open nature of the quantum system, namely, chemical reactions and environment induced relaxation, in the form of the linear superoperators $\hat{\hat{K}}$ and $\hat{\hat{R}}$, respectively. Here, $\left[\hat{A},\hat{B}\right] = \hat{A}\hat{B} - \hat{B}\hat{A}$ denotes the commutator, and the spin Hamiltonian $\hat{H}(\Omega)$ comprises the Zeeman interaction with the geomagnetic field, hyperfine interactions with surrounding nuclear spins, the electron-electron dipolar (EED) coupling, and the exchange interactions. Specifically,

$$\hat{\hat{H}}(\Omega) = \sum_{K\in\{A,B,C\}} \hat{\hat{H}}_K(\Omega) + \sum_{K\neq L\in\{A,B,C\}} \hat{\hat{H}}_{K,L}, \tag{2.2}$$

with $\hat{\hat{H}}_K(\Omega)$ and $\hat{\hat{H}}_{K,L}$ give in angular frequency units by

$$\hat{\hat{H}}_K(\Omega) = \omega_0 \cdot \hat{\mathbf{S}}_K + \sum_j^{N_K} \hat{\mathbf{S}}_K \cdot \mathbf{A}_{Kj} \cdot \hat{\mathbf{I}}_{Kj}, \tag{2.3}$$

and

$$\hat{\hat{H}}_{K,L} = -J_{KL}\left(\frac{\hat{1}}{2} + 2\hat{\mathbf{S}}_K \cdot \hat{\mathbf{S}}_L\right) + d_{KL}\left(\hat{\mathbf{S}}_K \cdot \hat{\mathbf{S}}_L - 3\left(\hat{\mathbf{S}}_K \cdot \mathbf{n}_{KL}\right)\left(\hat{\mathbf{S}}_L \cdot \mathbf{n}_{KL}\right)\right), \tag{2.4}$$

$\hat{S}_K$ and $\hat{\mathbf{I}}_{Kj}$ denote the vector operators of electron spin $K \in \{A,B,C\}$ and of nuclear spin j in radical K, respectively. For spin-$\frac{1}{2}$ particles in their respective sub-Hilbert spaces, the spin operators as used here are related to the Pauli operators by $\hat{S}_{K,j,a} = \frac{1}{2}\hat{\sigma}_a$, where $a \in \{x,y,z\}$.

The sum in Eq. (2.3) runs over all N_K magnetic nuclei with hyperfine tensor A_{Kj} in radical K. $\omega_0 = g\mu_B\hbar^{-1}\mathbf{B}_0$, with $\mathbf{B}_0(\Omega)$ denoting the applied magnetic field (of assumed 50 μT intensity; Larmor precession frequency: $g\mu_B\frac{\|\mathbf{B}_0(\Omega)\|}{h} \simeq 1.4\,\mathrm{MHz}$)

in the coordinate frame of the protein, as specified by the combined polar and azimuthal angles Ω. Note that the geomagnetic field is weak enough that differences in g-factors of the three electron spins can be neglected (in particular, $g \simeq 2$). $2J_{KL}$ is the energy difference of the singlet and triplet states of pair (K,L) due to the exchange coupling. The electron-electron dipolar coupling [second term in Eq. (2.4)] has been considered in the point-dipole approximation. The dipolar coupling constant is given by $d_{KL} = \mu_0 g^2 \mu_B^2/(4\pi r_{KL}^3 \hbar)$, with r_{KL} denoting the distance of the centers of spin density of radicals K and L. n_{KL} is a unit vector parallel to the line joining the centers of the two radicals.

The superoperator $\hat{\hat{K}}$ accounts for chemical reactions of the radical triad. Specifically, following the Haberkorn approach,[106] $\hat{\hat{K}}$ can be expressed as

$$\hat{\hat{K}}\hat{\rho}(t,\Omega) = -\frac{1}{2}k_X\left[\hat{\hat{P}}_{AC}^{(S)},\hat{\rho}(t,\Omega)\right]_+ - \frac{1}{2}k_S\left[\hat{\hat{P}}_{AB}^{(S)},\hat{\rho}(t,\Omega)\right]_+ - \frac{1}{2}k_T\left[\hat{\hat{P}}_{AB}^{(T)},\hat{\rho}(t,\Omega)\right]_+ - k_f\hat{\rho}(t,\Omega), \tag{2.5}$$

where k_X and k_f are the rate constants of radical scavenging and for spin-independent generation of the signaling state, respectively. k_S and k_T denote the rate constants of singlet and triplet pair recombination in the primary RP. Here, $[,]_+$ denotes the anti-commutator and $\hat{\hat{P}}_{KL}^{(S)}$ and $\hat{\hat{P}}_{KL}^{(T)} = \hat{1} - \hat{\hat{P}}_{KL}^{(S)}$ are the singlet and triplet projection operators in the subspace of the electron spins of radicals K and L, respectively. The former can be expressed as $\hat{\hat{P}}_{KL}^{(S)} = \frac{1}{4}\hat{I} - \hat{S}_K \cdot \hat{S}_L$. Equation (2.5) is of the truncated Lindblad form (the inclusion of "shelving" states for the reaction products would reveal its complete Lindblad form; see *e.g.*, Refs. 59 and 107) and accommodates minimal reaction-related singlet-triplet-dephasing of the reacting pair.[97,108] We will refer to k_f^{-1} as the "lifetime" of the radical system.

We treat spin relaxation in terms of the generic Lindbladian in diagonal form

$$\hat{\hat{R}}\hat{\rho}(t,\Omega) = \sum_n \gamma_n \frac{1}{2}\left(2A\hat{A}_n\hat{\rho}(t,\Omega)\hat{A}_n^\dagger - \hat{\rho}(t,\Omega)\hat{A}_n\hat{A}_n^\dagger + \hat{A}_n\hat{A}_n^\dagger\hat{\rho}(t,\Omega)\right) \tag{2.6}$$

where the $\hat{A}_n$ are jump operators and the γ_n are the associated noise rates. In the sections titled Results, we shall present simulations for random-field relaxation, for which $\hat{A}_n \in \{\hat{S}_{K,x},\hat{S}_{K,y},\hat{S}_{K,z}\}$ and the three associated coupling coefficients are assumed identical (corresponding to uncorrelated, *i.e.*, incoherently modulated field noise in the three space dimensions). For the Kth radical, these assumptions lead to

$$\hat{\hat{R}}_K\hat{\rho}(t,\Omega) = \gamma_K\left(\sum_{i\in\{x,y,z\}} S_{K,i}\hat{\rho}(t,\Omega)S_{K,i} - \frac{3}{4}\hat{\rho}(t,\Omega)\right), \tag{2.7}$$

which is equal to the phenomenological relaxation superoperator popular with magnetic resonance applications with equal spin-lattice (T_1) and spin-spin relaxation times (T_2), *i.e.*, $\gamma_K = T_{1,K}^{-1} = T_{2,K}^{-1}$. Equations (2.6) and (2.7) generally apply to Markovian noise, which is deemed applicable to describe the wider system-bath coupling

effects (as, *e.g.*, the discussion in Ref. 59). Alternative descriptions based on Bloch-Redfield theory[47,73] and spin-boson models[109] have been employed (which likewise are Markovian or have been applied in this limit).

Equation (2.1) is here solved subject to the initial condition

$$\hat{\rho}(0,\Omega) = \hat{P}_{AB}^{(T)} / \mathrm{Tr}\left[\hat{P}_{AB}^{(T)}\right] \tag{2.8}$$

which corresponds to an unpolarized triplet state of the AB-radical pair, in line with its assumed generation from the fully reduced FADH^{-} and triplet oxygen, in the presence of an initially uncorrelated radical $\mathrm{C}^{\bullet}$. Encounters of initially uncorrelated radicals (F-pairs/radical cluster) give rise to qualitatively comparable MFEs.[61]

The quantum yield of the signaling state, once all radicals have reacted, is given by

$$Y_S(\Omega) = k_f \int_0^\infty \mathrm{Tr}\left[\hat{\rho}\right] dt = k_f \mathrm{Tr}\left[\hat{\bar{\rho}}(\Omega)\right], \tag{2.9}$$

with $\hat{\bar{\rho}}(\Omega) = \int_0^\infty \hat{\rho}(t,\Omega)\, dt$ denoting the accumulated density operator. The directional dependence of the yield dictates the performance of the reaction as a compass sensor. We use as fidelity measures the absolute (Δ_S) and the relative (Γ_S) anisotropy of the yield of the signaling state, which are defined as follows:

$$\Delta_S = \max_\Omega [Y_S(\Omega)] - \min_\Omega [Y_S(\Omega)] \text{ and } \Gamma_S = \frac{\Delta_S}{\langle Y_S \rangle}, \tag{2.10}$$

where

$$\langle Y_S \rangle = \frac{1}{4\pi} \int Y_S(\Omega) d\Omega. \tag{2.11}$$

Assume that the spin relaxation is fast and local to $\mathrm{B}^{\bullet}$ (*i.e.*, acting on radical $\mathrm{B}^{\bullet}$, the superoxide radical anion, only). In the limit that the associated $\gamma_n \to \infty$, B-coherences are eradicated and B-population differences vanish. In this scenario, the spin dynamics of the system can be described in terms of the reduced density operator,

$$\hat{\sigma}(t,\Omega) = \mathrm{Tr}\left[\hat{\rho}(t,\Omega)\right] \tag{2.12}$$

or

$$\langle a,b|\hat{\sigma}(t,\Omega)|c,d\rangle = \langle a,\uparrow,b|\hat{\sigma}(t,\Omega)|c,\uparrow,d\rangle + \langle a,\downarrow,b|\hat{\sigma}(t,\Omega)|c,\downarrow,d\rangle \tag{2.13}$$

for which the spin-states of the B-radical have been traced out (a and c and b and d stand for the spin states of radical A and C, respectively; hyperfine interactions have been assumed to be absent for $\mathrm{B}^{\bullet}$). $\hat{\sigma}(t,\Omega)$ obeys an effective equation of motion of the form

$$\frac{d}{dt}\hat{\sigma}(t,\Omega) = -i\left[\hat{\hat{H}}'(\Omega), \hat{\sigma}(t,\Omega)\right] + \hat{\hat{K}}'\hat{\sigma}(t,\Omega) + \hat{\hat{R}}'\hat{\sigma}(t,\Omega) \tag{2.14}$$

where $\hat{\hat{H}}'(\Omega)$ is the Hamiltonian pertinent to A and C only, *i.e.*, $\hat{\hat{H}}'(\Omega) = \hat{\hat{H}}_A(\Omega) + \hat{\hat{H}}_C(\Omega) + \hat{\hat{H}}_{A,C}(\Omega)$; $\hat{\hat{R}}'$ is the relaxation superoperator in the AC-subspace; and the recombination superoperator obeys

$$\hat{\hat{K}}'\hat{\sigma}(t,\Omega) = -\frac{1}{2}k_X\left[\hat{P}_{AC}^{(S)},\hat{\sigma}(t,\Omega)\right]_+ - \left(k_f + \frac{k_S}{4} + \frac{3k_T}{4}\right) \tag{2.15}$$

Equations (2.14) and (2.15) suggest that the spin dynamics of the three-radical system in the limit of fast spin relaxation in $B^\bullet$ resemble that of a radical pair composed of $A^\bullet$ and $C^\bullet$ with the effective singlet recombination rate $k_S' = k_X$ and modified decay rate $k_f' = k_f + \frac{k_S}{4} + \frac{3k_T}{4}$. Equation (2.15) is to be solved subject to the random initial condition, $\hat{\sigma}(0,\Omega) \propto \hat{1}$. This applies both to $\hat{\rho}(0)$ given by Eq. (2.8) and F-pair/triad initial conditions. The majority of simulations described here will be conducted in the limit of infinitely fast spin relaxation in $B^\bullet$, for simplicity, reduction of the number of parameters, and in the expectation that this limit is, in fact, closely realized for a freely tumbling superoxide. Hyperfine parameters are reported for the molecular frames of the $FADH^\bullet$ and $Y^\bullet$ radicals in the supplementary material (Tables A.2-A.4). The identity of the scavenger radical within the protein, *i.e.*, sequence number, impacts on the spin dynamics via the relative orientation of radicals and, for models including the electron-electron dipolar coupling, the inter-radical distance.

2.5 Results

For context, we first consider a radical pair model of the reoxidation reaction. We adopt the prototype model of a triplet-born radical pair comprising the flavin semiquinone, $FADH^\bullet$, and superoxide anion radical, $O_2^{\bullet-}$ (hyperfine parameters are reported in Table A.4 in the supplementary material). Assuming that the superoxide is mobile allows us to neglect its electron-electron dipolar interactions, which have a suppressive effect on the magnetic field effects from radical pair reactions in general and in flavin-containing radical pair models of the cryptochrome charge recombination in particular.[25,27,55] We consider a "short-lived" ($k_f^{-1} = 1\,\mu$s) and "long-lived" ($k_f^{-1} = 10\,\mu$s) radical pair, with lifetimes chosen to elicit marked sensitivity of the geomagnetic field but still obeying lifetime bounds derived from the inference of avian magnetoreception by radio-frequency electromagnetic fields[48] and the expected spin relaxation times of cryptochrome-bound flavin radicals (*i.e.*, for longer lifetimes, spin relaxation in the flavin will strongly attenuate the effect).[47] The radical pair recombination has been accounted for subject to the frequent assumptions $k_S = k_f$ and $k_T = 0$. Modeling spin relaxation in the superoxide anion radical by Eq. (2.7), we predict the dependence of the relative anisotropy [Eq. (2.11)] of the quantum yield of signaling state formation on the relaxation rate constant γ_B, as shown in Fig. 2.3(a).

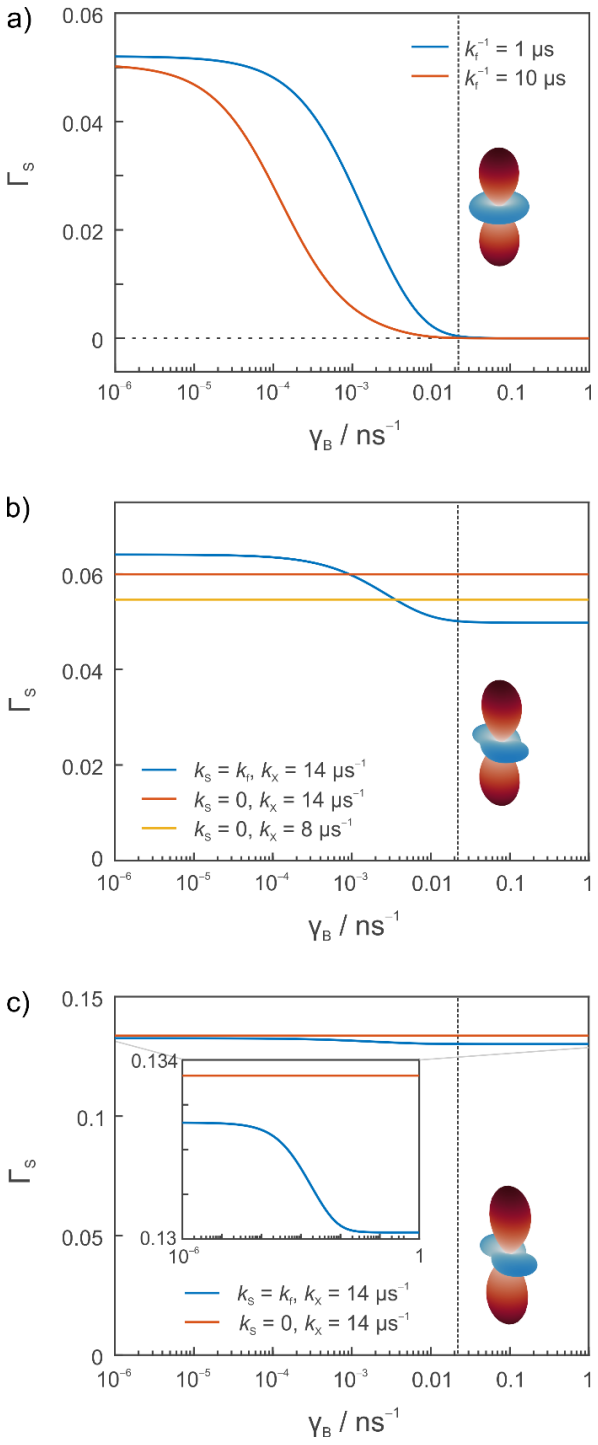

Figure 2.3: Directional magnetic field effects of radical pair and triad systems of topology $FADH^{\bullet}/O_2^{\bullet-}$ or $FADH^{\bullet}/O_2^{\bullet-}/Y^{\bullet}$ subject to random-field spin relaxation in $O_2^{\bullet-}$. a) $FADH^{\bullet}/O_2^{\bullet-}$ for $k_f^{-1} = 1\,\mu$s and $10\,\mu$s, $k_S = k_f$ and $k_T = 0$; b) and c) $FADH^{\bullet}/O_2^{\bullet-}/Y^{\bullet}$ for $k_f^{-1} = 1\,\mu$s and $10\,\mu$s, respectively, different k_S and k_X as indicated in the legends, and $k_T = 0$. The $Y^{\bullet}$ has been modelled after Y319 in *Dm*Cry. For the three-radical systems, the hyperfine interaction of N5, N10 and H5 in $FADH^{\bullet}$ and of the two ortho-protons in $Y^{\bullet}$ have been considered; a) additionally included Hβ1 and H6 in $FADH^{\bullet}$. The inserts on the right illustrate the anisotropy of the yield of the signalling state evaluated for $\gamma_B = 0.022\,\text{ns}^{-1}$, the relaxation rate expected for a viscous cellular environment, and the conditions represented by the blue lines. These diagrams are not drawn to scale.

In the absence of spin relaxation ($\gamma_B \to 0$), the model yields marked anisotropy of the yield of the signaling state of the order of 5% for both radical pair lifetimes considered. As the relaxation rate increases, the effects are, however, quickly attenuated, whereby the long-lived pair is more susceptible to the noise process. For the superoxide anion radical, the predominant source of the spin relaxation in weak magnetic fields is the spin-rotational interaction, the dephasing effect of which is directly proportional to the rotational correlation time.[86] Estimating the latter based on the Stokes-Einstein relation and using parameters from Ref. 86, the relaxation rate of superoxide freely tumbling in an aqueous solution is estimated as $\gamma_B = 1.8 \times 10^9\,\mathrm{s}^{-1}$, *i.e.*, γ exceeds the range of γ-values considered in Fig. 2.3. Allowing for the fact that the dynamic viscosity of hydrophobic cellular compartments surpasses that of water (80 mPa.s vs 1 mPa.s for water),[110] the intracellular spin-rotational relaxation rate is, in fact, expected to be smaller: $\gamma_B = 2.2 \times 10^7\,\mathrm{s}^{-1}$ (*i.e.*, the system loses coherences on a timescale of $\gamma_B^{-1} = 45\,\mathrm{ns}$).

However, the MFEs are strongly attenuated (for the here more favorable $k_f^{-1} = 1\,\mu$s, from 5.2 % to < 0.04 %; worse for $k_f^{-1} = 10\,\mu$s), thereby making obvious that the model of a mobile superoxide is irreconcilable with the demand of providing a sensitive compass in the geomagnetic field.

We next consider the extension of the radical pair model by a scavenging reaction with a third radical as shown schematically in Fig. 2.1 and Scheme 2.2. We assume that the signaling state is induced by the semiquinoid form of FAD.[34] The scavenging reaction correspond to the oxidation of $\mathrm{FADH}^\bullet$ by the tyrosine radical, thereby re-forming the fully oxidized resting state of FAD, which is also formed via the oxidation of the semiquinone by $\mathrm{O}_2^{\bullet-}$. Overall, the reaction products are thus the activated protein or its resting state. For definiteness, we arbitrarily identify the scavenger radical with the neutral tyrosine radical corresponding to Y319 as present in the crystal structure of *Dm*Cry. This residue is separated by 10.2 Å from the flavin (OH-N5 distance) and thus, in principle, well positioned to serve as scavenger of the flavin semiquinone based on the mere criterion of distance; beyond that, we do not want to imply mechanistic relevance of this system. For a moderately fast scavenging rate of $k_X \simeq 10\,\mu\mathrm{s}^{-1}$, Figs. 2.3(b) and 2.3(c) again show the dependence of the relative reaction yield on the rate of spin relaxation, γ_B, in the superoxide radical. It is apparent that the three-radical model predicts MFEs that exceed those of the RPM-based model, in particular, for the longer lifetime of $k_f^{-1} = 10\,\mu s$ [Fig. 2.3(c)] and that, importantly, the effects are robust to spin relaxation in the superoxide radical anion. Specifically, we find that the anisotropy is unaffected by $\mathrm{B}^\bullet$-spin relaxation if $k_S = k_T = 0$. For non-zero recombination in the primary pair, *e.g.*, $k_S = k_f$, the spin relaxation has an attenuating effect, but effects remain large even for $\gamma_B \to \infty$.

The diminishing effect of primary pair recombination in this limit is consistent with the observation [as expressed in Eqs. (2.14) and (2.15)] that, for $\gamma_B \rightarrow \infty$, the radical-triad dynamics correspond to that of the AC-pair but with decreased lifetime, *i.e.*, increased effective $k_f^{'}$. As the effective lifetime is decreased for $k_S > 0$ [see Eq. (2.15)], the sensitivity to the magnetic field is reduced, which is particularly pronounced for systems with lifetimes close to the "detection limit" for the geomagnetic field (*i.e.*, for the simulations with $k_f^{-1} = 1\,\mu$s; the time of at least one Larmor precession, *i.e.*, $\simeq 700$ ns, is required to elicit a marked response to the magnetic field). Figure 2.3 also shows the anisotropy of the MFE for $\gamma_B = 0.022\,\text{ns}^{-1}$, the relaxation rate expected for a viscous cellular environment, as an inset. A comparable directionality of the radical-pair and radical-triad systems is observed (while the size of the effects is markedly different).

For the calculations on triad systems with explicit spin relaxation taken into account, we have been able to include the five largest hyperfine interactions. Subsequent simulations will assume the extreme relaxation limit, $\gamma_B \rightarrow \infty$, for simplicity and efficiency while also being in line with the spin relaxation rates as estimated above. In this limit, we will be able to consider the eight largest hyperfine-coupled nuclei, yielding a more realistic description of the spin dynamics in these triad systems. As might be expected in view of the combined simulation data published for various radical pair systems,[3,63,72] this increase in complexity is associated with a (modest) decrease in Γ_S.

Figure 2.4(a) shows the dependence of the relative anisotropy of the flavin semiquinone/superoxide/Y319 triad system on the rate constant of scavenging for $k_f^{-1} = 1$ and $10\,\mu$s. Spin relaxation in the superoxide anion has been accounted for in the $\gamma_B \rightarrow \infty$ limit; EED interactions have initially been neglected (see below). The data reveal substantial MFEs for scavenging rate constants $k_X \simeq 10 \times k_f$. For $k_f^{-1} = 1$ and $10\,\mu$s, the effect peaks at $k_X = 13\,\mu\text{s}^{-1}$ and $k_X = 6\,\mu\text{s}^{-1}$, respectively. With increasing lifetime, the maximally attainable Γ_S increases and the associated scavenging rate constant k_X decreases. A similar trend is obtained for the absolute orientational spread of the reaction yield, Δ_S, except for that the $k_f^{-1} = 10\,\mu$s data appear to peak at lower k_X ($k_X = 0.9\,\mu\text{s}^{-1}$ for $k_f = 0.1\,\mu\text{s}^{-1}$; see the supplementary material). Figures 2.4(b) and A.2 in the supplementary material provide comparable data for Y319 from *Cl*Cry4 and Y388 from *Er*Cry4. The latter is the tyrosine residue closest to FAD according to a homology model taken from Ref. 111 (FAD-N5-OH-distance: 13.8 Å). Tyrosine atomic coordinates for *Cl*Cry4 were taken from the crystal structure (PDB ID: 6PU0), *i.e.* without the unresolved phosphate-binding loop (PBL). The *Cl*Cry4 PBL however does not contain any tyrosine residue. Y319 in *Cl*Cry4 is

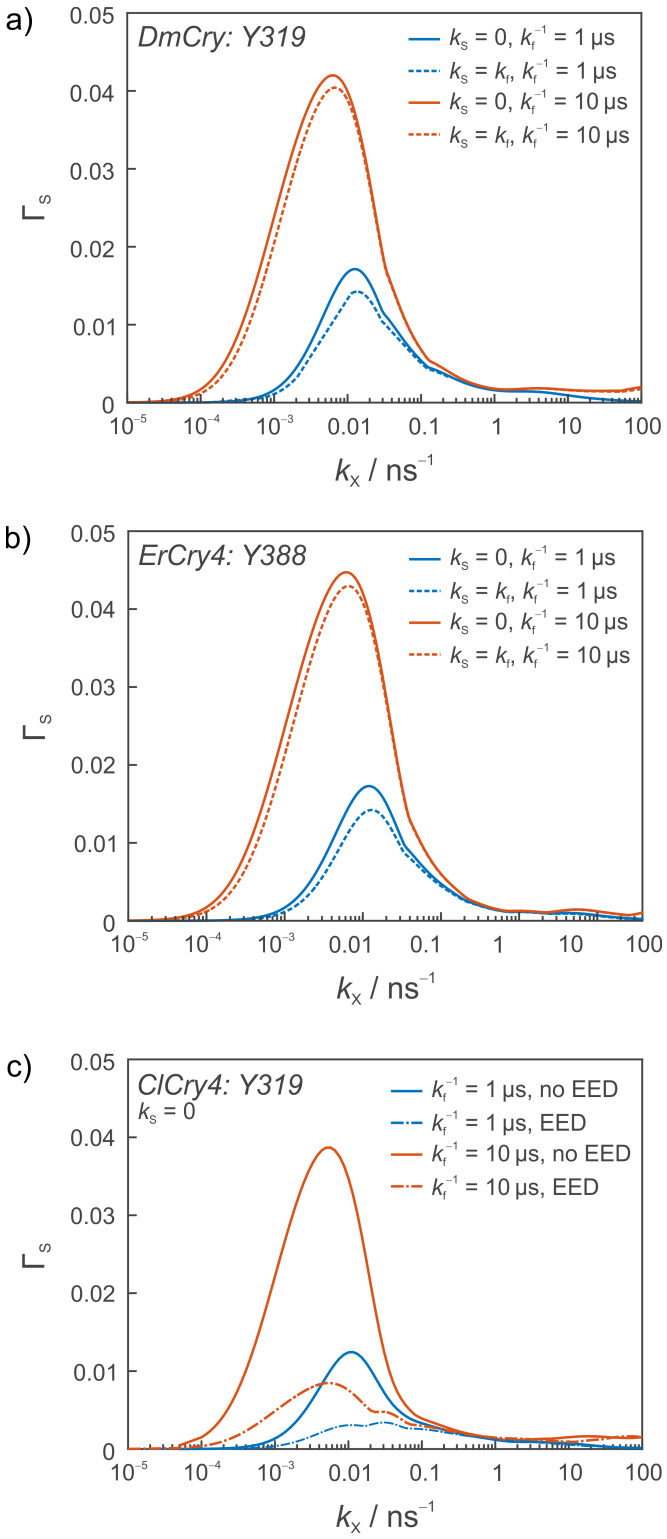

Figure 2.4: Directional magnetic field effects evaluated for models of $FADH^{\bullet}/O_2^{\bullet -}/Y^{\bullet}$ in the limit of infinitely fast spin relaxation in $O_2^{\bullet -}$ presented as a function of the scavenging rate constants k_X. The scavenger radical $Y^{\bullet}$ has been identified with a) Y319 in *Dm*Cry, b) Y388 in *Er*Cry4, and c) Y319 in *Cl*Cry4, respectively. k_S and k_f are specified in the legends; $k_T = 0$. All simulations included the hyperfine interactions of N5, N10, H5, H6, Hβ1 in $FADH^{\bullet}$ and Ho1, Ho2, and Hβ2 in $Y^{\bullet}$. For a) and b), EED interactions have been neglected; c) provides simulations with (dashed-dotted lines) and without (solid lines) EED interactions.

a surface-exposed tyrosine extending the tryptophan tetrad. Radical formation at this site has been implicated with the photo-reduction.[30] Despite different relative orientations of these tyrosine residues compared to Y319 in *Dm*Cry, the predicted anisotropies of the three systems are comparable, as is shown in Fig. 2.4. In Figs. 2.4(a) and 2.4(b), we summarize simulations for $k_S = k_f$ in addition to $k_S = 0$. It is apparent that in the presence of significant scavenging, the effect of primary pair recombination, *i.e.*, k_S, is minor, which is in agreement with the findings in the original publication for flavin/tryptophan radical pairs scavenged by radicals devoid of hyperfine interactions.[29] Figures A.3 and A.4 in the supplementary material further explore the dependence of the MFE on the reaction yield and its anisotropy on the intensity of the applied magnetic field. The simulations predict large relative anisotropies, up to 30%, at fields below 10 mT (for larger fields, the anisotropy is reduced) and huge MFEs of the reaction yield of several 100%. It is interesting to note that these MFEs monotonically increase with the applied field without going through an anti-phased low-field feature, as typical for the RPM under the conditions applying for magnetoreception.[99]

The electron-electron dipolar interaction of radicals is inevitably significant in magnetosensitive radical recombination reactions, both in radical pair and radical triad scenarios, where radicals are restrained at a distance allowing for mutual recombination, typically by distant electron transfer.[25,55] Nonetheless, EED interactions have traditionally been neglected for simplicity, reduction of computational effort, and possibly on conceptual grounds, as the RPM places an emphasis on the hyperfine-driven spin-state conversion. Recently, unexpected rich MFEs have been predicted for three-radical systems due to the EED coupling alone,[26,83] while the suppressive effect of EED interactions on the low-field sensitivity has raised doubts about the RPM hypothesis of magnetoreception.[25] Both observations motivate the exploration of the profound effects of EED coupling in the scavenged $FADH^{\bullet}/O_2^{\bullet-}$ systems.

In the limit of fast $O_2^{\bullet-}$ relaxation, the EED-interactions involving $O_2^{\bullet-}$ are effectively averaged. Thus, the spin dynamics are independent of the location of $O_2^{\bullet-}$ relative to the flavin and tyrosine radicals that governs its EED coupling [see Eq. (2.4)]. EED interactions will still impact on the MFEs via the $FADH^{\bullet}/Y^{\bullet}$ coupling. Possibly not unexpected in view of the suppressive effect found in Ref. 25, we find that here too the directional MFEs are strongly suppressed by the EED coupling. This is demonstrated for Y319 in Fig. 2.4(c).
For $k_f^{-1} = 1\,\mu$s, Γ_S of this system is reduced from 1.3×10^{-2} to 3.4×10^{-3} , whereby a larger k_X is necessary to elicit this maximal effect. For Y319 in *Dm*Cry, the suppression is even stronger, which is in line with the larger EED coupling present at

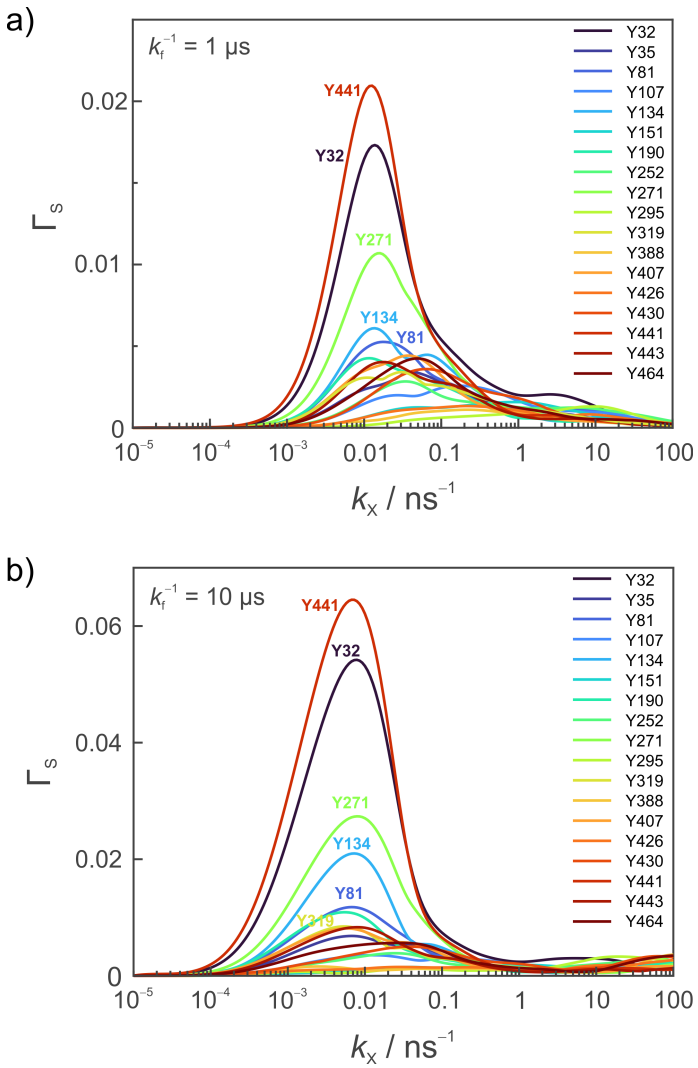

Figure 2.5: Directional magnetic field effects evaluated for various FADH$^\bullet$/$O_2^{\bullet-}$/Y$^\bullet$ radical triads based on the crystal structure of *Cl*Cry4 for $k_f^{-1} = 1\,\mu$s (a) and $10\,\mu$s (b). The simulations have assumed infinitely fast spin relaxation in $O_2^{\bullet-}$, $k_S = k_T = 0$ and included the hyperfine interactions of N5, N10, H5, H6, Hβ1 in FADH$^\bullet$and Ho1, Ho2, and Hβ2 in Y$^\bullet$. The effect of the EED coupling was fully taken into account. The systems differ in the assumed position of the Y$^\bullet$, which is indicated in the legend in terms of the residue number in the crystal structure of *Cl*Cry4 (PDB ID: 6PU0).

the shorter inter-radical distance. For this system with $k_f^{-1} = 1\,\mu$s, Γ_S is reduced from 1.7×10^{-2} to a mere 2.3×10^{-3}. Moreover, the peak of sensitivity of this system is shifted to markedly larger scavenging rate constants k_X ($8.2\,\text{ns}^{-1}$ as opposed to $0.013\,\text{ns}^{-1}$ without EED). Figure A.5 illustrates the dependence of the MFE on k_X for various tyrosine sites.

While the suppressive effect of the EED coupling is discouraging, the effect is expected to strongly vary with distance and orientation of the radicals involved. This led us to carry out a systematic exploration of the suitability of the various tyrosine sites in the cryptochrome protein to sustain large three-radical MFEs. These data are the main results of this contribution. We opted to use *Cl*Cry4 and *Dm*Cry as template structures (for which the crystal structures have been resolved, at least in part[30,112]) and again considered lifetimes of $k_f^{-1} = 1$ and $10\,\mu$s. The primary radical recombination rate constant was set to $k_S = 0\,\mu\text{s}^{-1}$, as the predictions are broadly insensitive to this choice. The exchange coupling of the scavenger and the flavin semiquinone was neglected in order to reduce the number of parameters to the manageable set of k_X and tyrosine-location in the protein (experimental values of the exchange interaction are available for the terminal tryptophans of the triads/tetrads of selected cryptochromes and photolyases, for which they appear to be negligibly small).[56] The eight largest hyperfine interactions, five in $\text{FADH}^\bullet$ and three in $\text{Y}^\bullet$, have been taken into account. A summary of these simulation parameters, compiled in table form for convenience, is available in Appendix A (Table A.1). Also provided are the relative positions and orientations of $\text{FADH}^\bullet$ and $\text{Y}^\bullet$ radicals for *Cl*Cry4 (Figure A.1 and Table A.2) and *Dm*Cry (Table A.3). Figure 2.5 summarizes the dependence of the directional MFEs for the 18 tyrosine residues in *Cl*Cry4. The maximal Γ_S's range from 1.1×10^{-3} to 0.021 and 2.6×10^{-3} to 0.065 for $k_f^{-1} = 1$ and $10\,\mu$s, respectively. Here, we find that for many tyrosine residues in *Cl*Cry4, the MFEs remain large in the presence of EED coupling. This applies, in particular, for (in the order of decreasing maximal Γ_S) Y441, Y32, Y271, Y134, Y81, and Y190, for which large effects are observed for both $k_f^{-1} = 1$ and $10\,\mu$s. Note further that for these systems, the maximal MFEs occur at the "usual" scavenging rate constants of $k_X \simeq 10\,\mu\text{s}^{-1}$ and that the longer lifetime, *i.e.*, $k_f^{-1} = 10\,\mu$s, gives rise to larger sensitivity, as expected. Figure A.5 provides a similarly exhaustive exploration for the tyrosine residues in *Dm*Cry for $k_f^{-1} = 1\,\mu$s, both in the presence and absence of EED coupling. Maximal Γ_S's are of the order of 2% and 1% in the absence and presence of EED coupling, respectively. If the EED interaction is ignored, the largest effects are predicted for Y328, Y317, and Y319; with EED coupling included, the MFEs of the two surface-exposed residues Y90 and Y211 exceed those of other sites by more than a factor of three at their respective optimal k_X.

2.6 Discussion

2.6.1 Magnetosensitivity of the reoxidation

The potential magnetosensitivity of the cryptochrome reoxidation reaction has been widely discussed following up on works of Ritz et al., proposing the involvement of molecular oxygen, and later Maeda et al., proposing superoxide.[77,100] The flavin semiquinone/superoxide radical pair is central to this hypothesis.[82,101,102] In terms of its hyperfine interaction structure alone, this model promises superior magnetosensitivity, vastly exceeding that of flavin/tryptophan radical pairs.[72,103] However, in free solution, superoxide is subject to fast spin relaxation as a consequence of its orbitally degenerate ground state and thus non-zero angular momentum, which gives rise to huge g-tensor anisotropy and eventually swift spin relaxation via the spin-rotational mechanism.[86] It is for this reason that the model has widely been viewed as improbable,[102] leading to the widespread practice of postulating a radical, usually denoted $Z^{\bullet}$,[72] which shares superoxide's favorable features in terms of being devoid of hyperfine interaction but is freed of its stigma of fast spin relaxation. The recent observations of dark-state magnetosensitivity, however, have brought the superoxide hypothesis back into the spotlight of cryptochrome's magnetosensitivity.[11,64,65] Further indirect support has been found in the observation of magnetoreception being affected by green/red light in some experiments and its feasibility under low light conditions.[76] Note, however, that as for now, no consensus as to the identity of the radical pair has been reached.

A frequent argument suggests that $FADH^{\bullet}/O_2^{\bullet -}$ could be feasible if the superoxide's rotational tumbling was hindered and/or its molecular symmetry reduced, *i.e.*, its angular momentum quenched.[69,102] This implies that the radical would have to strongly interact with its environment, *i.e.*, be essentially immobilized. This notion, however, is equally unsuccessful as immobilization at a feasible reaction distance[2] gave rise to larger, non-averaged EED coupling, which in model calculations effectively suppresses the magnetosensitivity of the radical pair recombination in weak magnetic fields.[25]

2.6.2 Magnetosensitivity enabled by three-radical interactions

We here suggest that this impasse can be overcome by a model involving three radicals, whereby the primary flavin semiquinone superoxide radical pair is scavenged in a spin selective recombination reaction with a third radical. This model was conceptually introduced in Ref.,[82] where the authors demonstrated vastly enhanced

directional sensitivity and resilience to spin relaxation in the non-scavenged radical of the primary pair, at least for simple model systems and neglecting the EED interaction. Here, we have subjected this idea to test under more realistic conditions, whereby we focus on the hypothetical scavenging reaction from a long-lived tyrosine radical inside of the protein for concreteness. We have realized a systematic survey for 18 tyrosine residues in the vicinity of the FAD cofactor in *Cl*Cry4, whereby a realistic but necessarily simplified model of the hyperfine structure, the relative orientation of the radicals, and their unavoidable EED coupling have been considered. In the limit of fast spin relaxation in the superoxide, the spin dynamics have been found to essentially correspond to that of the radical pair of $FADH^\bullet$ and $Y^\bullet$, subject to an F-pair initial condition, spin-selective recombination due to the scavenging reaction, and an altered lifetime. While thus showing similarity to strongly asymmetric radical pair recombination reactions,[113] the model permits the radical pair generation via dark-state reactions, such as the direct oxidation of the fully reduced FAD with molecular oxygen under production of superoxide. The fast relaxation of the superoxide could in this model offer an advantage, as it averages the large EED coupling of the $FADH^\bullet/O_2^{\bullet-}$ pair at the short reaction distance for hydroperoxide formation (a study has identified a likely binding site of $O_2^{\bullet-}$ in immediate vicinity of H5 of $FADH^\bullet$),[2] which otherwise exerted a strongly suppressive effect on the magnetosensitivity. While this suppression can, in principle, be overcome in slowly relaxing three-radical schemes, as has been shown in Refs. 25 and 27, it requires comparable EED coupling of the involved radicals. This, however, implies that all three radicals had to be close in space, which could turn out impractical/improbable in practice. In this sense, the fast relaxation in $O_2^{\bullet-}$ is recognized to simplify the model prerequisites.

We have here found that the three-radical scheme $FADH^\bullet/O_2^{\bullet-}/Y^\bullet$ with quickly relaxing $O_2^{\bullet-}$ predicts comparably larger anisotropy of the MFEs even if the suppressive effect of the EED coupling is accounted for. Specifically, the model delivers yield anisotropies exceeding those of the realistic model of $FAD^{\bullet-}/W^{\bullet+}$ even when the suppressive EED is neglected in the latter.[3,63] Several auspicious Y-residues have been identified in *Cl*Cry4 that sustained large MFEs. Inspecting the location of the radicals relative to the FAD, one realizes, however, that particularly large MFEs arise from distant Ys typically located at the protein's surface (see Fig. 2.1), *i.e.*, the data appear to reflect an intrinsic tendency to reduce the EED coupling by increasing the inter-radical distance. Indeed, we find a strong correlation of the maximally attainable relative anisotropy Γ_S (for the optimal k_X) and the inter-radical distance. For $k_f^{-1} = 1\,\mu$s, Pearson's correlation coefficient of the FAD-N5-Y-OH-distance and Γ_S amounts to $R = 0.82$ for the combined *Dm*Cry and *Cl*Cry4 data; for $k_f^{-1} = 10\,\mu$s in *Cl*Cry4, we find $R = 0.79$ (the correlation of Γ_S and dipolar interaction strength, which scales with r^{-3}, is weaker; $R = -0.49$). Further note that the simple correlation

of the MFE and distance appears to be a consequence of essentially reducing the system dynamics to that of the pair, *i.e.*, this tendency had not been identified for slowly relaxing three-radical systems in Ref. 27.

2.6.3 Scavenging rates vs inter-radical interactions

The effect requires an efficient scavenging reaction with the rate constant $k_X \simeq 10\,\mu s^{-1}$ or more for small inter-radical distances. Thus, a balance needs to be struck between reducing the EED coupling by increasing the inter-radical distance and the need to sustain this reaction rate. Among the Ys identified for *Cl*Cry4 to potentially give rise to sizable effects (if a suitable k_x could be realized), Y319 has attracted particular attention ($\Gamma_S = 8.5 \times 10^{-3}$ for $k_f^{-1} = 10\,\mu s$).[82] Y319 extends the highly conserved electron transfer pathway provided by the tryptophan tetrad (W_A, W_B , W_C , and W_D in Fig. 2.1; the Y319-W_D distance is only 3.9 Å).[52] Is it conceivable that the very same pathway that facilitates the charge separation in the photo-reduction could enable the scavenging as previously hypothesized?[82] The smallest tyrosine-to-isoalloxazine distance (R) amounts to 17.1 Å (between O in Y319 and C7M in FAD). If we assume that the scavenging reaction proceeds by diabatic, long-distance electron transfer, we can estimate the scavenging rates using the Moser-Dutton ruler,[114]

$$\log_{10} k_x \simeq 13 - \frac{\beta}{2.3}(R - 3.6) - 3.1\frac{(\Delta G_{et} + \lambda)^2}{\lambda}. \tag{2.16}$$

where the first term, $\frac{\beta}{2.3}(R-3.6)$, is an electronic term proportional to the strength of the coupling between the donor and acceptor species, taken to follow an exponential decay in the electron tunneling rate proportional to $e^{\beta/R}$; where R is the edge-to-edge distance separating the donor and the acceptor, and β is proportional to the square root of the barrier height. The second term depends on the energetic requirements to going from the reactant (*i.e.* before electron transfer) to product (after electron transfer) states: it includes the driving force ΔG_{et}, the free energy difference between the reactant and product states ; and the reorganisation energy λ, the energy required to reorganise nuclear coordinates upon electron transfer.
In the most favorable activation-less limit ($\Delta G_{et} = -\lambda$, $\Delta G_{et}^{\neq} = 0$) and using typical values for β (which represents the exponential decay of the coupling-matrix element-squared with distance) ranging from 0.9 and 1.4 $Å^{-1}$,[115,116] one obtains values of k_X between 6×10^5 and $5 \times 10^8\,s^{-1}$. Thus, provided that the coupling is efficient, the required k_X is at least not infeasible. However, it should be noted that the electron transfer rates would have to be modulated throughout the photo-cycle. In particular, the charge recombination ought to be slow in the fully reduced state (to avoid premature reoxidation of the flavin) and fast once the re-oxidation was initiated by reaction with molecular oxygen. That such modulation is, in principle, possible

is hinted at in several studies. A recent molecular dynamics investigation of the photo-activation of *Cl*Cry4 identified significant changes of the FAD-W_D distance, and thus electron transfer rates, set in motion by the charge redistribution associated with the photoreduction.[34] Metabolite binding and (de-)protonation reactions can strongly modulate electron transfer rates in cryptochromes.[117]

The requirement could also be fulfilled if the $FADH^\bullet/Y^\bullet$ recombination is in the Marcus inverted region, while the less exergonic $FADH^\bullet/Y^\bullet$ is close to activationless. While experimental insights do not yet allow a serious assessment of the feasibility of a three-radical processes involving Y319, it is reassuring that Y319 appears to enhance the efficiency of photo-reduction in *Cl*Cry4 in vitro, thereby hinting at the possibility of formation of a long-lived tyrosine radical at this location.[30] It is also worth mentioning that the mechanism as suggested here correctly predicts the enhancement of the signaling state yield in modest magnetic fields (0.5 mT) as observed for the dark-state MFEs in plants (while the radical-pair mechanism will predict a decrease for the triplet-born $FADH^\bullet/O_2^{\bullet-}$ - radical pair due to the low-field effect).[65] Finally, note that while the MFE predicted for Y319 in *Cl*Cry4 is not among the largest observed here, further enhancement appear realizable by optimizing the relative position of the radicals in space, even when keeping the inter-radical distance constant. That this is possible in principle is, *e.g.*, demonstrated by Y134 in *Cl*Cry4, for which large MFEs ($\Gamma_S = 0.021$) are predicted despite its smaller distance from FAD compared to Y319.

In view of the systematic study of *Cl*Cry4 presented above, it is furthermore remarkable that the optimal k_X tends to increase with decreasing distance, at least for FAD-Y distances smaller than $\simeq 25$ Å; for larger distances, the distance dependence is weak. Thus, at least in part the deleterious effect of large electron-electron dipolar couplings at small reaction distances appears to be compensated by increased scavenging reaction rate constants. This is not unknown for radical pair reactions, to which the spin dynamics of the radical triad system are here effectively reduced due to the assumed fast spin relaxation in superoxide. Specifically, Kominis and coworker previously showed that the effect of the exchange coupling can be ameliorated by fast triplet recombination via the quantum Zeno effect, *i.e.*, a decreased decay rate of quantum states subject to frequent measurement, reaction events, or other decoherence generating processes.[118,119] It appears that here a similar principle is at play. However, the compensation results from the fast singlet recombination that the scavenging reaction equates to in the limit of fast $O_2^{\bullet-}$ relaxation. Indeed, following Ref. 118, a simple model based on the coherent interconversion of degenerate singlet and triplet states with frequency ω subject to fast singlet recombination with rate k_X shows that one of the eigenstates of the Liouvillian decays with rate $4\omega^2/k_X$. This

quantum Zeno scaling, *i.e.*, the larger the interrogation rate k_X, the slower the decay, can enhance the sensitivity to weak magnetic fields. Note that while a fast triplet recombination is not expected in the avian compass system,[120] here the asymmetric relativity is introduced indirectly via the scavenging processes, for which a variety of processes are conceivable.

2.6.4 Chemical requirements of the tyrosyl radical hypothesis

Here, we have focused on the requirements that would enable a $FADH^{\bullet}/O_2^{\bullet-}/Y^{\bullet}$-magnetosensor from the point of view of spin dynamics. In addition, such a system is obviously constrained by its chemistry.[82] First and foremost, the Y-radical has to be formed. Ideally this radical ought to be persistent to enable "on-demand" magnetoreception, for which the "charging" (*i.e.*, the accumulation of scavenger radicals) of the compass and its readout (*i.e.*, light-independent reoxidation) are temporally separated to also work in the night.

As for $Y^{\bullet}$-formation, the process could be facilitated by photo-activation and accompany the photoreduction as suggested above for Y319 in *Cl*Cry4.[82] It could also be realized by chemical, *i.e.*, dark, one-electron oxidation of tyrosine by mechanisms that include oxidation by hydrogen peroxide and peroxidases, hydroxyl radical- and metal-catalyzed oxidations, and electron or hydrogen transfer to other radicals.[121] In fact, dark-state tyrosyl radicals are part of the enzymatic catalytic cycle of, for example, ribonucleotide reductase, prostaglandin synthase, and lactoperoxidase and are also formed on myoglobin and hemoglobin during reaction with hydrogen peroxide (see Ref. 121 and references therein).

As for the lifetime constraint, long-lived tyrosine radicals have been observed as a product of the photo-reduction in the animal-like cryptochrome in the green alga *C. reinhardtii* (lifetime: 2.6 s)[31] and a cryptochrome from *A. thaliana* (100 μs).[32] Arguably, these lifetimes are too short to allow ample radical accumulation under light for later readout in the dark, but it could still rationalize the flickering-light experiments. On the other hand, more persistent tyrosyl radicals are well known in biochemistry. The classical example is provided by the radical of the redox-active tyrosine residue Y_D in the photosystem II, which exhibits lifetimes up to hours, depending on preparation.[33] Although for now no such long-lived tyrosyl radical has been observed in avian cryptochromes (or other magnetosensitive animal cryptochromes), its occurrence is not infeasible and, in our opinion, should be considered a target of experimental efforts.

In general, chemical factors cannot currently be assessed beyond speculation. The true magnetoreceptor is not identical to free cryptochrome, as recently discussed.[53] Protein-protein interactions, immobilization, and association with the appropriate signaling partners are deemed essential to realize sensitivity to magnetic fields of around 50 μT in vivo, all of which will impact on the feasibility of $FADH^{\bullet}/O_2^{\bullet-}/Y^{\bullet}$.

It has become clear from the discussion that several requirements (k_X, scavenger location, chemistry) have to be met for the three-radical processes to function as a sensitive compass as originally envisaged. We think that it is not unconceivable that such a complex but more sensitive mechanism has resulted as the apex of an evolutionary optimization process. One could imagine that rudimentary magnetosensitivity was present in the photo-reduction but succeeded by a three-radical process realized on the basis of the pre-existing, basic building blocks. This could have offered greater sensitivity (limited by the lacking symmetry of hyperfine interactions in $W^{\bullet+}$ and by EED interactions; see Refs. 72, 3, and 122) and reception on demand/despite low light levels, for which the accuracy of the photo-reduction-based compass is likely insufficient.[76]

2.6.5 Ascorbyl radical: A better model?

We here focus on a mechanism within cryptochrome and have hence assumed the scavenger in the form of tyrosine radicals, putatively generated in the preceding photo-reduction. This was a deliberate decision for this study made for concreteness but does not present a necessity. In fact, alternative choices could be more favorable. Assume, for example, that the oxidation equivalent made available in the photo-reduction, via the tryptophan tetrad, ends up in a stable radical derived from a radical scavenger (in the original sense of the term), such as, for example, ascorbic acid, $AscH_2$. Following the reaction cycle as in Fig. 2.1, but with the ascorbyl radical ($Asc^{\bullet-}$) instead of the tyrosine residue, could give rise to a $FADH^{\bullet}/O_2^{\bullet-}/Asc^{\bullet-}$ radical triad. Figure 2.6 shows the directional MFEs calculated for this system as a function of the rate of the $FADH^{\bullet}/Asc^{\bullet-}$-recombination reaction. Huge Γ_S's of the order of 60% appear feasible for this system. This large effect could, however, come at the cost of less tight control (compared to $FADH^{\bullet}/O_2^{\bullet-}/Y^{\bullet}$), as it involved a freely diffusing $Asc^{\bullet-}$. It is interesting to note that the $FAD^{\bullet-}/Asc^{\bullet-}$-radical pair has been previously suggested in the context of the photo-reduction as a more potent radical pair[72] but rejected as the formation of the ascorbyl radical from the primary $FAD^{\bullet-}/W^{\bullet+}$ could not compete with its recombination.[123] This is not a limitation here as the $Asc^{\bullet-}$ formation precedes the radical triad processes and could thus be realized on a slow timescale either via the photo-reduction or independent pathways.

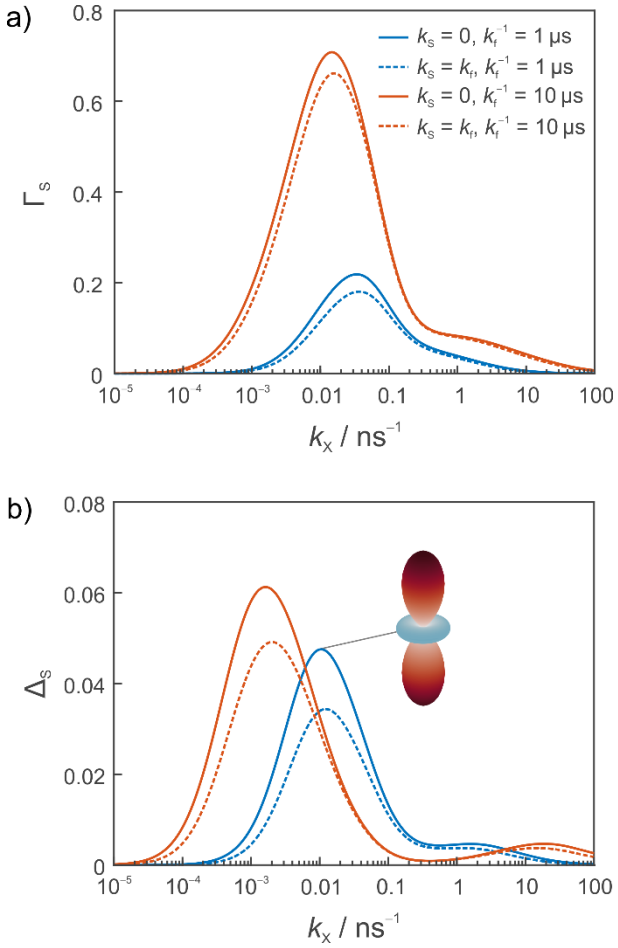

Figure 2.6: Directional magnetic field effects evaluated for $FADH^{\bullet}/O_2^{\bullet -}/Asc^{\bullet -}$ radical triad, where $Asc^{\bullet -}$ denotes a freely diffusing ascorbyl radical. The relative anisotropy (a) and absolute spread of the reaction yield of the signalling state are shown in a) and b), respectively. k_f and k_S are indicated in the legend of a), which applies throughout. The simulations have included the hyperfine interactions of N5, N10, H5, H6, Hβ1 in $FADH^{\bullet}$ and the isotropic interaction of H4 in $Asc^{\bullet -}$. The model does not depend on the identity of the cryptochrome.

2.6.6 Superoxide MFEs beyond magnetoreception

Eventually, we want to point out that superoxide containing radicals have been suggested to underpin a broad range of magnetic field and isotope-sensitive reactions beyond the established paradigm of cryptochrome magnetoreception. Usselman et al. used oscillating magnetic fields at the Zeeman resonance to impact on reactive oxygen species (ROS) partitioning and thus cellular bioenergetics, which the authors attributed to the $FADH^{\bullet}/O_2^{\bullet -}$ - radical pair.[124,125] Sherrard et al. demonstrated that exposure to weak magnetic fields can induces ROS production in human cells and that this process requires the presence of the cryptochrome receptor.[126] Smith and co-workers suggested that isotope effects on xenon-induced anesthesia[127] and the

lithium treatment of bipolar disorder[128] could both be linked to transient, superoxide containing radical pairs. Zhang et al. demonstrated that hypomagnetic fields attenuate hypocampal neurogenesis and cognition in mice and that this effect is correlated with a reduction of reactive oxygen species.[129] While in these contexts magnetosensitivity appears to emerge as a serendipitous side effect, the suggested processes share much similarity with the $FADH^{\bullet}/O_2^{\bullet-}$ -model of cryptochrome magnetoreception. Here too, the question of fast spin relaxation in $O_2^{\bullet-}$ appears pertinent. While it is unlikely that a complex three-radical processes of the marking $FADH^{\bullet}/O_2^{\bullet-}/Y^{\bullet}$ could be relevant here too, because the complexity of the mechanism likely mandated evolutionary optimization, a $FADH^{\bullet}/O_2^{\bullet-}/Asc^{\bullet-}$ process appears possible. Highly reactive radicals are quickly sequestered in biological systems, usually under the formation of persistent, less reactive species, such as $Asc^{\bullet-}$, which could engage in the suggested three-radical process. In this context, it is interesting to note that many observations of dark-state MFEs appear to implicate a relation with oxidative stress[130] and thus the overall radical concentration, in line with the expectations of the three-radical hypothesis.

2.6.7 Suggested experiments

The reoxidation of cryptochrome and its putative magnetosensitivity remain a mystery. Here, we have suggested a way by which this processes could elicit magnetosensitivity despite its involvement of quickly relaxing reactive oxygen species, such as superoxide. It is clear that many questions about feasibility and concrete implementation, including the identity of the scavenger radical, remain speculative. We hope nonetheless that this theoretical analysis is able to instigate dedicated experiments. A simple experiment could be built around the cyclic photo-reduction and dark re-oxidation of a cryptochrome *in vitro*. Magnetic fields could be applied selectively during the dark reoxidation, while the fluorescence of the flavin cofactor could be used to readout the oxidation yield during the photo-reduction cycle. Probing the magnetosensitivity of the processes while varying the frequency of photo-reduction and reoxidation cycles, optionally in the absence and presence of, *e.g.*, ascorbic acid, would allow valuable, needed insights to solve the cryptochrome puzzle. In addition, the identification of putatively long-lived tyrosyl radicals in avian cryptochromes and, in particular, their assemblies *in vivo* is suggested.

2.6.8 Conclusions

In summary, we have presented comprehensive simulations of radical triad systems comprising the flavin semiquinone, superoxide, and a tyrosine radical in cryptochrome. Assuming that the tyrosine radical can undergo a spin-selective recombination reaction with the flavin radical, this model delivers sizable directional

magnetic field effects in the geomagnetic field, even if the superoxide is subject to fast spin relaxation and electron-electron dipolar interactions are fully accounted for. Specifically, we have shown that in the limit of infinitely fast spin relaxation in the superoxide, the spin dynamics observables correspond to those of the flavin semiquinone tyrosine system with random initial spin configuration, spin-selective recombination, and an altered effective lifetime. For the model to elicit marked magnetosensitivity in the geomagnetic field, the scavenging reaction ought to proceed swiftly, *i.e.* with rate $k_X \simeq 10^7\,\mathrm{s}^{-1}$ or larger. This requirement and a systematic exploration of the effect for the tyrosine residues in pigeon cryptochrome 4 show that Y319 is a possible candidate to facilitate such enhanced three-radical MFEs. Being located at the end of the tryptophan tetrad, Y319 appears to form long-lived tyrosine radicals that could act as scavengers of $\mathrm{FADH}^\bullet$, generated in the reoxidation of FADH^-, via a long-range electron transfer processes mediated by the tryptophan tetrad.

The aim of this work was to test the hypothesis of a scavenging-enhanced MFE in a more realistic context than previously explored. In particular, the complexity arising from many hyperfine-coupled nuclear spins, the relative orientations of radicals, and the electron-electron dipolar coupling have been considered. The requirement to sustain a fast scavenging reaction while simultaneously reducing the EED coupling has been identified as the limiting factors in the employed $\mathrm{FADH}^\bullet/\mathrm{O}_2^{\bullet-}/\mathrm{Y}^\bullet$ model. In the limit of fast relaxation in the $\mathrm{O}_2^{\bullet-}$, the location of the superoxide relative to the other radicals is inconsequential, *i.e.*, radicals at close contact can be accommodated, but the processes is more susceptible to the electron-electron dipolar coupling in the $\mathrm{FADH}^\bullet/\mathrm{Y}^\bullet$Here, slowly relaxing, *i.e.*, immobilized $\mathrm{O}_2^{\bullet-}$ could provide the additional degrees of freedom needed to compensate the mutual dipolar coupling and further boost the magnetosensitivity.[27] Fast relaxation in $\mathrm{O}_2^{\bullet-}$ reduces the spin dynamics to that of an effective radical pair system that has lesser degrees of freedom to compensate for the delirious effect of the mutual EED coupling.

The $\mathrm{FADH}^\bullet/\mathrm{O}_2^{\bullet-}/\mathrm{Y}^\bullet$ system here has been elected for study for concreteness, but we also acknowledge that systems involving a freely diffusing scavenger radical besides the quickly relaxing superoxide might fare better in sustaining large MFEs, as they avoid the suppressive effect of the electron-electron dipolar interaction by design. With this in mind, $\mathrm{FADH}^\bullet/\mathrm{O}_2^{\bullet-}/\mathrm{Asc}^{\bullet-}$, where $\mathrm{Asc}^{\bullet-}$ is a freely diffusing stable radical resulting from a radical scavenger, such as ascorbic acid, has been realized as an exquisitely magnetosensitive system. The simplicity and general abundance of radical scavenger-derived radicals suggests that this potent spin chemical scheme could be relevant for many recent observations or suggestions of magnetic field and isotope effects involving reactive oxygen species. Overall, we find that the three-

radical model involving a scavenging reaction is feasible in principle. The issue of the electron-electron dipolar coupling suppressing the effect can be sidestepped for freely diffusing systems and mitigated in systems of three immobilized radicals by suitable placement of the radicals.

2.7 Acknowledgements

We gladly acknowledge the use of the University of Exeter High-Performance Computing facility and GENCI supercomputers (Grant No. A0080706913). This work was supported by the UK Defence Science and Technology Laboratory (Grant No. DSTLX-1000139168), the Office of Naval Research (ONR Award No. N62909-21-1-2018), and the EPSRC (Grant No. EP/V047175/1).

2.8 Chapter conclusion and perspectives

In this study, we have investigated the ability of a tyrosine radical $Y^\bullet$ to function as a scavenger in a realistic [$FADH^\bullet$-$O_2^{\bullet-}$-$Y^\bullet$] radical triad, using spin dynamics simulations parametrised with radicals positions and relative orientations taken from a model of pigeon cryptochrome 4 *cl*Cry4. Importantly, $O_2^{\bullet-}$ spin relaxation and electron-electron dipolar (EED) coupling between radicals were included in the simulations. The inclusion of these physical effects and the use of geometrical data taken from an avian cryptochrome, as opposed to plan or drosophila protein, constitute the main novelty of this research.

In a first time, following recent experimental data implicating a dark-state form of the flavin as the magnetosensitive form, we tested the feasibility of a [$FADH^\bullet$-$O_2^{\bullet-}$] radical pair with a realistic $O_2^{\bullet-}$ relaxation rate. Even neglecting EED coupling – a conceptually valid approximation for a free-diffusing radical –, no significant relative singlet yield anisotropy (Γ_S) could be achieved. As a measure of the directional sensitivity, this result indicates no performant magnetic compass could be realised with this radical pair.

The main focus of the study is on the performance of a [$FADH^\bullet$-$O_2^{\bullet-}$-$Y^\bullet$] scavenged compass, here treated in the presence of EED coupling and with immediately relaxing $O_2^{\bullet-}$. This setup effectively reduces the spin dynamics of the system to those of a [$FADH^\bullet$-$Y^\bullet$] pair with altered lifetime. It was found that sizable MFEs, exceeding those achieved by a [$FAD^{\bullet-}$-$W^{\bullet+}$] RP, could be achieved in the case of rather fast scavenging, *i.e.* for scavenging rates of the order of $k_X \simeq 10^7\,\mathrm{s}^{-1}$ or faster.

In particular – and this is the main finding of this study – Y319 was identified as a promising scavenger for a [$FADH^{\bullet}$-$O_2^{\bullet -}$-$Y^{\bullet}$] triad. Its location and orientation is ideal in several respects: first, it is located far enough from the flavin so that EED couplings have significantly decayed, achieving an optimal Γ_S of 8.5×10^{-3}. Second, its distance to the flavin makes it possible for the optimal scavenging rate to be attained. Lastly, Y319 is located only 3.9 Å away from the terminal tryptophan W_D, involved in the photoreduction of FAD^* into $FAD^{\bullet -}$, and Y319 itself seems to be implicated in this process.

These results, while extremely encouraging, warrant further research on multiple fronts. Electron-electron dipolar coupling has been identified as having a very strong suppressive effect on MFEs; an effect which could be overcome with slowly-relaxing 3-radical systems.[25,27] The possibility to realise a slowly-relaxing [$FADH^{\bullet}$-$O_2^{\bullet -}$-$Y^{\bullet}$] triad *via* $O_2^{\bullet -}$ immobilisation by the cryptochrome is explored in Chapter 4. The dependence of EED coupling strength on not only distance, but also relative orientation, calls into question the accuracy of Γ_S computed on a single structure. An analysis of tyrosine flexibility in a dynamic environment, as well as a study of the sensitivity of EED coupling to small and large reorientations, would allow to conclude on the performance achievable by these tyrosine residues in a biological environment. Other points that need dedicated research efforts is the computation of accurate electron transfer rates between $FADH^{\bullet}$ and Y319, and the estimation of $Y^{\bullet}$ lifetimes in avian cryptochromes.

Another avenue to improve the description of the spin dynamics for all triads considered in this study is the computation of dedicated hyperfine coupling (HFC) tensors for the flavin radical, taking into account the dynamical nature of the cryptochrome protein into which it is embedded. This is the subject of Chapter 3.

Finally we explored the possibility of a [$FADH^{\bullet}$-$O_2^{\bullet -}$-$Asc^{\bullet -}$] radical triad, which in the context of reoxidation does not suffer from the mechanistic limitation of formation from [$FAD^{\bullet -}$-$W^{\bullet +}$]. While still hypothetical, we report extremely large Γ_S values for an ascorbyl scavenger. We suggest an experimental study to verify whether its involvement, at least *in vitro*, is possible.

CHAPTER 3

PARAMETRISING THE SPIN HAMILTONIAN: DYNAMICAL AND ENVIRONMENT EFFECTS ON THE FLAVIN HYPERFINE STRUCTURE.

3.1 Chapter introduction

The following chapter presents a comprehensive computational study of the hyperfine coupling (HFC) tensors describing the magnetic structure of the cryptochrome-bound flavin. As mentioned in Chapter 1, the hyperfine interactions of a radical electron with its neighbouring magnetic nuclei is one of the contributor to the spin Hamiltonian, which means that a correct description of this effect is needed to accurately simulate the spin dynamics of a radical pair or triad. This work was notably carried out with the aim to better parametrise the spin Hamiltonian employed in Chapter 2, in order to verify the scavenging abilities of the promising Y319 identified therein.

Due to the continued research interest in both these spin systems, we consider in this study both oxidation states of the flavin relevant to magnetoreception processes: the radical anion $FAD^{\bullet -}$ formed from the photoreduction, and the radical semiquinone $FADH^{\bullet}$ from the dark-state reoxidation by triplet O_2. The motivation for computing an updated set of tensors for these radicals is the fact that studies on the hyperfine structure of flavins, until now, either neglect dynamical effects,[131] include the environment using an implicit solvent model,[132] approximate the flavin by a truncated analogue,[3,71] or work on proteins not implicated in avian magnetoreception.[133] The latter study concludes that the presence of at least the immediate environment is necessary to achieve a correct description of the hyperfine structure of flavins. While we eventually reach a broadly opposite conclusion – their

assessment is based on the presence of a hydrogen bond to the flavin, which is not present in the model of pigeon cryptochrome we used, but which is notoriously impactful to the electronic structure of the flavin[134] –, this assessment inspired us to compute HFC tensors for these flavins while taking into account dynamical effects. Precisely, we evaluate here the impact of structural fluctuations of the flavin and of the wider protein environment on flavin HFC tensors, as well as the effect of electronic polarisation by its immediate chemical environment.

This is done *via* a long (800 ns) Molecular Dynamics simulation of the flavin within a *Columba livia* cryptochrome 4 (*cl*Cry4). Taking a cluster approach where we explicitly include neighbouring residues into the calculation of flavin HFC tensors, and which we enrich with a QM/MM approach where the rest of the protein is included as point charges, we report an average set of tensors for atoms of interest. We also report the distributions of tensor element values along the dynamics.

The stepwise introduction of dynamical effects realised in this Chapter also allows us to gauge their respective sizes and to decorrelate some of their impact on specific tensors. In particular, we find the electronic polarisation to have, in most cases, a surprisingly weak effect on the flavin hyperfine structure, with the bulk of the variations induced by geometrical distortions due to thermal energy. We however found some specific instances of electronic polarisation impacting the shape of the N5 tensors, with implications to the spin dynamics of a compass operated by such a flavin.

This is a reproduction of the article entitled "*Ab initio* derivation of flavin hyperfine interactions for the protein magnetosensor cryptochrome" published in the Physical Chemistry Chemical Physics (PCCP) journal and available at https://doi.org/10.1039/d1cp05804e. The Supporting Information (SI) are provided in Appendix B.

This work is the result of a collaboration, and was carried out both at the University of Exeter and at Université Paris-Saclay. In terms of contributions: the histidine oxidation state assignment, residue cluster delineation, basis set benchmark, MD simulations (preparation and production), aDFT calculations of magnetic properties and subsequent statistical analysis, and the computation of final HFC tensors, were carried out by Jean Deviers. Creation of most figures, the computation of final HFC tensor standard deviation, graphical representation of the average and variance of final HFC tensors, and providing the initial structure for the protein and the flavin, were the work of Daniel Kattnig. This project was carried out in close collaboration with both universities, and under the monitoring by Daniel Kattnig, Aurélien De la Lande and Fabien Cailliez, with whom frequent discussion were absolutely essential to complete this work.

3.2 Abstract

The radicals derived from flavin adenine dinucleotide (FAD) are a corner stone of recent hypotheses about magnetoreception, including the compass of migratory songbirds. These models attribute a magnetic sense to coherent spin dynamics in radical pairs within the flavo-protein cryptochrome. The primary determinant of sensitivity and directionality of this process are the hyperfine interactions of the involved radicals. Here, we present a comprehensive computational study of the hyperfine couplings in the protonated and unprotonated FAD radicals in cryptochrome 4 from *C. livia*. We combine long 800 ns molecular dynamics trajectories to accurate quantum chemistry calculations. Hyperfine parameters are derived using auxiliary density functional theory applied to cluster and hybrid QM/MM (Quantum Mechanics/Molecular Mechanics) models comprising the FAD and its significant surrounding environment, as determined by a detailed sensitivity analysis. Thanks to this protocol we elucidate the sensitivity of the hyperfine interaction parameters to structural fluctuations and the polarisation effect of the protein environment. We find that the ensemble-averaged hyperfine interactions are predominantly governed by thermally induced geometric distortions of the flavin. We discuss our results in view of the expected performance of these radicals as part of a magnetoreceptor. Our data could be used to parametrize spin Hamiltonians including not only average values but also standard deviations.

3.3 Introduction

Magnetoreception is widespread in the animal kingdom.[8] Despite the phenomenon being well established, the sensory mechanism–and even the underlying principle–has remained opaque for decades.[40] In birds and a few other species, a compass sense has been attributed to a radical pair recombination reaction in the protein cryptochrome.[1,17,42] This spin-selective reaction acquires magnetosensitivity, because the electron spin states of the radical pair coherently interconvert between singlet and triplet states, as the electron spins couple to the applied and local magnetic fields. The latter are caused by the magnetic moments of nuclear spins in the radicals, *i.e.* arise via hyperfine interactions. In this way, hyperfine couplings, including the isotropic Fermi contact and the anisotropic dipole-dipole contributions, are critical in determining the magnetosensitivity and its directionality in the geomagnetic field, which governs the sensitivity of the compass.

The concept of a radical pair model of magnetoreception was originally suggested by Schulten *et al.*.[42] Later, Ritz *et al.* suggested the flavo-protein cryptochrome in the animals' eyes as the actual host of the magnetosensitive radical recombination process.[17] This proposition has since been supported by ample theoretical insight

and biological evidence.[1,135,136] Indeed, there is now a wealth of behavioural studies which confirm the existence of a light-dependent inclination compass, which can be scrambled by radio-frequency electromagnetic fields, as expected for the radical pair model.[1] However, the details of the sensor and its associated pathways have remained elusive so far.

Cryptochromes contain a non-covalently bound flavin adenine dinucleotide (FAD) cofactor, which is tightly linked to its function as a magnetosensor.[137] This flavin exists in two important radical forms, the anion radical ($FAD^{\bullet -}$) and its protonated semiquinone form ($FADH^{\bullet}$), which both have been implicated as members of the magnetosensitive radical pair intermediate. The photo-reduction of fully oxidised flavin in the cryptochrome gives rise to a radical pair, comprising the $FAD^{\bullet -}$ and a surface-exposed tryptophan radical cation, which has been found to be magnetosensitive *in vitro* in the isolated protein, albeit at magnetic fields significantly exceeding the geomagnetic field.[53] $FADH^{\bullet}$ can result from protonation of the anion radical or oxidation of the fully reduced flavin cofactor, $FADH^{-}$. The latter reaction has been suggested to underpin magnetoreception in the dark.[11,65–67,138] While there is ongoing debate about the identity[63,72,102] of the partner radical and even the number[25,27,29,37,82] of radicals involved, the flavin radical, either protonated or in is anionic form, is a central cornerstone of all models.

The hyperfine interaction parameters in the involved radicals are crucial in determining the directional sensitivity of the compass. The hyperfine couplings (HFCs) of the flavin radicals are generally perceived as ideal for its putative function in a directional sensor.[1,3,72] This is the result of the hyperfine structure being dominated by the HFCs of the two central nitrogen atoms of the isoalloxazine ring system, N5 and N10 (see Fig. 3.1), which are strongly anisotropic, close to axial and collinear. In the absence of other strong HFCs, this gives a dominant directionality to the spin dynamics.[72] Particularly large anisotropic magnetic field effects in the geomagnetic field result if these flavin radicals are combined with radicals devoid of hyperfine interactions, *i.e.* in so-called reference-probe configurations.[72,103] On the other hand, partner radicals without overarching symmetry of their hyperfine couplings strongly attenuate magnetic fields effects.[3,63]

Interestingly, the hyperfine structure can impact the spin dynamics in a non-obvious way too: in combination with anisotropic hyperfine interactions in the partner radical (e.g. as provided by a protein-bound tryptophan radical), the flavin anion HFC structure can give rise to a spike in the recombination yield of long-lived radical pairs, which results from a level anti-crossing phenomenon when the magnetic field is parallel to the isoalloxazine ring plane.[3] This remarkable observation emphasizes the truly quantum nature of cryptochrome magnetoreception, as the feature is only apparent in fully quantum spin dynamics simulations, but absent in

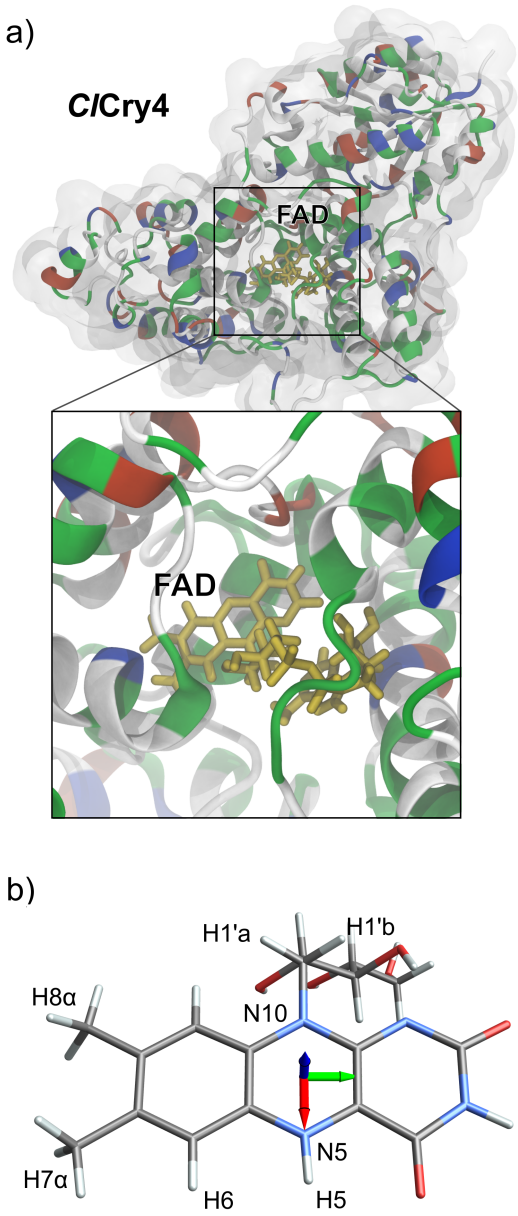

Figure 3.1: Graphical representation of (a) the pigeon cryptochrome 4 protein (*Cl*Cry4; PDB ID: 6PU0 with phosphate binding loop reconstructed) and (b) the FAD cofactor in its semiquinone form $FADH^{\bullet}$. (a) shows the chemical environment of the flavin. Residues coloured in blue are cationic; in red, anionic; and in green, polar. (b) introduces the numbering scheme for pertinent nuclei and the standard orientation used throughout this paper. Red axis = **x**, green = **y**, blue = **z**. In the anion radical $FAD^{\bullet -}$, the hydrogen labeled H5 is absent. H7α and H8α are generic labels for the 3 hydrogens born by the methyl groups on the isoalloxazine ring.

semi-classical realisations of the modeling.[139] The effect too relies on the hyperfine interactions of N5 and N10, specifically on the small but, importantly, nonzero transverse components. A small increase in their magnitude has been shown to enhance the effect.[3]

Many theoretical studies have been dedicated to understanding the electronic structure and properties of flavins in proteins. The reader is referred to Kar *et al.* for a review focusing on electronic spectra.[140] On the other hand, theoretical studies aiming to calculate hyperfine tensors for flavin radicals are much fewer, and either neglect dynamical effects,[131] include the environment using an implicit solvent model,[132] approximate the flavin by a truncated analogue,[3,71] or work on proteins not implicated in avian magnetoreception. Indeed, hyperfine interactions and *g*-matrices have only been predicted for the bound flavin radicals in glucose oxidase from *A. niger*, whereby a QM/MM molecular modeling approach was chosen.[133] The authors' conclusion, that incorporation of at least the nearest protein environment of the cofactor radicals proved to be vital for a correct reproduction of shifts in *g*-matrix components, supports the idea that accurate coupling parameters for the simulation of the avian magnetic compass must be computed in an avian protein, as we do here. Note however that the MD simulations reported in ref. 133 were based from short MD simulations of only 10 ps. Extensive exploration of the coupling parameters over long simulations are thus needed and will be reported in this article.

Similarly, the hyperfine interactions in the flavin radicals are expected to be sensitive to their protein environment; the HFCs can for example be modulated by substrate binding, altered geometries of hydrogen bonds, or the surrounding amino acids, as has been shown experimentally[134,141–146] and theoretically.[122,133,147,148] In addition to these static environmental effects, hyperfine interactions are dynamically modulated due to the thermal motions of the radicals in the protein–an unavoidable consequence of "warm, wet and noisy" biological environments. If the hyperfine interactions are modulated on a timescale fast relative to the timescale of spin evolution, this induced noise in the hyperfine parameters give rise to spin relaxation.[47] If, on the other hand, the modulation is slow, the magnetosensitive response is that of an inhomogeneous ensemble rather than that of a single radical pair. Procopio and Ritz have investigated the performance of the compass in response to such inhomogeneities in the hyperfine parameters and found that the choice of radical pair hyperfine parameters greatly influences the directional sensitivity.[122]

Despite the critical importance of the hyperfine parameters of flavin in the cryptochrome for assessing the radical pair hypothesis, little is actually known about them. Electron paramagnetic resonance (EPR) spectroscopy can reveal some of the hyperfine parameters of flavin radicals in cryptochromes and remotely related flavo-enzymes, such as Light, Oxygen, or Voltage sensing (LOV) and Blue-Light-

Utilizing flavin adenine dinucleotide (BLUF) domains.[149,150] Conventional EPR spectroscopy, in particular if carried out at high frequencies, allows measuring some components of the anisotropic HFCs of N5, N10, and H5. ENDOR spectroscopy shows the fingerprints of H5, H6, the protons of the methyl group at C8, *i.e.* H8α, and often one of the two β-protons attached to C1'. Time-resolved EPR can reveal a few HFCs of flavins in members of radical pairs.[81] While particular components of selected nuclei are thus accessible spectroscopically, the interactions of weakly coupled nuclei and the principal orientations are currently only inferable from computational approaches.

Many previous theoretical studies of spin dynamics in cryptochrome have relied on hyperfine tensors calculated on an isolated lumiflavin, ignoring environmental effects. Recently, the crystal structure of cryptochrome 4 (*Cl*Cry4) of *Columba livia* (PDB ID: 6PU0) has been resolved (for a large part of the protein), which now, for the first time, provides the prospect of assessing the flavin hyperfine interactions in the environment of an avian cryptochrome.[30] Here, we derive hyperfine interaction parameters for the most relevant spin-bearing atoms on $FAD^{\bullet -}$ and $FADH^{\bullet}$ in *Cl*Cry4 using Auxiliary Density Functional Theory (DFT).[151–154] We employ a cluster model that considers the flavin and its immediately surrounding amino acids in the quantum region; as well as a QM/MM scheme ($MD_{QM/MM}$), for which the flavin and the side-chains of the cluster residues are kept in the quantum region while the rest of the protein environment is included as a set of point charges. We therefore reach in both models a more accurate description of polarizing environment of the flavin radical than previously described in the literature, therefore leading to more realistic HFCC evaluations. We sample conformational ensemble using long-time scale classical dynamics trajectory (800 ns) whereby snapshots are extracted at representative time intervals. This allowed us to provide accurate hyperfine coupling parameter fluctuations for an avian cryptochrome, which will inform future, more realistic spin dynamics simulations. The results of the cluster and QM/MM approaches are compared.

3.4 Simulation setup and computational details

3.4.1 Initial protein structure

Our model is based on the X-ray diffraction-resolved structure of *Columba livia* cryptochrome 4 (*Cl*Cry4, PDB ID: 6PU0).[30] The unresolved segment of the protein (residues 228-244) was reconstructed as described in ref. (34). The protonation state of aminoacid residues was assigned with the use of multiple pK_a-predictors (Yasara,[155,156] DelPhiPka,[157–159] pdb2pqr[160,161]) and ambiguous cases were resolved

through visual inspection of the hydrogen-bonding pattern at the site in question. Finally, the histidine residues with index 3, 7 and 54 were found to be positively charged and doubly protonated at physiological pH (AMBER residue name: HIP); histidine residues 64, 353, 405 and 471 were neutral and singly protonated at the ε-site (HIE); all 13 remaining histidine residues were assigned as neutral and protonated at the δ-position (HID). A representative protein conformation is provided in the Supplementary Information (SI).

3.4.2 MD simulations

We carried out molecular Dynamics (MD) simulations using the Amber 18 package with the ff14SB force field for the protein; the flavin radicals $FAD^{\bullet -}$ and $FADH^{\bullet}$ were modeled based on previously established RESP atomic charges.[162,163] The TIP3P model was used for water molecules. Cl^- was added to neutralise the system; additional Na^+ and Cl^- ions were used to realize a NaCl concentration of 50 mM. A standard series of energy minimisation, heating and equilibration steps was then applied, following the protocol in Fox *et al.*,[164] in order to allow the system to relax and stabilise its density to $1.006\,\mathrm{g\,cm^{-3}}$, for box dimensions of approximately $90 \times 92 \times 102\,\mathrm{\AA}^3$.

The production run for the solvated protein/flavin complex was performed in the NVT ensemble and spanned 800 ns for each protonation state of FAD, with $T = 313\,\mathrm{K}$ and a time step of 2 fs. A Langevin thermostat was employed to maintain the temperature, and the SHAKE algorithm was used to constrain the length of hydrogen bonds.[165,166] A cutoff of 9.0 Å was applied for non-bonded interactions.

3.4.3 DFT calculations

Magnetic properties were calculated using auxiliary-density-functional theory (aDFT) as implemented in deMon2k.[167] aDFT makes use of variationally fitted electronic densities to speed-up the calculation of classical electronic repulsion and exchange-correction (XC) contributions, including exact exchange.[168] The details of the aDFT methodology to compute HFC tensors will be published elsewhere. The calculated tensors include Fermi contact, spin-dipole and paramagnetic spin orbit-spin orbit coupling contributions. We tested and benchmarked the calculation of HFC tensors testing various basis sets (more details presented in SI and discussed below).

It transpired from our tests that an accurate evaluation of HFC tensors involving flavin nuclei requires a detailed description of the electron density on the flavin and a adequate representation of the surrounding electron density. We also tested a mixed basis set scheme for the flavin, where a high-precision basis set is used on magnetic nuclei and a cheaper one for the other atoms. It emerged that using such a scheme, as opposed to the “full basis” approach where the high precision

basis set is applied on all flavin atoms, allows a significant speed-up at a moderate accuracy cost (see figures B.2 and B.3 of the SI). We thus selected for the flavin atoms the combination of EPR-III/GEN-A2* atomic orbitals and auxiliary basis sets for magnetic nuclei, and a combination of DZVP-GGA/GEN-A2 basis functions for the remaining flavin atoms and the close environment. We chose the B3LYP (Becke, Lee, Yang and Parr) XC functional[91,169,170] based on previous studies showing its suitability for evaluating HFC tensors with good accuracy.[171] An adaptive grid ensuring an accuracy of 10^{-6} Ha on the diagonal elements of the XC matrix was used.[172] The unrestricted Kohn-Sham formalism was chosen as the SCF procedure. A dynamic level shifting of 0.1 Ha was applied to facilitate convergence.

Inclusion of the full protein environment with a QM/MM scheme: To complement the cluster approach outlined in the previous paragraph, we also set up a QM/MM partitioning scheme, whereby the truncated flavin *and* the "minimal cluster" are explicitly included in the subsequent DFT calculation to compute hyperfine coupling tensors on the flavin, while all the other atoms in the system–*i.e* the ribityl and adenosine moieties of the flavin, the backbone atoms of the "minimal cluster" residues, all other residues in the protein, water molecules and ions– are included as point charges that polarise the distribution of electronic density of the QM region. These point charges were the same as those used in the MD simulations to generate the trajectories. The additive QM/MM methodology we chose was described in detail in Ref. [173].

Note that the delineated QM/MM approach does not constitute an incremental increase in the quality of the description over the cluster approach described above, for which the minimal cluster is directly subject to the DFT calculation of HFC tensors. This is the consequence of the standard methodology for partitioning proteins into QM and MM parts, which mandates to only include side-chains, and not the backbone atoms, into the QM framework. The rational for this is that in a QM/MM scheme, a "link atom" is inserted at the point where the cut is made, to avoid nonphysical dangling bonds by saturating the valence of the QM region. If the cut were done, as in the cluster scheme from above, at the backbone C-N bond between the amino group and the next residue's carboxyl group, then the link atom would be inserted on the N atom and along the axis of this cut N-C bond, yielding a terminating amine with a sp^2 nitrogen instead of a properly pyramidalised sp^3. This strained geometry of the QM region makes it extremely difficult to converge the DFT calculations. Besides, a more realistic model is obtained when cutting and protonating an apolar bond rather than a polar one.

3.4.4 Metrics

We consider in this work various parameters to quantify HFC tensors. Let A_{11}, A_{22} and A_{33} be the eigenvalues of the HFC tensor. We refer to the isotropic HFC as

$$a_{iso} = \frac{(A_{11} + A_{22} + A_{33})}{3} \tag{3.1}$$

We order the principal components, A_{11}, A_{22} and A_{33}, according to their separation from the isotropic value (Haeberlen convention). That is, we assign $\{A_{11}, A_{22}, A_{33}\}$ to the labels $\{A_{xx}, A_{yy}, A_{zz}\}$ such that

$$|A_{zz} - a_{iso}| \geq |A_{xx} - a_{iso}| \geq |A_{yy} - a_{iso}|, \tag{3.2}$$

i.e. A_{xx}, A_{yy}, A_{zz} are a permutation of A_{11}, A_{22}, A_{33}. We then define the anisotropy and the asymmetry of HFC tensors as

$$\Delta A = A_{zz} - \frac{A_{xx} + A_{yy}}{2} = \frac{3}{2}(A_{zz} - a_{iso}) \text{ and} \tag{3.3}$$

$$\eta = \frac{A_{yy} - A_{xx}}{A_{zz} - a_{iso}}, \tag{3.4}$$

respectively. These parameters are independent of the coordinate system used.

The uncertainty on the mean of HFC tensors' eigenvalues is computed as follows:

$$U(A_{ii}) = \frac{t \times s}{\sqrt{N_{eff}}}$$

where t is the Student's t-factor – here, $t = 1.96$ for a confidence level of 95.5% –, s is the standard deviation of the sample and N_{eff} is the effective size of this sample, computed using the R function `coda::effectiveSize(x)`.[174,175] `coda::effectiveSize(x)` computes $N_{eff} = N \times \frac{\lambda^2}{\sigma^2}$, where λ^2 is the sample variance and σ^2 is an estimate of the spectral density at frequency zero.

Following the rules of combination of uncertainties, we calculate the uncertainty of the mean a_{iso} using:

$$U(a_{iso}) = \frac{U(A_{yy}) + U(A_{zz}) + U(A_{zz})}{3}$$

and on the mean of ΔA using:

$$U(\Delta A) = U(A_{zz}) + \frac{U(A_{xx}) + U(A_{yy})}{2}$$

3.5 Results

We have aimed to sample the dynamic heterogeneity of hyperfine coupling parameters of the flavin radicals bound in a representative cryptochrome. To this end, we have run extensive MD simulations of $FAD^{\bullet -}$ and $FADH^{\bullet}$ in *Cl*Cry4, as described in the "Simulation setup and computational details" section. For both $FAD^{\bullet -}$ and $FADH^{\bullet}$, we extracted 400 geometries, evenly spaced by 2 ns across the entire length of the 800 ns MD trajectories.

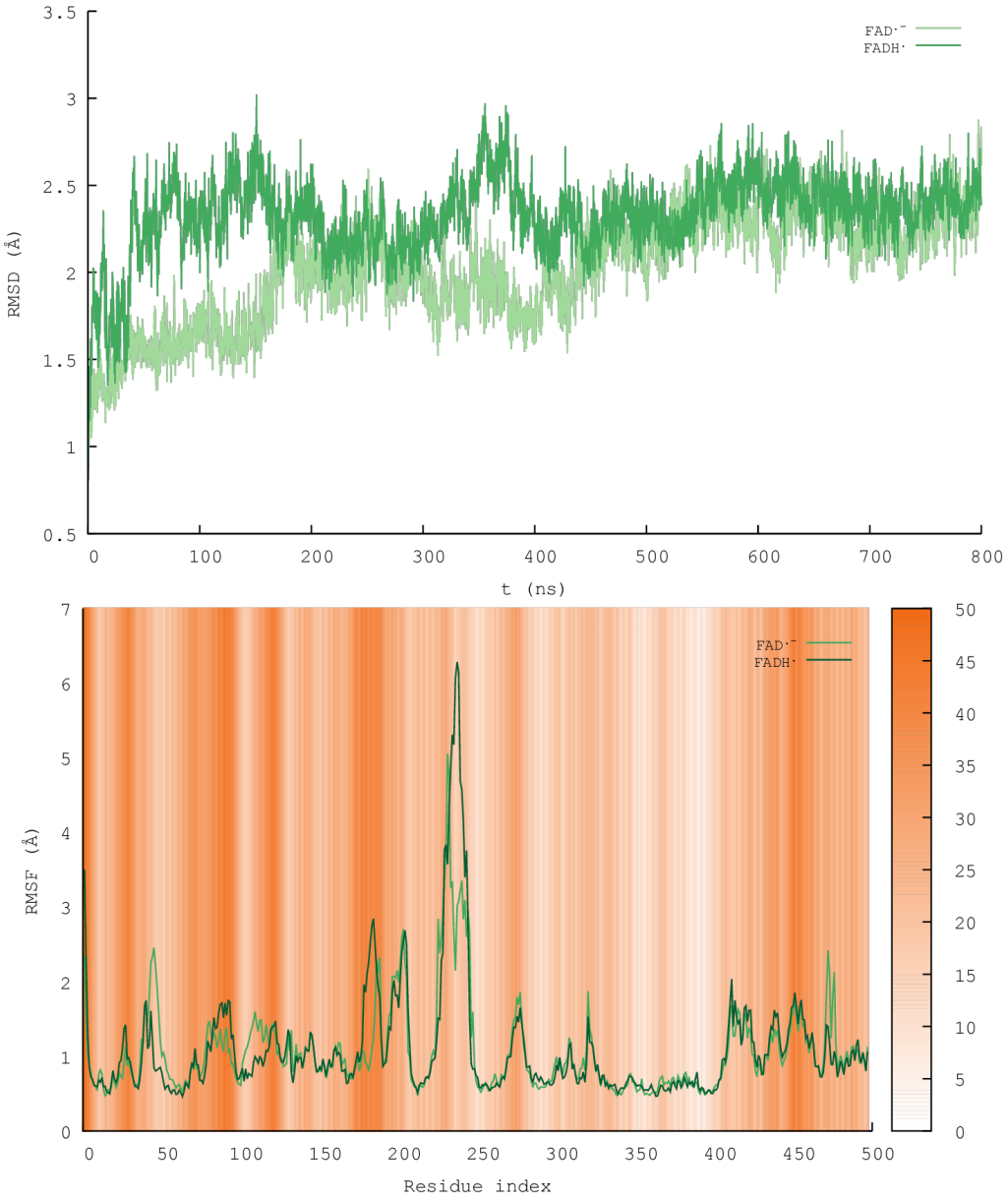

Figure 3.2: Various geometrical markers of the flavin-binding 6PU0 protein along a 800-ns MD trajectory in the two protonation states of the flavin radical ($FAD^{\bullet -}$ in light green and $FADH^{\bullet}$ in dark green): (top) RMSD of the backbone atoms; (bottom) RMSF of each residue's CA (backbone) atom, with distance to the center-of-mass of the flavin (in Å) represented by background colour.

Validation of the Molecular Dynamics simulations: Figure 3.2 (top) reports the Root-Mean-Square Deviations (RMSD) of the positions of the protein backbone atoms (CA, C, O, N in the AMBER naming convention) along a 800 ns MD trajectory of solvated 6PU0 protein containing either the $FADH^{\bullet}$ or the $FAD^{\bullet -}$ flavin cofactor. This metric, along with visual examination of the protein structure along the trajectory, reveals a preserved secondary structure throughout the simulation. Figure 3.2 (bottom) offers with the RMSF (Root-Mean-Square Fluctuations) a time-averaged, residue-disaggregated view which allows to identify the mobile regions of the protein. For both protonation states of the flavin the most flexible section of the backbone corresponds to the unresolved and reconstructed loop (residues 228 to 244), in agreement with Ref. 34. The background colour of Fig. 3.2 (bottom) indicates the distance between the centre of masses (COM) of the residue in question and the isoalloxazine moiety of the flavin. We note that the residues closest to the flavin (visible as pale bands), *i.e* those that constitute its chemical environment, are mostly residues with low RMSF. This suggests the immediate chemical environment of the flavin remains comparably constant throughout the simulation, although this claim can here only be made for the backbone atoms and not the side-chains.

A hydrogen-bonding analysis, performed using the `Cpptraj`[176] software on purely geometrical criteria, revealed no H-bonding involving the flavin isoalloxazine moiety as either a donor or acceptor, which has implications for its magnetic properties; indeed, it was shown that H-bonding to the isoalloxazine perturbs the spin density distribution in this area.[134] Water molecules infrequently enter the flavin binding cavity, and when they do, typically hover closer to the ribityl chain atoms than to the isoalloxazine. Counter-ions, namely Na^{+} and Cl^{-}, were never found within 10 Å of the isoalloxazine.

Another geometrical marker relevant in the context of magnetoreception that was tracked along the trajectory is the inter-residue distance in the electron-transfer (ET) chain. This is reported in Fig. S1 (a) and (b), and we note that these distances remain stable throughout both simulations. This is expected to ensure the efficient and reliable formation of a flavin - tryptophan or flavin - tyrosine radical pairs, both of which have been proposed as agents in magnetosensitive reactions schemes.

Before conducting extensive HFC tensor calculations on structures sampled from the MD trajectories, we validated our sampling protocol and benchmarked the quantum chemistry method to be used.

Validation of the HFC calculation method: A multitude of XC functionals have been suggested for calculating hyperfine coupling parameters. The B3LYP functional in combination with the EPR-II or EPR-III basis set, from the Barone group,[177] is well established.[178–180] Jakobsen and Jensen[180] have recently suggested a series

of double-ζ to pentuple-ζ polarisation-consistent basis sets with additional tight functions optimised for the calculation of hyperfine interactions, named pcH-ζ. In addition, we have also considered the B3LYP/N07D scheme, likewise proposed by Barone and coworkers,[179] which has been found remarkably accurate for a large set of radicals whilst being computationally cheap. Comparing the runtimes and isotropic hyperfine couplings parameters for a $FADH^{\bullet}$ relaxed in vacuum (Figure B.2**a** in the SI), we find that, for our application, B3LYP/EPR-III offers the best compromise between accuracy (assessed relative to pcH-3, the most expensive basis set tried) and computational effort. A further speed-up could be achieved with the use of the "mixed basis set" approach, in which the EPR-III basis set is only applied on the atoms for which magnetic properties are calculated, while a double-ζ basis set is used for the rest of the flavin. Figure B.3 in the SI shows the magnitude of the error associated with this approximation. We further confirmed that the aDFT framework did not introduce artefacts in the calculation of HFC tensors (see Table B.3 in the SI) and have thus decided to use this approach for the rest of the study.

Delineation of a minimal chemical environment for the flavin: Having validated the classical MD approach and chosen a suitable method for calculating hyperfine coupling tensors, we next set out to explore electronic and steric effects of the protein environment on the hyperfine couplings of the flavin. A possible strategy would be to rely on a hybrid QM/MM methodology in which the flavin would be described at the quantum mechanical level while the environment (protein or solvent) would be described by MM point charges. Repeating such QM/MM calculations along a classical MD simulation would then provide distributions of HFCC. In the study of flavin bound in glucose oxidase from Pauwles et al, the QM regions was for example restricted to a lumiflavin fragment. This MD+QM/MM strategy enforces spin localization on the flavin moieties, and assumes that electron density polarization is adequately captured by sets of point charges. For *C. livia* cryptochrome, our calculations indicate that spin density largely localize on flavin, (see Table B.6 in the SI). However, due to the presence of both polar and apolar, charged and neutral residues (see Fig. 3.1), individual residues may have variable effects on the distribution of electronic/spin density on the flavin. Therefore, we aim in this work to reach an accurate electrostatic embedding by including in the QM region not only the flavin but also the closest residues and to investigate HFCC fluctuations along long (800 ns) MD simulations. To select a list of amino acid residues to be described at the DFT level, we analysed 10 configurations from the MD trajectories, separated by time intervals of 20 ns.

For each snapshot, the following procedure was applied: first, all residues within 5 Å of the isoalloxazine moiety were extracted from the MD trajectory. Residues

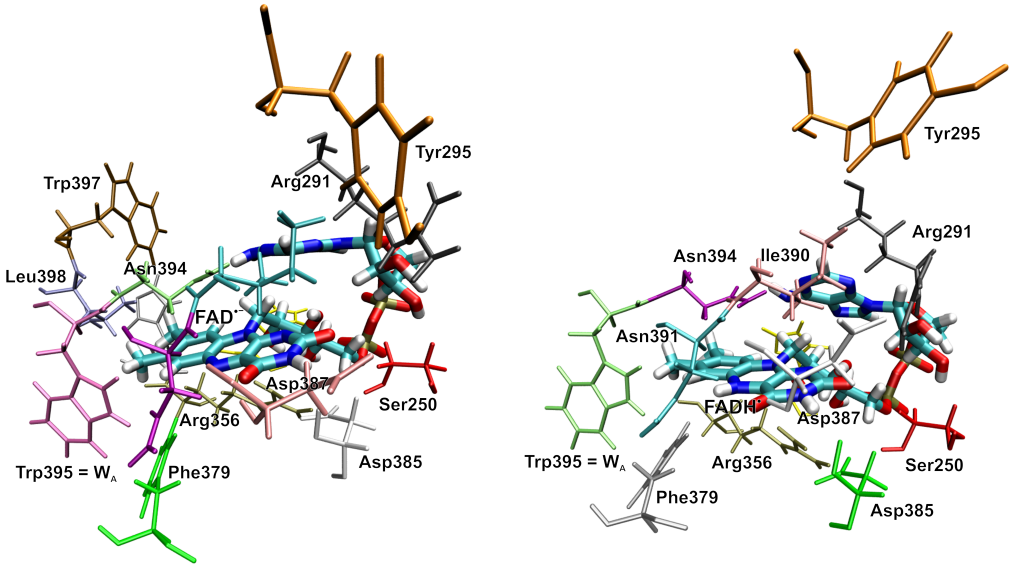

Figure 3.3: Graphical representation of the "minimal clusters" for $FAD^{\bullet -}$ (left) and $FADH^{\bullet}$ (right).

were truncated at the backbone atoms (*i.e.* cut between the carboxyl and amino groups) and hydrogen atoms were added to complete the unsaturated valences. The resulting 5-Å cluster consisted of 331 atoms in addition to the flavin, and is expected to provide a good approximation of the cofactor's steric and electronic environment. However, treating such a large number of atoms proves computationally demanding, considering that we seek to evaluate the average over long trajectories. Specifically, it was expected that selected residues could safely be removed from this cluster, thereby reducing its size and decreasing the computation effort at a marginal cost in accuracy.

In order to build such a "minimal cluster", residues were selected as follows: the individual polarising impact of each residue was measured by first computing the HFC tensors of atoms of interest for the isolated flavin in vacuum, and comparing them with the same tensors computed with this neighbouring residue explicitly included. Residues involved in a salt bridge or strong hydrogen bond were included with their counterparts: in these cases, instead of a pair, a triad (flavin - D385 - R356), or even a tetrad of molecular fragments (flavin - D387 - Y295 - R291, where hydrogen bonding also occurs with salt-bridging charged atoms) were considered at once. In order to compare the hyperfine tensors, the isotropic HFC constant, a_{iso}, and the tensor anisotropy, ΔA, were computed for the pertinent atoms on the flavin (see Fig. 1). Polarising residues were identified as those that induced a variation (Δa^i_{iso} or $\Delta\Delta A^i$) greater than one standard deviation above or below the average deviation (over all 10 selected conformers) for any considered atom i.

The final clusters so determined, shown in Figure 3.3, contained 272 atoms for

$FADH^{\bullet}$ (S250, R291, Y295, H353, R356, F379, D385, D387, I390, N391, N394, W395, $FADH^{\bullet}$) and 333 atoms for $FAD^{\bullet-}$ (S250, R291, Y295, H353, R356, H357, F379, D385, D387, I390, N391, N394, W395, W397, L398, $FAD^{\bullet-}$). Finally, the validity of the approach was once again verified by comparing flavin-borne HFC tensors calculated in the minimal cluster with those derived for the complete cluster (Tables B.4 and B.5 in SI). Δa_{iso} and $\Delta\Delta A$ for $FADH^{\bullet}$ and for $FAD^{\bullet-}$ are small in magnitude and typically do not exceed 2% of the corresponding quantity. The exception is H7α on $FADH^{\bullet}$, whose very small a_{iso} value makes the relative error comparatively large. However, such a small HFC has a correspondingly minuscule impact on the spin dynamics of a magnetosensor and therefore did not warrant increasing the cluster size.

Calculation of flavin HFC tensors: With the methodology validated and the minimal representative cluster established, we set out to assess the inhomogeneity of hyperfine interactions induced by the protein environment by sampling the representative set of geometries from the long-time MD trajectories. Hyperfine coupling tensors were calculated for 400 representative geometries of the flavin in its cluster, as determined above, extracted from the MD simulations at intervals of 2 ns using deMon2k. This interval was selected to exceed the (short-time) autocorrelations of the isotropic HFC constants, thereby permitting to compute reliable statistical quantities from an unbiased sample (Table B.7 in SI). We can verify with Figure B.4 (in the SI) that the conformational space explored by the flavin over this length of time is representative of the entire trajectory. MD-generated geometries were rotated and aligned to the flavin molecular axis system (as represented in Figure 3.1b and chosen in consistency with previous spin dynamics studies).[63] This procedure also implies that the fluctuations of hyperfine couplings reported here reflect variations of the polarising environment and of the conformation of the flavin itself, and not the librational motions of the flavin in its binding pocket, which is a source of spin relaxation.[47] Averaging the set of hyperfine interactions so obtained, a representative prediction of hyperfine interactions of the flavin in the protein environment has been realized. We report hyperfine coupling tensors for the relevant flavin atoms, for both the radical semiquinone ($FADH^{\bullet}$) and radical anion ($FAD^{\bullet-}$), in the SI. The principal components of these average hyperfine coupling tensors are reported in Table 3.2.

Decorrelation of structural and polarisation effects: For comparison, we also calculated a similar set of hyperfine coupling tensors from the extracted flavin geometries, without the surrounding cluster. In doing so, we aimed to quantify the electronic polarising effect of the environment, relative to the influence of structural

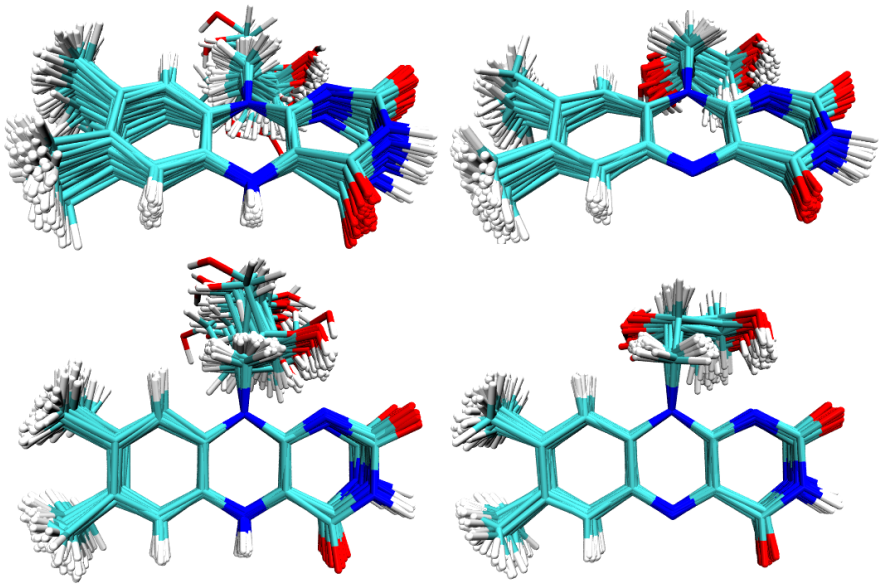

Figure 3.4: Flavin structural fluctuations during the MD simulations, represented by the superposition of 80 snapshots extracted from the trajectories for $FADH^{\bullet}$ (left) and $FAD^{\bullet-}$ (right).

fluctuations within the flavin. Figure 3.4 shows this structural variability for 80 snapshots from the extracted sample after alignment. The root-mean-square distance within these sets, calculated on the heavy atoms of the isoalloxazine moiety, is equal to 0.369 Å for $FADH^{\bullet}$ and 0.137 Å for $FAD^{\bullet-}$.

Figure 3.5 is a graphical representation of average HFC tensors of $FADH^{\bullet}$ and $FAD^{\bullet-}$. To this end, we represented the hyperfine tensors by surfaces which, for direction $\mathbf{r}$, are at a distance from the nucleus proportional to $\mathbf{r}^{\mathbf{T}}\mathbf{A}\mathbf{r}$. These graphical representations are scaled identically, making them directly comparable. In a similar way, we evaluated the standard deviation, taking the covariance of all tensor components into account. As can be seen, the hyperfine structure is generally dominated by the hyperfine constant of N5 and, for the semiquinone form, H5. The hyperfine interactions of the hydrogens of the methyl groups, (H7α and H8α on figure 3.1b), are averaged over the methyl group rotation: for this reason, a single effective parameter is reported throughout the paper for these groups. The largest variance is seen for the H8α protons and, for the semiquinone form, for H5.

The environment changes the shape and magnitude of hyperfine interactions. As can be seen in Figure B.8 in the SI, which resembles Fig. 3.5, on the scale of these plots, these changes appear subtle. The effect is there most clearly seen for H5 and N5, which is a simple consequence of their sheer size relative to other hyperfine couplings. A better quantitative appreciation of the environment effects can be obtained from Table 3.2, which reports the principal components of the

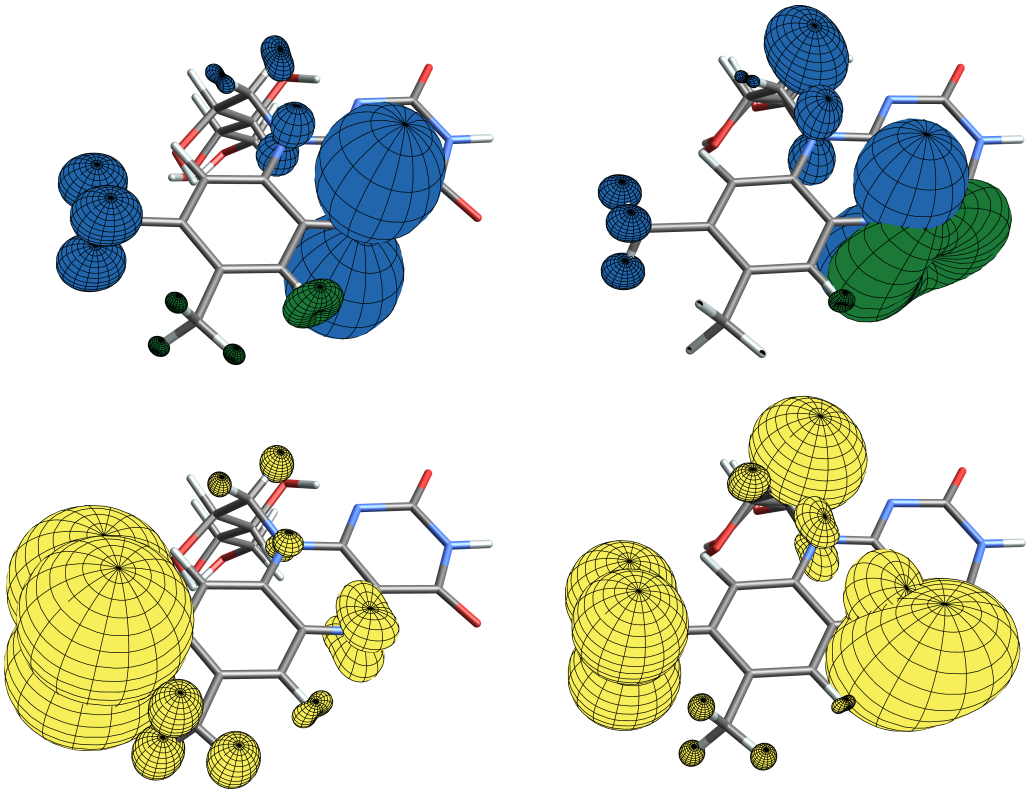

Figure 3.5: Graphical representation of average (top; blue/green surfaces) hyperfine coupling tensors and the standard deviation (bottom; yellow surfaces) for $FAD^{\bullet -}$ (left) and $FADH^{\bullet}$ (right), calculated using aDFT on MD-generated geometries within a "minimal" chemical environment.

averaged HFC tensors, with and without the environment. Table 3.1 provides the associated isotropic coupling constants and anisotropies in addition to a comparison with HFC parameters calculated on the relaxed structure (obtained using PBEh-3c, as implemented in Orca[181,182]) *in vacuum*. The statistical uncertainties associated with these calculated averages are reported in Table B.11 of the SI.

On average, the absolute deviation of the absolute value of tensors components induced by the inclusion of the environment is 0.448 ± 0.937 ($MD_{cluster}$) or 0.302 ± 0.819 ($MD_{QM/MM}$) MHz for the neutral semiquinone; the largest change is $\Delta A_{zz} = +1.186 \pm 0.809$ MHz, which occurs for N5 ($MD_{QM/MM}$). For the radical anion, the average absolute deviation is more reliable, equal to 0.729 ± 0.297 ($MD_{cluster}$) or 0.614 ± 0.283 ($MD_{QM/MM}$) MHz, and the largest change is $\Delta A_{zz} = +2.856 \pm 0.659$ MHz for N5. N10 is also significantly affected, with $\Delta A_{zz} = +2.393 \pm 0.525$ MHz ($MD_{cluster}$) or $+2.404 \pm 0.471$ MHz ($MD_{QM/MM}$). The relatively large statistical uncertainty associated to the magnitude of the shift in HFC-derived values arises from the combination of uncertainties on the MD_{vac} and $MD_{cluster/QMMM}$ datasets, and makes it difficult to accurately gauge the impact of electronic polarisation on the flavin's HFC tensors.

atom	a_{iso} (MHz)				ΔA (MHz)			
	Opt_{vac}	MD_{vac}	$\text{MD}_{cluster}$	$\text{MD}_{QM/MM}$	Opt_{vac}	MD_{vac}	$\text{MD}_{cluster}$	$\text{MD}_{QM/MM}$
N5	15.050	16.379	17.408	16.712	53.660	55.411	58.152	56.225
N10	5.916	5.931	6.828	6.882	19.418	16.586	18.830	18.767
H1'a	2.805	2.754	3.580	3.400	3.819	3.675	3.913	3.782
H1'b	6.559	5.232	5.992	6.302	3.866	3.549	3.729	3.612
H8α	12.392	10.118	10.342	9.847	2.869	2.501	2.349	2.369
H7α	-3.668	-3.461	-3.273	-3.238	1.773	1.596	1.609	1.597
H6	-10.125	-9.243	-8.064	-8.440	7.723	6.999	6.622	6.674

(a) $\text{FAD}^{\bullet-}$

atom	a_{iso} (MHz)				ΔA (MHz)			
	Opt_{vac}	MD_{vac}	$\text{MD}_{cluster}$	$\text{MD}_{QM/MM}$	Opt_{vac}	MD_{vac}	$\text{MD}_{cluster}$	$\text{MD}_{QM/MM}$
N5	11.987	16.829	17.129	17.153	43.793	45.475	46.522	46.768
N10	7.209	7.499	7.855	7.568	21.492	19.752	20.741	20.129
H1'a	3.423	2.247	2.438	2.413	3.886	3.596	3.667	3.631
H1'b	7.423	14.002	14.740	13.810	3.930	3.700	3.773	3.733
H8α	7.476	5.656	6.544	6.047	1.910	1.594	1.661	1.608
H7α	-0.950	-0.901	-0.684	-1.122	1.407	1.271	1.339	1.302
H6	-4.755	-3.584	-3.285	-3.528	4.596	4.464	4.513	4.459
H5	-22.675	-18.591	-19.159	-19.366	31.631	33.211	33.822	34.008

(b) $\text{FADH}^{\bullet}$

Table 3.1: Isotropic HFC and tensor anisotropy calculated using aDFT for (**a**) $\text{FAD}^{\bullet-}$ and (**b**) $\text{FADH}^{\bullet}$. The "Opt_{vac}" datasets were calculated on a single flavin conformer on its relaxed geometry in vacuum; "MD_{vac}" is the average of values calculated on the MD-derived flavin geometries with its environment excluded; "$\text{MD}_{cluster}$" corresponds to the average HFC parameters calculated on the MD-derived flavin geometries within the "minimal cluster"; and "$\text{MD}_{QM/MM}$" to the same quantity calculated with the QM/MM scheme described above. All HFC calculations were obtained using aDFT with the B3LYP functional and the mixed basis set scheme of EPR-III/GEN-A2* on the flavin's magnetic nuclei, and DZVP-GGA/GEN-A2 on the other flavin atoms and surrounding cluster. All calculations were performed in deMon2k 6.0.2.

Examination of individual HFC tensor components: To better visualize the HFC tensor components and their dependence on the protein environment, we have further studied the distributions of the projections of HFC tensors onto the averaged, normalised eigenbasis, $\mathbf{v}_{j\in\{1,2,3\}}$. Specifically, for each snapshot the projection of the hyperfine tensor $\mathbf{A}_n$ in the molecular frame (where n samples the set of $N = 400$ geometries for which HFCs were calculated) in the directions $\mathbf{v}_j$, $A_n^{(v_j)}$, was obtained by calculating $\|\mathbf{A}_n\mathbf{v}_j\|$. Histograms of these projections are reported in Figure 3.6 for the N5 atom, and for the N10 and H5 atoms in the SI (Figure B.9). Note that only the HFC parameters for the nitrogen atoms and H5 are well representable in this way, as their symmetry gave consistent eigenvector directions across the set of diagonalised tensors. The $\mathbf{v}_3$ eigenvector corresponds to the long axis of the HFC; it

atom	A_{YY}			A_{XX}			A_{ZZ}		
	MD_{vac}	$MD_{cluster}$	$MD_{QM/MM}$	MD_{vac}	$MD_{cluster}$	$MD_{QM/MM}$	MD_{vac}	$MD_{cluster}$	$MD_{QM/MM}$
N5	1.793	1.720	1.665	1.548	1.523	1.462	47.145	48.143	48.332
N10	1.058	1.076	0.997	0.771	0.807	0.720	20.667	21.682	20.988
H1'a	1.178	1.344	1.322	0.919	1.087	1.083	4.645	4.883	4.834
H1'b	13.015	13.689	12.754	12.522	13.275	12.377	16.469	17.255	16.299
H8α	5.218	6.106	5.610	5.031	5.875	5.411	6.718	7.652	7.119
H7α	-1.232	-1.025	-1.456	-1.417	-1.234	-1.656	-0.053	0.209	-0.254
H6	-4.677	-4.388	-4.635	-5.467	-5.191	-5.394	-0.608	-0.277	-0.556
H5	-23.190	-23.857	-24.172	-36.132	-37.009	-37.233	3.550	3.389	3.306

(a) $FADH^{\bullet}$

atom	A_{YY}			A_{XX}			A_{ZZ}		
	MD_{vac}	$MD_{cluster}$	$MD_{QM/MM}$	MD_{vac}	$MD_{cluster}$	$MD_{QM/MM}$	MD_{vac}	$MD_{cluster}$	$MD_{QM/MM}$
N5	-1.922	-1.827	-1.8771	-2.261	-2.125	-2.203	53.320	56.176	54.216
N10	0.516	0.666	0.7386	0.290	0.436	0.515	16.989	19.382	19.393
H1'a	1.747	2.477	2.3442	1.311	2.074	1.934	5.204	6.189	5.921
H1'b	4.330	5.034	5.3805	3.768	4.464	4.816	7.598	8.478	8.710
H8α	9.372	9.691	9.1594	9.196	9.427	8.955	11.786	11.907	11.426
H7α	-3.843	-3.663	-3.6253	-4.143	-3.956	-3.915	-2.397	-2.200	-2.173
H6	-10.858	-9.769	-10.1102	-12.293	-10.773	-11.218	-4.577	-3.649	-3.990

(b) $FAD^{\bullet-}$

Table 3.2: Principal components of the HFC tensors for atoms of **(a)** $FADH^{\bullet}$ and **(b)** $FAD^{\bullet-}$. The labels "$MD_{cluster}$" and "$MD_{QM/MM}$" refer respectively to the averaged tensors calculated for the flavin in a QM cluster and in a QM/MM protein environment; "MD_{vac}" refers to the tensors calculated on the same set of flavin geometries, but stripped from its protein environment.

aligns closely with the z-axis for the two N-atoms, and with the y-axis for H5. The so derived distributions give a more complete picture of the impact of the environment on the distributions of hyperfine interactions.

The inclusion of the environment is shown to have both a shifting and broadening effect on the distributions of $MD_{cluster}$ N5 and N10 along $\mathbf{v}_3$ i.e. on the longitudinal component $A^{(v_3)}$ of the tensors. Interestingly, while the lengthening effect applies to both protonation states, the presence of the chemical environment broadens the distributions of N5 and N10's $A^{(v_3)}$ for $FADH^{\bullet}$, but does not significantly affect the shape of the corresponding distributions in $FAD^{\bullet-}$. $A^{(v_1)}$ and $A^{(v_2)}$, i.e. the projections on the transverse axes are found to be affected for the N10 nucleus on both flavin protonation states, although to a generally weaker extent. Since these figures are included to convey qualitative insight into the effect of electronic polarisation on the distributions of HFC tensor projections, and into the shape of these distributions themselves, then only the projections from $MD_{cluster}$ tensors are reported; all the

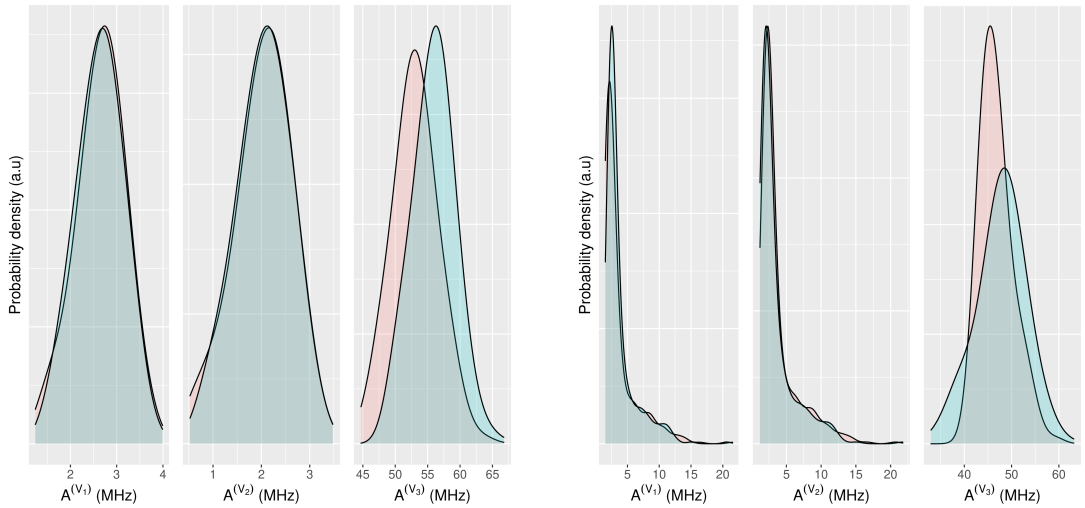

(a) $FAD^{\bullet -}$ (b) $FADH^{\bullet}$

Figure 3.6: Projection of the N5 HFC tensor for (a) $FAD^{\bullet -}$ and (b) $FADH^{\bullet}$ onto their average eigenvectors $\mathbf{v}_i$. Blue (resp. red) histograms refer to values calculated in $MD_{cluster}$ (resp. MD_{vacuum})

above comments also hold true for $MD_{QM/MM}$ projections, which differ only in the details.

Graphs in Figure B.5 in the SI report, respectively, the distributions of isotropic hyperfine couplings and the tensor anisotropy for the pertinent flavin atoms, calculated on the extracted geometries from the MD simulation. These quantities were again derived from the MD-extracted flavin geometries with and without its "minimal" environment, and correspond to the MD_{vac} and $MD_{cluster}$ datasets. Due to the non-normality of distributions (especially for N5 and N10), the average, quartiles, minimum and maximum of each set are reported. Average and standard deviation values for all tensor elements are also available in the SI (Section B.1.18 and B.1.19).

3.6 Discussion

We have calculated the hyperfine interactions of $FAD^{\bullet -}$ and $FADH^{\bullet}$ taking structural fluctuations and polarisation effects from the protein environment into account. Structural dynamics were accounted for by sampling molecular dynamics trajectories of 800 ns, *i.e.* a time span approaching the lifetime of radical pairs implicated with magnetoreception. Environment effects were included by a cluster approach, whereby a sensitivity analysis was used to elect the residues contributing to the cluster, allowing to model the environment on the full quantum level whilst keeping the computational demands manageable. We have observed that the hyperfine interactions are determined both by structural fluctuations, governed and confined by the protein, and by the polarising effects of the environment on the electronic structure. To gauge the relative importance of these two contributions, we shall compare the

hyperfine parameters derived for the relaxed structure of the isolated radicals in vacuum, and the average values of the extracted structures, both with and without environmental effects included *via* the cluster and QM/MM model.

We will first focus the discussion on the isotropic hyperfine coupling constant and the anisotropy, as defined in the Metrics section, which are reported in Table 3.1 **(a,b)**. A change in a_{iso} could reflect a scaling of the whole tensor, or a change in individual principal components. The latter aspect is captured in the anisotropy, which is also the central parameter determining the directionality of the magnetic field effect for the radical pair, and which we shall discuss thereafter. It should however not be forgotten that some changes in the hyperfine parameters are undetectable by these two metrics; these can always be assessed from the complete tensors, as reported in the SI (sections B.1.18 and B.1.19), and from the plots of the average HFC tensors (Figure 3.5, **(a,b)**). Some characteristics of these will be discussed here in terms of individual tensor components and their distributions, before we comment on differences with previous HFC calculations and experimental data, as well as between our $MD_{cluster}$ and $MD_{QM/MM}$ datasets.

Isotropic HFC: Analysing the isotropic hyperfine coupling constants (Table 3.1), we remark the following trends: on average, the absolute change in a_{iso} due to structural fluctuation is equal to 0.9 ± 0.1 MHz for the radical anion, and 2.5 ± 0.4 MHz for the semiquinone. Electronic polarisation by the close environment, on the other hand, induces on average an absolute change of 0.7 ± 0.3 MHz ($MD_{cluster}$) or 0.6 ± 0.3 MHz ($MD_{QM/MM}$) for $FAD^{\bullet -}$, and 0.4 ± 0.9 MHz ($MD_{cluster}$) or 0.3 ± 0.8 MHz ($MD_{QM/MM}$) for $FADH^{\bullet}$. As these effects are not necessarily additive, but may partly compensate each other, the average absolute change registered in a_{iso} upon consideration of the combined effect is about 1.3 ± 0.2 MHz ($MD_{cluster}$) or 1.2 ± 0.1 MHz ($MD_{QM/MM}$) for the anion, and 2.5 ± 0.6 MHz ($MD_{cluster}$) or 2.4 ± 0.5 MHz ($MD_{QM/MM}$) for the semiquinone.

Atoms which are particularly strongly affected by structural effects are the H8α methyl, with a deviation of about -2.3 ± 0.2 MHz, H1'b ($\Delta a_{iso} \simeq -1.3 \pm 0.2$ MHz) and N5 ($\Delta a_{iso} \simeq +1.3 \pm 0.2$ MHz) for the anion; and, even more so, H1'b ($\Delta a_{iso} \simeq +6.5 \pm 2.0$ MHz), N5 ($\Delta a_{iso} \simeq +5 \pm 0.4$ MHz) and H5 ($\Delta a_{iso} \simeq +4.6 \pm 0.8$ MHz) in the semiquinone. The inclusion of the environment seems to have a weaker impact overall, although the generally large statistical uncertainties make it difficult to conclude: the largest effects on $FAD^{\bullet -}$ atoms are deviations of $\Delta a_{iso} \simeq +1.2 \pm 0.2$, $+1.0 \pm 0.4$ and $+1.0 \pm 0.3$ MHz for H6, H1'b and N5 respectively; and $FADH^{\bullet}$ exhibits a remarkable insulation to electronic polarisation by its immediate chemical environment, with all environment-induced deviations staying below 1 MHz – the largest one occurring for H8α ($\Delta a_{iso} \simeq +0.9 \pm 0.3$ MHz).

HFC anisotropy: A similar analysis can be made for the tensor anisotropy (Table 3.1): on average, the absolute change in value due to structural fluctuation is equal to 0.9 ± 0.1 MHz for $FAD^{\bullet -}$ and 0.7 ± 1.1 MHz for $FADH^{\bullet}$. The average uncertainty on $FADH^{\bullet}$ ΔA is however contaminated by the very large uncertainty on the H1'b atom ($\Delta\Delta A = 6.463 \pm 5.493$ MHz), which arises because of its poor sampling in the MD_{vac} dataset: only 27 A_{zz} and 30 A_{yy} values are uncorrelated. Removing $\Delta A^{H1'b}$ from the calculation of the average deviation of anisotropy yields $\Delta\Delta A = 0.8 \pm 0.4$ MHz for $FADH^{\bullet}$. Polarisation by the cluster induces on average an absolute change of 0.8 ± 0.2 MHz ($MD_{cluster}$) or 0.5 ± 0.2 MHz ($MD_{QM/MM}$) for $FAD^{\bullet -}$, and 0.4 ± 3.833 MHz ($MD_{cluster}$) or 0.3 ± 3.183 MHz ($MD_{QM/MM}$) for $FADH^{\bullet}$ – again contaminated by a huge uncertainty on $\Delta\Delta A^{H1'b}$. The average absolute change registered by ΔA upon addition of these two effects is about 1.0 ± 0.1 MHz ($MD_{cluster}$) or 0.8 ± 0.1 MHz ($MD_{QM/MM}$) for the anion, and 0.8 ± 2.8 MHz ($MD_{cluster}$) or 0.9 ± 2.1 MHz ($MD_{QM/MM}$) for the semiquinone.

For both protonation states of the flavin, the N10 atom is most affected by structural fluctuations: ΔA registers a decrease of 2.8 ± 0.1 MHz for the anion, and of 1.6 ± 0.1 MHz for the semiquinone. The N5 atom is the second most affected, with $\Delta\Delta A \simeq +1.8 \pm 0.1$ and $+1.6 \pm 0.6$ MHz for $FAD^{\bullet -}$ and $FADH^{\bullet}$, respectively. The subsequent polarisation by the chemical environment most strongly impacts the same two nitrogen atoms, increasing the average tensor anisotropy in $FAD^{\bullet -}$ of N5 by 2.7 ± 0.1 MHz and N10 by 2.2 ± 0.2 MHz, respectively, while increasing ΔA^{N5} by 1.3 ± 1.2 MHz in $FADH^{\bullet}$. This relatively large uncertainty again arises from poor sampling, as the $MD_{QM/MM}$ dataset contains only 57 independent A_{zz} values for N5.

In the case of N5 and N10, the HFC interactions of which are strongly axial and nearly collinear (see Figure 3.5), a variation in tensor anisotropy can reveal a weakening or strengthening of their axial character. Since the directional sensitivity of the magnetic compass depends on the strong axiality of this particular interactions, any change in ΔA for these atoms has implications regarding compass performance. Still, it should be noted that the variations reported here are modest: indeed, the static, vacuum picture of $FAD^{\bullet -}$ (Table 3.1, column "Opt_{vac}") underestimates the tensor anisotropy of N5 by about 5-8% and overestimates that of N10 by only 3%; similarly, relaxed $FADH^{\bullet}$ in vacuum underestimates ΔA by about 6% for N5 and overestimates it by about 3-6% for N10. For both protonation states, H8α is the atom for which the relative error of the static picture is the largest, overestimating ΔA by 17-18% in $FAD^{\bullet -}$ and 12-15% in $FADH^{\bullet}$.

Individual tensor components: While tensor anisotropy reveals some information on the directionality of hyperfine couplings, a finer appreciation can be gained by comparing their eigenvalues A_{xx}, A_{yy} and A_{zz}, assigned as detailed in the Metrics sec-

tion. For the strongly anisotropic atoms N5 and N10, A_{zz} is proportional to the length of the longest axis of the HFC tensor, and its direction nearly coincides with the z-axis. We note that when in a dynamic environment, N5 has significantly smaller transverse components (A_{xx} and A_{yy}, see Table 3.2), *i.e* by 30 to 50%, than predicted for the static flavin in vacuum (cf. Tables B.8 and B.9 in the SI). This has implications for the ability of the system to generate a "spike" in the orientation-dependent singlet recombination yield at long coherence times, the so-called "quantum needle" proposed to explain the remarkable angular precision of the compass: indeed, scaling down the transverse components of nitrogen tensors is expected to weaken this spike.[3] N10, on the other hand, show either a marked increase in the magnitude of its transverse components, in the case of $FADH^{\bullet}$, or a simultaneous increase of A_{yy} and decrease of A_{xx} for $FAD^{\bullet-}$, resulting in roughly interchanged values of these two components going from the static to the dynamic flavin representation.

Distributions: The distributions of selected principal tensor components are reported in Figure 3.6 and in the SI (Figure B.5): the red and blue histogram reflect the projected tensor components including only structural fluctuations or including both structural fluctuations and polarisation effects, respectively. We notice that inclusion of the environment has both a shifting and a broadening effect on the distribution of N5 and N10 $A^{(v_3)}$, *i.e.* on the size of the tensors along their longest axis. Interestingly, while the boosting effect of the environment on the average value of A^{v_3} applies to both nitrogen tensors and protonation states of the flavin, the broadening is only apparent for the $FADH^{\bullet}$ nitrogen tensors. The reason for this shift, which arises from a different distribution of spin density on the flavin, is not attributed to the formation of a hydrogen bonds, e.g. between N5 and a nearby residue, but is a nonspecific environmental effect.

H5 is also mildly affected by the presence of the environment, registering a slight decrease in a_{iso} and increase in ΔA (Table 3.1). The very asymmetric distribution of a_{iso}^{H5} (Figure B.6(a)), trailing to large values, can be linked with the "out-of-planeness" of H5 with respect to the isoalloxazine rings. This is shown in the SI in Figure B.10, which seeks to illuminate the relation between extreme HFC values for $FADH^{\bullet}$ H5 and geometric parameters, such as the improper angle of H5 with the isoalloxazine rings. An angle of 0° places H5 and the 3 other atoms in the same plane.

QM/MM: Average values and distributions of a_{iso} and ΔA, calculated with the QM/MM scheme described in the Results section, are reported in Figure B.7 of the SI. Both the interquartile amplitude and mean values are very similar to those calculated with the "$MD_{cluster}$" scheme. Indeed, the largest differences between

these sets arise for $FAD^{\bullet-}$ N5 a_{iso} (0.7 MHz, *i.e* 4.0% change) and ΔA (1.9 MHz *i.e* 3.3% change). Considering only atoms with large and strongly anisotropic hyperfine coupling tensors (namely N5, N10, and H5), $FADH^{\bullet}$ N10 shows similarly sized relative deviation ($\Delta a_{iso} = 3.7\%$ and $\Delta\Delta A = 3.1\%$), although these changes correspond to smaller absolute value. The remaining atoms ($FAD^{\bullet-}$ N10, $FADH^{\bullet}$ N5 and H5) are on the other hand very similarly described by the QM/MM and cluster models, with deviations between their respective averaged quantities below or equal to 1.1%.

For other atoms, with smaller and/or more isotropic hyperfine coupling tensors, the relative change is contained within 0.8-7.6%, except for $FADH^{\bullet}$ H7α a_{iso} for which the cluster and QM/MM descriptions differ by 64%; however, this only corresponds to a deviation of 0.4 ± 0.2 MHz.

It is difficult to decide which approach, $MD_{cluster}$ and $MD_{QM/MM}$, best captures the effect of the electronic polarisation on flavin-borne hyperfine coupling tensors. While $MD_{QM/MM}$ includes both an accurate (*i.e* DFT-level) description of the polarising effect of the polar residues in the vicinity of the flavin, and a more rudimentary (MM) description of the rest of the protein and of the ribityl-adenosine moieties of the flavin, it also relies on a point-charge description of the backbone atoms of all neighbouring residues, which places potentially overpolarising charges close to the flavin. On the other hand, $MD_{cluster}$ treats all atoms at the DFT level, ensuring that the included chemical environment, including backbone atoms, polarises the flavin through a reasonably realistic electron density, instead of a collection of over-localised atomic charges. This gain in accuracy is balanced by the fact that the chemical environment is incomplete, limited to residues for which the election process as detailed in "Delineation of a minimal chemical environment for the flavin" indicated sizeable effects, and also lacks the ribityl-adenosine complex of the flavin. These approximations, made to keep computational demands manageable, prevent us from suggesting a hierarchy in the accuracy of results obtained from the $MD_{QM/MM}$ and $MD_{cluster}$ approaches.

Importantly, both $MD_{QM/MM}$ and $MD_{cluster}$ results suggest that the impact of polarisation on the average value of a_{iso} and ΔA is small, especially compared to that of structural fluctuations within the flavin.

Lumiflavin: The "Opt_{vac}" dataset for $FAD^{\bullet-}$, which paints a minimalist, completely static picture of the magnetic properties of the flavin, allows us to judge the suitability of the radical lumiflavin anion as approximation for cryptochrome-bound $FAD^{\bullet-}$. DFT-calculated HFCs of isolated lumiflavin have frequently been employed in the literature to support spin dynamics calculations, such as those presented in.[3,72] Structurally, the lumiflavin corresponds to the isoalloxazine moiety of the

radical flavin anion, with a methyl group on the N10 atom, where the ribityl chain would start in FAD.

Considering the isotropic hyperfine couplings (Figure B.6**c** in the SI), the only, but quite sizable, error ($\Delta a_{iso} \simeq 7\,MHz$) arises for this methyl-group. For the flavin, the corresponding hydrogens (H1'a, H1'b) cannot be considered equivalent, as the ribityl chain prevents their equivalencing by rotation. For all other atoms however, the isotropic hyperfine couplings appear to be (surprisingly) well approximated based on the lumiflavin analogue.

The tensor anisotropy is reasonably well reproduced for N5 (Figure B.6**d**, in the SI), but less so for N10. For the methyl groups (*e.g.* H8α), the reported HFCs were obtained by equating the anisotropic components to zero, as they were expected to be averaged out by the fast rotation of the methyl group. However, as can be seen from the "$MD_{cluster}$" dataset of $FAD^{\bullet-}$, which effectively introduces this rotational averaging via sampling from the MD trajectory, some anisotropy remains. Inspecting the shapes of the averaged H8α tensors (Figure 3.5, right), we note this anisotropy emanates from an elongation of the HFC, along the axis of rotation and in a direction pointing towards the central ring – *i.e.* towards the center of spin density.

Experimental HFCs: Although no experimental HFCs have so far been realized for *Cl*Cry4, we can compare our results with measurements for other cryptochromes, as listed in the SI in Table B.1 and B.2. We note a large variability among studies, which might arise from both intrinsic differences and different experimental conditions. Data have also been reported for light oxygen voltage (LOV) domains and blue light sensor using FAD (BLUF) proteins,[149,183,184] but the cofactor (FMN instead of FAD in LOV), photo-cycle and reactivity are entirely different, suggesting that no obvious parallels can be draw beyond the distant similarity in the sense of involving a (likely) radicalized flavin cofactor.

The largest discrepancy between HFC parameters derived here and experimental results arises for the N10 atom: the $A_{\|}$ component of N10, which can be identified with A_{zz}, has been measured to be significantly larger than predicted, with experimental values ranging from 23.1 to 27.9 MHz (Table B.1 and B.2 in the SI) compared to $A_{zz} = 19.3\,MHz$ (Table 3.2) as derived here for $FAD^{\bullet-}$. This same discrepancy exists for $FADH^{\bullet}$. On the other hand, previous theoretical studies have found values similar to ours; and, as can be inferred from Figure B.2**(b)** (in the SI), this particular atom does not seem to be sensitive to basis sets effects. We are therefore tempted to attribute this discrepancy to different experimental conditions (*e.g.* low temperature leading to more confinement and and sampling, different pH, etc.) or to an effect not included here, such as water binding or marked structural differences of the binding pocket compared to the crystal structure. On the other hand, such stark deviations

are not expected to manifest as a result of structural fluctuations or the polarising effect of the environment alone, as our data show.

3.7 Conclusion

In this study, we have reported a set of hyperfine coupling tensors for the cryptochrome-bound flavin radicals derived from long-time MD and a aDFT-based cluster approaches. These average tensors, calculated on a statistically significant number of biologically relevant geometries of the flavin and its close chemical environment, are expected to provide a realistic description of the magnetic properties of this magnetosensitive system under biologically relevant conditions. For each protonation state of the flavin considered in this paper, *i.e.* the radical anion $FAD^{\bullet -}$ and the neutral radical semiquinone $FADH^{\bullet}$, we report detailed hyperfine parameters accounting for dynamic effects.

Our calculations include the structural variability of the flavin and its environment due to thermal fluctuations, and the polarisation of the electronic and spin density of the flavin by neighbouring residues. To account for the latter effect, we defined a minimal polarising cluster of amino acids, of a size suited for efficient aDFT calculations, which can be re-used in the computation of other spin-density-dependent molecular properties. This "cluster" was also completed with the rest of the protein environment, approximated by a set of atomic point charges. The fluctuation in magnetic properties induced by these dynamical effects, which cannot be estimated from the fully static picture of a single flavin conformation in vacuum, are shown to be largely of geometrical origin, while the effect of electronic polarisation by the chemical environment is weaker. Even though the average shift of HFCs due to these dynamical effects is surprisingly small (of the order of 1 or 2 MHz for the isotropic hyperfine coupling), they induce deformations to hyperfine coupling tensors that are critical for the operation of a magnetic compass and which are expected to impact on its performance. This is e.g. the case for the induced changes of the nitrogens' A_{zz} component, or of N5's transverse components. The step-wise introduction of structural and polarising effects allowed to decorrelate and gauge their respective impact. In the same spirit, the particularly asymmetric distribution of H5's HFCs could be linked to a geometrical feature of the flavin. The new set of averaged hyperfine coupling tensors derived here for the two pertinent protonation states of the flavin radical involved in putative magnetosensitive radical pairs, will be valuable to better parametrise the spin Hamiltonian for future spin dynamics calculations. Beside average values, distributions are also reported: these could be used to inform the dynamics of HFC parameters as vital for open quantum systems spin dynamics calculations or to model the inhomogeneous distribution of hyperfine

parameters expected to prevail in a biologic sample. All in all, we expect this study to help to better model the phenomenon of avian magnetoreception, and to provide a step towards elucidating its widely debated mechanisms.

3.8 Acknowledgments

We gladly acknowledge GENCI for generous computational resources (project number A0080706913) and the UK Defence Science and Technology Laboratory (DSTLX-1000139168) for financial support.

3.9 Chapter conclusion and perspectives

In this study, we report an updated set of average hyperfine coupling tensors calculated on the $FAD^{\bullet -}$ (radical anion) and $FADH^{\bullet}$ (radical semiquinone) forms of the cryptochrome-bound flavin. The long MD simulations (800 ns) from which these tensors were computed allow to obtain converged statistics for the magnetic properties of both oxidation states of the flavin involved in a credible magnetosensitive radical pair ($[FAD^{\bullet -}\text{-}W^{\bullet +}]$) or triad ($[FADH^{\bullet}\text{-}O_2^{\bullet -}\text{-}Y^{\bullet}]$). Besides, the length of the simulation approaches the expected lifetime of a radical pair or triad, which should exceed one Larmor period ($\simeq 700$ ns) to gain sensitivity to the geomagnetic field. We therefore hope to have sufficiently sampled the range of perturbations encountered by the hyperfine structure of a radical flavin during the length of one magnetic orientation event.

The inclusion of dynamical effects in the computation of HFC tensors, in this case of structural fluctuations due to thermal energy and of electronic polarisation by the immediate environment, constitutes the main novelty of this research. The former effect was included by setting up a MD simulation of the flavin within the cryptochrome protein, sampling conformations accessible at 313 K; while the latter effect was accounted for by defining a minimal polarising cluster of amino acids with a sensitivity analysis. This “cluster” was also completed with the rest of the protein environment, approximated by a set of atomic point charges.

The changes registered by HFC tensor elements, attributable to dynamical effects, are shown here to be mostly caused by structural fluctuations, while the impact of polarisation by the immediate chemical environment is weaker. We note that on average, the overall HFC shift is quite small: typically 1 or 2 MHz for a_{iso}. However,

the deformations to HFC tensors, resulting from the inclusion of dynamical effects, are expected to impact the performance of a magnetic compass operated by such tensors. Most notably, this outcome is expected from the changes in the nitrogens' A_{zz} component, or of N5's transverse components. The design of this study, where structural and polarising effects were introduced in a stepwise manner, allowed to decorrelate the respective impact of structural fluctuations and electronic polarisation on flavin-borne tensors. In particular, we were able to link the extremely asymmetric distribution of H5's a_{iso} values to a specific geometrical feature of the flavin. Finally, besides average values, standard deviation for every tensor elements were reported.

There are a few developments which we hope could build on this research. First, the provided set of average tensors could be used to parametrise a spin Hamiltonian in future spin dynamics calculations. Updated tensors could also be added individually, in order to test the hypotheses made in this article on the consequences of some changes in the shape of the tensors; for instance, whether the enhanced axial character of N5 in a dynamical environment really does increase the anisotropy of the singlet yield. Such an approach would also inform us on the sensitivity of the spin dynamics to a moderate fluctuation of the tensor, an event which, as demonstrated here, is expected to occur frequently during the lifetime of a radical pair or triad.
Second, the distributions reported could be used to inform the dynamics of HFC parameters as vital for open quantum systems spin dynamics calculations or to model the inhomogeneous distribution of hyperfine parameters expected to prevail in a biological sample.
Finally, the minimal cluster delineated in this article, although shown to have only a small polarising effect, could be used for the calculation of other dynamical electronic properties of the flavin susceptible to electronic polarisation.
All in all, we expect this study to help to better model the phenomenon of avian magnetoreception, and to provide a step towards elucidating its widely debated mechanisms.

CHAPTER 4

LOCALISATION AND IMMOBILISATION OF THE SUPEROXIDE RADICAL BY THE CRYPTOCHROME PROTEIN.

4.1 Chapter introduction

In this chapter, we explore the possibility that the Cryptochrome protein is able to immobilise a superoxide radical at its surface for extended periods of time. Such a small and mobile molecule as $O_2^{\bullet -}$, for which spin relaxation occurs primarily through spin-rotational interaction – *i.e.* the coupling of its spin magnetic moment and the molecule rotation axis when quickly tumbling in solution –, can be expected to delay its otherwise nearly immediate spin relaxation if prevented to rotate. Naturally, to achieve such long spin relaxation times as those necessary to, for instance, operate a [$FADH^{\bullet}$-$O_2^{\bullet -}$] radical **pair** ($\simeq 10^2$ ns – see Chapter 2, Fig. 2.3(a)), it is not sufficient to perfectly immobilise the $O_2^{\bullet -}$ radical: the binding must also be maintained for at least the same length of time, since diffusion entrains immediate relaxation.

Following this assessment, we investigate here the ability of a *cl*Cry4 protein to bind and immobilise, through nonbonded interactions, a $O_2^{\bullet -}$ radical. It should be noted that we investigate here a $FADH^{\bullet}/O_2^{\bullet -}/Y^{\bullet}$ radical triad which we assume to be already formed; and we understand that another study on the binding of O_2, which seems to be a necessary condition for its reduction by $FADH^-$ to generate the spin-correlated $FADH^{\bullet}/O_2^{\bullet -}$ RP under consideration here, should be done before concluding on the feasibility of the 3-radical compass proposed here in *cl*Cry4. Geometrical data from a number of Molecular Dynamics simulations are reported,

both for $O_2^{\bullet-}$ and for the biologically available Cl^- ion with which competition for the binding sites could be an issue. Several binding sites, 5 of which are of particular chemical interest as they're located in the vicinity of the flavin, are identified.

Parallel to this study, we investigate the ability of a putative $O_2^{\bullet-}$ formation site in the cavity of the flavin, where the reoxidation of $FADH^-$ could take place, to bind $O_2^{\bullet-}$. While extremely long binding and rotational correlation times are recorded, the inability of $O_2^{\bullet-}$ to ever populate this cavity casts some doubt on its relevance for *cl*Cry4 reactivity. Microsecond spin relaxation times are estimated for this site. We then explore the idea of another formation site, from which $O_2^{\bullet-}$ easily diffuses out to populate previously identified binding sites. While long binding times are still recorded, the statistics appear quite different to the case where $O_2^{\bullet-}$ can diffuse from the bulk.

Another round of MD simulations is then launched, where a $O_2^{\bullet-}$ radical is left to diffuse out from these 5 chemically relevant sites, while the binding time and the rotational correlation time within the site is monitored. These values are finally used to estimate achievable spin relaxation times, which routinely attain 10^2 ns timescales and, in extreme cases, approach the microsecond. However, a proper statistical treatment of the average ability of these binding sites to bind and immobilise a $O_2^{\bullet-}$ is not achievable from these data. We preliminarily conclude that such moderately long spin coherence times might enhance the magnetosensitivity of a $FADH^\bullet/O_2^{\bullet-}$ RP, particularly with a radical lifetime shorter than $10\,\mu$s.

Note that we are not simply focusing on the [$FADH^\bullet$-$O_2^{\bullet-}$] RP case; in our view, the formation of this particular radical pair, which has a plausible mechanism in the reoxidation of $FADH^-$ by $^3O_2$, implies the presence of a third radical somewhere, following the flavin photocycle and general reaction scheme presented in Chapter 1, Figure 1.1; and the focus of this thesis remains on the investigation of three-radical, scavenged reaction schemes. Indeed, we finally test the magnetosensitivity of a $FADH^\bullet/O_2^{\bullet-}/Y^\bullet$ radical triad, in the limit of slow $O_2^{\bullet-}$ spin relaxation. EED couplings, previously found to have an extremely strong quenching effect on MFEs, are fully taken into account by locating the $O_2^{\bullet-}$ in the previously identified binding sites. We find in particular Y319, identified in Chapter 2 as a promising scavenger, to be fairly insensitive to $O_2^{\bullet-}$ relaxation, even when located near enough to sustain large EED couplings with the other radicals.

4.2 Introduction

The $O_2^{\bullet-}$ ion, or superoxide, is a reactive oxygen species (ROS) involved in various metabolic processes within the cell, such as respiration through the electron-transfer

flavoprotein (ETF) complexes,[185] phagocytosis,[186] or phosphorylation-induced signaling[187] to initiate such processes as mitosis, cell differentiation, or apoptosis.[188,189] In mammalian cells, $O_2^{\bullet -}$ radicals are typically formed in flavo- or quinoenzymes through a one-electron transfer from a reduced flavin or quinone donor to molecular oxygen, possibly creating a radical pair in the process[190] – a mechanism supported by the reported susceptibility of some oxidative-stress-related processes to magnetic field effects (MFEs).[191,192] The emergence of magnetic field effects, or MFEs, denotes a sensitivity of the spin dynamics of a radical pair to an external magnetic field (see Chapter 1): this phenomenon is thought to be the basis for a mechanism of avian magnetoreception in the cryptochrome protein,[1] for which superoxide has been suggested as a potential radical[29] – although its involvement remains controversial.[69,101] The main enzymes involved in ROS production are the ETF complexes I and III, located in the mitochondrial membrane, and the NADPH oxidase (Nox 2), which triggers the extracellular respiratory burst of phagocytic cells[193] – a quick and toxic exhalation of ROS, some of which can diffuse back into the cell through transmembrane ion channels.[194] Superoxide generation and release can be the desired outcome, for instance as a phagocytising agent released from the NADPH oxidase; or it can be, as in the case of $O_2^{\bullet -}$ leaking from the ETF chain, a toxic phenomenon which needs to be controlled. Indeed, although a moderately oxidative ion, high concentrations of $O_2^{\bullet -}$ in cells are a source of oxidative stress,[195] either through its own action or through conversion – spontaneous or catalysed – into more potent oxidants such as H_2O_2 or the hydroxyl radical $HO^{\bullet}$. While a baseline level of these species is required for normal cell function, their presence is thought to participate in the cell-degrading process of aging, and chronically elevated oxidant levels have been linked to the onset of various pathologies.[196] Indeed, ROS have been shown to alter cellular function through at least two mechanisms: either by oxidising iron-sulphur clusters and releasing one Fe, thereby damaging ETF complexes I and III; or by abstracting electrons from various chemical species present in the cell, such as DNA, RNA, fatty acids, or steroids. This latter mode of attack results in a variety of cell damages, such as toxic/mutagenic DNA lesions,[197] increased membrane rigidity through lipid peroxidation,[198] or the closing of ion transport channels.[199]

Homeostatic control of intracellular ROS levels is carried out by an arsenal of enzymatic and molecular scavengers, organised in “lines of defence” according to their nature and function.

- The first line consists of metalloenzymes tasked with neutralising free $O_2^{\bullet -}$: typically, superoxide dismutase (SOD) converts superoxide into H_2O_2, which is then processed to harmless molecules by catalase or glutathione peroxidase (GPX).[200]

- The second line of defence comprises molecular scavengers which reduce ROS into non-radical molecules, becoming themselves free radicals of lesser toxicity in the process. This class of antioxidants notably includes vitamin E, ascorbic acid[201] and glutathione.[202]

- The 3$^{\text{rd}}$ and 4$^{\text{th}}$ lines of defence are not directly concerned with ROS neutralisation, but respectively with damage repair (*e.g.* polymerase for DNA damage) and antioxidant transport.

In the context of the three-radical model of magnetoreception, in which $O_2^{\bullet -}$ has been proposed to participate, electrostatic guidance to reaction site (*i.e.* within $\simeq$ 20 Å of the flavin cofactor) and long-time trapping at the protein surface are two features which could both facilitate the efficient operation of the magnetic compass and prevent oxidative damage to the surrounding cell components.

The ability of proteins to sequester small molecules for extended (*e.g.* tens of nanoseconds) lengths of time is well documented. Especially relevant to the case at hand is the computational study by Salerno and colleagues,[203] in which binding sites for molecular oxygen in the ETF flavoprotein were identified. Interestingly, none of these sites contained arginine (residue code: R), while this residue is consistently cited as the most important feature of a superoxide binding site[204,205] – although glutamine (G), but especially lysine (K), also appear to be involved in electrostatic guidance of $O_2^{\bullet -}$.[206–208]

In this chapter, we will investigate whether extended binding is also possible in the cryptochrome protein, and whether such binding can give rise to sufficient immobilisation of the $O_2^{\bullet -}$ radical as to delay the onset of spin relaxation. After a validation step, we shall identify $O_2^{\bullet -}$ binding hotspots at the cryptochrome surface, in particular those located within efficient electron-transfer range to the flavin. Finally, the reorientation times of $O_2^{\bullet -}$ within these binding sites will be calculated, allowing us to estimate spin relaxation times which could then be used to parameterise future spin dynamics simulations.

4.3 MD study: methodological aspects

In this section, the various trajectory sets which shall be used later for analysis are presented, and technical simulation details are provided. In a second time, he force-field used throughout these simulations is validated.

4.3.1 Simulation setup and strategy

Investigating the ability of an avian cryptochrome protein to bind a $O_2^{\bullet -}$ radical could be done via a classical Molecular Dynamics (MD) study, in which the interactions between atoms are classically approximated by calibrated harmonic potentials, allowing to propagate the positions and velocities of the whole system over long (*i.e.* up to microsecond) timescales. Such timescales are of the same order as the magnetosensitive step of the flavin-containing radical pair/triad reaction cycle. Besides, for the [$FADH^{\bullet}/O_2^{\bullet -}$] radical pair case, a previous spin dynamics investigation required coherence to be maintained over $\sim 10^2$ ns for sizable Magnetic Field Effects (MFEs) to manifest.[37] No such coherence lifetimes could be observed without a strong binding of approximately the same length, as the rapid tumbling of $O_2^{\bullet -}$ in solution is the main mechanism for its spin relaxation. For these reasons, the Molecular Dynamics method was the obvious choice for propagating our system, as any quantum representation of such a large number of atoms is prohibitively slow. The `AMBER` code also uses GPU acceleration to further speed up execution; a technology we had access to and which allowed us to sample the system remarkably fast: for instance, a system of $\sim 90,000$ atoms could be propagated, with a timescale of 2 fs, over 500 ns in just over 80 hours.

Importantly, force-field- (FF-) based MD simulation method has demonstrated its ability to correctly describe the modalities of non-bonded interactions we suspect to be relevant for binding a superoxide ion: namely, Coulombic attraction and hydrogen bonding. It was also previously used for a similar purpose, to identify binding pockets of molecular oxygen at the surface of a flavoprotein,[209] or superoxide formation site near the flavin.[2]

All Molecular Dynamics (MD) simulations in this chapter were performed using the `AMBER` 18 package,[210,211] specifically the `SANDER` code for energy minimisations and the GPU-accelerated `PMEMD.cuda` code[212,213] for equilibration, heating and production runs. GPU acceleration with a GeForce RTX 2080 Ti GPU allowed to reach an impressive average of ~ 150 ns/day for a simulation of $\sim 90,000$ atoms in the NVT ensemble with PME.

The first set of simulations, dedicated to locating superoxide, were run on 10 different initial configurations of a 89,637-atom system, consisting of a *Columba livia* Cryptochrome 4 protein binding a flavin adenine dinucleotide radical in its neutral semiquinone form $FADH^{\bullet}$. In a first time, a single configuration of this complex is created, solvated with a 10-Å TIP3P water molecule padding. The $92 \times 94 \times 125$ Å^3 square cuboid box also contains 21 $O_2^{\bullet -}$ molecules (43 mM, *i.e.* a largely supraphysiological concentration), and the whole system is neutralised with 17 Na^+ ions. A similar set of 10 500-ns simulations, containing 21 Cl^- ions instead of $O_2^{\bullet -}$, was also generated.

System minimisation, heating and equilibration followed a protocol detailed in Ref. 164. These steps yielded an equilibrated system of dimensions $87 \times 89 \times 117\,\text{Å}^3$. In all equilibration and heating phases, the target temperature was set to $T = 313\,\text{K}$ (40 °C, an average of diurnal/nocturnal core temperature of *Columba livia*)[214] with Langevin dynamics.[215] All runs in the NpT ensemble aimed at a target pressure of 1 bar, enforced by a Berendsen barostat.[216] All preparation and production runs employed a 2 fs timestep, the Particle-Mesh Ewald (PME) summation method for computing electrostatic interactions,[217] and the SHAKE algorithm.[165] Post-treatment of the trajectories, namely frame alignment and re-imaging, was performed with `cpptraj`.

4.3.1.1 $O_2^{\bullet-}$ binding sites search: FD-SUP dataset

To investigate the interactions between an avian cryptochrome protein and the $O_2^{\bullet-}$ radical, we chose to set up a system of a *Columba livia* cryptochrome 4 protein, solvated in water, and containing 21 $O_2^{\bullet-}$ radicals. While largely supraphysiological, the $O_2^{\bullet-}$ concentration has been obtained from a similarly-sized MD study,[209] in which 20 O_2 did not interact among themselves while affording a faster sampling of the protein-O_2 interactions.

In order to gain more insight into the nature of the protein-$O_2^{\bullet-}$ binding, and to uncover potential competition for binding sites with other negatively charged species already present around the protein, a comparable system was set up, with Cl^- ions instead of $O_2^{\bullet-}$ radicals.

The initial structure for the pigeon Cryptochrome 4 protein (PDB code: 6PU0) was taken from a previous MD simulation:[34] it was chosen from a clustering analysis on the conformations adopted along the trajectory, which identified the most frequently occurring conformation. This previous MD simulation used the original crystallised form of the *Columba livia* protein,[30] for which the loop poorly resolved by X-Ray Diffraction (XRD) had been reconstructed in Ref. 34. It is modeled with the ff14SB force-field for proteins and ions.[84] The GAFF2 all-atom force-field[210] was used to model the $FADH^\bullet$ and $O_2^{\bullet-}$ radicals. The former was modified with a set of RESP atomic charges established in Ref. 162, and the latter with the appropriate electronic charges and equilibrium bond length.

After a successful preparation of this unique initial configuration, 9 additional copies of it were made and $O_2^{\bullet-}$ radicals were moved to new locations in each of them, while the solvent molecules and protein-$FADH^\bullet$ complex remained in place. The new spatial configurations of $O_2^{\bullet-}$ radicals in the box were generated using the `PackMol` software.[218] A short (3,000 steps) energy minimisation of the solvent and SUP molecules, while constraining the positions of the protein-$FADH^\bullet$ complex with the application of a 500 kcal.mol^{-1} harmonic potential, was used to remove steric tension

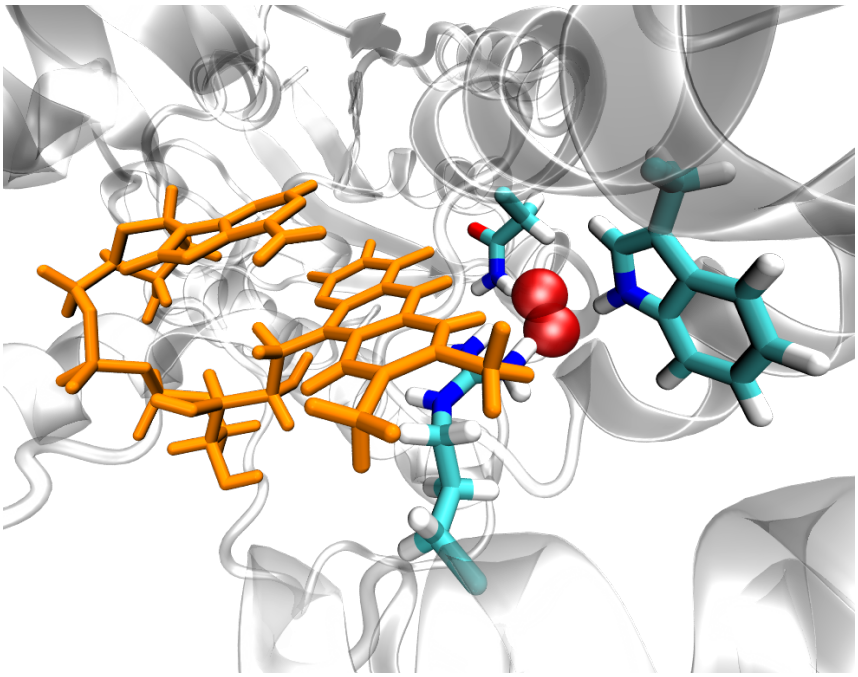

Figure 4.1: Representation of $O_2^{\bullet -}$ in the binding cavity from Ref. 2. $FADH^{\bullet}$ is shown in orange, and ASN393, TRP397 and ARG358 surrounding a $O_2^{\bullet -}$ radical are highlighted.

from all these 10 starting configurations, before regenerating atomic velocities with a 400 ps heating simulation in the NpT ensemble to $T = 313$ K. A production run in the NVT ensemble was then launched from all 10 initial configurations, for 500 ns.

The sets of 10 500-ns trajectories thus generated, for $O_2^{\bullet -}$- and Cl^--containing systems, are respectively referred to as the **FD-SUP** and **FD-CL** trajectory sets. FD stands for "free-diffusing" and highlights the fact that anions are allowed to freely explore both bulk and bound states – a feature which will not be present in other trajectory sets presented later in the Chapter.

4.3.1.2 $O_2^{\bullet -}$ binding in the flavin cavity: C-SUP

We also investigate a binding pocket located close to the $FADH^{\bullet}$. Identified by Mondal and co-workers[2] in the *dm*Cry protein (a drosophila cryptochrome), it was proposed as a formation site for the superoxide radical; a triplet oxygen $^3O_2$ would enter the pocket, reduce the $FADH^-$ by a fast electron transfer, and then remain in the cavity, held by strong electrostatic interactions and possibly H-bonding. Figure 4.1 shows the initial localisation of $O_2^{\bullet -}$ in this binding cavity.

The dynamics of $O_2^{\bullet -}$ inside the binding pocket were simulated by setting up a Molecular Dynamics study where one $O_2^{\bullet -}$ radical was placed inside the binding pocket. The same initial *cl*Cry conformation as the FD-SUP dataset was used. The system was left to evolve for 400 ns at $T = 313$ K in the NVT ensemble, after which τ_2 and γ_B values were computed. In order to investigate the reorientation

dynamics of $O_2^{\bullet -}$ into the binding pocket, we require a more finely time-defined MD trajectory; indeed, a 200 ps interval between two consecutive geometries does not permit computing τ_2 reorientation times shorter than 200 ps. For this reason, the MD simulation was carried out with a Δt between consecutive geometries of 10 ps. This trajectory is referred to as **C-SUP**, with C standing for "cavity".

4.3.1.3 $O_2^{\bullet -}$ diffusing away from a putative formation site: E-SUP

The observation that the $O_2^{\bullet -}$ formation site in the flavin-binding cavity, *i.e.* the starting point for the C-SUP simulation, is never populated by a free-diffusing $O_2^{\bullet -}$ throughout the FD-SUP dataset led us to propose an alternative $O_2^{\bullet -}$ formation site, also located suitably close to $FADH^{\bullet}$. The set of diffusion trajectories generated from an initial configuration of $O_2^{\bullet -}$ in this binding site is referred to as **E-SUP**, for "escaping $O_2^{\bullet -}$".

In order to study the diffusion dynamics of a newly created $O_2^{\bullet -}$, we set up an MD simulation of the *cl*Cry protein, solvated in a TIP3P water box extending 10 Å away from the protein on each side, and an appropriate ion concentration, as well as one $O_2^{\bullet -}$ radical. We hypothesised the initial $O_2^{\bullet -}$ fixation point to be as close to the isoalloxazine moiety of the $FADH^{\bullet}$ as possible, without entering the $FADH^{\bullet}$-binding cavity, as this domain seems to be impenetrable to $O_2^{\bullet -}$ radicals in all 10 500-ns simulations. Additionally, the fixation point was picked to be between a histidine (HIE353), an asparagine (ASN394) and a tryptophan (TRP290) residues, all polar aminoacids and therefore hypothesized to be capable of maintaining O_2 in place for the electron transfer. All these constraints located the $O_2^{\bullet -}$ residue, at $t = 0$ of the simulation, 3.5 Å away from the $FADH^{\bullet}$ C8 methyle group; see Figure 4.2.

The system was equilibrated and heated in much the same way as the other MD simulations in the NVT ensemble presented in this chapter; the details of the steps can be found in Ref. 164. The difference is that here, the single $O_2^{\bullet -}$ molecule was held firmly in place with the application of an harmonic potential. After this, a short 40-ns MD simulation in the NVT ensemble was run, saving structures every 200 ps. Again, the $O_2^{\bullet -}$ radical is kept in place near the flavin by a strong harmonic potential. Geometries from this first dynamics were extracted and used as starting points for restarted simulations, where the escape path of $O_2^{\bullet -}$ and its interaction with the identified binding sites would be monitored.

To do so, 5 frames were chosen from the initial NVT run to serve as starting configurations: frame 10 (*i.e.* after 2 ns), 50 (10 ns), 100 (20 ns), 150 (30 ns) and 200 (40 ns). Taking starting conformations sufficiently spaced out in the dynamics allows to sample different conformations of the protein and of the side-chains, thereby better representing the overall protein structure. From there, each starting conformation was copied into 20 identical replicas, from each of which an MD simulation would be

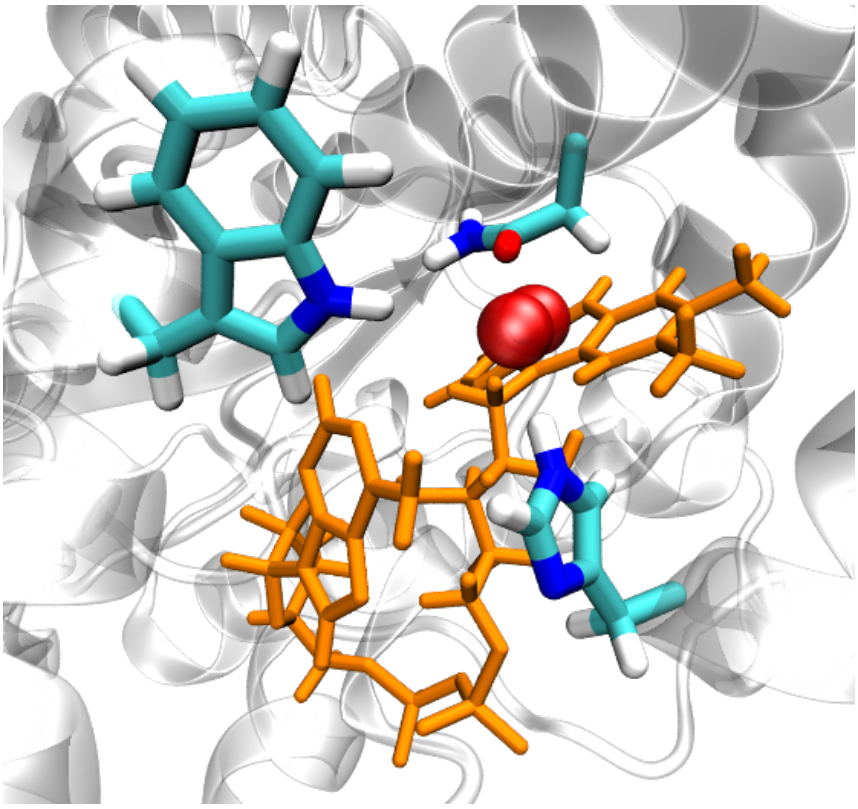

Figure 4.2: Representation of the hypothesized $O_2^{\bullet -}$ fixation point. $FADH^{\bullet}$ is shown in orange, and HIE353, ASN394 and TRP290 surrounding a $O_2^{\bullet -}$ radical are highlighted.

started.

4.3.1.4 $O_2^{\bullet -}$ diffusing out of binding sites: T-SUP

Finally, the reorientation dynamics of $O_2^{\bullet -}$ when bound by the protein, in each of the 5 binding sites identified from analysing the FD-SUP trajectory set, were investigated. This is achieved by running another MD study where $O_2^{\bullet -}$ radicals are originally placed into the sites of interest. Their motions inside the site are monitored, and the simulation is terminated once $O_2^{\bullet -}$ has diffused out of the site. Here again, a Δt between two consecutive geometries of 10 ps was employed, in order to be able to compute relatively short reorientation times τ_2. The same criteria for identifying binding ($d_{\mathrm{SUP-residue}} \leq 3.0$ Å) and for defining sites (Table 4.3) as before are in use here. In order to also obtain reference values for the reorientation time of a freely tumbling $O_2^{\bullet -}$ radical in the bulk, an additional MD study is set up, where 5 $O_2^{\bullet -}$ and an appropriate salt concentration are placed in a TIP3P water box. For free $O_2^{\bullet -}$ for which the reorientation time is expected to be even shorter, a Δt of 100 fs was chosen.

Starting geometries, with $O_2^{\bullet -}$ inside of each binding site, are extracted from the FD-SUP set of trajectories, where $O_2^{\bullet -}$ radicals diffuse from the bulk onto the protein surface. Ideally, starting configurations from the E-SUP would have been

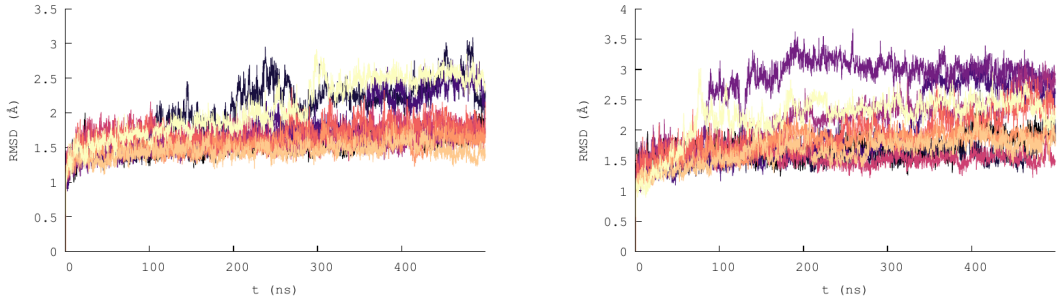

(a) $O_2^{\bullet-}$ (b) Cl^-

Figure 4.3: Root-Mean-Square Deviation (RMSD) of the positions of *cl*Cry backbone heavy atoms, for the 10 500-ns trajectories of solvated *cl*Cry containing $FADH^\bullet$ and 21 (a) $O_2^{\bullet-}$ or (b) Cl^- ions.

more relevant to the chemistry of the problem investigated, and could have given rise to longer binding times; but the chronology of the project meant that E-SUP data were not available at the time of starting this round of simulations.

For each binding site, 5 $O_2^{\bullet-}$-site binding configurations were extracted from the FD-SUP trajectories. These frames were all chosen from a long binding event, to increase the chance of it corresponding to a strongly binding configuration. Site 4, deemed to be of lower interest at the time of setting up this study, was investigated with only 2 starting configurations, as a compromise to the large resources in memory this project demanded. For all sites, initial geometries were picked semi-randomly, only satisfying the criterion that upon visual inspection, $O_2^{\bullet-}$ did not look particularly weakly bound and about to unbind.

Finally, in order to generate correct binding statistics, each starting configuration was copied into 20 identical replicas, for a total of 100 trajectories for each site (except site 4, with only 40). The set of trajectories created from these starting configurations will be referred to as **T-SUP**, for trapped-SUP. Initial velocities consistent with a temperature of 313 K were regenerated with a short heating phase, before running an MD simulation in the NVT ensemble until $O_2^{\bullet-}$ diffused out of the site.

4.3.2 Model validation

4.3.2.1 Protein structure analysis

Figure 4.3 reports the Root-Mean-Square Deviations (RMSD) of the positions of backbone heavy atoms, for each of the 10 trajectories. Most trajectories are characterised by a stable RMSD of $\sim 1.5-2$ Å, which suggests a nearly constant secondary and tertiary structure of the protein. Others tend to exhibit a jump, followed by an elevated but stable RMSD following that. On average though, trajectories containing $O_2^{\bullet-}$ radicals have a lower (RMSD= 1.70 ± 0.65 Å) RMSD than those containing Cl^- (RMSD= 1.93 ± 0.98 Å). Both systems were successfully equilibrated to the target

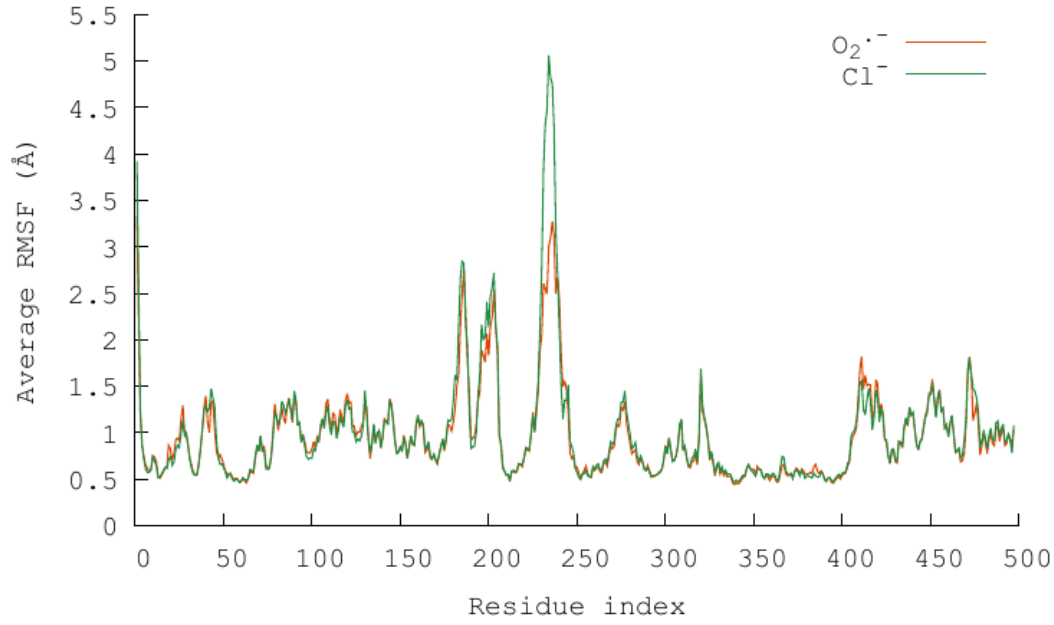

(a)

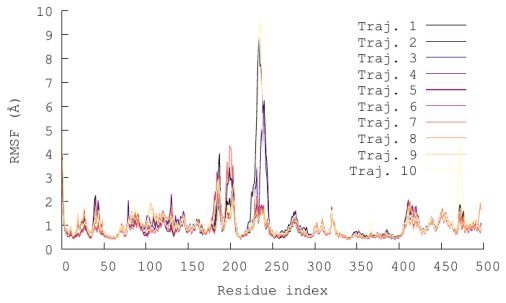

(b) $O_2^{\bullet -}$

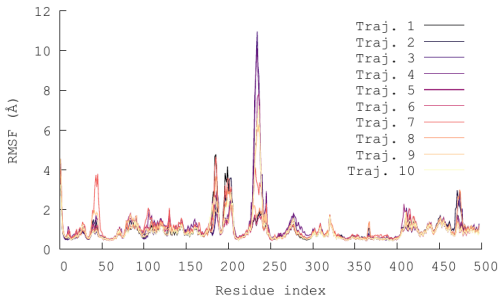

(c) Cl^-

Figure 4.4: Root-Mean Square Fluctuations (RMSF) of the positions of *cl*Cry backbone heavy atoms, for the 10 500-ns trajectories of solvated *cl*Cry binding $FADH^{\bullet}$ and 21 (b) $O_2^{\bullet -}$ or (c) Cl^- ions. The average RMSF curve for both these data sets is reported in (a).

pressure and temperature, and both have the same ionic strength; their great similarity makes it unlikely that the apparent difference in stability arises from a systematic bias introduced by the anion.

This feature could be better understood using the Root-Mean Square Fluctuation of atomic positions, or RMSF (Fig. 4.4), calculated as the average of all RMSD values for a given residue along the trajectory. This residue-disaggregated view allows to identify the most mobile parts of the protein, which exhibit a large RMSF (*i.e.* a large time-averaged RMSD). Here, the most flexible sections of the backbone are identified as the phosphate-binding loop (or PBL; residues 228 to 244), a result confirmed in other studies.[34] There does exist a variability in the magnitude of each peak, but their location remains consistent across both data sets. Indeed, the most mobile loop remains by far the 228-244 (in gold on Fig. 4.5), followed by two adjacent peaks

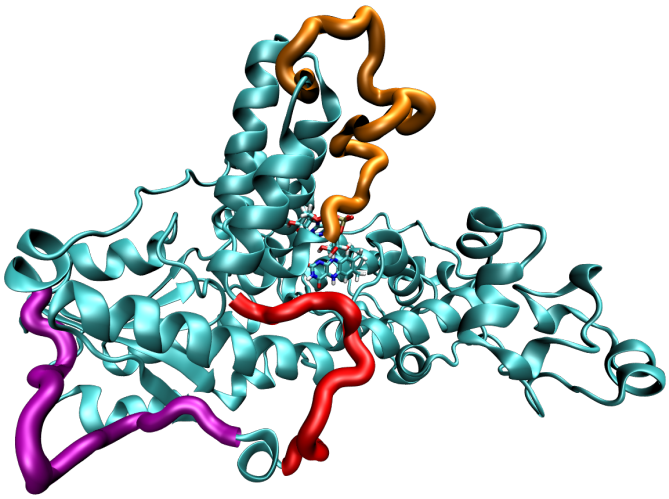

Figure 4.5: Graphical representation of the starting conformation of the 6PU0 protein, where the 3 most flexible residue ranges are highlighted. Residues 228 to 244 (phosphate-binding loop) is in gold, 180-195 in purple, 200-210 in red.

roughly ranging the 180-195 (purple) and 200-210 (red) residues. Highlighted in Fig. 4.5 on the 6PU0 protein in its initial conformation, these three mobile ranges correspond unsurprisingly to unstructured, solvent-exposed loops. The lack of secondary and tertiary structure to these areas is the cause for their great flexibility. This is also illustrated by the presence of a short (5-residue) alpha helix between the purple and the red segments, responsible for the dip in the RMSF curve separating the two unstructured loops. This feature remains present throughout the simulation.

While the overall RMSF profile of both sets of $O_2^{\bullet -}$ and Cl^- trajectories is qualitatively similar, an average RMSD difference remains, with a larger proportion of Cl^--containing trajectories exhibiting increased overall flexibility. Fig. 4.4 (a) allowed us to verify that it however did not arise from the denaturation of an area otherwise stable in all $O_2^{\bullet -}$-containing simulations - an effect that, if it could have been ascribed to the action of the anion, would have both been unexpected and would have made the comparison between $O_2^{\bullet -}$ and Cl^- binding areas trickier. Indeed, it seems that the lower average RMSF in the PBL peak is not due to a systematic electrostatic effect, as sizable RMSF for this region can be achieved for some trajectories in both $O_2^{\bullet -}$ and Cl^- datasets. In these conditions, the apparent difference is probably independent of the anion and simply a statistical artefact arising from the small sample size, of only 10 500-ns trajectories per dataset.

To conclusively link the sudden RMSD jumps observed in 4.3, more present in the Cl^- dataset, and the increased PBL flexibility of the latter, we also report (in

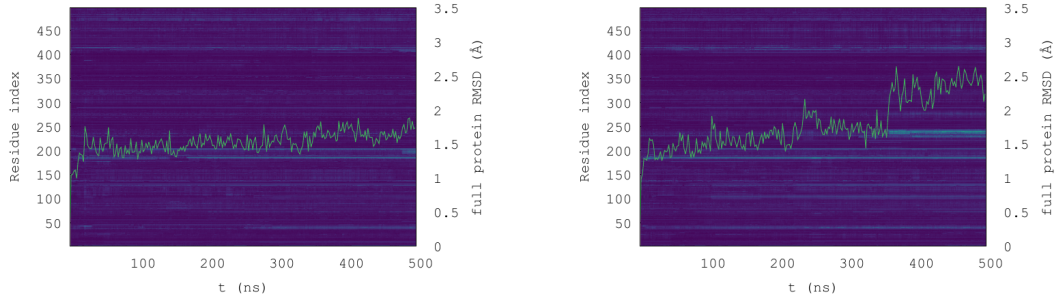

(a) Traj. 1

(b) Traj. 3

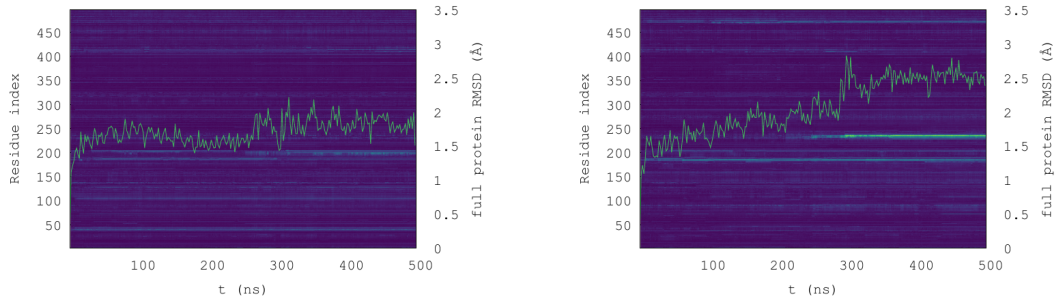

(c) Traj. 7

(d) Traj. 10

Figure 4.6: Per-residue RMSD of the backbone heavy atoms (AMBER names: N, CA, C, O) along some of the 10 500-ns MD trajectories of *cl*Cry with 21 $O_2^{\bullet -}$ radicals. A lighter spot at coordinates (x,y) denote a large RMSD for residue y at time x. The average RMSD for the full protein, as shown in Fig. 4.3, is superimposed. All axes scaling and colourscales are harmonised, allowing a direct visual comparison across subfigures. The remaining 6 trajectories are provided in Appendix C.

Fig. C.1 and C.2, and C.3 and C.4) below the per-residue RMSD as a function of the simulation time. The full-protein RMSD curve, as reported in Fig. 4.3, is also superimposed onto this representation, so that its features, such as sudden increases or "jumps" as mentioned above can be correlated in time with an increase or decrease of RMSD of a particular region.

The large RMSD jumps observed in Fig. 4.3 could be identified, both by matching with the RMSF and by visual inspection, to the release of the phosphate-binding loop. This is particularly evident for Cl^-, in trajectories 3 (Fig 4.7 (c)) and 4 (Fig. 4.7 (d)). The same phenomenon of synchronised full-protein RMSD jump and PBL RMSD increase can also be found in the $O_2^{\bullet -}$dataset, *e.g.* for trajectories 3 (Fig. 4.6 (c)) and 10 (Fig. 4.6 (j)). Other than this, areas of chronically elevated RMSD correspond to the high-RMSF peaks in Fig. 4.4, in particular the two peaks at 180-195 and 200-210. Interestingly, these seem to be also able to give rise to full-protein RMSD elevation ($O_2^{\bullet -}$: trajectory 7 from $\simeq 250$ ns; Cl^-: trajectories 1 and 8), although not nearly achieving the same magnitude as the PBL. This could be due to their shorter length compared to the latter, affording them fewer degrees of freedom across their constitutive dihedrals, bond angles and lengths; perhaps also their more constrained

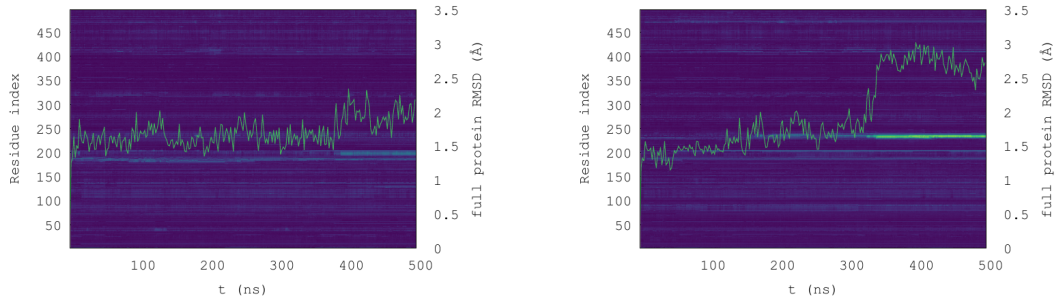

(a) Traj. 1

(b) Traj. 3

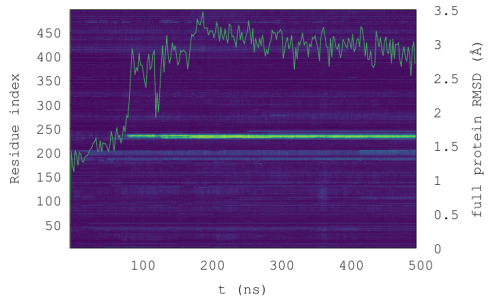

(c) Traj. 4

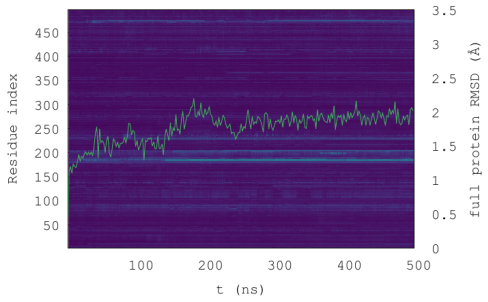

(d) Traj. 8

Figure 4.7: Per-residue RMSD of the backbone heavy atoms (AMBER names: N, CA, C, O) along some of the 10 500-ns MD trajectories of *cl*Cry with 21 Cl^- radicals. A lighter spot at coordinates (x,y) denote a large RMSD for residue y at time x. The average RMSD for the full protein, as shown in Fig. 4.3, is superimposed. All axes scaling and colourscales are harmonised, allowing a direct visual comparison across subfigures. The remaining 6 trajectories are provided in Appendix C.

linearity, as they are more stretched out between two very structured (and therefore rigid) sections of the protein (see Fig. 4.5).

4.3.2.2 Binding energetics: force-field vs. DFT

Another aspect of the model requiring validation is the description of nonbonded interaction between anions ($O_2^{\bullet -}$, Cl^-) and the protein. Given the inability of this implementation of MD to describe chemical event such as bond formation, we expect nonbonded interaction – namely, Coulomb and van der Waals – to be the only relevant modality of interaction in this system. Besides, superoxide is only a weak oxidising and reducing agent, whose known reactivity is with alkyl halides – not present in this protein – and with thiols, although at a fairly slow rate.[219,220] No particular electrostatic affinity of $O_2^{\bullet -}$ with thiol aminoacids, *i.e.* cysteine and methionine, has been detected in the present study, and we therefore do not expect that disregarding chemical reactivity of $O_2^{\bullet -}$ invalidates the conclusions reached in this study.

As mentioned in the general Methods section in the introduction, nonbonded interactions are modeled in this force field by the Coulomb term, parametrised by atomic charges, and by the van der Waals term taking the form of a Lennard-Jones potential. While the atomic electronic charges of $O_2^{\bullet -}$ have been fixed to -0.5 per O atom, the Lennard-Jones parameters were taken directly from the GAFF2 force field for molecular oxygen. This could constitute a source of error as the extra electron in $O_2^{\bullet -}$ is expected to increase the size of its electron cloud. On the other hand, GAFF2 nonbonded parameters for Cl^- already exist and should not carry much systematic error when describing the interactions with standard residues such as aminoacids.

Intermolecular nonbonded interactions can be calculated by computing the interaction energy E_{int}:

$$E_{\text{int}}^{\text{AB}} = E^{\text{AB}} - \left(E^{\text{A}} + E^{\text{B}}\right), \tag{4.1}$$

where E^{AB} is the potential energy of the complex of molecules A and B, and E^{A} is the potential energy of molecule A alone; resp. with B. These quantities can be easily obtained from a 0-step MD simulation, where the energy of the system is computed but the positions of the atoms are not propagated. We chose to run these 0-step MD simulations in the NVT ensemble. This ensured perfect comparability with the production NVT runs which we seek to validate.

The interaction energy was computed on a complex of $O_2^{\bullet -}$ and ARG. As will be shown in more details later, this is a recurring interaction pattern for which MD-generated geometries are abundant, and one which is of particular significance for superoxide immobilisation. Here, E_{int} were computed for 36 consecutive conformations of the ARG-$O_2^{\bullet -}$ complex, extracted as a subtrajectory of one of the 500-ns trajectories obtained above. Since the phenomenon under investigation here is long, uninterrupted immobilisation of $O_2^{\bullet -}$ by the protein, it seemed that more relevant energetic figures would be obtained by treating a subtrajectory rather than individual snapshots, where $O_2^{\bullet -}$ could be in a brief encounter with ARG not necessarily giving rise to extended binding.

Such extended binding event were much rarer for Cl^-, although this ion also exhibits a preference for complexing with ARG. For this reason, and for better comparability with the ARG-$O_2^{\bullet -}$ complexes, the ARG-Cl^- complex geometries were obtained by taking the geometries in the subtrajectory mentioned above and simply mutating the $O_2^{\bullet -}$ into Cl^-. Finally, the arginine residue, truncated at the backbone and leaving an unsaturated valence at the amino N and carboxylate O, was capped at both ends by a methyle and an acetyl group. This method allowed to avoid creating a nonstandard residue for arginine. We expect the aliphatic part of the ARG side-chain

to insulate the diamine head from any potential induction effect from these capping residues.

To sample correctly the range of $O_2^{\bullet -}$ binding geometries with an ARG residue, a short geometry optimisation in MM was performed on these structures. The arginine side-chain, its backbone and the anion were kept from relaxing by applying a very strong harmonic potential, while the capping residues were allowed to relax. This protocol served the purpose of correcting the initial geometries of the capping residues, particularly in their dihedrals and bond angles with respect to the backbone of the arginine, as this unchemical tension would artificially raise the energy of the residues, and completely prevent convergence when a QM energy calculation is done on these same geometries. For Cl^--ARG binding geometries, which had been generated by arbitrarily locating Cl^- on one of the $O_2^{\bullet -}$ atoms, a slightly different protocol was used: while the arginine side-chains and backbone positions were still constrained, both the anion and capping residues were allowed to relax. This protocol permit to approximate a more realistic binding configuration for Cl^- ions.
The two sets of ion-arginine binding geometries thus created will be referred to as $\left[O_2^{\bullet -} - \mathrm{ARG}\right]$ and $\left[Cl^-_{\mathrm{opt}} - \mathrm{ARG}\right]$. The "opt" subscript in the latter set recalls the fact that Cl^- was allowed to relax its position with respect to the arginine, therefore realising an idealised binding configuration not necessarily present in the actual dynamics, unlike $\left[O_2^{\bullet -} - \mathrm{ARG}\right]$ geometries.

Finally, interaction energies were computed on these sets of geometries. In order to validate them against a more accurate method, *i.e.* one not relying on generic, fitted potential, but instead describe the electronic structure of the complex, interaction energies $E_{\mathrm{int}}^{\mathrm{ARG-SUP}}$ were then computed on the same geometries using DFT, at the CAM-B3LYP/def2-TZVP level of theory in Gaussian 16. A dispersion correction to the energy was added, in the form of the D3BJ method.

Comparing the energies of a single fragment E^{A} and a complex E^{AB} in DFT is trickier than in MM, because of the use of a basis set to spatially distribute electron density. When in a complex, electron density of *e.g.* the arginine can access $O_2^{\bullet -}$-bound basis set function – especially when diffuse, *i.e.* large, basis functions are used –, effectively allowing delocalisation and further decrease in total energy. On the other hand, these basis functions are not present when the arginine is considered in isolation. The E^{ARG} term is therefore effectively computed on a poorer basis set than $E^{\mathrm{ARG-SUP}}$, rendering the comparison inappropriate. The resultant error, termed Basis Set Superposition Error (BSSE), can be corrected by computing the energies of each individual fragment in the full basis set, by placing "ghost atoms" (*i.e.* atoms with no nuclei or electrons but holding basis functions) where

Complex	$E_{\text{int}}^{\text{MM}}$ (kcal/mol)	$E_{\text{int}}^{\text{QM}}$ (kcal/mol)
$\left[O_2^{\bullet-} - \text{ARG}\right]$	-92.0 ± 3.6	-113.0 ± 3.9
$\left[Cl^-_{\text{opt}} - \text{ARG}\right]$	-86.1 ± 1.8	-109.0 ± 1.9

Table 4.1: Average and standard deviations of the interactions energies of 2 complexes over a 36-frame subtrajectory, computed at the MM and QM (DFT) level.

the other molecule would be. This method is implemented in Gaussian 16 with the *Counterpoise* keyword.[221,222] For these clusters, the BSSE amounts to $\simeq 4$ kcal/mol, a chemically significant error.

We focus here on the accuracy of the force field for each ion, taking the DFT-calculated values as reference (see Table 4.1). In both cases, the force-field underestimates E_{int} by about 20%; specifically, -21.2 kcal/mol *i.e.* 19% for $O_2^{\bullet-}$, and -22.8 kcal/mol *i.e.* 21% for Cl^-. The crucial point here is that $O_2^{\bullet-}$ interaction energies are not overestimated by the force-field, meaning that the length and quality of immobilisation of binding events observed in the dynamics could constitute a sort of "worst-case scenario", and the rotational correlation times computed therein could be longer in reality. While it may seem strange for Cl^-, a common biological ion for which force-field parameters were derived with great care, one must keep in mind that these parameters were not fitted to reproduce ion-residue interaction energies, but rather "solvation free energies, radial distribution functions, ion-water interaction energies and crystal lattice energies and lattice constants" (cited from the AMBER website).[223]

The aim here is not to compare the $O_2^{\bullet-}$ and Cl^- cluster, as the set of geometries on which E_{int} were calculated are not comparable; indeed, the $\left[Cl^-_{\text{opt}} - \text{ARG}\right]$ probably represents a "best-case scenario", an optimal binding configuration which perhaps wouldn't be sampled, or not as often, in an actual dynamic. This leads us to be critical of the actual E_{int} values computed here, which perhaps overestimates those encountered in the MD simulation. This hypothesis is supported by the E_{int}^{MM} computed on a third dataset, $\left[O^{\bullet-}_{2,\text{opt}} - \text{ARG}\right]$, containing $O_2^{\bullet-}$-ARG geometries taken from the same subtrajectory, but where the $O_2^{\bullet-}$ was also left to relax its position with respect to the arginine. These conformations show increased MM interaction energies of $E_{\text{int}}^{MM} = -99.62 \pm 2.38$ kcal/mol, which suggest stronger binding than in the $\left[O_2^{\bullet-} - \text{ARG}\right]$ set. Besides the averaged picture, each of the $\left[O^{\bullet-}_{2,\text{opt}} - \text{ARG}\right]$ structures registered an increase in E_{int} after letting $O_2^{\bullet-}$ relax.

We can therefore make the proposition that relaxed geometries artificially boost the interaction energies, thereby suggesting that Cl^- interacts in a significantly

weaker fashion with the protein than $O_2^{\bullet-}$ does; however, we cannot be certain that the subtrajectory chosen samples sufficiently the range of binding geometries accessible to both ions – especially since binding events often involve multiple residues at once. The comparison between $O_2^{\bullet-}$ and Cl^- binding will therefore remain outside of the scope of this chapter, and more research will be needed to conclude on whether there exist or not competition between these ions for occupying some specific binding sites. We can at least draw the conclusion that the FF used here does not overestimate $O_2^{\bullet-}$ binding to the protein, and that $O_2^{\bullet-}$ seems to exhibit a more marked preference for binding arginine residues than Cl^- does.

4.3.2.3 $O_2^{\bullet-}$ vs Cl^- binding capabilities: energetics of desolvation

This section examines the interaction of the two anions present in our system, $O_2^{\bullet-}$ and Cl^-, with water molecules, and with the different degree of solvation they maintain when bound to the protein vs. in the bulk. Due to the stabilising nature of solvation, the removal of water molecules to approach the protein surface comes with an energy penalty, the free energy of desolvation, which we estimate in this section.

The radial distribution function, or RDF, between a molecule i and the water molecules w is given by function $g_{iw}(r)$ defined in Eq. 4.2. It is a measure of the angle-averaged density of w with respect to i at distance r, and is typically used to uncover such structures as solvation shells.

$$g_{iw}(r) = \frac{1}{4\pi r^2 N_w \Delta r} \sum_{t=0}^{T} \sum_{j=1}^{N_w} \delta \left[|\vec{r_i}(t) - \vec{r_j}(t)| - r \right], \tag{4.2}$$

where T is the simulation length, N_w the total number of water molecules, and $\frac{1}{4\pi r^2 \Delta r}$ the normalisation volume on a grid of spacing Δr.[224] In this study, we use the radial distribution function to characterise the solvation structure of water around $O_2^{\bullet-}$ and Cl^- ions. For both anions, the question we pose is: "how many water molecules have to be removed for an anion to leave the bulk and adsorb onto the protein, and what is the energy cost associated with it". The criterion for adsorption onto the protein will be defined in more details later in the study (cf. Figure 4.13): a $O_2^{\bullet-}$ radical is considered to be in a *bound* state when found within 2.75 Å of the protein surface, and a Cl^- ion within 3.00 Å.

In order to account for the dynamics of desolvation and resolvation, which may not occur immediately after the ligand has entered or left the 3.00 Å cutoff around the protein, we chose to err on the side of caution and to define the *bulk* state for $O_2^{\bullet-}$ and Cl^- atoms as when the anion is at $d_{prot.-ion} \geq 10.0$ Å away from the protein.

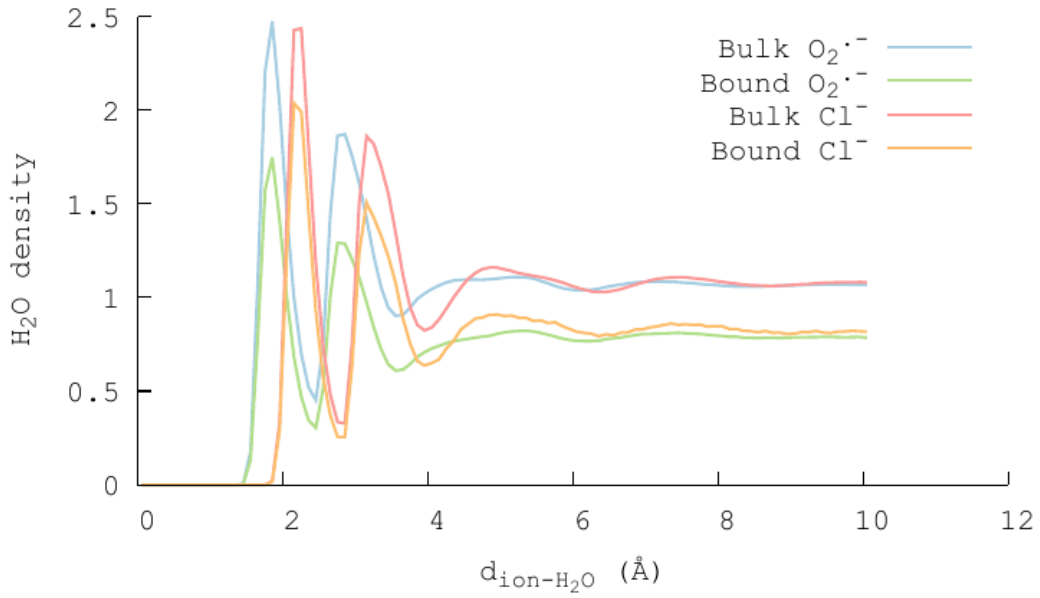

Figure 4.8: Radial Distribution Functions (RDF) of the $O_2^{\bullet -}$ and Cl^- ions with respect to H_2O, when realising a bound ($d_{prot.--ion} \leq 3.0\,Å$) or bulk ($d_{prot.--ion} \geq 10.0\,Å$) configuration. Computed over all frames from the 10 500-ns MD simulations, and all 21 ions, which satisfied the distance criteria.

In this way, we expect that its full solvation shell has reformed.

Figure 4.8 reports the RDFs of water with respect to $O_2^{\bullet -}$ and to Cl^-, separating the cases when the ion is in the *bound* and *bulk* state. This was computed over the 500-ns MD simulations containing respectively 21 $O_2^{\bullet -}$ and 21 Cl^- ions.

Examining Figure 4.8, we remark that both $O_2^{\bullet -}$ and Cl^- have a fairly far-ranging solvation structure: for both bulk states, we can identify 4 solvation shells, each materialised by a water density peak. The first two, occurring near 2 and 3 Å away from the ion, are the most well-defined, and occur at the same value of $d_{prot.--ion}$ for the protein-bound and bulk state.

Comparing $O_2^{\bullet -}$ and Cl^- solvation structure, we remark that the first and second solvation shell, as well as their peak water densities, occur at shorter distance for $O_2^{\bullet -}$ as they do for Cl^-. This is consistent with a phenomenon also observed in Figure 4.13, that $O_2^{\bullet -}$ tends to approach the protein surface closer.

Integrating the g_{iw} function yields the number of water molecules as a function of distance from molecule i, and therefore can be used to count the number of water molecules in a given solvation shell. The resulting function is given in Figure 4.9, and a numerical breakdown is given in Table 4.2.

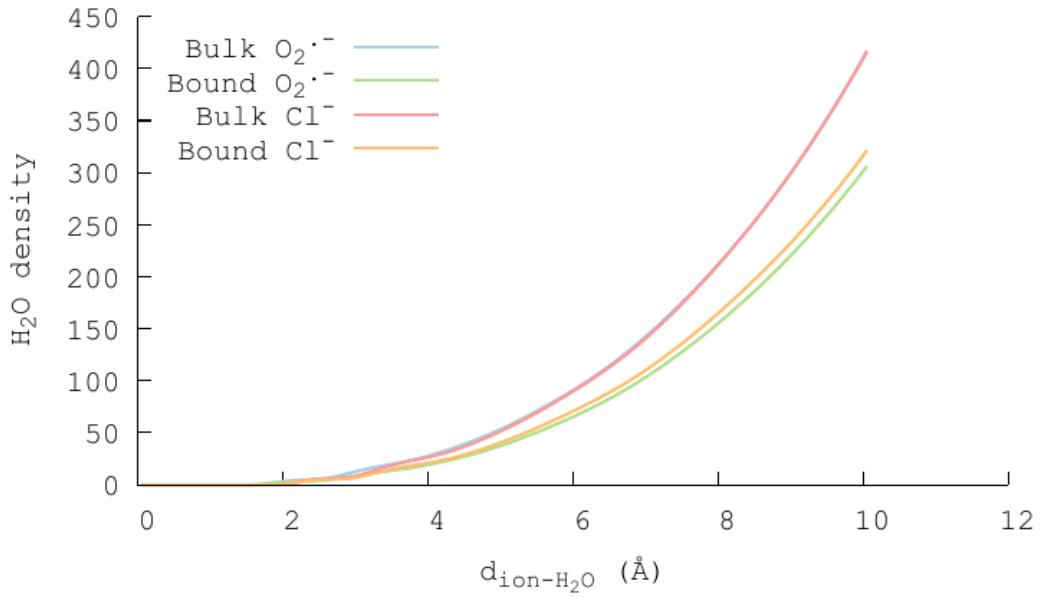

Figure 4.9: Integrated number of water molecules from the Radial Distribution Functions (RDF) of the $O_2^{\bullet -}$ and Cl^- ions with respect to H_2O, when in a bound ($d_{prot.-ion} \leq 3.0$ Å) or bulk ($d_{prot.-ion} \geq 10.0$ Å) configuration. Computed over all frames from the 10 500-ns MD simulations, and all 21 ions, which satisfied the distance criteria.

	1st shell			2nd shell		
	d (Å)	$N^{bulk}_{H_2O}$	$N^{bound}_{H_2O}$	d (Å)	$N^{bulk}_{H_2O}$	$N^{bound}_{H_2O}$
$O_2^{\bullet -}$	2.45	5.22	3.63	3.55	20.57	14.17
Cl^-	2.85	6.92	5.61	3.95	25.71	20.62

Table 4.2: Solvation shell boundary distances and integrated number of water molecules for $O_2^{\bullet -}$ and Cl^- ions, when in a bound and bulk state.

Figure 4.9 and Table 4.2 allow us to estimate the number of water molecules displaced in the binding of the ion to he protein surface, *i.e.* in the transition from *bulk* to *bound* state. We focus here only on the first solvation shell, which contains water molecules with which the ion interacts most strongly with and which should therefore contribute the majority of the total free energy of desolvation.

The free energy of desolvation can be computed for a molecule or group of molecules as the energy difference between this molecule in complete solvation and the same molecule in the gas-phase, *i.e.* in vacuum.[225] The former situation is modeled using an implicit solvation model, such as in our case, the polarisable continuum model (PCM). This method, notably implemented in DFT, consists in placing the molecule inside a cavity lined with a polarisable charge density which reproduces the dielectric constant of the solvent.[226] The charge densities of the molecule and of the solvent cavity mutually polarise each other. The advantage of

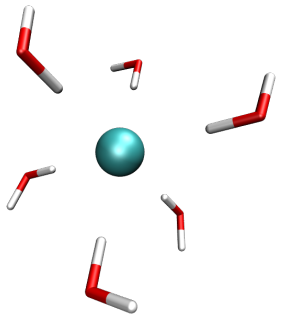

(a) 1st H_2O shell around Cl^- ion

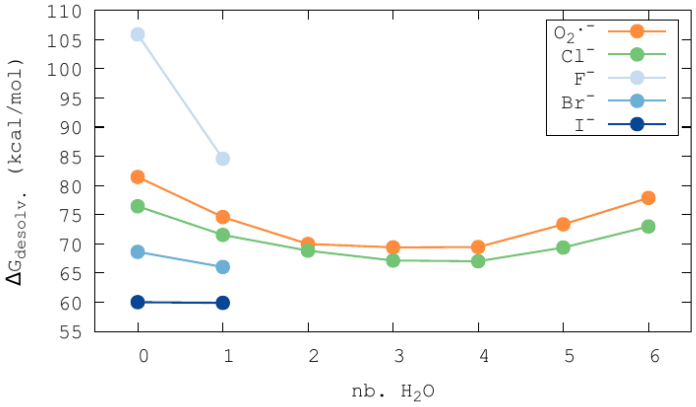

(b) $\Delta G_{\text{desolv.}}$ of various hydrated ions

Figure 4.10: (a) Model hexa-hydrated Cl^- ion, hand-built in `Molden`. (b) Free energies of desolvation of a N-hydrated ion X (X = $O_2^{\bullet -}$, Cl^-, F^-, Br^-, I^-), computed using DFT at the CAM-B3LYP/def2-TZVPP level in `Gaussian 16`, with and without a PCM implicit solvation.

using a PCM instead of an explicit solvation, where water molecules are provided in a given geometry and are explicitly part of the DFT calculation, is the built-in treatment of entropic effects: indeed, a PCM approximates the average solvation pattern around the solute, by effectively modeling all possible solvent arrangements. On the other hand, explicit solvation is dependent on the geometries sampled, and it is difficult to determine whether the sampling is sufficient.

$$\Delta G_{\text{desolv}} = E^{\text{gas}} - E^{\text{PCM}} + C \tag{4.3}$$

For this reason, we computed the ΔG_{desolv} of $O_2^{\bullet -}$ and Cl^- following Equation 4.3, where E^{gas} and E^{PCM} are respectively the energy of our system in the gas-phase and with PCM solvation. $C = -RT.\ln(55.5)$, with 55.5 M the molarity of water. These energies were computed using DFT as implemented in Gaussian 16, at the CAM-B3LYP/def2-TZVPP level of theory with GD3BJ empirical dispersion. Cavities of the PCM models were defined with the Unified Atom model calibrated based on Kohn-Sham DFT calculations. When implicit solvation was included, *i.e.* for the calculation of E^{PCM}, its implementation in the Integral Equations Formalism (IEF-PCM) was used.

Since both anions do not shed the entirety of their solvation shell when entering a bound state with the protein, the desolvation energy associated to this binding event corresponds to the desolvation energy of the anion in its bound-state, partial solvation shell. In order to model this, we built an explicit solvation shell around the

anion, assuming an octohedral coordination geometry for simplicity. No geometry optimisation was performed, but the H_2O molecules were placed at a distance informed by the RDFs shown in Figure 4.8. Their relative orientation to the anion, shown in Figure 4.10 (a), with the hydrogen pointing at the anion, was informed both by chemical intuition – electrostatic interactions favour this solvation pattern, with H atoms with a positive partial charge neutralising the anion – and by the $g_{\text{ion}-\text{O}}$ and $g_{\text{ion}-\text{H}}$ functions, shown as a RDF in the Annex. The $g_{\text{ion}-\text{H}}$ function shows a density peak at a shorter distance than $g_{\text{ion}-\text{O}}$, indicating the H_2O H atoms are pointing towards the anion.

This solvation shell was built for both $O_2^{\bullet-}$ and Cl^- anions in a stepwise manner, adding one H_2O molecule at the time and computing $\Delta G_{\text{desolv.}}$ on this partial solvation shell geometry. This process was also partially repeated for other halide anions not present in the system. These results are reported in Figure 4.10 (b).

Solvation energies for single ions are well reproduced, registering a deviation of about 5 kcal/mol with respect to reference values computed from experimental data.[227] Using data reported in Table 4.1, the desolvation free energy of a $O_2^{\bullet-}$ solvated by 3.63 water molecules, *i.e.* its bound-state hydration shell, is $\Delta G^{O_2^{\bullet-}}_{\text{desolv.}} \simeq 70\,\text{kcal.mol}^{-1}$; and for a Cl^- surrounded by 5.61 H_2O, $\Delta G^{Cl^-}_{\text{desolv.}} \simeq 72\,\text{kcal.mol}^{-1}$. Their very similar desolvation energies do not permit to rationalise the large discrepancy in binding abilities they apparent in *e.g.* Figure 4.13, or in the isodensities shown in Figure 4.11. Naturally, the estimation made here is not nearly quantitative, chiefly due to the absence of entropic effects in the first solvation shell and to its arbitrary conformation. Nevertheless, the very similar desolvation energies of $O_2^{\bullet-}$ and Cl^- ions, all other things being equal, is an indicator that desolvation is not a strong factor, if at all, in the binding capabilities of each ion to the protein.

4.4 Localisation of $O_2^{\bullet-}$ binding sites

Having measured the limitations of the force-field approach, this section focuses on the analysis of the ion-protein interactions, specifically the localisation, frequency and duration of binding events. Furthermore, interaction sites of particular interest for the operation of a magnetic compass are defined, and their ability to properly immobilise a superoxide radical is evaluated. Rotational correlation times of superoxide in these sites are computed, as a proxy for spin relaxation times. The ability of superoxide to populate these sites of interest, after diffusing from a putative formation site, is also explored. Finally, we try to rationalise the binding modalities of $O_2^{\bullet-}$ with its preferred interaction partner arginine, looking especially at hydrogen-bonding.

4.4.1 Probability density distribution

Ion binding sites at the surface of the protein can be uncovered by searching for areas of high ion concentration across the dynamics. In order to maximise sampling, this search is done over all 10 500-ns MD simulations, for both Cl^- and $O_2^{\bullet-}$. After alignment of all protein structure onto a frame of reference, so that the protein stays well in place in its Cartesian frame over all 5 μs of combined dynamics, the average probability of finding an ion at each point of this frame can be evaluated on a 3D grid using the `VMD` plugin `VolMap`. Such areas, termed hotspots, are represented below in Fig. 4.11 as red isosurfaces.

Here, the integration was performed on a 3D grid with 1.0 $Å^3$ bins (1.0×1.0×1.0 Å). An isodensity of 0.015 therefore means that every bin within the isosurface has a 1.5 or higher percent chance of containing an ion, at any given frame.
While the comparison between $O_2^{\bullet-}$ and Cl^- binding patterns is out of the scope of this study, due to uncertainties in the description of their relative electrostatic binding behaviour, we can remark that $O_2^{\bullet-}$ binding to the protein is more frequent than with Cl^-, which is consistent with the observation that its interaction energy is likely higher – at least with arginine residues. Focusing on the $O_2^{\bullet-}$ binding areas, an interesting aspect is its distribution into localised sites, suggesting a particular affinity with specific residues. Finally, nearly all of these sites are located in the "crypt" of the cryptochrome, *i.e.* the concave area leading to the flavin binding cavity.

This particular affinity of the negative ions in this area of the protein can be better understood by looking at the electrostatic landscape. Figure 4.12 is a representation of the electrostatic potential at the surface of the protein, in a view here that looks down the "crypt" of the cryptochrome. This map was computed using the `APBS` plugin in `VMD`.

The notion of electrostatic guiding of a reactive species to its reaction site is an already documented phenomenon, notably for reactive oxygen species.[204–208] For the particular case of the cryptochrome, we could see the crypt of the protein as a funnel to bring $O_2^{\bullet-}$ within electron-transfer range of the flavin, thereby both favouring their efficient recombination, and preventing a ROS from diffusing out into the cell, mitigating its toxicity, and potentially enabling operation of a superoxide-containing magnetic compass.

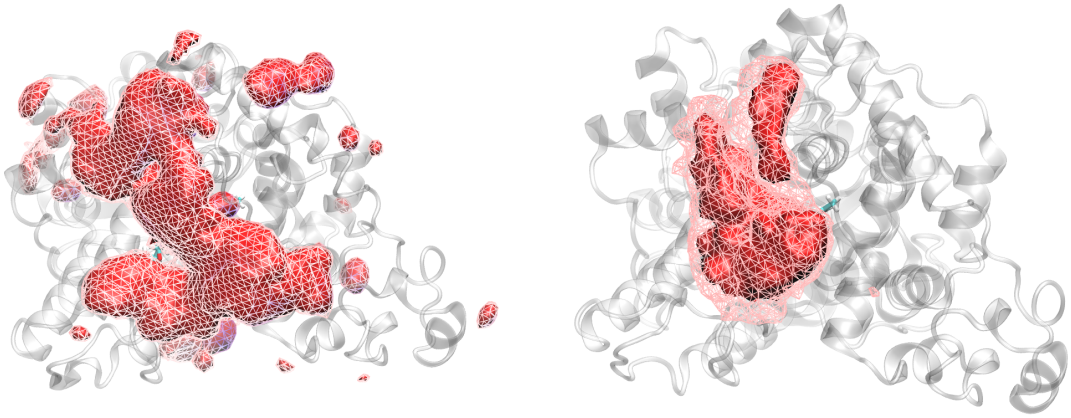

(a) $O_2^{\bullet -}$ hotspots: iso = 0.0066

(b) Cl^- hotspots: iso = 0.0066

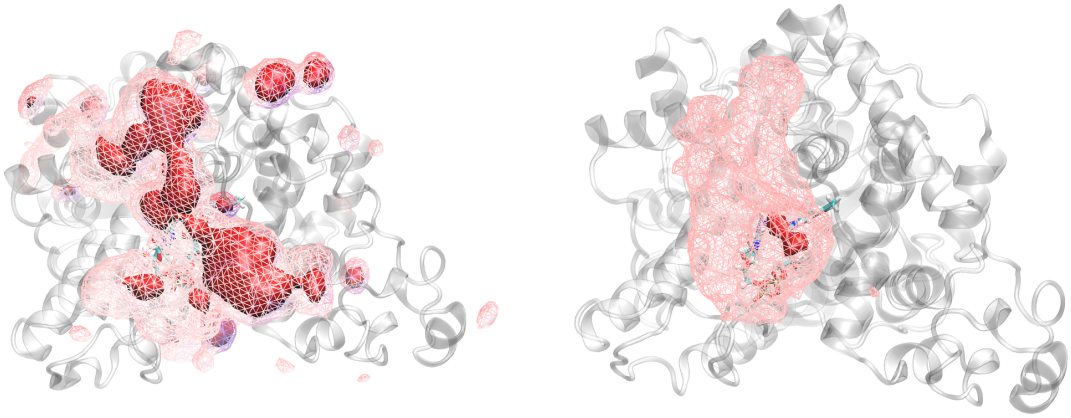

(c) $O_2^{\bullet -}$ hotspots: iso = 0.0150

(d) Cl^- hotspots: iso = 0.0150

Figure 4.11: Volumetric density maps of **(a,c)** $O_2^{\bullet -}$ and **(b,d)** Cl^- ions, computed using the `VMD` plugin `VolMap` over the 10 500-ns trajectories, concatenated and aligned onto the first frame of the Cl^--containing trajectory for best visual comparability. For all representations, wireframe meshes materialise an isodensity of 0.0060; solid surfaces, an isodensity of **(a,b)** 0.0066 or **(c,d)** 0.015.

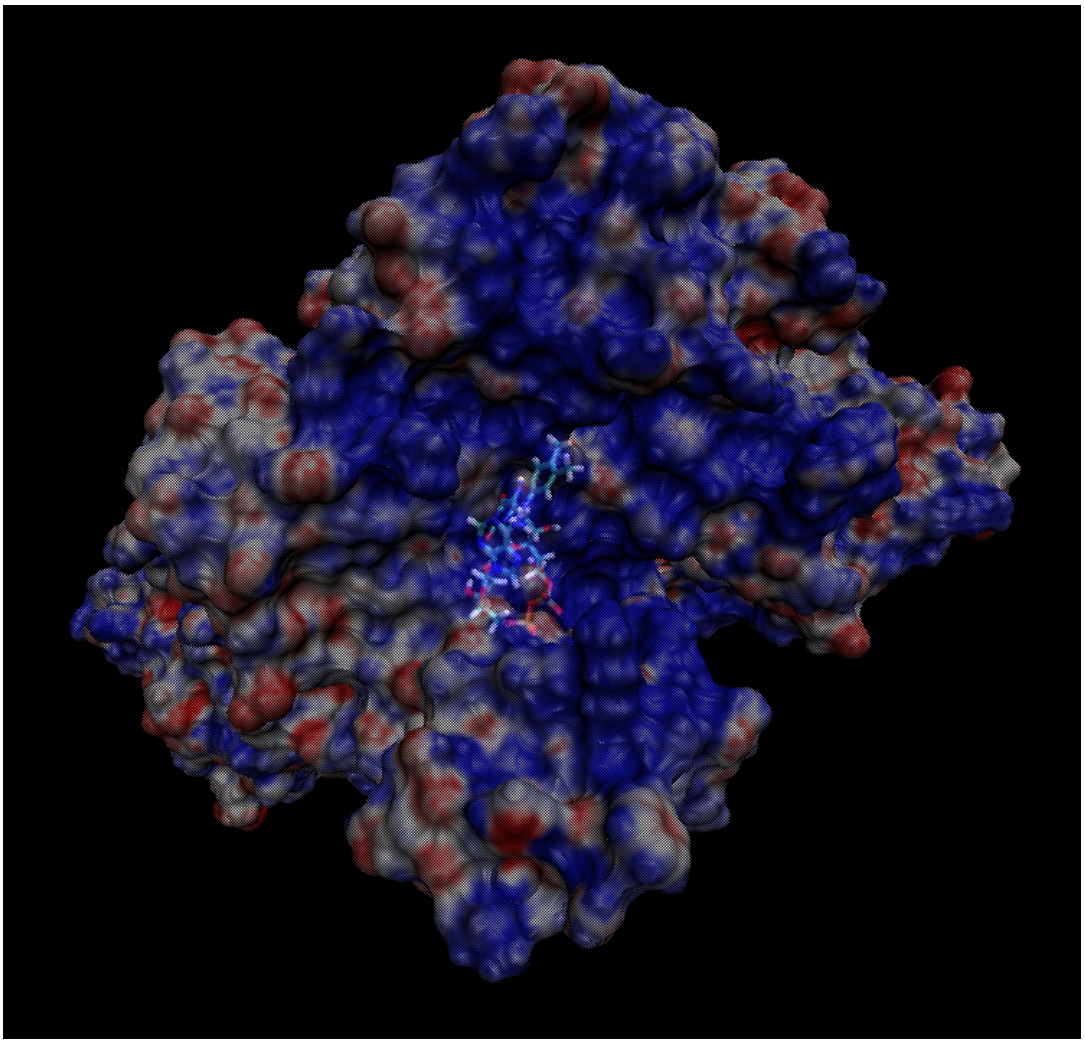

Figure 4.12: Electrostatic potential at the surface of the *cl*Cry protein. Blue (resp. red) zones denote positive (resp. negative) values. This view looks down the "crypt", the cavity leading to the flavin binding region.

4.4.2 Binding specifics: distance, duration, and partners

After locating areas of high ion concentration, a more accurate characterisation of binding events is useful. The first parameter of interest is the binding distance, *i.e.* "when bound, how far does the ion stay from the protein surface?". This is investigated in Fig. 4.13:

Fig. 4.13 reports, as a density plot with a bin width of 0.1 Å, the distance between each $O_2^{\bullet-}$ (or Cl^-) ion and the closest atom on the protein. For instance, a density of 0.05 at a distance of 2.5 Å means that an ion spends, on average, 5% of its time at 2.5 Å from the protein surface. Here, we only track ion density up to 10 Å away from the protein surface because we do not expect nonbonded interactions to allow for any significant immobilisation of the ion at such a large distance. This is indeed the case, as both densities appear well stabilised past $\simeq 7.5$ Å. Note that the densities for $O_2^{\bullet-}$ and for Cl^- are directly comparable, being computed on samples of identical size.

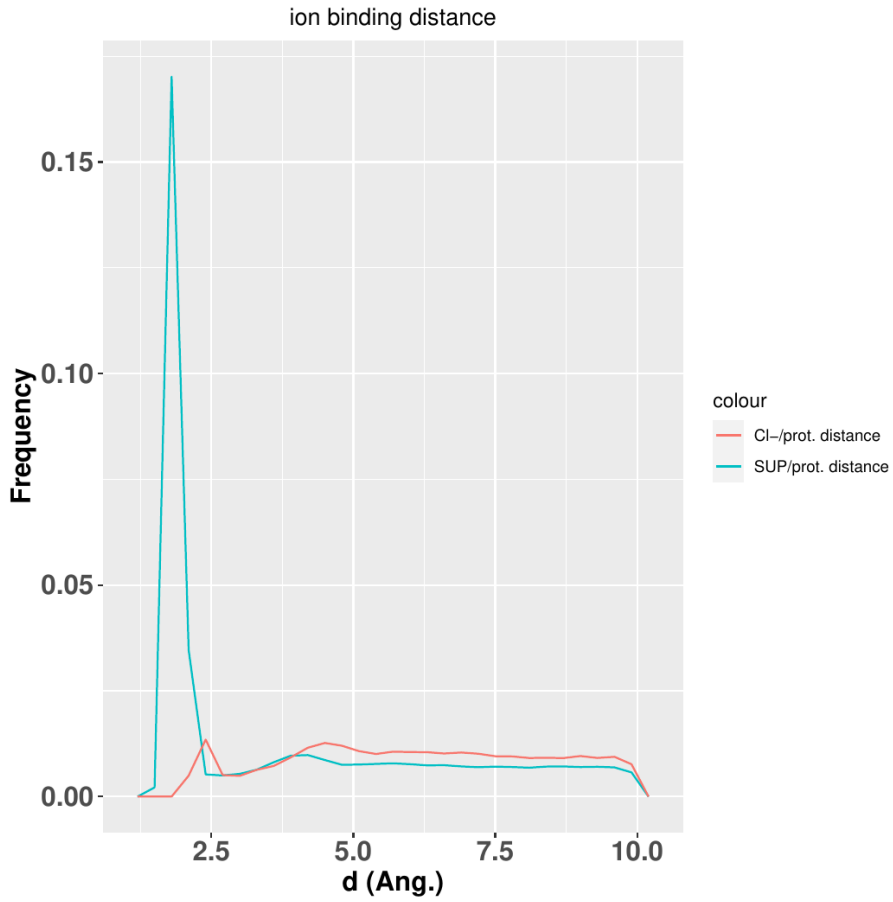

Figure 4.13: Density plot of the shortest distances between a protein atom and an ion, over 10 500-ns MD simulations (10×2500 frames) and averaged over 21 ions for each set. The ions are $O_2^{\bullet -}$ (blue) or Cl^- (red). Note that for $O_2^{\bullet -}$, the ion-protein distance is measured not from the center of mass, but from whichever O atom is closest. The apparent density drop-off at 10 Å is an artefact of the construction of this graph.

This representation highlights some key features of ion-protein binding. The most obvious is the much larger probability of presence of $O_2^{\bullet -}$ next to the protein than Cl^-. Integrating the first peak for both ions, $O_2^{\bullet -}$ has a 21% probability of being found within 2.75 Å of the protein surface, and Cl^- has a 3% probability of being within 3.00 Å. Within this first peak, $O_2^{\bullet -}$ is found on average at 1.87 Å from the surface, and Cl^- at 2.45 Å.

Interestingly, there is for both ions a second density peak, occurring at larger distances from the protein surface. This corresponds to the case where the ion is in interaction with the protein, but still solvated with its shell of water molecules. For $O_2^{\bullet -}$ at least, this binding modality is largely minor.

Fig. 4.14 shows the probability of having a given aminoacid as the nearest neighbour to a Cl^- and $O_2^{\bullet -}$ ion, during a binding event. Chance encounters, *i.e.* very

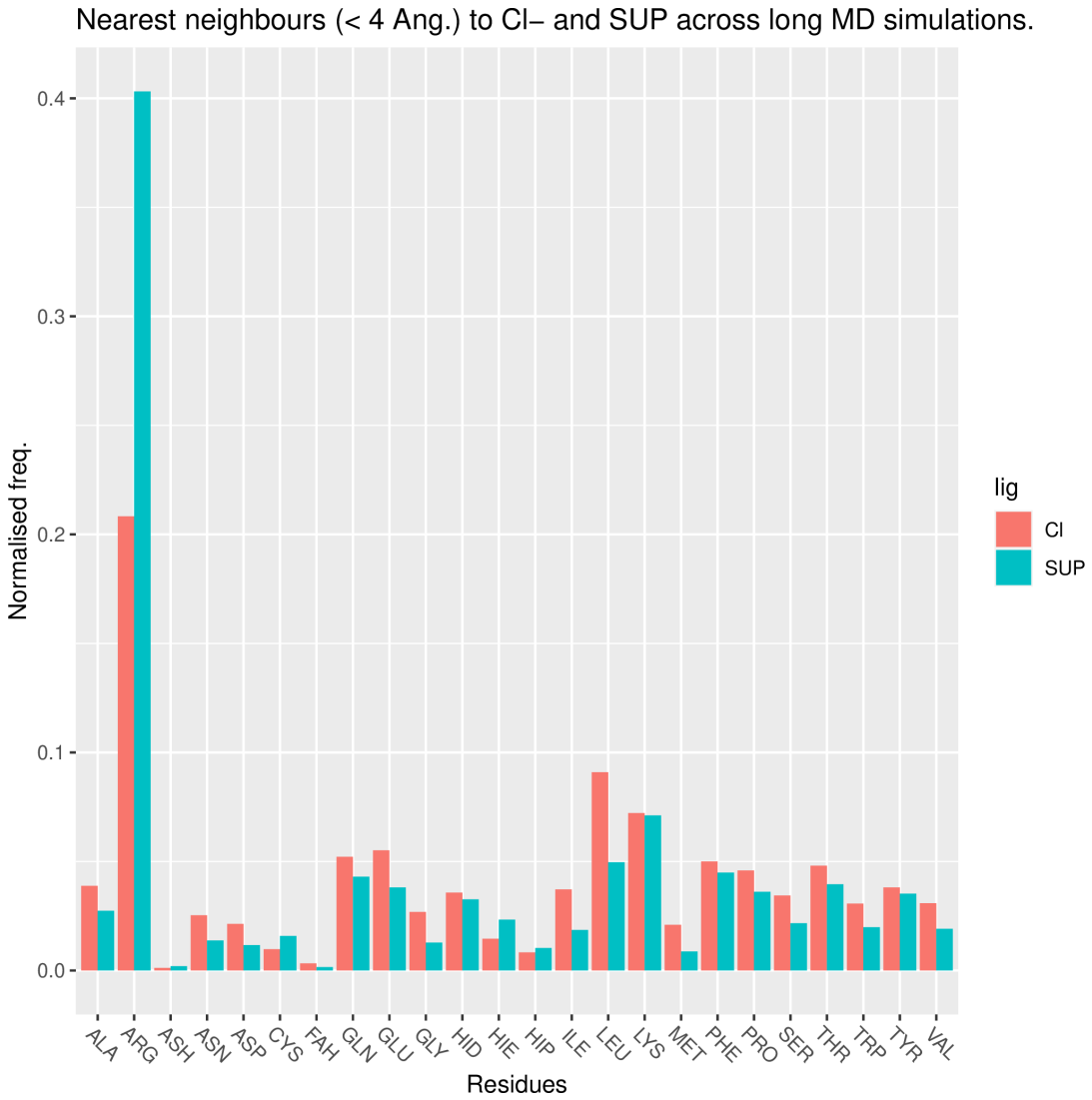

Figure 4.14: Probability for each ion to have a given aminoacid as its nearest neighbour, when the ion is within 4 Å of the protein surface for at least 2 consecutive frames. Averaged over all 10 500-ns MD simulations for both ions, *i.e.* over the FD-SUP and CL-SUP trajectory sets.

short or weak ion-residue encounters that do not trap the ion at the protein surface for an extended period of time, are excluded from the statistics by including only binding events extending over 2 or more consecutive frames. Since the Δt between 2 consecutive frames is 200 ps, this corresponds to a binding time of at least 200 ps.

$O_2^{\bullet-}$ shows well converged statistics, with only 44 % of its binding events being single-frame encounters, leaving 121,235 frames of strong ion-protein interactions. $O_2^{\bullet-}$ shows an overwhelming affinity with arginine (ARG, $\simeq$ 40 %), followed by lysine (LYS, $\simeq$ 7 %) then leucine ($\simeq$ 5 %). The affinity with ARG and LYS is readily explained by the fact that these residues are positively charged at physiological pH, resulting in a potentially strong Coulombic attraction. The other positively charged residue, histidine (HIP), shows a rather low affinity with $O_2^{\bullet-}$, probably

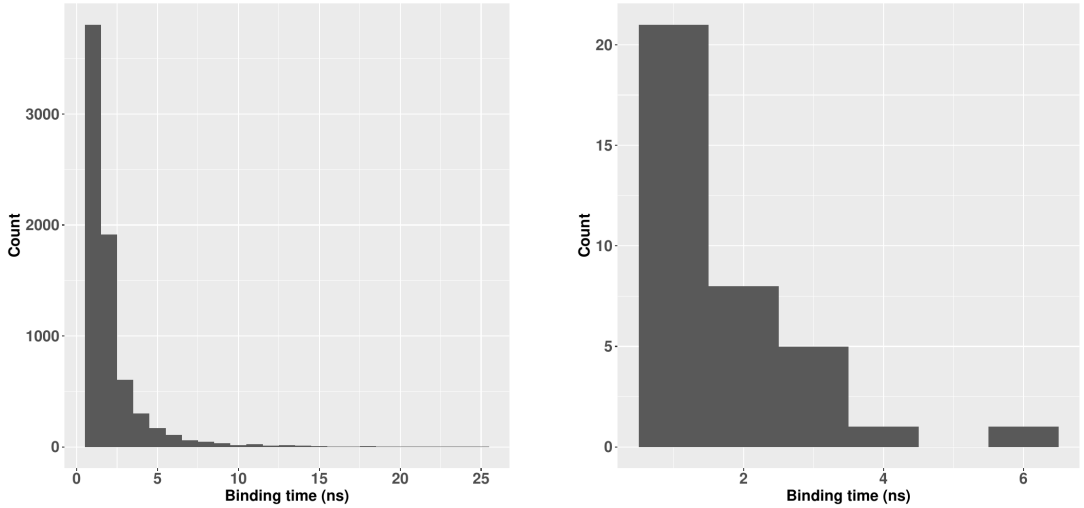

(a) $O_2^{\bullet-}$ (b) Cl^-

Figure 4.15: Histogram of the lengths of (a) $O_2^{\bullet-}$- and (b) Cl^--protein binding events, *i.e.* a minimum of 5 consecutive frames (1 ns) in which a given ion is located within 4 Å of a protein atom.

due to its low prevalence in the *cl*Cry protein at this pH; indeed, due to its pKa of $\simeq 6.8$, the assignment of the protonation state of histidines at physiological pH is a delicate process, which was detailed in Chapter 3. Most histidines turned out to be singly-protonated, neutral aminoacids. Regarding the LEU residue, a neutral and apolar aminoacid, its relatively high rate of $O_2^{\bullet-}$ binding is trickier to explain. Upon visual inspection of the crypt of the protein, in particular in the areas of high $O_2^{\bullet-}$ concentrations identified in Fig. 4.11, it could simply be due to the presence of LEU residues next to other residues susceptible to binding strongly a negative ion. Indeed, LEU314 is located right next to ARG486, one of the key aminoacids for immobilising $O_2^{\bullet-}$; same analysis for LEU354, located between ARG409 and ARG419, two fairly flexible residues which have been found to exchange $O_2^{\bullet-}$ radicals.

This figure is less reliable for Cl^-, for which the vast majority (88 %) of binding events occur on only one frame. These stats are therefore computed over only 3879 frames for Cl^-, out of a total of 525,000 (2,500 frames × 10 trajectories × 21 ions). A very similar analysis can be made: Cl^- shows a particularly strong affinity with arginine (ARG, $\simeq 20$ %), followed by leucine (LEU, $\simeq 9$ %) and lysine (LYS, $\simeq 7$ %).

Having identified which residues are most likely to bind these ions, let us have a look at the length of these binding events. Indeed, in order to delay the onset of $O_2^{\bullet-}$ spin relaxation, two conditions must be met: first, it must be hindered to rotate and second, the binding must persist for long enough to achieve the target rotational correlation time. A $O_2^{\bullet-}$ radical unbinding and going into the bulk relaxes immediately, so however strong protein-ion interactions might be, spin relaxation

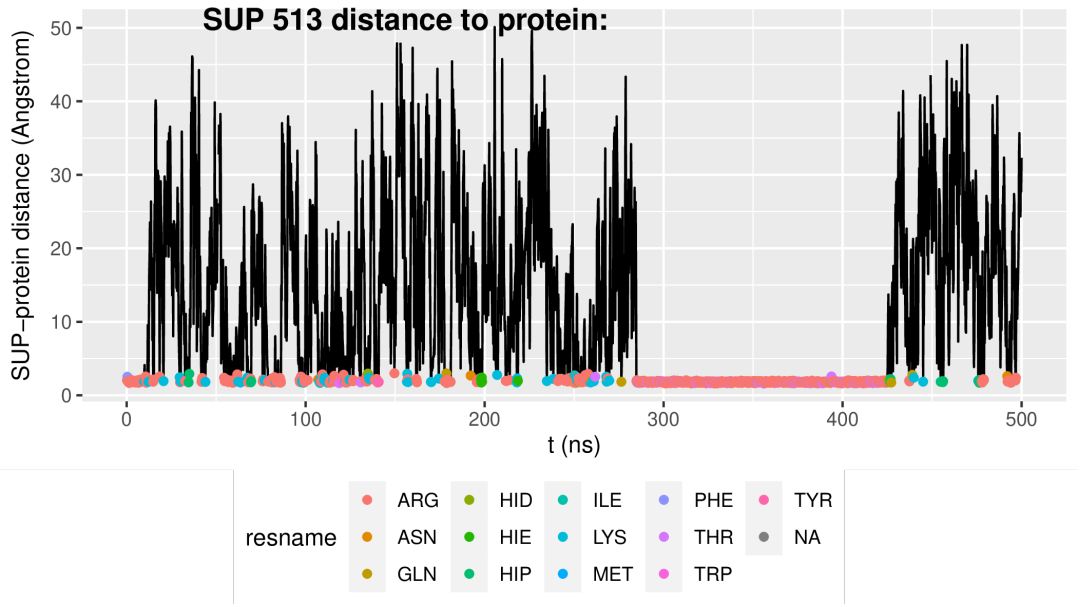

Figure 4.16: Distance between a $O_2^{\bullet-}$ ion (SUP 513 in AMBER notation) and the nearest protein atom, along a 500-ns MD simulation. The identity of the nearest residue is indicated by a dot whenever $d_{prot.-ion} \leq 4.0$ Å.

times are ultimately limited by binding times. In our case, a spin relaxation time of the order of $10^1 - 10^2$ ns would be required to increase the directional sensitivity of a 3-radical compass, or in the most extreme case to allow a $[FADH^\bullet - O_2^{\bullet-}]$ radical pair to generate sufficient magnetic field effects (MFEs).

Figure 4.15 reports binding times t_b for (a) $O_2^{\bullet-}$ and (b) Cl^- to *cl*Cry, again extracted from their respective 10 500-ns MD simulations. For both relevance and visualisation purposes, binding events shorter than 5 frames (1 ns) are omitted. Graph (a) is also truncated past $t_b = 25$ ns, not revealing a low density of binding events in excess of this value. Focusing on the $O_2^{\bullet-}$ results, we note that the vast majority of such binding events are shorter than 5 ns; however, crucially, longer binding events such as the one depicted in Fig. 4.16 are possible: for $O_2^{\bullet-}$, there are 133 binding events with $t_b \geq 10^1$ ns, and 2 with $t_b \geq 10^2$ ns. The longest event spans 148.6 ns.

4.4.3 Chemical considerations: sites of interest

In this section, after having identified binding sites for $O_2^{\bullet-}$ radicals able to trap them for tens or even hundreds of nanoseconds, we take a more chemically aware approach and delineate sites relevant to the context of the three-radical compass. We also examine the frequency and length of binding events in these sites from free-diffusing $O_2^{\bullet-}$, as well as the phenomenon of ion transport between sites.

While the 3-radical mechanism is able to retain solid levels of magnetic field sensitivity even after the extinction of one of the spin-selective recombination pathway, thanks to scavenging by the other radical partner, its optimal accuracy is realised when all spin-selective reaction channels are functioning. The aforementioned extinction can occur, for instance, through the onset of spin relaxation. In addition, spin relaxation should be slow; indeed, fast spin relaxation renders the recombination event completely independent from the orientation of the external magnetic field. Another possibility is that one radical diffuses away from its partner, altering the kinetics of its electron transfer and making it impossible to recombine fast enough to compete with the spin-independent reaction. $O_2^{\bullet -}$, as a radical in the *e.g.* [$FADH^{\bullet}$-$O_2^{\bullet -}$-$Y^{\bullet}$], is susceptible to suffering both these fates, as a free-diffusing diatomic radical. Fortunately, the cure to both these problems is the same: if by interacting strongly enough with the molecule, $O_2^{\bullet -}$ is prevented both from tumbling and from diffusing away, then its recombination channel would remain active. For electron recombination through long-range electron transfer to proceed fast enough and thereby compete with the spin-independent reaction, $O_2^{\bullet -}$ should remain within $\simeq 20\,\text{Å}$ of the flavin – more precisely, of its isoalloxazine moiety, where the vast majority of its spin density is concentrated.

Note that, while the preservation of spin coherence in $O_2^{\bullet -}$ in the absence of recombination could be useful, as its non-averaged EED coupling with the remaining radical pair was shown to enhance Γ_S for some configurations,[25,27] it is not an avenue we shall explore in this thesis. Here, we focus on the case where additional performance can be expected from a 3-radical compass by identifying a binding site for $O_2^{\bullet -}$ within 20 Å of the isoalloxazine. As shown in Figure 4.17, there is a significant concentration of $O_2^{\bullet -}$ within this range, although the peak density occurs for slightly longer distances – around 22 Å away.

In Figure 4.18, we identify 5 hotspots of $O_2^{\bullet -}$ concentration that satisfy the distance requirements mentioned above. Their constitutive residues are listed in Table 4.3. The naming of the sites is perfectly arbitrary and does not imply any sort of ordering.

A feature that needs explaining is the singling out of site 4, composed of only R409. Although separate from the hotspots of site 1 and site 2 in this representation, it is a fairly flexible residue which can reach into both of these sites, and has been noted in several instances along the simulations to transport a $O_2^{\bullet -}$ radical between site 1 and 2. This behaviour, where a $O_2^{\bullet -}$ can be held simultaneously by multiple residues, can be visualised in Figure 4.19. There, the binding of superoxide radicals to 4 arginines, either alone or together, is monitored along one 500-ns MD simulation.

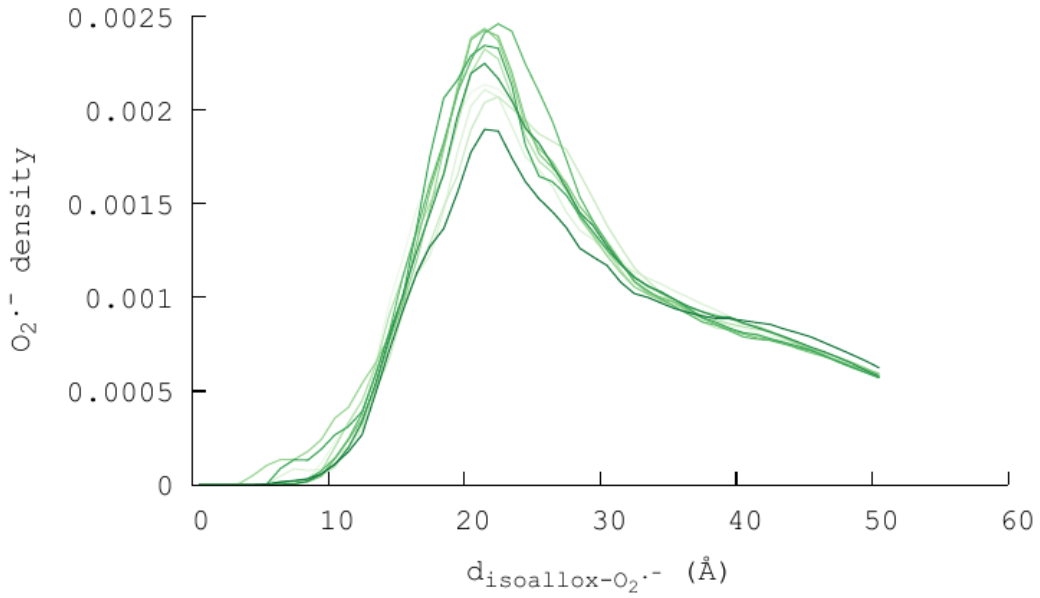

Figure 4.17: Radial Distribution Functions (RDF) of $O_2^{\bullet-}$ radicals, with respect to the center of mass of the $FADH^{\bullet}$ isoalloxazine moiety. Averaged over 21 ions for each of the 10 500-ns MD trajectories.

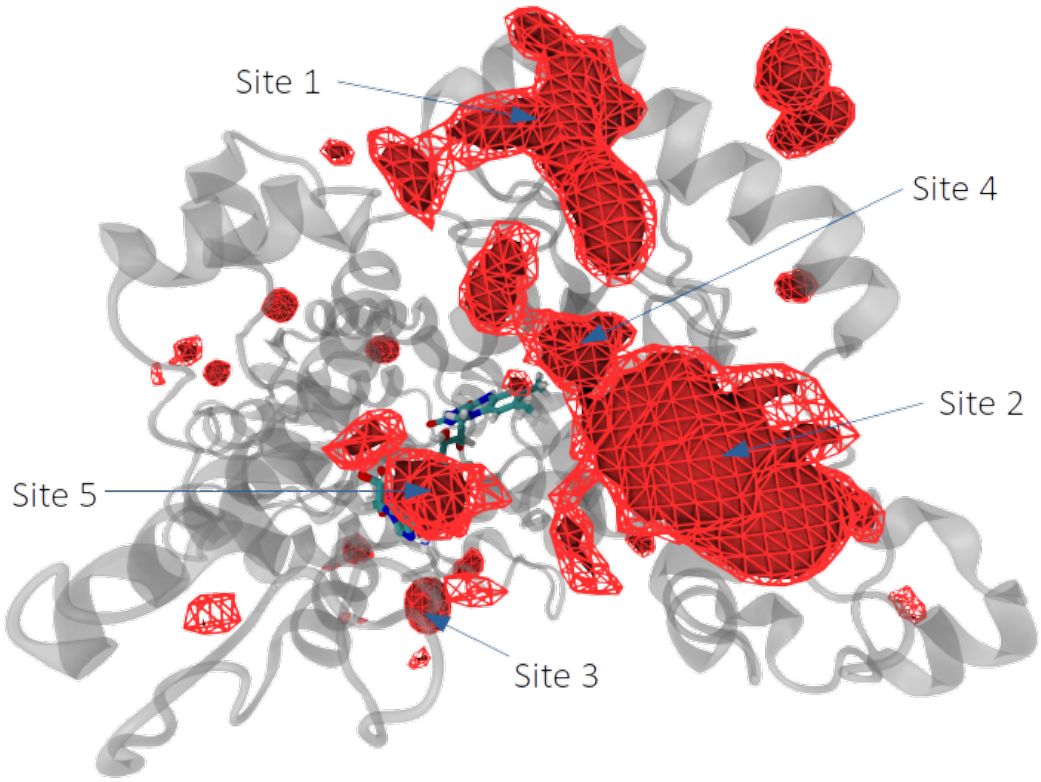

Figure 4.18: Volumetric density maps of $O_2^{\bullet-}$ radicals, computed using the `VMD` plugin `VolMap` over the 10 500-ns trajectories, concatenated and aligned onto the first frame of the Cl^--containing trajectory for best visual comparability. Wireframe meshes materialise an isodensity of 0.0155; solid surfaces, an isodensity of 0.0160. Sites 1 through 5 correspond to $O_2^{\bullet-}$ hotspots of potential chemical relevance in the operation of a 3-radical compass.

Site	Residues
1	R497, R486, R490
2	R415, R419
3	T209, R217, R218
4	R409
5	K234, R236

Table 4.3: Aminoacids involved in the binding of $O_2^{\bullet -}$ for each site. In the one-letter aminoacid naming convention: R = ARG, T = THR, K = LYS.

A single numeric ID is associated to each combination of arginines binding the same $O_2^{\bullet -}$, attributed according to the following rule: R365 (near site 1) has ID = 1, R409 (site 4) has ID = 2, R415 (site 2) has ID = 4, and R419 (site 2) has ID = 8. If a $O_2^{\bullet -}$ is held by both R365 and R409 simultaneously, *i.e.* stays within 3.0 Å of both, this configuration has ID = 1 + 2 = 3. The same logic applies to 3-arginine binding, although this configuration never appeared in practice.

The same representation was made for each of the 10 trajectories, and are provided in Appendix C, Figure C.5 and C.6; this one is quite representative of the whole. A recurring feature is that the most common binding patterns are single-arginine binding, as shown by the nearly-solid lines of ID 2, 4, and 8. The only significant double-binding that occurs is at ID 12, *i.e.* R415 + R419, both in site 2. While there are very occasional instances if ID 6 binding happening (R409 + R415, *i.e.* cross-site binding), this phenomenon is rare.

Treating sites 4 and 2 as only one would have made sense if $O_2^{\bullet -}$ transport between the two occurred with unbroken binding by the arginines, as in this way the radical would remain immobilised and not be allowed to relax; however, due to the flexibility of R409, which can also point in the opposite direction towards site 1 (this graph for trajectory 1, provided in appendix C, shows a very long binding event at ID 3, *i.e.* R365 + R409), then it also happens that $O_2^{\bullet -}$ has to diffuse into the bulk to reach the other site. For this reason, we chose to err on the side of caution and to treat R409 as a binding site of its own.

This representation also illustrates the impressive ability of R409, R415 and R419 as $O_2^{\bullet -}$ traps; although they are here in an environment with a largely supra-physiological $O_2^{\bullet -}$ concentration, they are nearly constantly occupied.

Figure 4.20 reports the number of occurrences and lengths of $O_2^{\bullet -}$ binding events into the 5 sites defined earlier. A numerical breakdown is also given in Table 4.4. Results are fairly similar to those reported in Figure 4.15; indeed, 77 of the 133

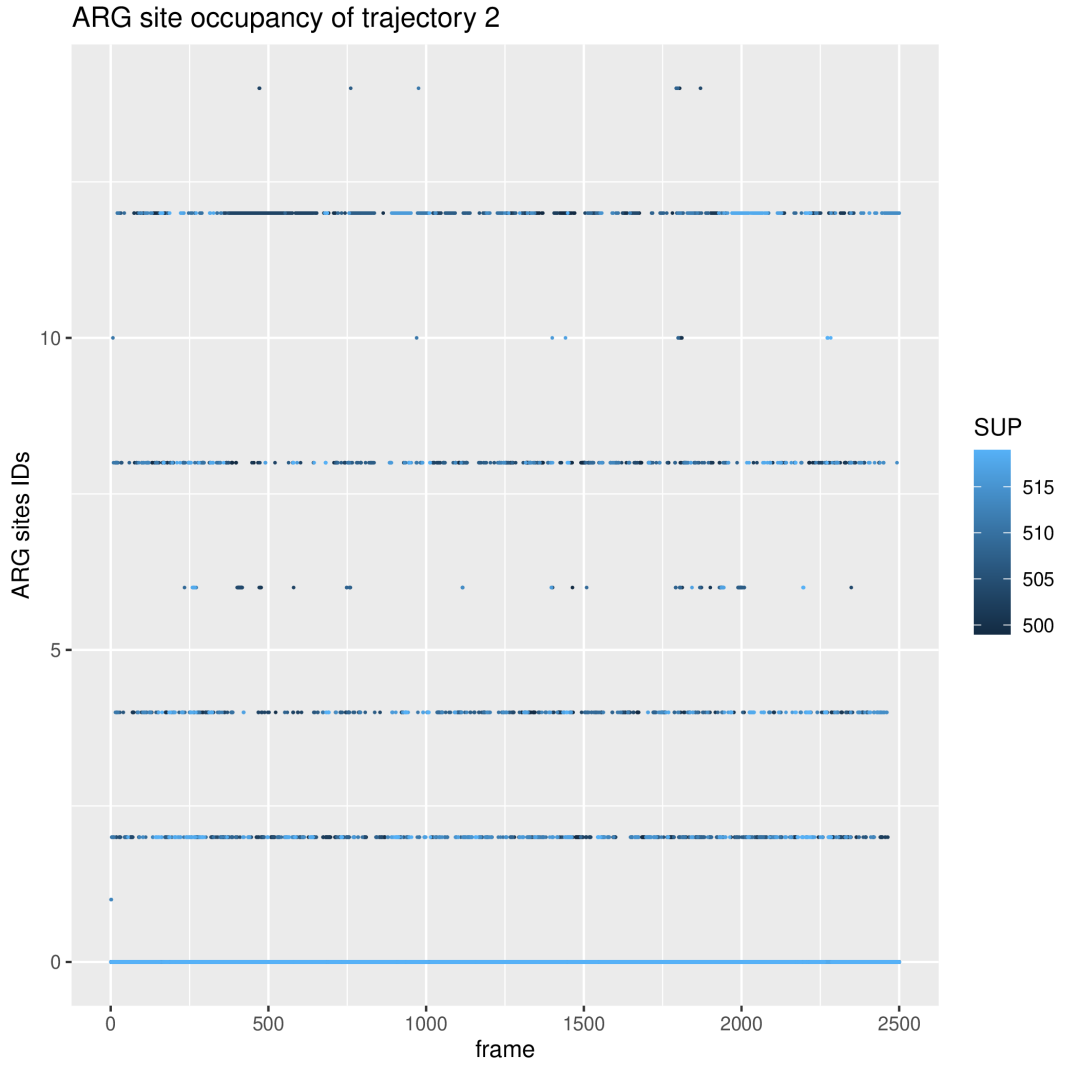

Figure 4.19: Occupancy of the various binding sites consisting of the possible combinations of R365, R409, R415, and R419. To each combination corresponds a unique ID, according to a naming protocol given in the main text.

Site	Total nb. of BE	nb of $t_b \geq 10^0$ ns BE	nb of $t_b \geq 10^1$ ns BE	nb of $t_b \geq 10^2$ ns BE
1	2113	764	26	0
2	3165	1339	44	0
3	304	94	5	2
4	2660	670	2	0
5	1961	432	0	0

Table 4.4: Number of binding events (BE), with binding length t_b in ns, from the 10 500-ns trajectories of 21 freely-diffusing $O_2^{\bullet -}$.

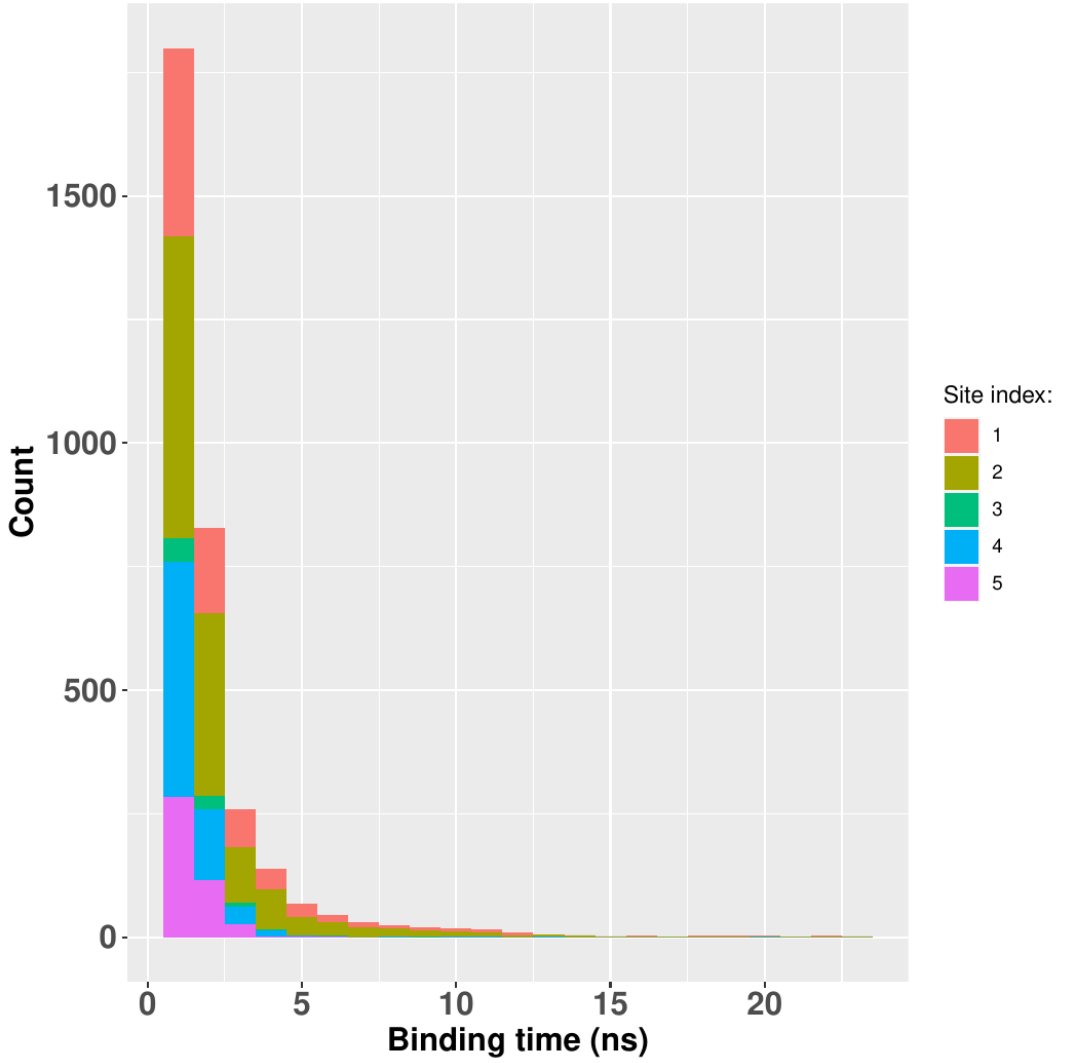

Figure 4.20: Histogram of the lengths of $O_2^{\bullet -}$-protein binding events, *i.e.* a minimum of 5 consecutive frames (1 ns) in which a given ion is located within 4 Å of a binding site defined in Figure 4.18.

$t_b \geq 10^1$ ns and both $t_b \geq 10^2$ ns events are retained. The longest binding event remains $t_b = 148.3$ ns, in site 3.

Out of a total of 10,203 recorded binding events, this dataset should present well-enough converged statistics to comment. In terms of the sheer number of binding events, site 2 is the most able to trap $O_2^{\bullet -}$ (31.0 % of all binding events), closely followed by site 4 (26.0 %), and with sites 1 and 5 performing a bit worse (20.7 % and 19.2 %, respectively). Site 3 has the least number of binding events, only 3.0 %, a situation perhaps explained by its localisation outside of the crypt.

It appears that very short, and consequently probably weak, binding events constitute the overwhelming majority: $t_b < 1.0$ ns occurs in about 67.7 % of the cases, a proportion rather consistent across binding sites. On the other hand, it means that a very sizable subset of binding events (about 32.3 %) give rise to extended $O_2^{\bullet -}$ trapping, for 1 ns or longer.

A clearer hierarchy in the capacity of each site to achieve extended binding is more apparent looking at $t_b \geq 10.0$ ns: sites 1 through 3 show similar performance, with about 1 to 2 percent of binding events lasting over 10 ns. Site 4 and 5, on the other hand, have zero or nearly zero probability of achieving such long binding. This could be due to the nature of site 4, a single ARG of great flexibility which is able to reach into site 2, and perhaps transfer its $O_2^{\bullet-}$ there, where a stronger immobilisation, by both R415 and R419, could happen. Regarding site 5, this site has the smallest proportion of $t_b \geq 1.0$ ns events, suggesting perhaps an intrinsic inability to interact strongly with $O_2^{\bullet-}$.

While these last values were quite noisy for site 3, which had only 5 $t_b \geq 10.0$ ns binding events, its quality seems confirmed by the fact that it is the only site to achieve $t_b \geq 100.0$ ns, with a maximum of 148.3 ns. This sort of binding lifetimes is what is required for $10^1 - 10^2$ ns $O_2^{\bullet-}$ rotational correlation times, and makes site 3 a very promising candidate for trapping superoxide and delaying its spin relaxation for the purpose of magnetosensitive spin dynamics.

Similarly, sites 1 and 2 have a similar proportion of $t_b \geq 10.0$ ns events, making it plausible that $t_b \geq 100.0$ ns is possible for them.

4.4.4 FADH$^\bullet$ and Y319 relative positions

In this section, we come back on a question left open in Chapter 2, now informed by the dynamical behaviour of FADH$^\bullet$ and Y319. In particular, the interrogation was: "given the dependence of EED coupling on inter-radical separation and orientation, is a static representation of FADH$^\bullet$ and Y319 throughout the spin dynamics simulation a reasonable assumption?".

Figure 4.21 (a) reports the distance separating FADH$^\bullet$'s N5 atom and Y319's OH atom across the accumulated 5 μs of FD-SUP trajectories. This atom selection is the same as that defined in Chapter 2, Table A.2, which was given to parameterise a subsequent spin dynamics calculations. In there, the inter-radical distance provided was $d_{\mathrm{F-Y}} = 25.2$ Å. In comparison, an average distance of 25.86 ± 1.53 Å was recorded in the FD-SUP dataset. In this case, the FADH$^\bullet$-Y319 geometry used in Chapter 2 seems perfectly adequate.

Besides average figures, the variability of $d_{\mathrm{F-Y}}$ values appears rather low; indeed, the reported double standard deviation of $d_{\mathrm{F-Y}}$, which visually approximates a Gaussian distribution, confines 95% of the sampled values between the rather narrow range of $[24.33, 27.39]$ Å. Again, we can be satisfied with the $d_{\mathrm{F-Y}}$ value used in Chapter 2, and expect no large energy differences arising from it. One way to verify this is to compute a dipolar coupling constant d_{KL} between radicals K and L, dependent only on the inter-radical distance. We recall here its expression:

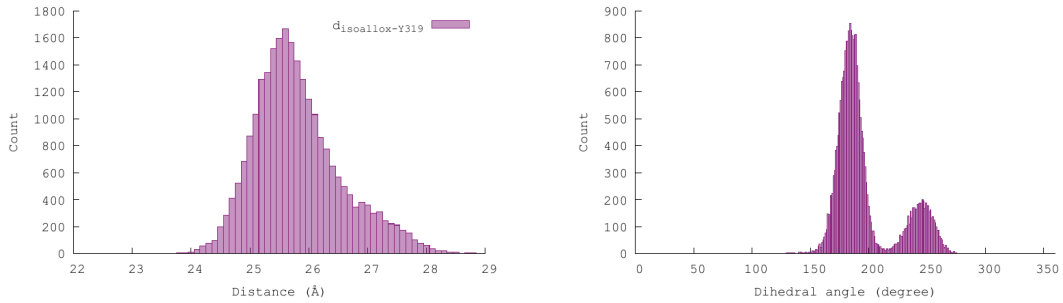

Figure 4.21: (a) Histogram view of the N5-OH distance between $FADH^{\bullet}$ isoalloxazine and Y319, across the FD-SUP trajectory set (*i.e.* 10 500-ns MD trajectories of $FADH^{\bullet}$ in *cl*Cry, also including 21 $O_2^{\bullet-}$ radicals). (b) Histogram view of the dihedral angles φ_{F-Y} value across the same FD-SUP dataset.

$d_{KL} = \mu_0 g^2 \mu_B^2/(4\pi r_{KL}^3 \hbar)$, with r_{KL} denoting the distance of the centers of spin density of radicals K and L. n_{KL} is a unit vector parallel to the line joining the centers of the two radicals. This constant enters into the calculation of the full EED coupling, given in Equation 2.4, and includes no orientational dependence. This therefore constitutes only a preliminary analysis.

The inter-radical separation used in Chapter 2 gives rise to $d_{KL} = -3.25\,\text{MHz}$, while the average distance reported in Figure 4.21 corresponds to a coupling of $d_{KL} = -3.01\,\text{MHz}$. This energy difference between the two is much weaker than the strength of the interaction of a radical with its hyperfine structure or with the magnetic field; we therefore don't expect the distance component of the guess $FADH^{\bullet}$-Y319 geometry provided in the spin dynamics simulations to have a significant impact on the outcome. Similarly, the double-standard-deviations range around $\langle d_{F-Y} \rangle$ only spans an energy range of 1.08 MHz.

The question now remains whether the relative orientation of $FADH^{\bullet}$ and Y319 used in Chapter 2, which played a part in the triad's appreciable magnetosensitivity, represents a statistically significant conformation in a dynamics. To verify this, we choose as a metric for relative orientation the φ_{F-Y} dihedral angle, reported in Figure 4.21 (b).

The φ_{F-Y} dihedral angle is defined by 4 points, and measures the angle between the plane containing points $\{1,2,3\}$, and the plane containing points $\{2,3,4\}$. It can be viewed as the relative orientation of the segment between points 1 and 2, and the segment between 3 and 4. Here, φ_{F-Y} is defined such that points 1 and 2 are atoms N3 and C7 on the isoalloxazine, and points 3 and 4 atoms CA and CZ on Y319. Both segments correspond to the long axis of the molecule: for the flavin, it is the length across the isoalloxazine, and for tyrosine, it goes along the side-chain to the phenol carbon.

We note that FADH$^\bullet$-Y319 relative orientations cluster into 2 main orientation ranges: the most prevalent one peaking at $\varphi_{\mathrm{F-Y}} = 186\,^\circ$, and a secondary orientation peaking at $\varphi_{\mathrm{F-Y}} = 246\,^\circ$. While the flavin does not maintain perfect planarity throughout a dynamic, as can be appreciated in Figure 3.4 in Chapter 3, and that some of the variance can probably be attributed to isoalloxazine bending, such a vast angle difference between the peaks can realistically only be attributed to a change in the Y319 side-chain orientation.

On the geometry used to inform the spin dynamics simulations in Chapter 2, $\varphi_{\mathrm{F-Y}} = 184.6\,^\circ$. Comparing with the range of dihedrals sampled in FD-SUP, this value is very close to the centre of the main peak. However, this geometry does not represent the second, albeit minority, preferential conformation of the tyrosine side-chain. We report later in the chapter, in section 4.7, Γ_S for a [FADH$^\bullet$-$O_2^{\bullet-}$-Y319] triad in this conformation, in order to verify whether appreciable MFEs are conserved.

4.5 Superoxide formation and diffusion into the sites.

The $O_2^{\bullet-}$ binding sites of chemical relevance identified in the previous section could be verified to give rise to significantly long occupancy times t_b from free $O_2^{\bullet-}$ diffusing from the bulk. In this section, we verify whether these sites can still be populated and trap radical for extended periods of time when the $O_2^{\bullet-}$ molecule diffuses from a putative formation point, near the flavin.

The proposed mechanism for the formation of a triad of radicals is as follows: the neutral flavin FAD gets photoexcited to FAD*, triggering a cascading electron transfer along a tryptophan tetrad. This first phase, called the photoreduction, results in the creation of a $\left[\mathrm{FAD}^{\bullet-} - \mathrm{W}^{\bullet+}\right]$ radical pair. For the second, slower phase, the unpaired electron on the terminal tryptophan is transferred to a stable radical, such as Y$^\bullet$. In the meantime, FAD$^{\bullet-}$ gets protonated and, under UV to 570 nm light, further reduced to FADH$^-$. Finally, dioxygen can approach the fully reduced flavin and reoxidise it to the radical semiquinone FADH$^\bullet$, itself converting to $O_2^{\bullet-}$ in the process. The reason for the addition of the reoxidation step, despite $\left[\mathrm{FAD}^{\bullet-} - \mathrm{W}^{\bullet+}\right]$ already being a radical pair capable of generating MFEs, is based on experimental evidence reported in Ref. 14. Essentially, it was found that the magnetic sense could still be used for navigation in the dark after a flash of light, after such a delay that all radical pairs created by the photoreduction step would have decayed already. However, the formation of FADH$^\bullet$ requires an additional electron transfer, suggesting the creation of a third radical.

Molecular oxygen, being rather abundant in biological media, and small enough

Site	Total nb. of BE	nb of $t_b \geq 10^0$ ns BE	nb of $t_b \geq 10^1$ ns BE	nb of $t_b \geq 10^2$ ns BE
1	15	12 (80.0%)	1 (6.7%)	0
2	164	134 (81.7%)	22 (13.4%)	1 (0.6%)
3	0	0	0	0
4	107	79 (73.8%)	7 (6.5%)	1 (0.9%)
5	212	149 (70.3%)	15 (7.1%)	0

Table 4.5: Number of binding events (BE), with binding length t_b in ns, from the 100 trajectories of $O_2^{\bullet -}$ diffusing from a formation site near the flavin.

to easily access the flavin binding site in the protein, is an ideal candidate for this role. Dedicated cellular structures also exist for the disposal of its radical form, due to its mild toxicity.

Analysis of the E-SUP trajectory set aims at examining the rate and duration of $O_2^{\bullet -}$ binding when diffusing from inside the cavity, and not from the bulk; for this reason, simulations were terminated when $O_2^{\bullet -}$ strayed too far away from the protein surface. On the other hand, the recapture events, which could occur as $O_2^{\bullet -}$ briefly goes into the bulk and then randomly reapproaches the protein surface, were thought to be already described by the previous study with bulk-born radicals. The criterion for identifying a $O_2^{\bullet -}$ radical having diffused into the bulk was a simple distance one: if $O_2^{\bullet -}$ found itself more than 10 Å away from any of the 5 binding sites or of the flavin, the simulation was terminated. This radius was determined from a visual examination of the cavity and of the spatial distribution of sites: it spanned the entire volume of the crypt, and also made a path allowing diffusion towards site 3. Likewise, the criterion for detecting a binding event with one of the sites is based on distance, as informed by results summarised in Figure 4.13: if $d_{\mathrm{SUP-residue}} \leq 3.0$ Å, where "residue" is an aminoacid involved in one of the 5 sites defined earlier, then $O_2^{\bullet -}$ is assumed bound to that site.

From these 100 MD simulations, 29 were terminated without a single binding event recorded. Over the remaining 71, the average simulation length is $\langle t_b \rangle = 41.11 \pm 53.69$ ns, ranging from 3.80 to 294.40 ns. Across this same set of 71 simulations, $O_2^{\bullet -}$ spends on average 30.33 ns bound to any of the 5 binding sites, *i.e.* 74 % of its time bound and the rest circulating between sites. However, it should be made clear that $O_2^{\bullet -}$ does not spend, on average, 30 ns is the same site before diffusing out into the bulk; indeed, over these 71 trajectories, there are 498 recorded binding events. A histogram view of their lengths and rates of occurrences is provided in Figure 4.22. A numerical breakdown is also given in Table 4.5.

Before comparing binding data between the "free-diffusing $O_2^{\bullet -}$" trajectories (Fig. 4.20) and the "escaping $O_2^{\bullet -}$" trajectories (Fig. 4.22), it should be noted that the latter has a much smaller sample size. For clarity throughout this section, we remind the

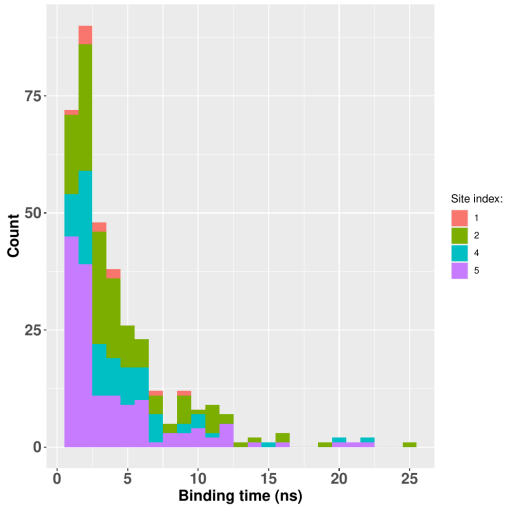

Figure 4.22: Histogram of the lengths of $O_2^{\bullet -}$- protein-sites binding events, as a $O_2^{\bullet -}$ radical diffuses away from a possible formation site near the flavin.

reader that we refer to the former set as “FD-SUP” and to the latter as “E-SUP”.

The total number of 498 binding events in E-SUP, over a total simulation time of 3,074.8 ns, is a fairly impressive hit rate: it amounts to 0.16 BE/ns (BE = binding event), against 0.09 BE/ns for FD-SUP. This is of course favoured by the ideal location of $O_2^{\bullet -}$ at the start of each simulation, where encounter rates with each of these binding sites is expected to be much higher than for a $O_2^{\bullet -}$ appearing in the bulk. Another factor that could favour this trend is the fact that $O_2^{\bullet -}$ in the E-SUP dynamics is likely often not fully solvated, staying constantly very close to the protein. This allows for quicker binding and closer contact with the partner residue(s), and a smaller desolvation penalty.

Here, site 5 registers the most binding events, amounting for 42.6 % of the total. Site 2 and 4, with 32.9 % and 21.9 % respectively, have similar prevalences as in FD-SUP. Site 3, already difficult to populate in FD-SUP, registers here 0 binding events. Finally, the biggest difference between the 2 sets is with site 1, which sees its contribution drop from 31.0 % to 3.0 %.

The very large difference in performance observed for sites 1 and 5 could be due to the importance of the angle of attack for populating a site; especially with very cluttered areas like site 1, where there is also likely a steric element to the trapping of $O_2^{\bullet -}$ into the site, it makes sense that some sides are always blocked by some residue and that $O_2^{\bullet -}$ can only enter it from some directions. This is a tentative explanation that would require further investigation.
Regarding site 3, its already low rate of population in the FD-SUP dynamics (3.0 %) makes it difficult to determine whether its total disappearance in the E-SUP set is

due a peculiarity of the E-SUP setup or simply to chance. In any case, its unusual location compared to the other sites, which require first a $O_2^{\bullet -}$ to exit the electrostatically attractive crypt to travel along the protein surface before reaching it, could be sufficient to explain this phenomenon. While a path is technically present for $O_2^{\bullet -}$ to reach site 3 without being considered "diffused away" and the simulation terminated, perhaps is it too narrow; or perhaps there is simply not sufficient electrostatic guiding to pull a $O_2^{\bullet -}$ straight to site 3 after having reached the edge of the crypt, requiring all encounters to proceed from the bulk.

Looking now at the breakdown per binding lifetimes, another interesting discrepancy appears: E-SUP binding events seem much more reliable, averaging 75.1 % success rate of exceeding 1.0 ns, against 32.3 % for FD-SUP. This trend persists for $t_b \geq 10.0$ ns, with an overall 9.0 % of all binding events in this range. While very homogeneous across all binding sites (except site 3, whose 0.0 % across the board was not included in these statistics), the best performing site is site 2. Sites 4 and 5 have nearly identical rates of binding for $t_b \geq 1.0$ ns (73.8 % and 70.3 %) and for $t_b \geq 10.0$ ns (6.5 % and 7.1 %). Site 1 has similar stats, but its very small sample size (12 and 1 binding events in the last two t_b ranges, out of a total of 15) makes it difficult to draw a definite conclusion.

This remarkable quality of binding in the E-SUP dynamics, whereby the vast majority of $O_2^{\bullet -}$-site encounters give rise to $t_b \geq 1.0$ ns binding, would require more investigations to explain. We remind here that the same definition was used for the binding sites, the same distance criterion applied, and the same Δt between two consecutive frames. In any case, should this arise from purely geometrical factors such as the angle of approach, or physical ones like the partial desolvation of $O_2^{\bullet -}$ due to continued proximity with the protein surface, then the remarkable efficacy of these sites to intercept a newly-formed $O_2^{\bullet -}$ radical could be an intended feature of the 3-radical compass. To verify whether the extent of immobilisation thus achieved is sufficient to significantly delay its spin relaxation, we now turn to the computation of rotational correlation times.

4.6 Superoxide immobilisation by the protein: binding, rotational correlation and relaxation times

In this section, we evaluate the ability of various areas of the protein to properly immobilise a $O_2^{\bullet -}$ radical, *i.e.* to both sequester it for extended periods of time and to prevent it from freely tumbling. The former property is quantified by the binding

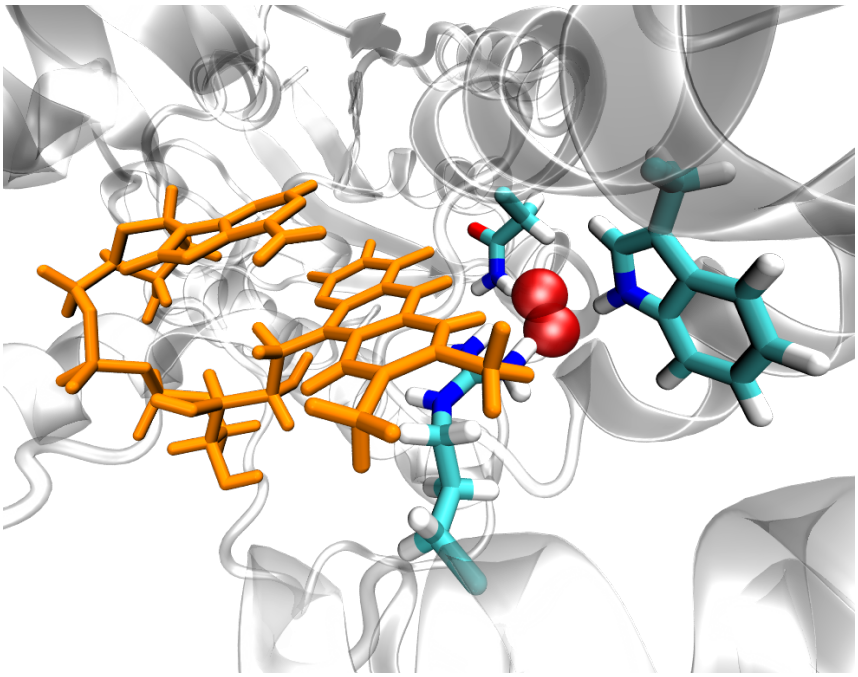

Figure 4.23: Representation of $O_2^{\bullet -}$ in the binding cavity from Ref. 2. $FADH^{\bullet}$ is shown in orange, and ASN393, TRP397 and ARG358 surrounding a $O_2^{\bullet -}$ radical are highlighted.

time t_b, the latter by the rotational correlation time τ_2. Finally, a corresponding relaxation time γ_B is estimated from τ_2, assuming a spin-rotational mechanism of relaxation.

4.6.1 $O_2^{\bullet -}$ in the $FADH^{\bullet}$ binding pocket

In this section, we investigate the binding capabilities of a putative $O_2^{\bullet -}$ formation pocket, and superoxide reorientation dynamics therein. This formation site, located in the flavin binding cavity, was identified by Mondal and colleagues in Ref 2 in a *dm*Cry protein. While this binding pocket is also present in *cl*Cry4, where an empty space exists in front of the $FADH^{\bullet}$ H5 atom, we suspect adverse steric effects might be involved in our model of avian cryptochrome. Indeed, despite the potential for strong attractive interactions with the flavin, this pocket was never populated by either of the 21 $O_2^{\bullet -}$ in the 5 μs of the FD-SUP trajectory set. However, it was not verified whether a neutral triplet oxygen could diffuse inside; it is possible that the barrier is electrostatic rather than steric.

This section relies on the analysis of the C-SUP trajectory set.

4.6.1.1 Binding times t_b

A definite binding time t_b could not be estimated in this simulation, as $O_2^{\bullet -}$ never diffused out. This finding is consistent with the fact that no exchanges between the

binding cavity and the outside of the protein were observed, even in longer studies containing more numerous anions. In fact, strong electrostatic interactions are also present. In particular, 3 residues, depicted in Figure 4.23, maintain very close proximity with $O_2^{\bullet -}$ throughout the simulation. From `cpptraj` geometrical criteria for identifying H-bonding (donor-acceptor distance $d_{\mathrm{DA}} \leq 3.0\,\text{Å}$ and donor-hydrogen-acceptor angle $\widehat{\mathrm{DHA}} \leq 150\,°$), we note that $O_2^{\bullet -}$ is constantly involved in H-bonding with at least one of these 3 residues, at any point during the simulation.

4.6.1.2 Rotational correlation times τ_2

Rotational correlation times were then computed as outlined in Chapter 1, by integrating the time-correlation function of the 2$^{\mathrm{nd}}$-order Legendre polynomial of $O_2^{\bullet -}$ molecular orientation. A very impressive rotational correlation time of $\tau_2 = 3869\,\text{ns}$ was achieved, suggesting an extremely strong immobilisation of $O_2^{\bullet -}$ in the cavity. The rotational correlation time can be understood as the time it takes for all memory of the initial orientation to be lost.

4.6.1.3 Spin relaxation times γ_B

As described in Chapter 1, a spin relaxation time can be derived from τ_2. Due to the extremely weak strength of the geomagnetic field, we can assume spin relaxation occurs *via* the Spin-Rotational Interaction (SRI) mechanism, whereby the magnetic moment of the radical spin couples with the rotation axis of the molecule. The calculation of γ_B requires an accurate estimation of the $O_2^{\bullet -}$ g-tensor, which is quite sensitive to its immediate electronic environment. To calculate it, a geometry was extracted from the dynamics of $FADH^{\bullet}$ in the binding pocket. Its g-tensors was computed by Daniel Kattnig using DFT at the B3LYP/def2-TZVP level, including dispersion corrections with the D3BJ scheme. The rest of the protein environment was included as point charges, and the atoms nearest to the $O_2^{\bullet -}$ were modeled more accurately using effective core potentials (ECPs).

Using Equation 1.15, a relaxation time of 3869 ns, *i.e.* 3.5 μs was found for $O_2^{\bullet -}$ in the binding pocket. This is extremely significant and suggests a sustained coherence throughout most of the radical pair's lifetime, which is typically bound between 1 and 10 μs, and which some estimations place at 3 μs.[48] There is a possibility that non-averaged EED couplings at such a short distance could exert a strongly suppressive effect of magnetosensitivity. In the radical pair model, such a phenomenon proves fatal to MFEs, as such a strong interaction tends to lift the near degeneracy of singlet and triplet states, thereby rendering interconversion extremely slow and effectively abolishing it.[25] This effect is also visible in $FADH^{\bullet}/O_2^{\bullet -}$ radical pairs

(Chapter 2, Fig. 2.3 (a)) or effective $FADH^{\bullet}/Y^{\bullet}$ radical pairs (Chapter 2, Fig. 2.5). The formation of $O_2^{\bullet -}$ in the binding pocket, according to the mechanism proposed in Ref. 2, would therefore likely not allow a $FADH^{\bullet}/O_2^{\bullet -}$ radical pair to function, due to the inability of $O_2^{\bullet -}$ to diffuse out in the *cl*Cry structure and to mitigate its strong EED coupling with the flavin.

For non-relaxing 3-radical systems, as could exist in *cl*Cry4 if the proposed $Y^{\bullet}$ is not neutralised itself by a scavenger (in the classic sense of the term), strong EED coupling between 3 radicals, even in such a geometry where radicals are far from equidistant, do not necessarily abolish MFEs. Systems containing more than 2 radicals have their spin dynamics governed by a complex interplay of EED- and hyperfine-driven interconversion, and large MFEs have been realised for a $FADH^{\bullet}/O_2^{\bullet -}/Y^{\bullet}$ triad in such a configuration, with $O_2^{\bullet -}$ within 5 Å of $FADH^{\bullet}$.[27] In this case, the very slow relaxation of $O_2^{\bullet -}$ could actually enhance the magnetosensitivity of the radical triad. We suggest verifying, *e.g. via* a MD study similar to that in Ref 2, the ability of a $^3O_2$ molecule to enter this cavity in a *cl*Cry4, as was found in *dm*Cry.

Alternatively, the FD-SUP trajectory set (10 500-ns MD simulation of *cl*Cry4 and 21 $O_2^{\bullet -}$ radicals) evidenced the presence of $O_2^{\bullet -}$ in close proximity to the flavin (see Figure 4.17: $O_2^{\bullet -}$ has non-zero density as close as 4 Å away from the isoalloxazine). We proposed in section 4.5 to study the diffusion path of $O_2^{\bullet -}$ near the flavin, from a putative fixation point where it could oxidise $FADH^-$, to binding sites where its spin relaxation could also be delayed, and three-centres EED coupling maintained. We now investigate in the next section the spin relaxation times achievable by a $O_2^{\bullet -}$ radical trapped in one of these sites.

4.6.2 $O_2^{\bullet -}$ in the binding sites

In this section, we compute binding times and rotational correlation times for a $O_2^{\bullet -}$ radical trapped in one of the previously defined sites. This section consists of an analysis of the T-SUP trajectory set, where a $O_2^{\bullet -}$ radical is initially trapped into one of the 5 sites defined earlier and left to diffuse out. The same criteria for identifying binding ($d_{\mathrm{SUP-residue}} \leq 3.0$ Å) and for defining sites (Table 4.3) as before are in use here. The binding times t_b obtained from these simulations are reported in Figure 4.24; and a numerical breakdown is given in Table 4.6.

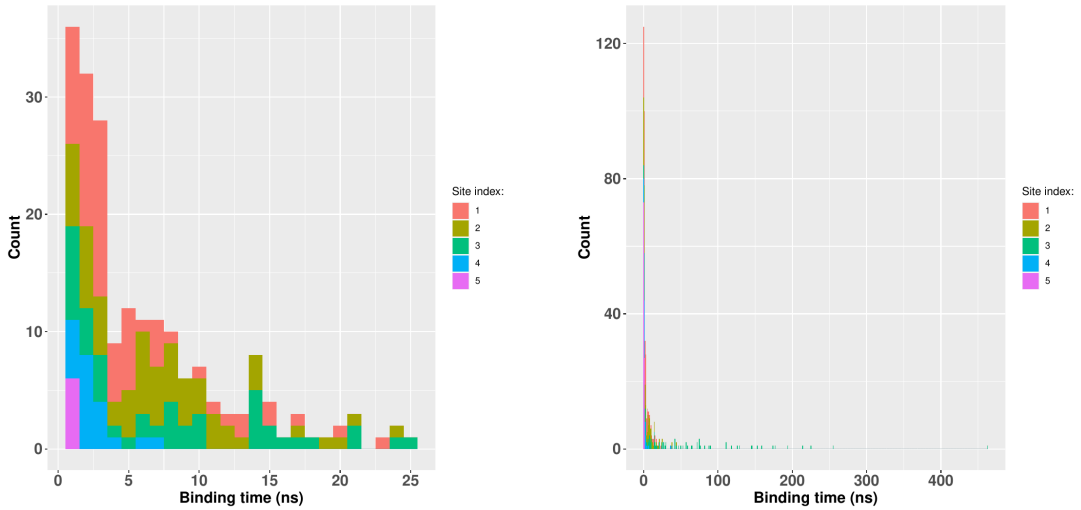

Figure 4.24: Histogram of the lengths of $O_2^{\bullet -}$-protein binding events, calculated for each site on 20 MD trajectories for each of 5 initial binding configurations, for a total of 100 trajectories. (a) and (b) differ only by the plot range.

Site	Total nb. of BE	nb of $t_b \geq 10^0$ ns BE	nb of $t_b \geq 10^1$ ns BE	nb of $t_b \geq 10^2$ ns BE
1	100	67 (67.0%)	11 (11.0%)	0
2	100	66 (66.0%)	18 (18.0%)	0
3	100	88 (88.0%)	58 (58.0%)	16 (16.0%)
4	40	21 (52.5%)	1 (2.5%)	0
5	100	6 (6.0%)	0	0

Table 4.6: Number of binding events (BE), with binding length t_b in ns, from the 440 restarted trajectories of $O_2^{\bullet -}$ diffusing from a binding site.

4.6.2.1 Binding times t_b

The most striking feature of this binding profile, made evident in Figure 4.24 **(b)**, is the remarkable performance of site 3 in achieving long t_b: it is the only site in which $t_b \geq 100$ ns is realised in the T-SUP dataset, with a maximum of $t_b = 463.07$ ns, and it also dominates the $25 \leq t_b \leq 100$ ns range, with numerous contributions from site 2. This is qualitatively consistent with the already observed abilities of these two sites to realise long-lived $O_2^{\bullet -}$ trapping.

Comparison with the previous trajectory sets is however not the main point of focus here, because of the bias introduced in the selection of starting frames, supposed to eliminate the weakly-interacting configurations. Indeed, due to the computationally extensive nature of this study, the aim is to determine whether long binding and rotational correlation times are achievable in these sites, rather than to offer a statistically exact account of their prevalence.

In this respect, our choice of starting configurations seems adequate for site 3,

for which the extremely long binding times promised in the FD-SUP set could be replicated. Similarly for site 1, 2 and 4, although this last one ideally should be investigated further. On the other hand, the $t_b = 10^0 - 10^1$ ns binding capabilities of site 5 were not reproduced in the 100 trajectories proceeding from its 5 chosen starting configurations. It is difficult to conclude whether the range of t_b and τ_2 reported for this site in the present study really reflects, or contains, the best performance achievable for this site; and further research with additional starting frames is desirable.

Figure C.7, provided in Appendix C (Figure C.7), reports the characteristic $O_2^{\bullet -}$ binding times for each site and for our set of simulations, computed by integrating a function $f(t)$ such that $f(t) = \frac{N^t_{\text{SUP=bound}}}{N_{\text{tot.}}}$, where $N_{\text{tot.}}$ is the total number of trajectories for a given site, and $N^t_{\text{SUP=bound}}$ is the number of trajectories where $O_2^{\bullet -}$ is still bound at time t, *i.e.* the number of trajectories with $t_b \geq t$.

4.6.2.2 Rotational correlation times τ_2 and spin relaxation times γ_B

Having verified that long binding times could be achieved for the sites under investigation, we next set out to compute rotational correlation times τ_2 for $O_2^{\bullet -}$ radicals when in a binding configuration, in order to gauge the quality of the immobilisation realised by the binding aminoacids. τ_2 values are calculated as detailed in Chapter I, and serve as a proxy for evaluating the superoxide spin relaxation rate.

Tables 4.7 through 4.11 report average t_b and τ_2 values computed on each of the 5 sets of 20 replica trajectories associated to each site. This breakdown per starting configurations, rather than a single $\langle t_b \rangle$ and $\langle \tau_2 \rangle$ value per site, was favoured due to the sometimes large intra-site variability.

It is important to note that these averages are not computed on the full set of 20 replica trajectories, but only on trajectories for which a meaningful τ_2, *i.e.* $\tau_2 \geq 10.0$ ps, could be computed. For each set, the actual number of trajectories on which $\langle \tau_2 \rangle$ and $\langle t_b \rangle$ are calculated is reported as N.

"N/A" refers to the case where none of the trajectories could give rise to $\tau_2 \geq 10.0$ ps, or as in the case of site 5 frame 1, to a τ_2 value at all. This can occur when binding times are extremely short (here: $\langle t_b \rangle = 0.11$ ns, with $t_b^{\max} = 0.26$ ns). With so few data points, the autocorrelation function of $C_2(t)$ (see Chapter 1) turns out extremely noisy, which could make fitting impossible. Beside, our strategy here is to fit either the first quarter of the ACF, or up to the point where it reaches 0

		Occupancy time (ns)	τ_2 (ps)	N
site 1	1	7.07 ± 9.18	108.8 ± 180.4	16
	2	1.26 ± 0.99	17.9 ± 7.4	5
	3	3.69 ± 3.02	99.9 ± 136.9	8
	4	3.92 ± 4.17	66.4 ± 52.4	12
	5	7.30 ± 6.46	103.6 ± 101.3	17

Table 4.7: Average binding times and rotational correlation times τ_2 of a $O_2^{\bullet -}$ radical to site 1, calculated from 20 MD trajectories for each of 5 initial binding configurations, for a total of 100 trajectories. Only 69 trajectories yielded $\tau_2 \geq 10.0$ ps and therefore were included in these statistics.

		Occupancy time (ns)	τ_2 (ps)	N
site 2	1	2.10 ± 1.69	18.2 ± 3.5	4
	2	6.30 ± 3.90	97.2 ± 65.8	18
	3	9.30 ± 9.62	92.5 ± 107.6	18
	4	10.87 ± 10.71	120.6 ± 212.7	17
	5	6.89 ± 5.32	56.9 ± 51.7	9

Table 4.8: Average binding times and rotational correlation times τ_2 of a $O_2^{\bullet -}$ radical to site 2, calculated from 20 MD trajectories for each of 5 initial binding configurations, for a total of 100 trajectories. Only 66 trajectories yielded $\tau_2 \geq 10.0$ ps and therefore were included in these statistics.

		Occupancy time (ns)	τ_2 (ps)	N
site 3	1	10.11 ± 17.11	36.7 ± 32.8	12
	2	6.86 ± 6.30	59.8 ± 57.3	17
	3	119.96 ± 113.23	116.2 ± 147.1	15
	4	65.76 ± 50.00	78.0 ± 108.3	19
	5	75.44 ± 71.02	59.8 ± 78.0	15

Table 4.9: Average binding times and rotational correlation times τ_2 of a $O_2^{\bullet -}$ radical to site 3, calculated from 20 MD trajectories for each of 5 initial binding configurations, for a total of 100 trajectories. Only 78 trajectories yielded $\tau_2 \geq 10.0$ ps and therefore were included in these statistics.

		Occupancy time (ns)	τ_2 (ps)	N
site 4	1	0.65 ± 0.00	27.8 ± 0.0	1
	2	3.96 ± 8.11	61.6 ± 63.5	17

Table 4.10: Average binding times and rotational correlation times τ_2 of a $O_2^{\bullet -}$ radical to site 4, calculated from 20 MD trajectories for each of 2 initial binding configurations, for a total of 40 trajectories. Only 18 trajectories yielded $\tau_2 \geq 10.0$ ps and therefore were included in these statistics.

		Occupancy time (ns)	τ_2 (ps)	N
	1	N/A	N/A	0
	2	0.52 ± 0.29	18.1 ± 9.0	4
site 5	3	0.59 ± 0.30	12.3 ± 0.5	2
	4	1.01 ± 0.13	15.0 ± 1.1	2
	5	0.69 ± 0.00	10.9 ± 0.0	1

Table 4.11: Average binding times and rotational correlation times τ_2 of a $O_2^{\bullet -}$ radical to site 5, calculated from 20 MD trajectories for each of 5 initial binding configurations, for a total of 100 trajectories. Only 9 trajectories yielded $\tau_2 \geq 10.0$ ps and therefore were included in these statistics.

Site	Initial frame	τ_2 (ps)	t_b (ns)	γ_B (ns)
2	2429	940.69	44.36	729.85
1	568	756.86	13.25	587.22
2	1755	454.95	8.43	352.98
1	1015	444.57	11.19	344.93
3	579	413.07	27.29	320.49
3	579	400.99	174.20	311.11
3	579	399.43	118.24	309.90
3	1463	390.69	41.86	303.12
3	1463	374.13	75.34	290.27
1	1484	334.72	15.32	259.70

Table 4.12: Top 10 τ_2 values of the T-SUP set, with their associated t_b and γ_B, and the site info.

– whichever comes first (typically the latter). A noisy ACF could reach 0 almost immediately, again rendering fitting impossible.

The maximum τ_2 values achieved across all sites are reported in Table 4.12.

An intriguing aspect of long-τ_2 trajectories is that they do not necessarily have the longest t_b. One could expect that extended binding of $O_2^{\bullet -}$ into a site would be achieved by setting up very strong interactions, and that these interactions would in turn necessarily prevent $O_2^{\bullet -}$ from rotating in the cavity. However, out of the 10 trajectories with the longest τ_2, 4 are shorter than the average trajectory in the truncated T-SUP set, which is of $\langle t_b \rangle = 23.36$ ns. What we refer to as "truncated T-SUP" set is the subset of T-SUP for which $\tau_2 \geq 10.0$ ps is achieved; *i.e.* it only includes trajectories for which a physically meaningful τ_2 could be computed. There could still be a correlation, as the average t_b in Table 4.12 is $\langle t_b \rangle = 52.95$ ns; but this latter figure is extremely noisy. This correlation phenomenon is examined in more details in a later section.

The degree of immobilisation imposed by the binding residues in these sites can be appreciated by comparing with τ_2 values computed for freely-tumbling, bulk $O_2^{\bullet-}$ radicals. Such trajectories were generated in a separate MD simulation, where 5 $O_2^{\bullet-}$ radicals were left to tumble around in a water box for 5 ns. Due to the expected very fast relaxation, the Δt between two consecutive geometries was reduced to 100 fs, allowing to compute meaningful rotational correlation times below 10 ps.

Bulk $O_2^{\bullet-}$ achieve an average τ_2 of $\langle\tau_2\rangle = 0.99 \pm 0.33$ ps. Direct, rigorous comparison with averages for the sites is not possible, as all $\tau_2 \leq 10.0$ ps could not be meaningful and therefore removed, sometimes severely depleting the statistics. However, we can do a rough comparison, with sites where e.g. $N \geq 15$, to observe that binding into a site can reliably increase the rotational correlation times of $O_2^{\bullet-}$ by a factor of $10^2 - 10^3$. Although highly sensitive to the choice of initial $O_2^{\bullet-}$-site configuration, as evidenced by the large intra-site variability of N (see *e.g.* site 2 and 4), we can cite site 2 in particular for its regularity in achieving 10^3 (or near) times better immobilisation than the bulk.

A more assured conclusion can be reached through comparison with site-bound $O_2^{\bullet-}$ τ_2 values in Table 4.12, where we compare the top 10 peak immobilisation ability across T-SUP trajectories. As already suggested by the averages, sites 1 through 3 are the best performers, routinely achieving 10^2 ps rotational correlation times, *i.e.* 1000 times longer than those for $O_2^{\bullet-}$ in solution. The very best immobilisation, although probably a rare event, is achieved by site 2 and corresponds to a τ_2 of almost 1 ns.

Using the same value for the $O_2^{\bullet-}$ g-tensor as in Section 4.6.1, superoxide spin relaxation times γ_B were computed, and are reported in Table 4.12. While not quite as impressive as the $O_2^{\bullet-}$ immobilisation realised in the flavin binding pocket, spin relaxation times approaching the microsecond timescale appear possible, and the 10^2 ns timescale is readily achievable by sites 1, 2 and 3.

Contrary to the case in the previous section, where $O_2^{\bullet-}$ stays extremely close to the flavin, the longer distances separating them here (all binding sites are located $\simeq 20$ Å away from $FADH^{\bullet}$) point to EED coupling at least partly decayed. In the limit case where EED couplings are completely abolished, our earlier study of the magnetosensitivity of a $FADH^{\bullet}/O_2^{\bullet-}$ RP in the presence of EED coupling predicts (Chapter 2, Figure 2.3 (a)) MFEs between 1 and 2 % for relaxation times in the region of 500 – 700 ns – particularly for a radical lifetime shorter than 10 μs, as is suggested by some experimental findings.[48] A repeat of this study, locating $O_2^{\bullet-}$ radicals inside these sites and taking electron-electron dipolar coupling and spin relaxation into account, would be useful to investigate a potentially promising RP configuration.

For the 3-radical case, significant magnetosensitivity was reported for a similar geometry, with $O_2^{\bullet -}$ located 18 Å away from $FADH^{\bullet}$.[27] Due to the sensitivity of EED coupling to not only distance, but also relative orientation, it would be useful to evaluate MFEs for such a system, parametrised with $O_2^{\bullet -}$ location and Γ_B values. Neglecting the impact of EED coupling on the triad's spin dynamics and considering only the addition of the $FADH^{\bullet}/O_2^{\bullet -}$ recombination channel, only a very small Γ_S gain is expected from extended $O_2^{\bullet -}$ coherence (see Chapter 2, Figure 2.3 (b)). It would nonetheless be useful to evaluate their impact on the spin dynamics, as they couple with hyperfine couplings to drive spin state interconversion.

All γ_B values reported in this last section are preliminary results and should inform an order of magnitude, rather than a precise value, of relaxation times associated with every long-τ_2 binding event. Indeed, the $O_2^{\bullet -}$ g-tensor used to convert τ_2 into γ_B is the one computed on a geometry of $O_2^{\bullet -}$ in the binding pocket, where a much stronger immobilisation is realised. More accurate spin relaxation times could be estimated by computing the $O_2^{\bullet -}$ g-tensor in sites 1, 2 and 3. In the meantime, we report here the likely possibility of realising 10^2 ns spin relaxation times for $O_2^{\bullet -}$ radicals immobilised around 20 Å away from the flavin, and possibly approaching 1 μs. This assessment, while preliminary, breathes some new life into the hypothesis of a magnetosensitive $FADH^{\bullet}/O_2^{\bullet -}$ RP, and warrants some research for the 3-radical possibility, whose spin dynamics could be significantly altered by long-lifetime, 3-centres EED coupling.

4.6.2.3 $O_2^{\bullet -}$: correlation of τ_2 and t_b with H-bonding

In this section, we seek to clarify the relationship between t_b and τ_2, as well as explore the possibility of the involvement of hydrogen bonding for immobilising $O_2^{\bullet -}$.

Across the truncated T-SUP set (*i.e.* only $t_b \geq 10$ ns), the rate of occurrence of hydrogen bonding, between a $O_2^{\bullet -}$ and the aminoacids composing the site currently trapping it, was monitored. Hydrogen bonding, or- H-bonding, is an electrostatic interaction modality involving a donor group attached to a hydrogen, and an acceptor group with a partial negative atomic charge.

H-bonding can be determined from purely geometrical factors, namely the distance separating the acceptor from the donor heavy atom and the angle $\widehat{\mathrm{DHA}}$ between the donor (D), hydrogen (H) and acceptor (A). In our analysis, we follow `Cpptraj` with default parameters and consider H-bonding exists for donor-acceptor distance $d_{\mathrm{DA}} \leq 3.0$ Å and $\widehat{\mathrm{DHA}} \leq 150\,^{\circ}$.

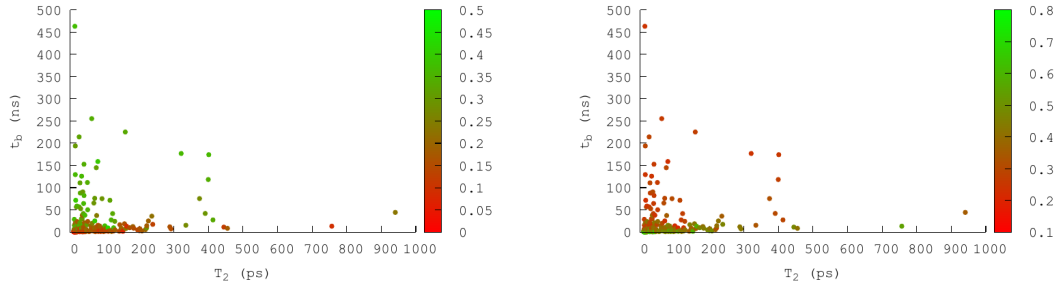

(a) **Double** H-bonding

(b) **No** H-bonding

Figure 4.25: t_b vs τ_2 values of the truncated T-SUP trajectory set, with the associated rate of (a) double H-bonding and (b) absence of H-bonding throughout the corresponding simulation.

In Figure 4.25, we report in graph form the τ_2, t_b, and proportion of a certain type of hydrogen bonding along each trajectory of the truncate T-SUP set. In particular, we look at the proportion of "double" H-bonding, *i.e.* the fraction of the trajectory where both $O_2^{\bullet -}$ atoms are simultaneously involved in a H-bond; and the "no-" H-bond case, where none of them is involved.

There is no evidence of a linear correlation between τ_2 and t_b (Pearson: 0.10). This goes against the intuitive reasoning mentioned earlier, which states that long $O_2^{\bullet -}$ trapping times and strong immobilisation could be realised in the same way, *i.e.* with strong interactions with the participating residues, and that therefore large τ_2 and t_b should group together. This representation shows almost the opposite effect: long t_b overwhelmingly have associated $\tau_2 \leq 100$ ps, and the 2 longest τ_2 both have $t_b \leq 50$ ns. The nearly vertical arrangement of points near $\tau_2 = 400$ ps illustrates the lack of correlation between these two properties: a very large τ_2 can be achieved with a $O_2^{\bullet -}$ binding time anywhere from 10 to 200 ns.

Since length of binding is not a predictor for quality of immobilisation, let us focus on one interaction modality between $O_2^{\bullet -}$ and its binding residues. The colourscales indicate, for each trajectory in the truncated T-SUP set, the proportion of (a) double H-bonding, and (b) the absence of H-bonding. No particular correlation can be detected upon visual inspection, for either double- or no-bonding. This is confirmed by the Pearson correlation coefficients, which are $r_{\tau_2/2Hb} = 0.06$ for τ_2 correlation with double-bonding and $r_{\tau_2/0Hb} = -0.10$ with the absence of H-bonding. Again, this is rather surprising: intuitively, one would expect that simultaneous binding of both atoms of $O_2^{\bullet -}$ would prevent it from reorienting. Here, only the signs of the linear correlation coefficients confirm this hypothesis; but while they hint at a positive correlation of τ_2 with double H-bonding, and an inverse correlation with the absence

of H-bonding, their magnitude is too small to assign the variance in τ_2 to either of these properties.

There is, on the other hand, a clearer correlation between t_b and the amount of hydrogen bonding in which $O_2^{\bullet -}$ is involved while in the binding site. Upon visual inspection of Figure 4.25, is seems that a larger proportion of double H-bonding correlates to larger t_b, while a larger fraction of no H-bonding at all correlates with short t_b. This observation is confirmed by Pearson correlation coefficients, which are $r_{t_b/2Hb} = 0.48$ with double-bonding and $r_{t_b/0Hb} = -0.44$. This moderately strong linear correlation makes intuitive sense, as one can expect that more numerous interactions between $O_2^{\bullet -}$ and the site stabilise the bound configuration and therefore increase trapping time.

The representation in Figure 4.25 only includes trajectories where $\tau_2 \geq 10.0\,\mathrm{ps}$, *i.e.* computed on the truncated T-SUP set. Including the full T-SUP set does however not change the conclusion: the Pearson correlation coefficient of t_b with double H-bonding is 0.49, and remains at -0.44 with no-H-bonding.

The lack of correlation between τ_2 and the simultaneous binding of both $O_2^{\bullet -}$ atoms is a surprising find, which warrants further investigation into the subject. Perhaps this could be traced to the great flexibility shown by arginine residues, which do not maintain a persistent H-bonding scaffolding to anchor the $O_2^{\bullet -}$ radical.

4.7 Non-relaxing superoxide in a binding site: what impact on the spin dynamics?

In this last section, we present the results of spin dynamics simulations carried out by Daniel Kattnig, testing again the relative performance of 18 *cl*Cry tyrosine residues to function as a scavenger, within a [$FADH^{\bullet}/O_2^{\bullet -}/Y^{\bullet}$] radical triad. This update on the simulations presented in Chapter 2 is parameterised by quantities computed in Chapters 3 and 4; namely, hyperfine coupling tensors for the flavin, and $O_2^{\bullet -}$ locations.

Due to the still large uncertainty on τ_2 and γ_B values achievable for $O_2^{\bullet -}$ inside any of its sites, but bolstered by the proof-of-principle that slow $O_2^{\bullet -}$ spin relaxation is possible, we report here results from spin dynamics simulation with a **non-relaxing** $O_2^{\bullet -}$, located in the previously defined binding sites. This is expected to affect the spin dynamics through two main mechanisms. First, its spin-selective

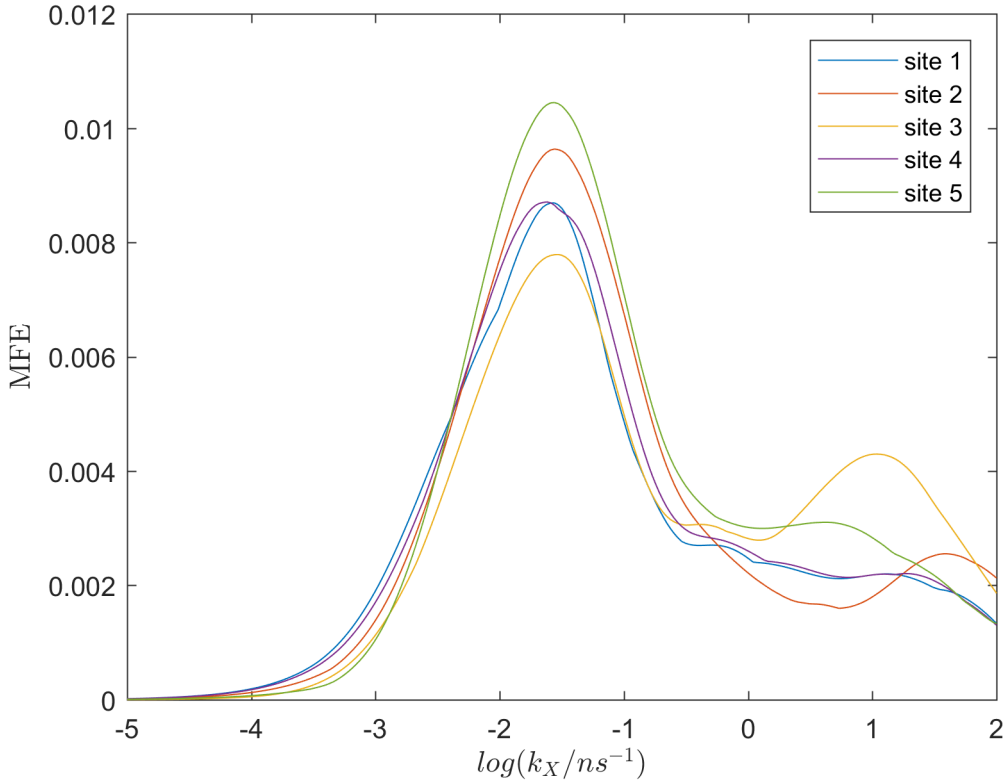

Figure 4.26: Γ_S as a function of scavenging rate k_X, obtained from a spin dynamics simulation of a $FADH^\bullet/O_2^{\bullet-}/Y319^\bullet$ radical triad in a *cl*Cry4 structure. $O_2^{\bullet-}$ is located in one of the 5 binding sites defined earlier, and is assumed not to undergo spin relaxation. We use a radical lifetime of $k_f^{-1} = 3\,\mu s$. The hyperfine structure of $FADH^\bullet$ is modeled by tensors for nuclei N5, N10, H5, Hβ1, Hβ2, H6, H7 and H8, as computed using QM/MM in Chapter 3. For $Y319^\bullet$, nuclei Ho1, Ho2 and Hβ2 are included. EED interactions are considered.

recombination channel with $FADH^\bullet$ remains active, since each binding site is located within $\simeq 20$ Å of the flavin. $O_2^{\bullet-}$ being devoid of hyperfine couplings, the $FADH^\bullet$-$O_2^{\bullet-}$ recombination dynamics approach those of the "reference-probe" configuration, a remarkably magnetosensitive system. Second, its non-averaged EED coupling with both other radicals in the triad is itself able to sustain spin-state interconversion, thereby affecting the overall spin dynamics. Interference of hyperfine- and EED-driven interconversion has been shown to give rise to very localised, but quite potent, MFEs in 3-radical systems.[25,27] We test here whether a non-relaxing $O_2^{\bullet-}$ located in one of these sites could achieve significant magnetosensitivity.

4.7.0.1 The slowly-relaxing $FADH^\bullet/O_2^{\bullet-}/Y319^\bullet$ triad

We report in Figure 4.26 achievable Γ_S values for Y319. It should be noted that all spin dynamics simulations reported in this section were carried out on a slightly different *cl*Cry4 geometry than that used for simulations in Chapter 2. This new geometry was extracted from an MD simulation from the FD-SUP trajectory set.

While interradical distances are left roughly unchanged (see Table 4.13), the relative orientation of $FADH^{\bullet}$ and Y319 is slightly modified. In particular, the φ_{FY} dihedral angle between the respective long axes of the $FADH^{\bullet}$ isoalloxazine and Y319 is $\varphi_{F-Y} = 252.2\,^{\circ}$, *i.e.* in the secondary preferential orientation of Y319.

Compared to MFEs reported in Chapter 2, which were of an optimal $\Gamma_S \simeq 8.5 \times 10^{-3}$ at $k_X \simeq 10\,\mathrm{ns}^{-1}$ in the limit of fast $O_2^{\bullet-}$ relaxation and a less complete $FADH^{\bullet}$ hyperfine structure, we report in the present study similar to slightly enhanced MFEs, ranging from 7.8×10^{-3} to 10.4×10^{-3}. While the many differences between the two studies do not allow to pinpoint it to a single factor, we can at least conclude that the addition of a third, slowly-relaxing radical in the vicinity of the $FADH^{\bullet}/Y^{\bullet}$ system does not quench its magnetosensitivity. In fact, the enrichment of $FADH^{\bullet}$ hyperfine structure with additional tensors is expected to bring about a decrease in the directional sensitivity of the compass, due to the mainly isotropic nature of the added tensors (all H tensors, including methyles). Instead, we report maximum MFEs of $\Gamma_S \simeq 10 \times 10^{-3}$ for a $O_2^{\bullet-}$ bound by site 5. Site 2 also outperforms the fast-relaxing $O_2^{\bullet-}$ case, with optimal $\Gamma_S \simeq 9.5 \times 10^{-3}$ achieved for a very similar scavenging rate.

Interestingly, the relative performance of the sites can't be linked to $FADH^{\bullet}$ or $Y^{\bullet}$ distance to $O_2^{\bullet-}$, or to the triad geometry; indeed, the best- and worse-performing configurations, with $O_2^{\bullet-}$ in sites 5 and 3 respectively, correspond to similar radical arrangements where $d_{F-site} \simeq 20\,\text{Å}$ and $d_{Y-site} \simeq 40\,\text{Å}$, with $d_{F-Y} = 27.6\,\text{Å}$. On the other hand, configurations with $O_2^{\bullet-}$ located in sites 1, 2 and 4 correspond to roughly equidistant radicals. Nonetheless, the Γ_S across sites remains small and differences can probably be explained by the interplay between HFC- and EED-driven spin dynamics.

The question now arises whether a non-relaxing $O_2^{\bullet-}$ is an appropriate approximation for the long relaxation times observed for bound $O_2^{\bullet-}$. Drawing on the results presented in Figure 2.3 from Chapter 2, the overall Γ_S gains from long $O_2^{\bullet-}$ coherence lifetimes are fairly small, of the order of 1 to 2 % for a $FADH^{\bullet}/O_2^{\bullet-}/Y^{\bullet}$ triad in the geometry considered there, and saturates for $O_2^{\bullet-}$ relaxation times of $\gamma_B \simeq 10^{-4}\,\mathrm{ns}^{-1}$, *i.e.* a coherence lifetime of about $10\,\mu$s. Note that this case is not necessarily applicable to the present study, as $O_2^{\bullet-}$ EED couplings were considered averaged out by diffusion in Chapter 2, which is not the case here. Using this model however, a $O_2^{\bullet-}$ relaxation time of $10\,\mu$s or slower would yield identical MFEs to the non-relaxing $O_2^{\bullet-}$ simulated here. This is more than 10 times slower than the largest γ_B recorded in our study, a relaxation time of $\gamma_B = 929\,\mathrm{ns}$ attained for site 2. The best relaxation times for other sites, $\gamma_B = 587\,\mathrm{ns}$ for site 1 and $\gamma_B = 320\,\mathrm{ns}$ for site 3, fall similarly

Tyrosine	d_{F-Y} (Å)
Y32	38.8
Y35	18.8
Y81	26.3
Y107	14.8
Y134	22.7
Y151	16.5
Y190	35.6
Y252	16.3
Y271	28.4
Y295	15.5
Y319	27.6
Y388	14.1
Y407	24.4
Y426	16.0
Y430	18.9
Y441	38.1
Y443	23.2
Y464	23.3

Table 4.13: Interradical distances between $FADH^\bullet$ N5 atom and the tyrosine's OH atom.

short. While we cannot be certain to have uncovered the $O_2^{\bullet -}$-binding configuration giving rise to the largest possible relaxation times, and that the non-relaxing limit could not therefore be relevant for one or some sites, current data leads us to consider the results reported in Figure 4.26 as over-optimistic estimations.

Nonetheless, it is encouraging that MFEs for a triad in the limit of slow $O_2^{\bullet -}$ relaxation are so close to the fast-relaxation limit. As Figure 2.3 teaches us that the $FADH^\bullet/O_2^{\bullet -}/Y^\bullet$ triad magnetosensitivity is fairly robust to fast $O_2^{\bullet -}$ spin relaxation in terms of its contribution to spin-selective recombination, it seems from results presented in Figure 4.26 that the effect of preserved $O_2^{\bullet -}$ EED coupling on the compass performance is also small. We therefore still consider Y319 as a fairly efficient scavenger.

4.7.0.2 Other $Y^\bullet$ scavengers in the limit of slow $O_2^{\bullet -}$ relaxation

In this section, we extend the study presented in the previous section to all tyrosines considered in Chapter 2 as potential scavengers in a $FADH^\bullet/O_2^{\bullet -}/Y^\bullet$ triad. Again, we consider the limit case where a site-bound superoxide does not undergo spin relaxation, preserving both its recombination channel with $FADH^\bullet$ and its EED coupling with both other radicals.

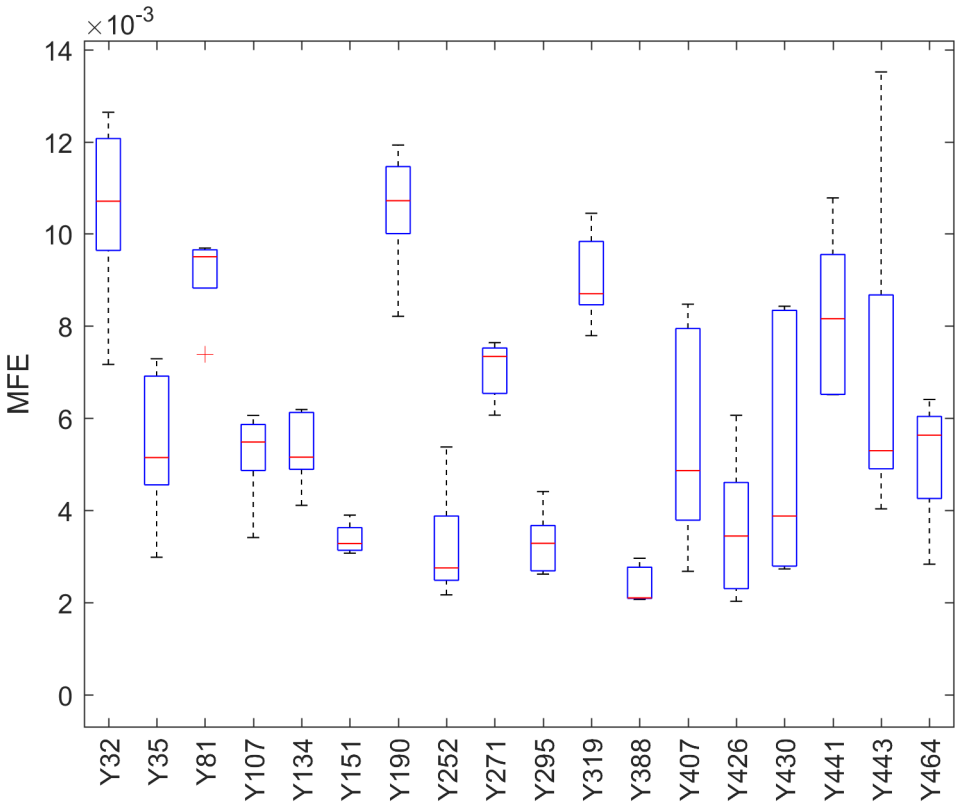

Figure 4.27: Maximum Γ_S, *i.e.* realised at optimal k_X, obtained from a spin dynamics simulation of a $FADH^{\bullet}/O_2^{\bullet -}/Y^{\bullet}$ radical triad where $O_2^{\bullet -}$ is located in each of the five binding sites defined earlier. The red lines materialise the median Γ_S across these 5 $O_2^{\bullet -}$ locations, and the boxes their distributions. Computed with radicals geometries extracted from a *cl*Cry4 structure. Again, $O_2^{\bullet -}$ is assumed not to undergo spin relaxation. We use a radical lifetime of $k_f^{-1} = 3\,\mu$s. The hyperfine structure of $FADH^{\bullet}$ is modeled by tensors for nuclei N5, N10, H5, Hβ1, Hβ2, H6, H7 and H8, as computed using QM/MM in Chapter 3. For $Y^{\bullet}$, nuclei Ho1, Ho2 and Hβ2 are included. EED interactions are considered.

We report in Figure 4.27 the distribution of maximum achievable anisotropies for 18 tyrosines. This study echoes that realised in Chapter 2, Figure 2.5, but assumes a non-relaxing $O_2^{\bullet -}$ located in each of the 5 binding sites defined earlier. $FADH^{\bullet}$ hyperfine structure uses tensors computed in Chapter 3. This set of calculations was also realised by Daniel Kattnig.

While direct comparison with data reported in Figures 2.5 (a) or (b) is not possible, notably due to the different radical lifetime used here ($k_f^{-1} = 3\,\mu$s vs. 1 or 10 μs), no Γ_S as high as 2 % is realised. There are however a number of $Y^{\bullet}$ residues able to elicit MFEs around or above 1 %: namely, Y32, Y81, Y190, Y319, Y441 and Y443. Considering these data in conjunction with $FADH^{\bullet}$-$Y^{\bullet}$ distances, provided in Table 4.13, however, the same trend outlined in Chapter 2 emerges: large MFEs are mainly realised by $Y^{\bullet}$ located far away from the flavin, presumably due to decayed EED

coupling. Interesting exceptions arise: Y81 and Y319, both separated from the flavin by 27 Å achieve Γ_S close to or exceeding 10×10^{-3}. Y443 also, while underperforming for all other sites, reaches optimal MFEs of nearly 1.4 % for site X. Its shorter separation from the flavin's N5 atom ($d_{N5-OH} = 23.2$ Å) makes it a promising scavenger in this particular geometry.

While both quite promising in terms of their potential performance as scavengers, we for now lack a mechanism to form these radical tyrosines in the *cl*Cry: both Y81 and Y443 are located rather far away from W_C and W_D, at respectively 32.2 Å and 23.1 Å away from the nearest. As such, it seems unlikely that they could be formed rather than Y319, which extends the tetrad. On the other hand, as solvent-exposed residues, there is the possibility that they could be formed from a free-diffusing radical, possibly a $O_2^{\bullet -}$.

All in all, this study highlights the rather special nature of Y319, which retains appreciable MFEs and shows its robustness with respect to $O_2^{\bullet -}$ relaxation, in the limits of immediate- and no-relaxation. With the rather large variability in $O_2^{\bullet -}$ spin relaxation rate estimated in this Chapter, Y319's ability to function as a scavenger irrespective of $O_2^{\bullet -}$ relaxing early or not could allow an inhomogeneous ensemble of *cl*Cry4 to be magnetosensitive across the board. The idea that quite different $O_2^{\bullet -}$ relaxation rates can be expected to arise from different *cl*Cry4 conformations is supported by the large in-site τ_2 variability pointed out in Section 4.6.2.

4.8 Chapter conclusions and perspectives

In this study, we have investigated the ability of an avian cryptochrome protein to trap $O_2^{\bullet -}$ radicals to its surface and to prevent them from tumbling, computing spin relaxation times that can be used to parameterise spin dynamics simulations of radical pairs or triads.

The force-field parameters used for describing $O_2^{\bullet -}$ nonbonded interaction with the protein, taken from the generic GAFF2 force-field, were found through interaction energy calculations to likely underestimate the binding energy with arginine residues, its preferred interaction partner. A similar conclusion was reached for the Cl^- ion. This latter species appears to concentrate in the crypt area of the protein, which was found to be extremely electrostatically welcoming to both these ions. While it is difficult to conclude due to the uncertainties on the quality of the force-field for nonbonded interactions, the much lower rate of binding and the reduced preference for arginine residues shown by Cl^- suggests no competition for populating binding sites should be expected between $O_2^{\bullet -}$ and Cl^-. As for $O_2^{\bullet -}$, the probable

underestimation of its electrostatic binding capabilities, suggested in the $\simeq 20\,\%$ underestimation of MM interactions compared to E_{int}^{QM}, allow us to expect the actual binding to therefore be stronger than observed here.

The discrepancy between QM- and MM-computed interaction energies is a first point on which we believe this research should be the starting point for more in-depth investigations. A first avenue of research could be the derivation of force-field parameters for $O_2^{\bullet -}$, in particular to reproduce its nonbonded interactions with aminoacids. This could allow us to first, validate the binding patterns identified in this study, as well as obtain definitive binding times and rotational correlation times; and second, to accurately compare $O_2^{\bullet -}$ and Cl^- binding rates and areas, in order to conclude on the issue of competition for the binding sites. Another option would be the use of multipolar and polarisable FF, such as AMOEBA.[228]

We also investigated the binding capabilities of a proposed formation site for $O_2^{\bullet -}$,[2] a cavity situated right next to the flavin from which a diffusing triplet oxygen could reoxidise FADH−, creating the $FADH^{\bullet}/O_2^{\bullet -}/Y^{\bullet}$ radical triad which is the focus of this thesis. Extremely long binding times and rotational correlation times arose from this configuration, and we could estimate a spin relaxation for $O_2^{\bullet -}$ trapped in the cavity. Such binding geometries, although subject to strong EED coupling, are potentially still significantly magnetosensitive in the context of scavenging;[27] but they would likely completely extinguish MFEs in a $FADH^{\bullet}/O_2^{\bullet -}$ radical pair. However, our large-scale MD study revealed no $O_2^{\bullet -}$ ever entering or exiting this cavity, possibly pointing to a different formation site for $O_2^{\bullet -}$.

We then examined the diffusion dynamics of a $O_2^{\bullet -}$ radical exiting another putative formation site, also extremely close to the flavin. In particular, we monitored its subsequent trapping by 5 identified binding sites, all located within roughly 20 Å of the flavin to permit efficient recombination, and thereby allow the operation of a 3-radical compass scavenged by a third residue. Interestingly, we found the binding times into the sites to be significantly different to those obtained from the FD-SUP dataset (a set of 10 500-ns simulations including 21 $O_2^{\bullet -}$ radicals, diffusing from the bulk), for sites 1, 3 and 5 in particular. While this discrepancy could be due to study design for site 3, we tentatively proposed phenomena such as angle of approach and ion desolvation to explain this effect. In any case, the quite different population rates of binding sites when $O_2^{\bullet -}$ is diffusing away from the flavin as opposed to coming from the bulk, should be the focus of more in-depth investigations. The former modality being probably more relevant to the avian compass case, we would gain from understanding why, and whether it really is the case that, site 5 binds so much better oncoming $O_2^{\bullet -}$ than was observed on the possibly better statistically resolved FD-SUP dataset.

The quality of the immobilisation realised in each site was probed by another

MD study, by placing a $O_2^{\bullet -}$ radical in a frame and monitoring its binding time and rotational correlation time. We recorded rotational correlation times up to nearly 10^5 times its value in solution. Besides this extreme result, factors of 10^4 were routinely achieved by several of these sites. However, we also noted a visibly great sensitivity of the binding rates and lengths on the initial configuration. This is also a point that would deserve an extension to this study, or a different study altogether: how to obtain statistically reliable estimates of average τ_2 and t_b per site. The current study only identified proofs of concept, without concluding on the prevalence of long or short binding events.

We then estimated spin relaxation rates associated with the largest τ_2 values recorded, and found that sustained coherence lifetimes approaching the microsecond timescales were possible, with the $10^2\,\mu$s timescale readily attained by 3 sites in particular. At the larger interactions distances, and therefore reduced EED coupling, afforded by the binding sites, non-negligible MFEs might be realisable for a $FADH^{\bullet}/O_2^{\bullet -}$ radical pair – a proposition that demands further investigation. Regarding the $FADH^{\bullet}/O_2^{\bullet -}/Y^{\bullet}$ triad, a spin dynamics study involving a non-relaxing $O_2^{\bullet -}$ radical placed in these binding sites revealed a relative insensitivity of the triad to $O_2^{\bullet -}$ relaxation; even with non-averaged, relatively short-range EED couplings. In particular, Y319 registered similar Γ_B values to the fast-relaxing case. Its broad range of operating conditions could be the key to magnetosensitivity arising from an inhomogeneous ensemble of *cl*Cry4 proteins.

Finally, we found that the proportion of double H-bonding of a $O_2^{\bullet -}$ radical when bound by a site is a fairly good predictor of the length of the binding event, but not of the associated rotational correlation time. This observation, with the point on different $O_2^{\bullet -}$ "sticking rate" whether coming from the crypt or from the bulk raised in a previous paragraph, suggest the mechanics of binding into a site to be a quite complex phenomenon, to which more research should be devoted.

All in all, we hope our research has provided new elements regarding the localisation and relaxation rate of $O_2^{\bullet -}$ and helped to clarify its role in the avian compass. In another domain, this notion of electrostatic trapping of ROS to mitigate its toxicity to the rest of the cell environment is one that we found very scarcely researched computationally, and hope that this chapter can kindle some research interest on the subject.

CHAPTER 5

GENERAL CONCLUSION

Magnetosensitivity, the remarkable trait exhibited by birds allowing them to orient using the geomagnetic field, is a well-documented but still poorly understood phenomenon. Thought to arise from truly quantum processes, namely the sustained coherence of the spin dynamics of a radical pair or triad, the actual mechanism is still the subject of debates. In this thesis, I investigate the magnetosensitivity arising from a radical triad, formed in the reoxidation reaction of a flavin within the cryptochrome protein. In particular, I consider the $FADH^{\bullet}/O_2^{\bullet -}/Y^{\bullet}$ radical system, where $Y^{\bullet}$ acts as a scavenger on the primary radical pair $FADH^{\bullet}/O_2^{\bullet -}$. The performance of a magnetic compass operated by these radicals, quantified by the singlet yield anisotropy Γ_S, is evaluated using spin dynamics simulations. To generate realistic estimates, the various processes determining the evolution of a radical system – *i.e.* the spin dynamics of the radicals, their reactivity and spin relaxation – must be parametrised to accurately reflect the conditions within an avian cryptochrome protein.

I began my investigation with an assessment of the magnetosensitivity expected from a $FADH^{\bullet}/O_2^{\bullet -}/Y^{\bullet}$ radical triad in a pigeon Cryptochrome 4, *cl*Cry4, using spin dynamics simulations. All 18 tyrosine residues present in the *cl*Cry4 proteins were investigated. The inclusion of inter-radical interactions and the use of radical positions and orientations taken from an avian cryptochrome, as opposed to a plant or fruit fly cryptochrome, is the main novelty of this research. Inter-radical distances and relative orientations determine the strength of electron-electron dipolar (EED) coupling, an oft-neglected physical effect which was found here to strongly reduce the magnetosensitivity of a radical triad. Informed by the very fast spin relaxation rate estimated for a $O_2^{\bullet -}$ radical near the protein, I worked in the limit of fast spin relaxation for $O_2^{\bullet -}$, which effectively reduced the spin dynamics of the

triad to that of a radical pair with altered lifetime. Within these conditions, I found that most $Y^{\bullet}$ residues could achieve magnetic field effects (MFEs) exceeding those expected from a realistic $FAD^{\bullet -}/W^{\bullet +}$ radical pair, for scavenging rates of the order of $k_X \simeq 10^7\ s^{-1}$ or faster. However, large MFEs were shown to correlate with large $FADH^{\bullet}$-$Y^{\bullet}$ separation distances, which might prevent fast scavenging *via* electron transfer to occur in most cases. Y319, on the other hand, was found to achieve rather large MFEs ($\Gamma_S = 0.85$, for a radical lifetime of $k_f^{-1} = 10\,\mu s$ and with EED coupling included) at a scavenging rate plausibly realisable in the *cl*Cry4 structure. This is the most significant finding of this study. Additional mechanistic justification was provided for the involvement of Y319 in cryptochrome magnetoreception. Finally, other potentially magnetosensitive systems were investigated. It was found that a $FADH^{\bullet}/O_2^{\bullet -}$ radical pair, involving a free-diffusing $O_2^{\bullet -}$, could not produce any MFEs due to fast spin relaxation. On the other hand, a $FADH^{\bullet}/O_2^{\bullet -}/Asc^{\bullet -}$ triad, where ascorbyl acts as a scavenger, proved considerably magnetosensitive.

This study was the first to employ radical positions and orientations taken from an actual avian cryptochrome structure. Given the considerable impact of EED interactions outlined here, this is a requirement for modeling the spin dynamics correctly. The research presented in Chapter 2 was published in the Journal of Physical Chemistry, and is available at Ref. 37.

In an effort to generate quantitative data on the magnetosensitivity of flavin-containing radical systems, I calculated hyperfine coupling (HFC) tensors computed on biologically relevant geometries of the flavin and of its immediate environment. The aim of this research was to include in the description of the flavin hyperfine structure dynamical effects to better reproduce the “warm, wet and noisy” protein environment. At the time of writing, other available tensors for the flavin did not include the environment in a satisfactory manner, and especially did not take into account flavin structural fluctuations over long timescales, which were found to be the factor inducing the largest changes to its hyperfine structure. It could also be verified that other perturbing factors, such as hydrogen-bonding to the flavin as identified in *A. niger* glucose oxidase, were not present in *cl*Cry4. In this study, structural dynamics were accounted for by sampling molecular dynamics trajectories of 800 ns, *i.e.* a time span approaching the lifetime of radical pairs implicated with magnetoreception. Environment effects were included by a cluster approach, whereby a sensitivity analysis was used to elect the residues contributing to the cluster. This cluster, which models the environment at a quantum level, was also enriched with point charges to include electrostatic interactions with the rest of the protein. This cluster could be re-used for the computation of other electronic properties of the flavin in *cl*Cry4. The main contributions of this work are the derivation of

an updated set of HFC tensors for both potentially magnetosensitive states of the flavin, $FADH^{\bullet}$ and $FAD^{\bullet -}$. The distribution of tensor elements along the dynamics are also reported. These can be used to parametrise a spin Hamiltonian, and also allow to model the inhomogeneity of hyperfine parameters expected to prevail in a biological sample. A notable result is the surprising insulation of the flavin from its chemical environment, with the majority of the variability in HFC tensor values arising from its structural distortions due to thermal motion.

The study presented in Chapter 3 also resulted in a publication, in the PCCP journal (Ref. 38). In the absence of EED coupling, as would arise *e.g.* in a radical pair involving a free-diffusing radical, HFC interactions determine the baseline spin dynamics that the geomagnetic field can then perturb. Including EED interaction, HFC- and EED-driven interconversion couple to give rise to significantly different spin dynamics. I therefore consider that the accurate description of the flavin hyperfine structure proposed here is key to correctly model a radical pair or triad, and hope that it can inform further investigation into the mechanism of cryptochrome-based avian magnetoreception.

In a main effort, I explored the possibility that *cl*Cry4 might trap $O_2^{\bullet -}$ radicals at its surface, inhibiting the fast tumbling that brings about fast spin relaxation. The phenomenon of $O_2^{\bullet -}$ binding has only previously been considered for a tightly bound $FADH^{\bullet}/O_2^{\bullet -}$ pair in *Dm*Cry, *i.e.* a non-avian protein, which cannot elicit magnetosensitivity due to strong EED coupling; and this investigation did not look into the consequence for $O_2^{\bullet -}$ relaxation times and for the performance of 3-radical compass.[2] The main results from this chapter are the locations of 5 $O_2^{\bullet -}$ binding sites, close enough to the flavin for spin-selective recombination to proceed efficiently, with a range of associated binding times (t_b) and rotational correlation times (τ_2). These were identified from multiple long-time MD studies, where $O_2^{\bullet -}$ radicals were allowed to diffuse from the bulk, from a putative formation site near the flavin, or placed inside the binding sites. Associated spin relaxation times (γ_B) were also computed for the largest τ_2, providing preliminary values for the longest spin coherence lifetimes achievable by a site-bound $O_2^{\bullet -}$. Moderately long ($10^2 - 10^3$ ns) γ_B-values were estimated, particularly three sites (labeled 1, 2 and 3 in the main study). Unfortunately, the current study did not allow to compute statistically reliable estimates of average τ_2 and t_b per site. This range of spin relaxation rates might allow a $FADH^{\bullet}/O_2^{\bullet -}$ radical pair to exhibit magnetosensitivity, although immobilisation of $O_2^{\bullet -}$ would give rise to deleterious non-averaged EED coupling. I also investigated the latter's impact on the performance of a scavenged, 3-radical system. I report Γ_S values for $FADH^{\bullet}/O_2^{\bullet -}/Y^{\bullet}$ triads in the limit of slow $O_2^{\bullet -}$ relaxation, as a limit case, where $O_2^{\bullet -}$ is located in the binding sites. A more complete $FADH^{\bullet}$ hyperfine structure (computed

in Chapter 3) was employed. Y319 in particular was found to be roughly insensitive to coherent $O_2^{\bullet-}$ location, achieving Γ_S between 7.8×10^{-3} and 10.4×10^{-3} across sites. These values are close to those obtained with a fast-relaxing, free-diffusing $O_2^{\bullet-}$.

As a quick recap of the work carried out in this thesis: I identified one tyrosine residue, in an avian cryptochrome protein, able to function as a scavenger in a $FADH^{\bullet}/O_2^{\bullet-}/Y^{\bullet}$ radical triad. After an effort to parametrise our spin dynamics model, by computing quantities able to better represent the hyperfine structure and electron-electron dipolar couplings, which together govern the baseline spin dynamics of a radical pair or triad, I verified its ability to elicit magnetosensitivity in a more realistic environment. Particularly promising is its ability to deliver significant MFEs across a broad ranges of conditions, with or without $O_2^{\bullet-}$ relaxation; this robustness could play a role in delivering a strong, consistent compass reading from an inhomogeneous ensemble of cryptochrome proteins.

Further developments of the work presented here could be an MD study using a polarisable force-field for superoxide, in order to conclude on its binding and rotational correlation times in the sites identified here. The computation of $O_2^{\bullet-}$ g-tensors within these sites would also allow to conclude on its spin relaxation time when bound to the protein. We also suggest, in the closing of Chapter 2, an experiment to explore the possible involvement of a theoretically promising ascorbyl radical, and to verify the existence of long-lived tyrosine radicals in the protein, identified here as efficient scavengers.

APPENDIX A

APPENDIX A

This appendix contains the Supporting Information of the article (DOI: 10.1063/5.0078115) provided in Chapter 2. Tables A.2 and A.3 contain parameters specifying the relative orientation of tyrosine (in *cl*Cry4 and *Dm*Cry, respectively) and flavin residues, with respect to an internally defined frame of reference. Table A.4 lists the $FADH^{\bullet}$ and $Y^{\bullet}$ hyperfine coupling tensors employed in the spin dynamics simulations. Figure A.2 provides the absolute anisotropy, given as a function of scavenging rate, for a $[FADH^{\bullet}/O_2^{\bullet-}/Y^{\bullet}]$ triad with relaxed $O_2^{\bullet-}$ and where the tyrosine is either *cl*Cry4 Y319, or its analogue in *Dm*Cry and textcolorErCry4. Figure A.3 gives a broad view of magnetic fields effects from a *Dm*Cry $[FADH^{\bullet}/O_2^{\bullet-}/Y319]$ triad with relaxed $O_2^{\bullet-}$, in the case where electron recombination in the primary radical pair is impossible, for $k_f^{-1} = 1\,\mu s$. Figure A.4 reports the corresponding data for $k_f^{-1} = 10\,\mu s$. Finally, Figure A.5 gives the relative yield anisotropies for all *Dm*Cry $[FADH^{\bullet}/O_2^{\bullet-}/Y^{\bullet}]$ triads with relaxed $O_2^{\bullet-}$.

A.1 Supporting Informations:

A.1.1 *Cl*Cry4 tyrosine radicals' locations

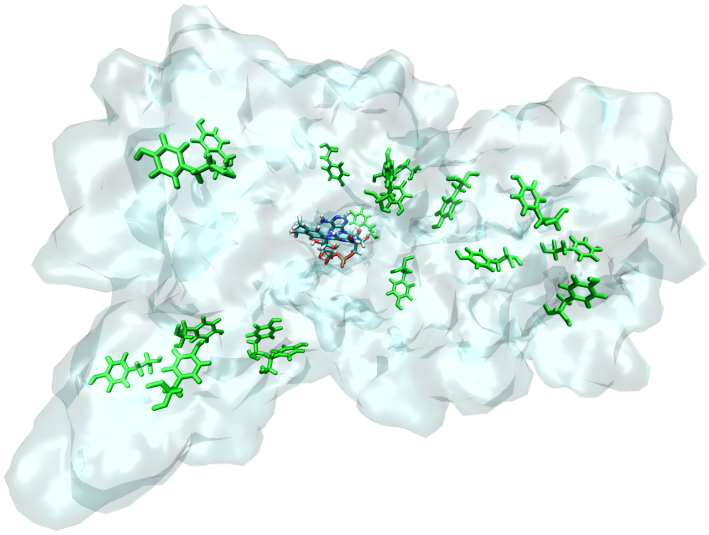

Figure A.1: Graphical representation of the relative positions of the semiquinone flavin $FADH^{\bullet}$ (in colour, center) and tyrosine radicals $Y^{\bullet}$ (in green) within the crystal structure of *Cl*Cry4 (in transparent blue).

A.1.2 Spin dynamics simulation parameters

Atomic coord.		Crystal structure (PDB ID: 6PU0)
Hamiltonian	Zeeman	Yes ($B_0 = 50\,\mu$T)
	EED	Yes (point-dipole approx.)
	Exchange	No
	Hyperfine	Yes (see Table A.4)
Rates	k_f^{-1}	1 and 10 μs
	k_s	0 μs^{-1}
	k_x	Variable: 10^{-5} to 10^{2} ns^{-1}

Table A.1: Simulation parameters for the spin dynamics results presented in the main text, Chapter 2, Figure 2.5.

A.1.3 FADH$^\bullet$ and Y$^\bullet$ relative orientations

Residue	α (°)	β (°)	γ (°)	x (Å)	y (Å)	z (Å)	d (Å)
Y32	177.2	77.9	108.6	-1.96	20.96	33.29	39.4
Y35	359.7	36.6	81.9	-4.44	13.03	13.55	19.3
Y81	131.0	85.9	258.4	5.44	22.39	11.87	25.9
Y107	276.2	94.3	147.4	0.78	11.46	10.96	15.9
Y134	349.8	61.6	169.0	15.52	-8.62	13.61	22.4
Y151	265.1	151.3	139.9	11.15	-10.90	5.02	16.4
Y190	134.0	124.3	121.5	-7.39	23.89	26.01	36.1
Y252	272.3	84.0	121.9	-10.06	-2.78	13.11	16.8
Y271	44.6	82.1	117.1	12.18	-22.15	14.72	29.2
Y295	304.3	92.5	308.7	5.04	3.14	8.98	10.8
Y319	175.2	57.8	298.4	1.35	4.94	-24.71	25.2
Y388	119.9	102.0	194.3	9.22	10.21	2.04	13.9
Y407	145.1	116.3	248.8	12.33	-6.25	-21.61	25.7
Y426	73.7	42.4	254.3	-12.40	-6.55	-4.30	14.7
Y430	55.6	165.7	292.5	-16.63	-6.40	-0.22	17.8
Y441	205.8	82.0	275.2	-22.47	-15.04	-25.10	36.9
Y443	173.4	131.4	51.0	-13.57	-13.79	-11.07	22.3
Y464	86.9	119.1	279.9	-16.32	-3.42	-15.35	22.7

Table A.2: Parameters specifying the relative orientation of the tyrosine and FAD residues in *Cl*Cry4 (PDB ID: 6PU0). α, β and γ are the Euler angles relating the FAD molecular frame to the Y frame; x, y, and z give the position of the Y-residues relative to the FAD (assessed in terms of the N5 and OH atoms, respectively) in the protein frame of reference. d denotes the distance of the radicals.

Residue	α (°)	β (°)	γ (°)	x (Å)	y (Å)	z (Å)	d (Å)
Y54	263.1	135.9	159.4	-1.89	-21.47	-7.32	22.8
Y90	331.2	64.0	342.2	8.12	-30.85	20.02	37.7
Y158	286.0	144.9	161.3	10.37	11.37	-1.43	15.5
Y211	173.2	129.1	139.6	-7.66	-26.74	0.48	27.8
Y250	126.6	25.4	187.5	12.12	7.52	-14.90	20.6
Y281	103.7	133.8	250.0	20.08	9.09	-1.50	22.1
Y317	169.0	87.4	255.6	3.88	11.22	6.23	13.4
Y319	239.0	99.3	154.1	8.33	-3.46	4.72	10.2
Y328	190.4	77.9	348.9	2.87	5.12	9.01	10.8
Y407	341.4	59.4	21.3	-10.14	-12.46	-0.23	16.1
Y453	93.4	137.3	71.3	-7.73	-1.96	-12.55	14.9
Y457	49.5	173.7	291.3	-5.37	-6.98	-15.38	17.7
Y483	344.2	129.8	142.5	-24.90	1.44	-29.04	38.3
Y491	85.3	122.2	290.3	-19.37	-0.58	-12.37	23.0

Table A.3: Parameters specifying the relative orientation of the tyrosine and FAD residues in *Dm*Cry (PDB ID: 4GU5). See the caption of Table S1 for detail.

A.1.4 FADH$^\bullet$ and Y$^\bullet$ HFC tensors

FADH$^\bullet$		Y$^\bullet$	
$\mathrm{N5} = \begin{pmatrix} -2.41 & -0.07 & -0.97 \\ -0.07 & -2.45 & 0.05 \\ -0.97 & 0.05 & 43.51 \end{pmatrix}$		$\mathrm{Ho1} = \begin{pmatrix} -25.96 & -7.79 & -0.04 \\ -7.79 & -11.84 & 0.02 \\ -0.04 & 0.02 & -21.77 \end{pmatrix}$	
$\mathrm{H5} = \begin{pmatrix} -2.39 & 1.87 & 0.51 \\ 1.87 & -40.64 & 0.03 \\ 0.51 & 0.03 & -27.86 \end{pmatrix}$		$\mathrm{Ho2} = \begin{pmatrix} -23.79 & 6.91 & -0.03 \\ 6.91 & -10.54 & -0.07 \\ -0.03 & -0.07 & -20.12 \end{pmatrix}$	
$\mathrm{N10} = \begin{pmatrix} 0.44 & 0.06 & 1.80 \\ 0.06 & -0.01 & -0.34 \\ 1.80 & -0.34 & 23.15 \end{pmatrix}$		$\mathrm{H}\beta 2 = \begin{pmatrix} 33.91 & -1.81 & 1.36 \\ -1.81 & 30.65 & -0.92 \\ 1.36 & -0.92 & 30.00 \end{pmatrix}$	
$\mathrm{H6} = \begin{pmatrix} -2.25 & -1.74 & 0.09 \\ -1.74 & -4.74 & -0.08 \\ 0.09 & -0.08 & -6.07 \end{pmatrix}$			
$\mathrm{H}\beta 1 = \begin{pmatrix} 10.34 & -0.86 & -1.24 \\ -0.86 & 7.56 & 0.37 \\ -1.24 & 0.37 & 6.91 \end{pmatrix}$			

Table A.4: Hyperfine interaction tensors of FADH$^\bullet$ and Y$^\bullet$ in their respective molecular frame.

A.1.5 FADH$^{\bullet}$/$O_2^{\bullet-}$/Y319 MFEs:

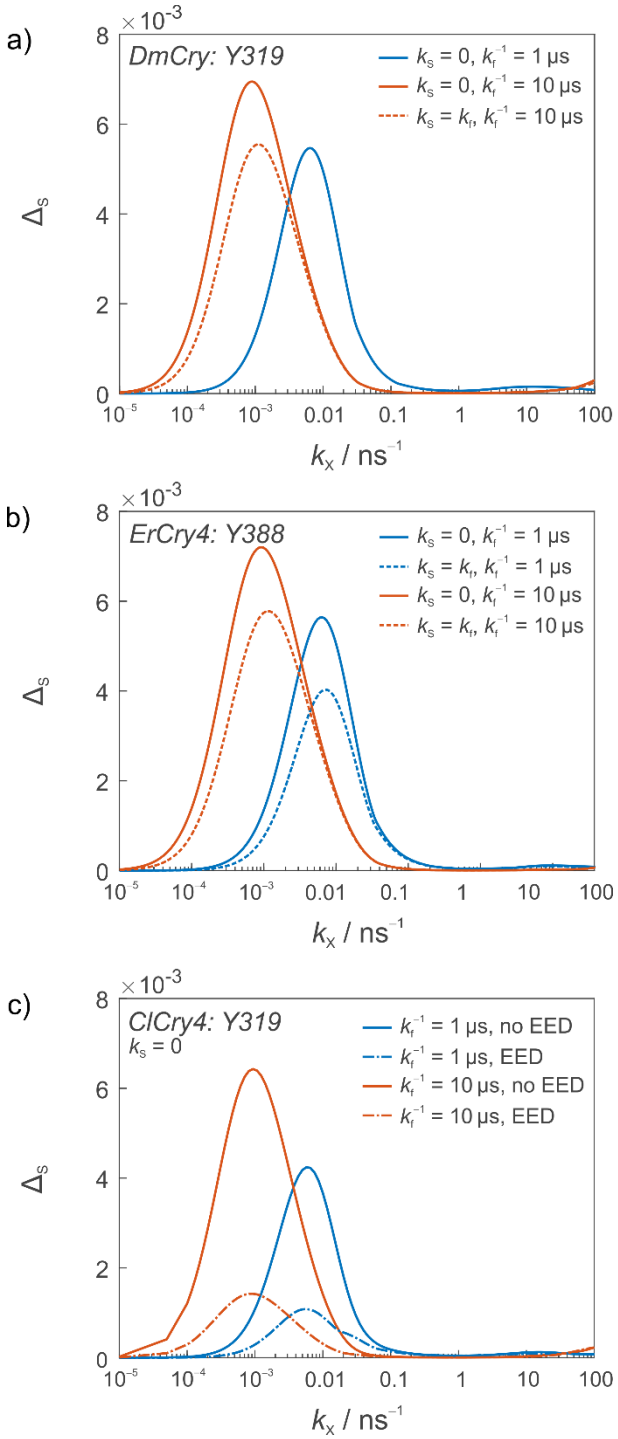

Figure A.2: Absolute anisotropy, *i.e.* the maximal difference of the yields of the signalling for different orientations of the magnetic field, evaluated for models of FADH$^{\bullet}$/$O_2^{\bullet-}$/Y$^{\bullet}$ in the limit of infinitely fast spin relaxation in $O_2^{\bullet-}$ presented as a function of the scavenging rate constants k_X . The scavenger radical Y$^{\bullet}$ has been identified with a) Y319 in *Dm*Cry, b) Y388 in *Er*Cry4, and c) Y319 in *Cl*Cry4. k_S and k_f are specified in the legends; $k_T = 0$. Additional details are as for Figure 2.4 in the main document, which reports the related dependence of Γ_S on k_X.

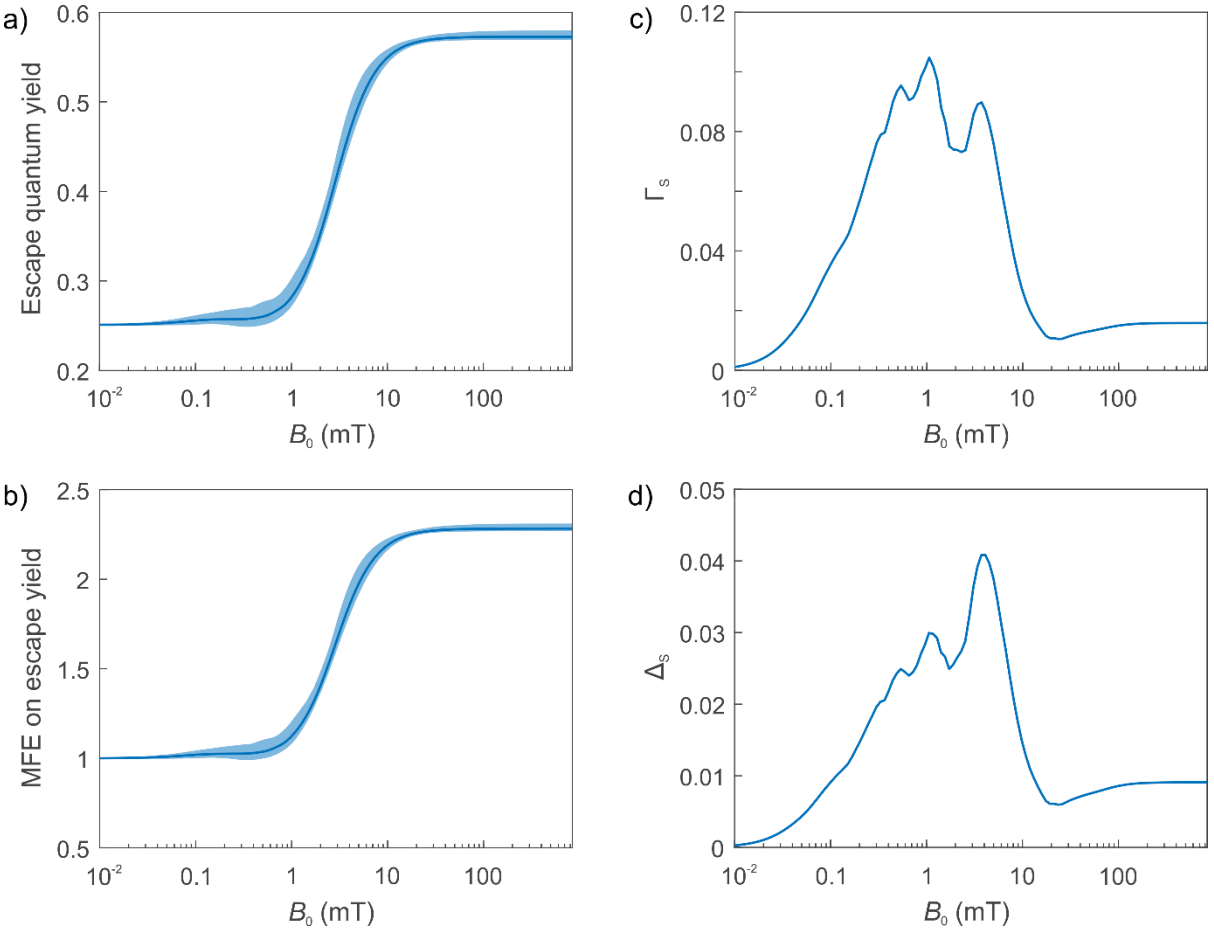

Figure A.3: Magnetic field effects in the $FADH^{\bullet}/O_2^{\bullet-}/Y319^{\bullet}$ radical triad in *Dm*Cry for $k_S = k_T = 0$, $k_f^{-1} = 1\,\mu$s, and instantaneous spin relaxation in the $O_2^{\bullet-}$ radical. The panels give a) the quantum yield of the "escape" product (*i.e.* the product of the k_f-reaction), b) the magnetic field effect, c) the relative anisotropy and d) the directional spread of this yield, all presented as a function of the intensity of the applied magnetic field, B_0. For a) and c) the shaded region illustrates the directional variability of the quantity under consideration; the solid line reports the orientational average.

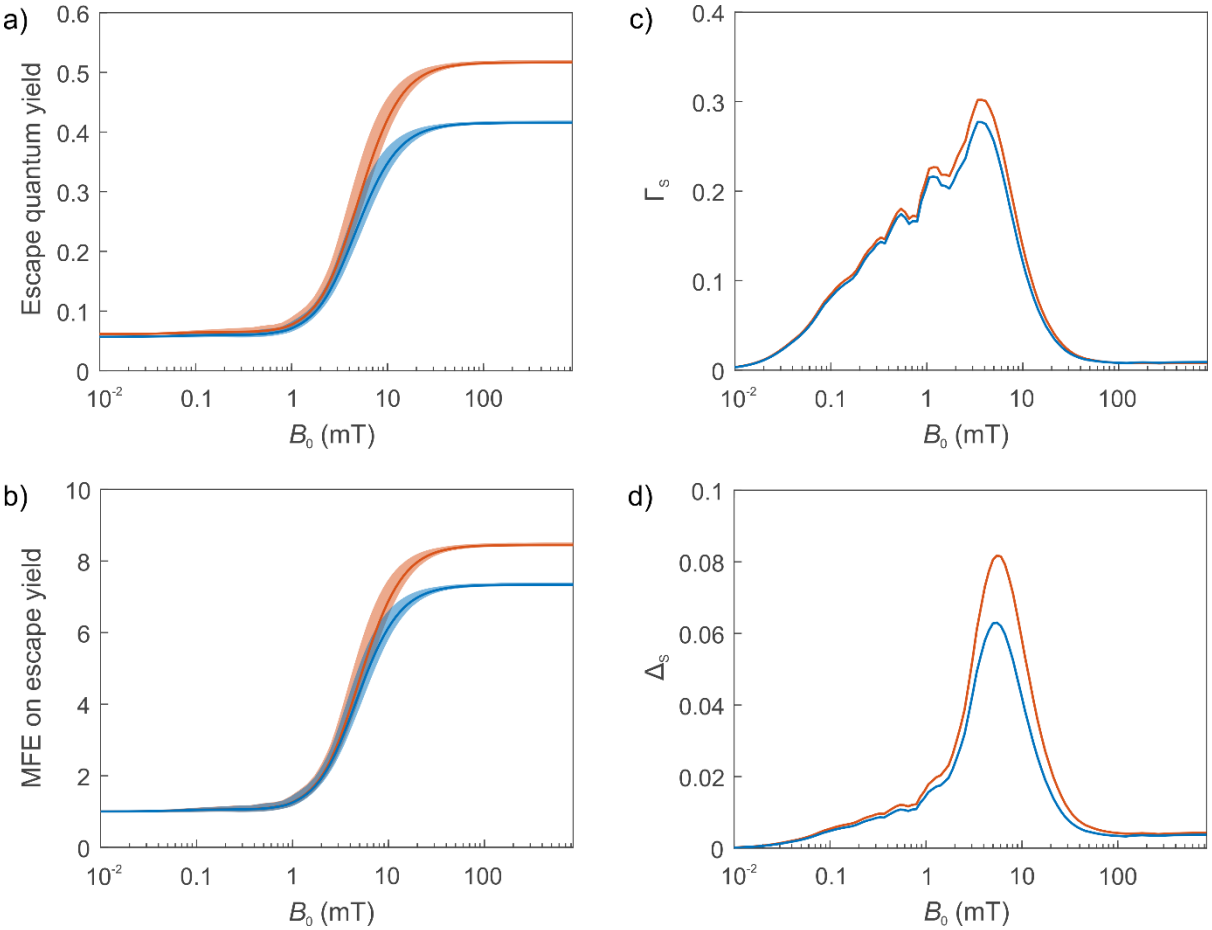

Figure A.4: Figure S3: Magnetic field effects in the $FADH^{\bullet}/O_2^{\bullet-}/Y319^{\bullet}$ radical triad in *Dm*Cry for $k_f^{-1} = 10\,\mu s$, $k_T = 0$, instantaneous spin relaxation in the $O_2^{\bullet-}$ radical and two rate constants of spin selective recombination of the singlet configuration of the $FADH^{\bullet}/O_2^{\bullet-}$-pair: $k_S = 0$ (red) and $k_S = k_f$ (blue). See the caption of Fig. A.3 for details.

A.1.6 *Dm*Cry FADH$^{\bullet}$/$O_2^{\bullet-}$/Y$^{\bullet}$

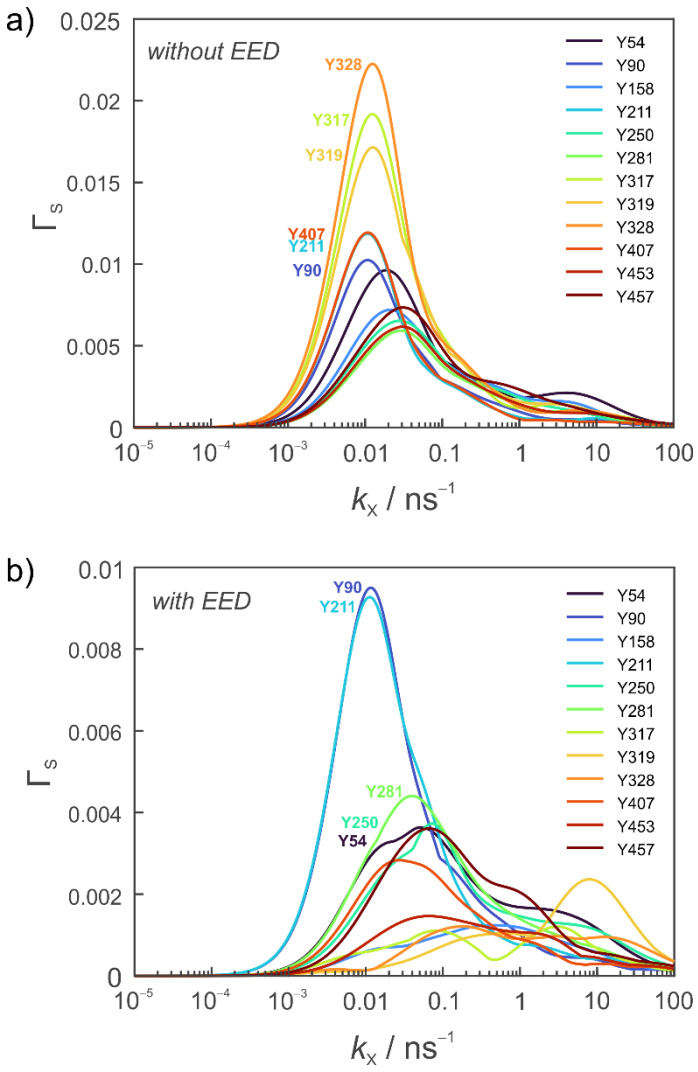

Figure A.5: Directional magnetic field effects of FADH$^{\bullet}$/$O_2^{\bullet-}$/Y$^{\bullet}$ radical triads from *Dm*Cry (PDB ID: 4GU5) for $k_f^{-1} = 1\,\mu$s without (a) and with (b) electron-electron dipolar (EED) interactions taken into account. The simulations have assumed infinitely fast spin relaxation in $O_2^{\bullet-}$, $k_S = k_T = 0$ and included the hyperfine interactions of N5, N10, H5, H6, Hβ1 in FADH$^{\bullet}$ and Ho1, Ho2, and Hβ2 in Y$^{\bullet}$. The identity of the tyrosine radical is reported in the legends.

APPENDIX B

APPENDIX B

This appendix contains the Supporting Informations of the article (DOI: 10.1039/d1cp05804e) provided in Chapter 3.

B.1 Supporting Information:

B.1.1 Experimental HFCs.

		A_{11}	A_{22}	A_{33}	$A_{\parallel}$	$A_{\perp}$	A_{iso}
			*Dm*Cry[81,146]				
$FAD^{\bullet -}$	N5	-	-	-	54.17	4.20	-
	N10	-	-	-	27.94	0.03	-
	H8α	-	-	-	-	-	12.39
$FADH^{\bullet}$	H8α	9.93	10.40	12.19	-	-	10.84
	H1'	-	-	-	-	-	-
	H5	-	-	-	-	-	-
			A. niger glucose oxidase[229]				
$FAD^{\bullet -}$	H8α	-	-	-	11.45	9.95	-
	N5	-	-	-	53.3	0.3	-
	N10	-	-	-	25.3	0.3	-
$FADH^{\bullet}$	H8α	-	-	-	8.45	6.85	-
	N5	-	-	-	53.5	0.5	-
	N10	-	-	-	30.5	0.5	-
	H5	-10.5	-33.91	-24.11	-	-	-
			X. laevis (6-4) photolyase[146,229]				
$FADH^{\bullet}$	H8α	-	-	-	8.13	6.50	-
	N5	-	-	-	51.2	0	-
	N10	-	-	-	27.2	0	-
	H5	-13.72	-38.41	-26.11	-	-	-
$FADH^{\bullet}$	H8α	6.24	6.59	8.04	-	-	6.96
	H1'	7.05	8.01	11.50	-	-	8.85
	H5	-	-25.90	-38.36	-	-	-

Table B.1: (Part 1 of 2) Experimental hyperfine couplings of flavin atoms, measured using EPR spectroscopy on various cryptochrome, glucose oxidase and photolyase proteins. All reported values are in MHz.

		A_{11}	A_{22}	A_{33}	$A_{\parallel}$	$A_{\perp}$	A_{iso}
E. coli DNA photolyase[229]							
$FADH^{\bullet}$	H8α	-	-	-	8.66	6.80	-
	N5	-	-	-	50.12	0	-
	N10	-	-	-	31.72	0	-
	H5	-8.50	-37.00	-24.90	-	-	-
C. reinhardtii Cryptochrome[81]							
$FAD^{\bullet-}$	N5	-	-	-	52.57	2.80	-
	N10	-	-	-	23.12	2.80	-
	H8α	-	-	-	-	-	10.65
A. thaliana Cryptochrome 1[146]							
$FADH^{\bullet}$	H8α	6.85	7.90	9.00	-	-	7.91
	H1'	8.99	8.99	11.49	-	-	9.82
	H5	-	-25.00	-37.02	-	-	-
Synechocystis Cryptochrome[146]							
$FADH^{\bullet}$	H8α	6.41	7.01	8.26	-	-	7.23
	H1'	7.84	8.55	11.39	-	-	9.26
	H5	-	-25.53	-38.36	-	-	-
T. thermophilus CPD photolyase[146]							
$FADH^{\bullet}$	H8α	6.61	6.99	8.47	-	-	7.36
	H1'	6.41	8.70	11.75	-	-	8.62
	H5	-	-25.30	-37.49	-	-	-
A. thaliana CPD photolyase[146]							
$FADH^{\bullet}$	H8α	6.54	7.21	8.40	-	-	7.38
	H1'	8.41	8.50	11.34	-	-	9.42
	H5	-	-24.60	-37.02	-	-	-

Table B.2: (Part 2 of 2) Experimental hyperfine couplings of flavin atoms, measured using EPR spectroscopy on various cryptochrome, glucose oxidase and photolyase proteins. All reported values are in MHz.

Tables B.1 and B.2 list experimentally available flavin ($FADH^{\bullet}$ and $FAD^{\bullet-}$) hyperfine coupling values, for comparison with those computationally obtained in Chapter 3. It should be noted that at the time of publishing, no experimental values exist for *cl*Cry4 (or any avian cryptochrome).

B.1.2 Validation of the MD simulations

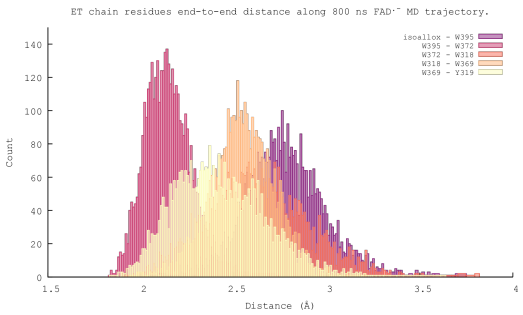

(a) $FAD^{\bullet -}$: ET chain inter-residues distances

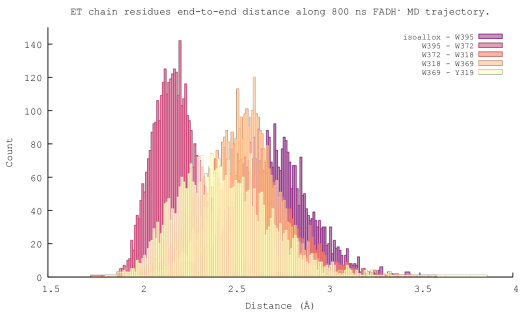

(b) $FADH^{\bullet}$: ET chain inter-residues distances

Figure B.1: Inter-residue distance of the electron-transfer chain (flavin, W395, W362, W318, W369, Y319), where the flavin is (a) $FAD^{\bullet -}$ and (b) $FADH^{\bullet}$.

B.1.3 Validation of the aDFT method.

Atom	Δa_{iso} (MHz)	$\Delta\Delta A$ (MHz)
N5	0.1516	0.1642
N10	0.0700	0.0490
H1'a	0.1260	0.0074
H1'b	0.0526	0.0042
H8α	0.0352	0.0094
H7α	0.0326	0.0078
H6	0.0270	0.0078
H5	0.2748	0.1014

(a) $FADH^{\bullet}$

Atom	Δa_{iso} (MHz)	$\Delta\Delta A$ (MHz)
N5	0.3188	0.1160
N10	0.1282	0.0774
H1'a	0.0708	0.0054
H1'b	0.0394	0.0028
H8α	0.1382	0.0092
H7α	0.0324	0.0034
H6	0.0904	0.0836

(b) $FAD^{\bullet -}$

Table B.3: Absolute difference between DFT and aDFT calculation on the same geometry, averaged over 5 **(a)** $FADH^{\bullet}$ and **(b)** $FAD^{\bullet -}$ structures.

B.1.4 DFT basis set benchmark.

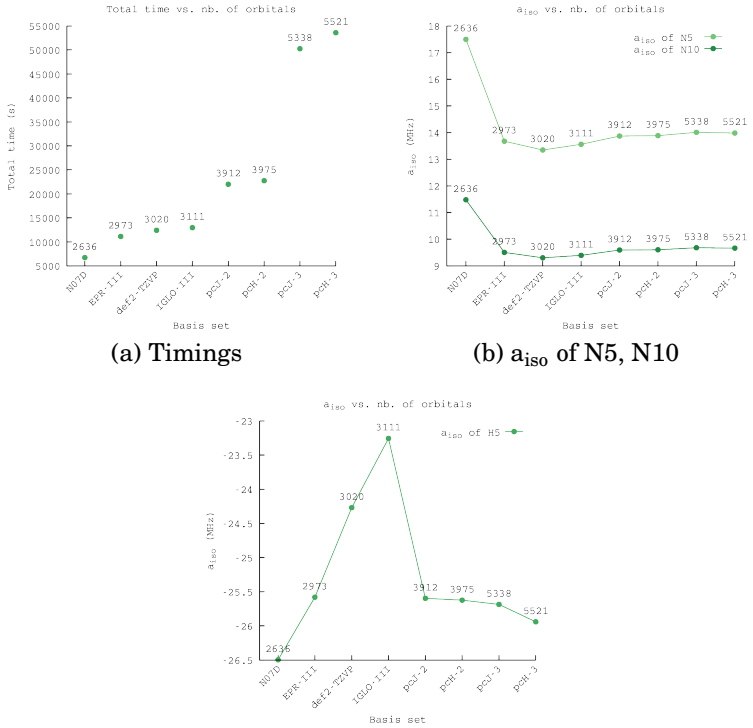

(a) Timings

(b) a_{iso} of N5, N10

(c) a_{iso} of H5

Figure B.2: **(a)** Timings and **(b,c)** a_{iso} benchmarks of various basis sets, using aDFT as implemented in deMon2k. All values calculated on an 295-atoms MD-generated conformation of FADH$^{\bullet}$ with a cluster of residues around. aDFT specs: B3LYP/basis/GEN-A2* for the flavin, B3LYP/DZVP-GGA/GEN-A2 on the neighbouring residues. The number of orbitals generated for the aDFT calculation are given above data points. Timings are for a single-point calculation parallelised onto 4 nodes (96 cores).

Residues included in the calculations: S250, R291, Y295, H353, R356, D385, D387, I390, N391, N394, W395, and FADH$^{\bullet}$ (FAH 498).

The basis sets tested here are listed in order of increasing completeness, N07D being the smallest one and pcH-3 the largest. Given that pcH-N and pcJ-N basis sets converge exponentially to the complete basis set limit, we take the a_{iso} calculated with pcH-3 to be the most accurate, and can visually estimate an extrapolation to the CBS. For the three atoms considered here, EPR-III emerged as the best compromise of computational lightness and accuracy.

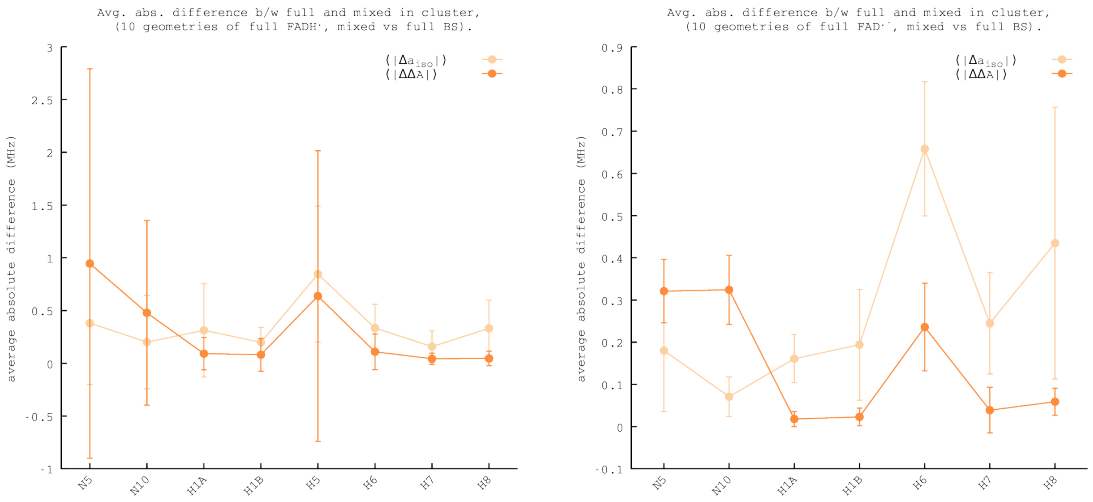

(a) FADH• (b) FAD•⁻

Figure B.3: Mean Absolute Error and standard deviations for a_{iso} and ΔA, calculated between a full and mixed basis set, on a set of 10 MD-generated geometries of (a) FADH• and (b) FAD•⁻ in their explicit cluster of residues. Magnetic properties were calculated using aDFT at the B3LYP/basis/aux-basis level, with the DZVP-GGA/GEN-A2 basis sets on the chemical environment of the flavin. For the "full basis" set, EPR-III/GEN-A2* was applied on all flavin atoms; and for "mixed basis", EPR-III/GEN-A2* was applied only on magnetically active flavin atoms (those listed in Figure B.3) and DZVP-GGA/GEN-A2 on the rest.

$\langle|\Delta a_{iso}|\rangle = \frac{\sum_{i=1}^{N=10}\left|a_{iso,i}^{mixed} - a_{iso,i}^{full}\right|}{N}$, and similarly for $\langle|\Delta\Delta A|\rangle$. Both are in MHz. Using a mixed basis set speeds up the calculation by a factor of 1.9, on average.

B.1.5 Validation of the minimal cluster.

Atom	minimal cluster		full cluster		$\Delta a = a^{full} - a^{minimal}$	
	a_{iso} (MHz)	ΔA (MHz)	a_{iso} (MHz)	ΔA (MHz)	Δa_{iso} (MHz)	ΔΔA (MHz)
H5	-24.920	35.261	-24.768	35.069	-0.152	-0.192
N5	14.161	48.680	14.062	48.395	-0.099	-0.285
N10	7.586	21.240	7.426	20.796	-0.160	-0.444
H1'a	7.407	3.679	7.299	3.630	-0.108	-0.049
H1'b	6.490	4.317	6.386	4.256	-0.104	-0.063
H8α	6.691	1.530	6.592	1.517	-0.099	-0.013
H7α	-0.665	1.222	-0.786	1.209	-0.121	-0.013
H6	1.589	3.434	1.579	3.404	-0.010	-0.030

Table B.4: Comparison between HFC tensors on FADH• in full and minimal cluster.

Atom	minimal cluster		full cluster		$\Delta a = a^{\text{full}} - a^{\text{minimal}}$	
	a_{iso} (MHz)	ΔA (MHz)	a_{iso} (MHz)	ΔA (MHz)	Δa_{iso} (MHz)	ΔΔA (MHz)
N5	17.437	60.257	17.474	60.473	0.037	0.216
N10	5.827	18.187	5.739	18.003	-0.088	-0.184
H1'a	5.228	3.451	5.173	3.415	-0.055	-0.036
H1'b	3.492	3.869	3.452	3.837	-0.040	-0.032
H8α	8.978	2.371	8.993	2.379	0.015	0.008
H7α	-3.081	1.554	-3.093	1.556	-0.012	0.002
H6	-7.968	5.830	-7.992	5.849	-0.024	0.019

Table B.5: Comparison between HFC tensors on $FAD^{\bullet-}$ in full and minimal cluster.

Δa_{iso} and ΔΔA are reported in Table B.4 for $FADH^{\bullet}$ and in Table B.5 for $FAD^{\bullet-}$. They are small in magnitude and typically do not represent more than 2% of the corresponding quantity. The exception is the case of H7α on $FADH^{\bullet}$, whose very small a_{iso} value makes the relative error comparatively large. However, such a small tensor has a correspondingly minuscule impact on the spin dynamics of a magnetosensor, and so increasing the cluster size for this tensor would yield only very marginal accuracy gains.

B.1.6 Distribution of spin density in the "minimal cluster" model.

Frame index	% of spin charge delocalised onto cluster atoms	
	$FAD^{\bullet-}$	$FADH^{\bullet}$
1	1.02	0.65
2	1.39	15.01
3	0.69	0.95
4	0.66	0.73
5	0.81	9.56
6	0.95	0.69
7	1.00	1.07
8	0.74	0.54
9	0.90	0.38
10	1.04	0.92

Table B.6: Percentage of the total spin charge ($S = 1$ for both $FAD^{\bullet-}$ and $FADH^{\bullet}$) localised on non-flavin atoms. The Löwdin atomic spin charges were calculated using aDFT at the B3LYP/EPR-III/GEN-A2* level for magnetically active isoalloxazine atoms and B3LYP/DZVP-GGA/GEN-A2 for the rest, on 10 geometries of the flavin cofactor in its minimal cluster, as defined in the main text, extracted from a 800 ns MD trajectory at 80 ns interval.

B.1.7 Autocorrelation times of a_{iso} and ΔA from $FAD^{\bullet -}$ and $FADH^{\bullet}$ atoms.

atom	a_{iso} (MHz)		ΔA (MHz)	
	N_{eff}	τ (ps)	N_{eff}	τ (ps)
N5	101.0	20.0	101.0	20.0
N10	83.7	24.1	44.6	45.3
H1'b	101.0	20.0	101.0	20.0
H1'a	101.0	20.0	101.0	20.0
H5	101.0	20.0	142.4	14.2
H6	101.0	20.0	58.8	34.4
H7α	66.0	30.6	45.8	44.1
H8α	101.0	20.0	101.0	20.0

(a) $FADH^{\bullet}$ in cluster - $N = 101$, $\Delta t = 20$ ps.

atom	a_{iso} (MHz)		ΔA (MHz)	
	N_{eff}	τ (ps)	N_{eff}	τ (ps)
N5	45.0	20.0	45.0	20.0
N10	8.3	108.3	45.0	20.0
H1'b	68.2	13.2	8.7	103.5
H1'a	45.0	20.0	45.0	20.0
H6	45.0	20.0	45.0	20.0
H7α	45.0	20.0	5.0	179.8
H8α	45.0	20.0	23.3	38.6

(b) $FAD^{\bullet -}$ in cluster - $N = 45$, $\Delta t = 20$ ps.

Table B.7: Autocorrelation times of a_{iso} and ΔA, calculated on relevant atoms of the (a) semiquinone and (b) radical anion flavin cofactor, in its minimal cluster as defined in the main text. The sample of structures on which these quantities were calculated are extracted from a MD trajectory, at an interval of $\Delta t = 20$ ps. N is the size of the sample; N_{eff} is the effective size of this sample, computed using the R function `coda::effectiveSize(x)`; $\tau = \Delta t \times \frac{N}{N_{eff}}$ is the autocorrelation time of the property considered.

B.1.8 RMSD of flavins' isoalloxazine heavy atoms along MD trajectories.

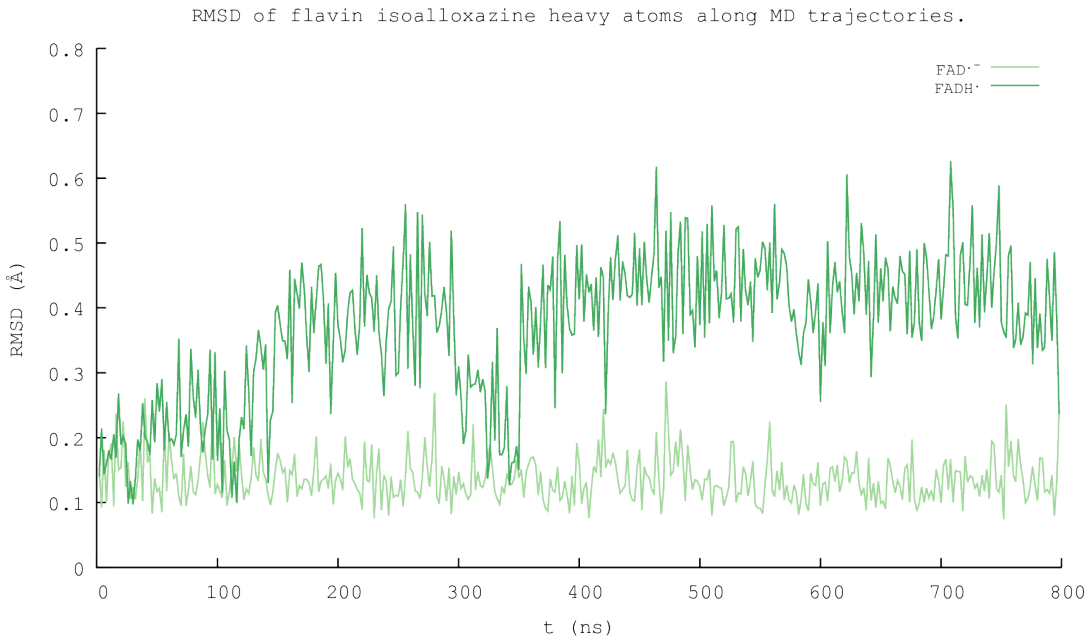

Figure B.4: Root-Mean-Square Deviation of the position of flavin atoms along the MD trajectories. For relevance and clarity, only the geometries on which magnetic properties were subsequently computed are included in this analysis. The time interval between two successive data points in therefore 2 ns.

B.1.9 The static picture: flavin optimised in vacuum.

atom	A_{YY}	A_{XX}	A_{ZZ}	a_{iso}	ΔA
N5	-2.655	-3.018	50.823	15.050	53.660
N10	-0.423	-0.690	18.861	5.916	19.418
H1'a	1.781	1.284	5.351	2.805	3.819
H1'b	5.519	5.021	9.136	6.559	3.866
H8α	11.516	11.356	14.305	12.392	2.869
H7α	-4.085	-4.433	-2.487	-3.668	1.773
H6	-11.751	-13.647	-4.976	-10.125	7.723

Table B.8: Principal elements, isotropic value and anisotropy of the HFC tensors, calculated on a single conformation of $FAD^{\bullet -}$ in vacuum using aDFT. The structure was obtained from a geometry optimisation at the PBEh-3c level, as implemented in Orca. All values are in MHz.

atom	A_{YY}	A_{XX}	A_{ZZ}	a_{iso}	ΔA
N5	-2.428	-2.793	41.182	11.987	43.793
N10	0.244	-0.154	21.537	7.209	21.492
H1'a	2.345	1.911	6.014	3.423	3.886
H1'b	6.555	5.670	10.043	7.423	3.930
H8α	6.924	6.754	8.749	7.476	1.910
H7α	-1.297	-1.542	-0.012	-0.950	1.407
H6	-6.114	-6.460	-1.691	-4.755	4.596
H5	-27.247	-39.191	-1.588	-22.675	31.631

Table B.9: Principal elements, isotropic value and anisotropy of the HFC tensors, calculated on a single conformation of $FADH^{\bullet}$ in vacuum using aDFT. The structure was obtained from a geometry optimisation at the PBEh-3c level, as implemented in Orca. All values are in MHz.

B.1.10 *In vacuo* lumiflavin vs. in-cluster $FAD^{\bullet -}$: principal components.

atom	A_{YY}		A_{XX}		A_{ZZ}	
	ref	$MD_{cluster}$	ref	$MD_{cluster}$	ref	$MD_{cluster}$
N5	-2.433	-1.827	-2.805	-2.125	49.237	56.176
N10	-0.404	0.666	-0.675	0.436	16.944	19.382
Hb	11.406	3.755	11.406	3.269	11.406	7.334
H8α	12.328	9.691	12.328	9.427	12.328	11.907
H7α	-3.968	-3.663	-3.968	-3.956	-3.968	-2.200
H6	-14.865	-9.769	-12.152	-10.773	-5.538	-3.649

Table B.10: Eigenvalues of the diagonalised HFC tensors for atoms of $FAD^{\bullet -}$. "ref" refers to the tensors calculated in [7] ; "$MD_{cluster}$" to the average tensors calculated on the flavin in its cluster. In this latter set, $\overleftrightarrow{Hb}$ = ($\overleftrightarrow{H1'a}$ + $\overleftrightarrow{H1'b}$)/2. All values are in MHz.

B.1.11 Flavin isotropic HFCs and tensor anisotropy.

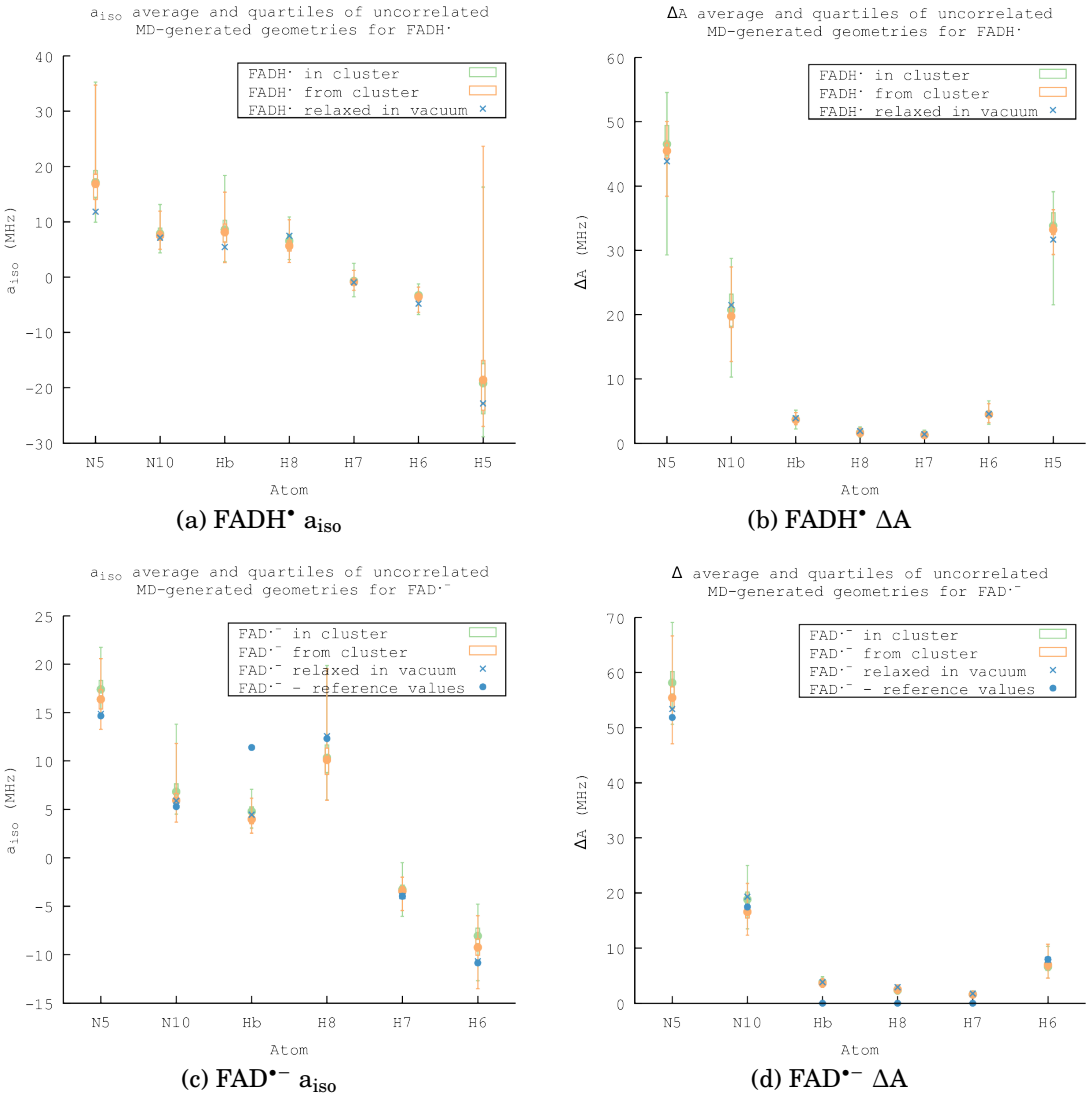

(a) FADH$^\bullet$ a_{iso} (b) FADH$^\bullet$ ΔA

(c) FAD$^{\bullet-}$ a_{iso} (d) FAD$^{\bullet-}$ ΔA

Figure B.5: average (dot) and quartiles (box) of the isotropic HFC and tensor anisotropy for selected atoms on (**a,b**) FADH$^\bullet$ and (**c,d**) FAD$^{\bullet-}$. Vertical bars span the entire distribution, locating the minimum and maximum value of a given sample. Green and orange data points were obtained on geometries taken from an MD run, while data points represented by blue crosses were calculated on a flavin optimised in vacuum using the PBEh-3c scheme. The dihedral angle of its ribityl chain with respect to the isoalloxazine moiety was constrained throughout the optimisation. Blue dots correspond to reference values calculated by Hiscock *et al.*[3]

B.1.12 Shifted representation of flavin isotropic HFCs and tensor anisotropy.

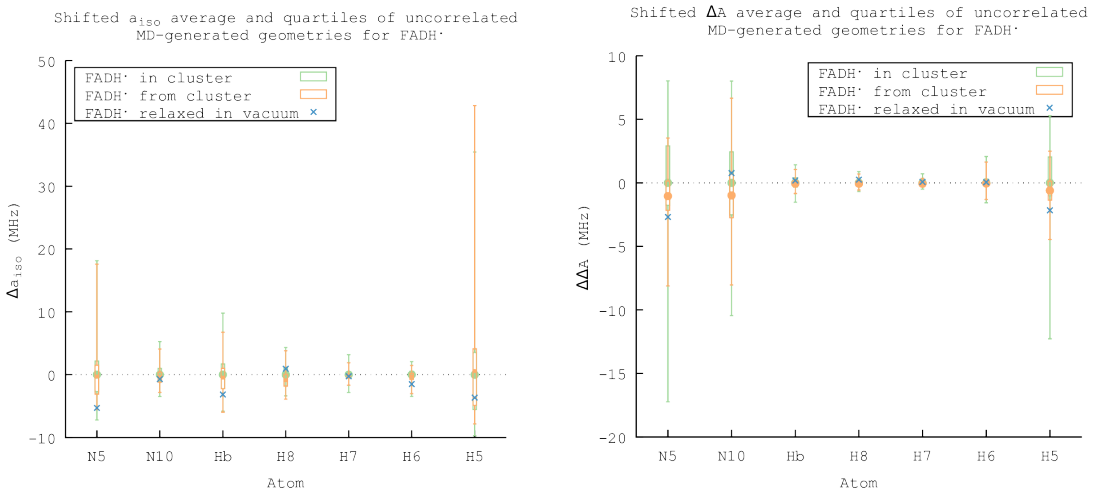

(a) $FADH^{\bullet}$ a_{iso} (b) $FADH^{\bullet}$ ΔA

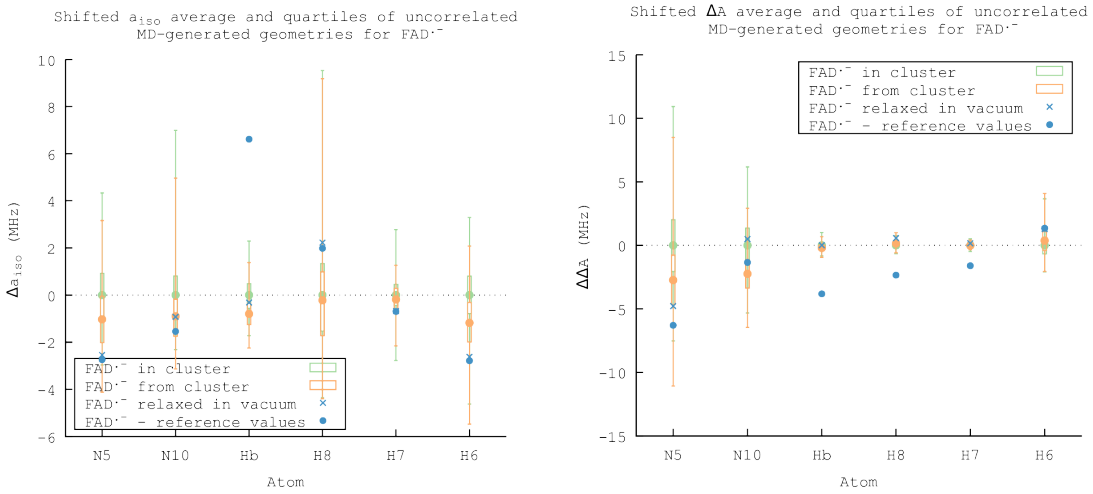

(c) $FAD^{\bullet -}$ a_{iso} (d) $FAD^{\bullet -}$ ΔA

Figure B.6: Shifted average (dot) and quartiles (box) of the **(a,c)** isotropic HFC and **(b,d)** tensor anisotropy for selected atoms on $FADH^{\bullet}$ and $FAD^{\bullet -}$. The average value of the flavin in cluster was subtracted from all values so as to better show the magnitude of the shift induced by polarisation. To regenerate values reported in Figure $B.5$, apply: $a_{\text{iso,aniso}} = \text{average}(a_{\text{iso,aniso}}^{\text{atom,in-cluster}}) + \Delta a_{\text{iso,aniso}}$.

B.1.13 Shifted representation of flavin isotropic HFCs and tensor anisotropy, including QM/MM tensors.

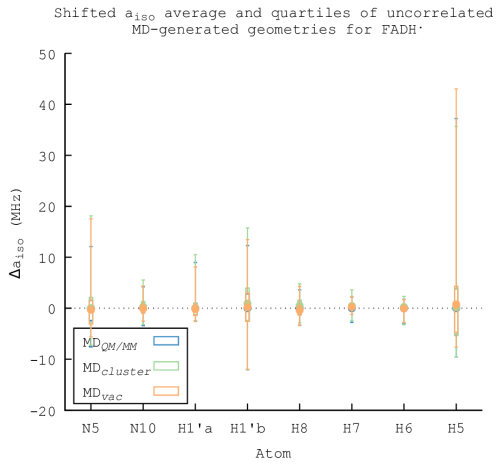

(a) FADH$^{\bullet}$ a_{iso}

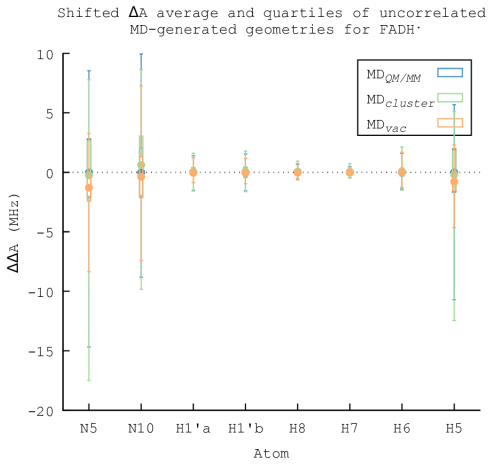

(b) FADH$^{\bullet}$ ΔA

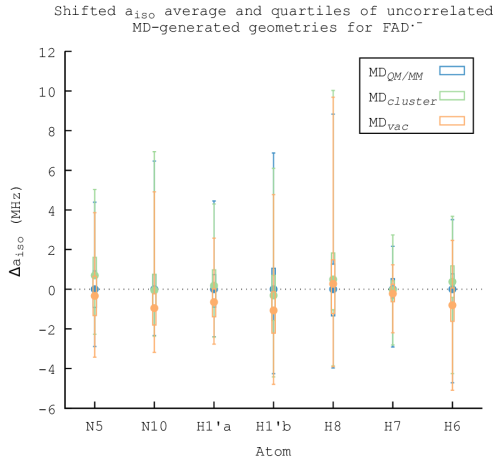

(c) FAD$^{\bullet-}$ a_{iso}

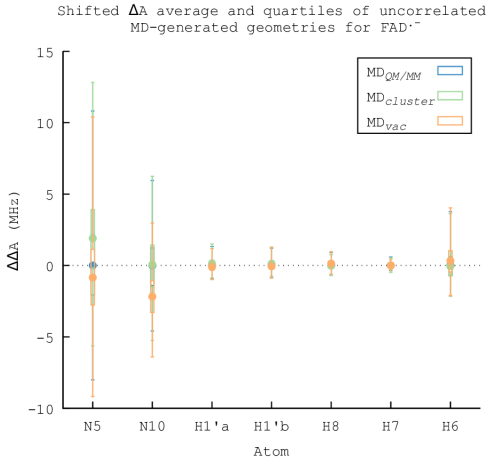

(d) FAD$^{\bullet-}$ ΔA

Figure B.7: Shifted average (dot) and quartiles (box) of the **(a,c)** isotropic HFC and **(b,d)** tensor anisotropy for selected atoms on FADH$^{\bullet}$ and FAD$^{\bullet-}$. The average value of the flavin in cluster was subtracted from all values so as to better show the magnitude of the shift induced by polarisation. To regenerate values reported in Figure $B.5$, apply: $a_{\text{iso,aniso}} = \text{average}(a^{\text{atom,in-cluster}}_{\text{iso,aniso}}) + \Delta a_{\text{iso,aniso}}$.

B.1.14 Visual representation of the flavin isotropic HFCs and of its variance, in and out of its minimal cluster.

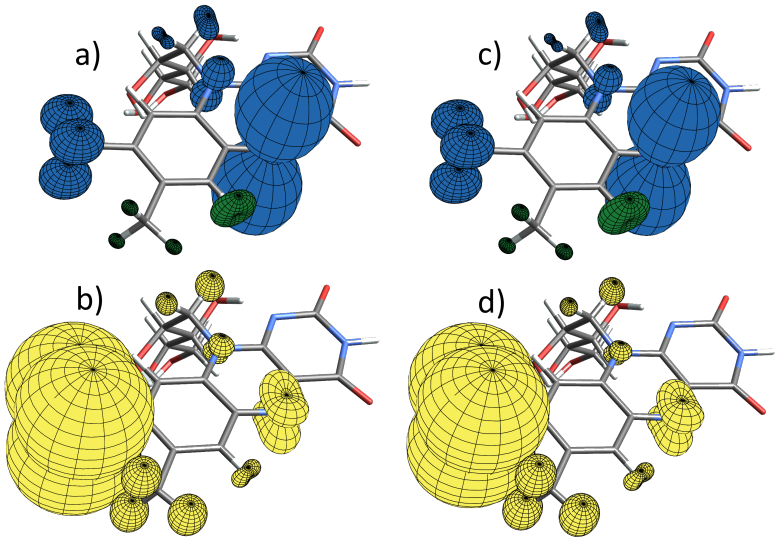

(a) $FAD^{\bullet -}$

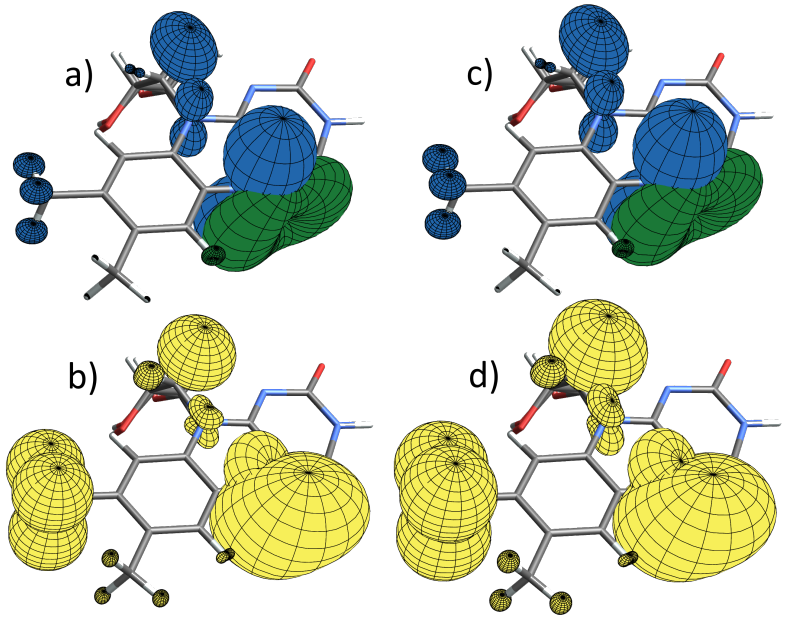

(b) $FADH^{\bullet}$

Figure B.8: Graphical representation of average $FAD^{\bullet -}$ and $FADH^{\bullet}$ hyperfine coupling tensors, calculated using aDFT on MD-generated geometries **(a)** without and **(c)** with a minimal chemical environment. The variance of average tensor elements is also plotted in a similar fashion, again **(b)** out of (MD*vac* dataset) and **(d)** in (MD*cluster* dataset) its minimal cluster.

B.1.15 Projections of HFC tensors onto average eigenbasis.

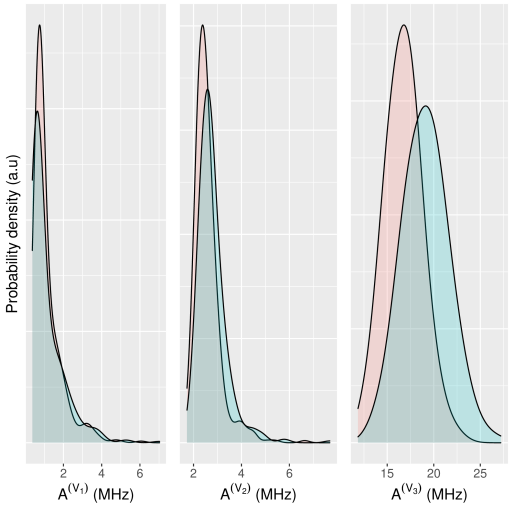

(a) $FAD^{\bullet -}$ N10

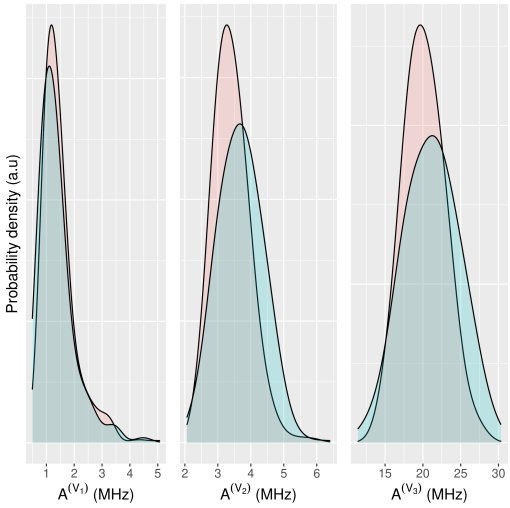

(b) $FADH^{\bullet}$ N10

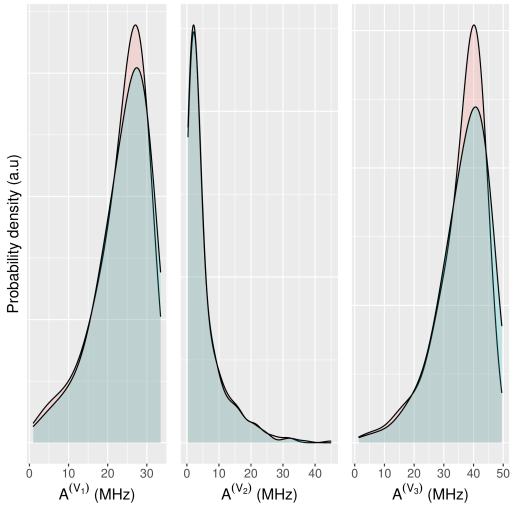

(c) $FADH^{\bullet}$ H5

Figure B.9: Projection of (a) $FAD^{\bullet -}$ N10, (b) $FADH^{\bullet}$ N10 and (c) $FADH^{\bullet}$ H5 HFC tensors onto their average eigenvectors V_i. Blue (resp. red) histograms are for calculations with (resp. without) inclusion of the environment, *i.e* in the $MD_{cluster}$ (resp. MD_{vac}) dataset.

B.1.16 Geometrical origin to extreme a_{iso} values: H5 improper angle.

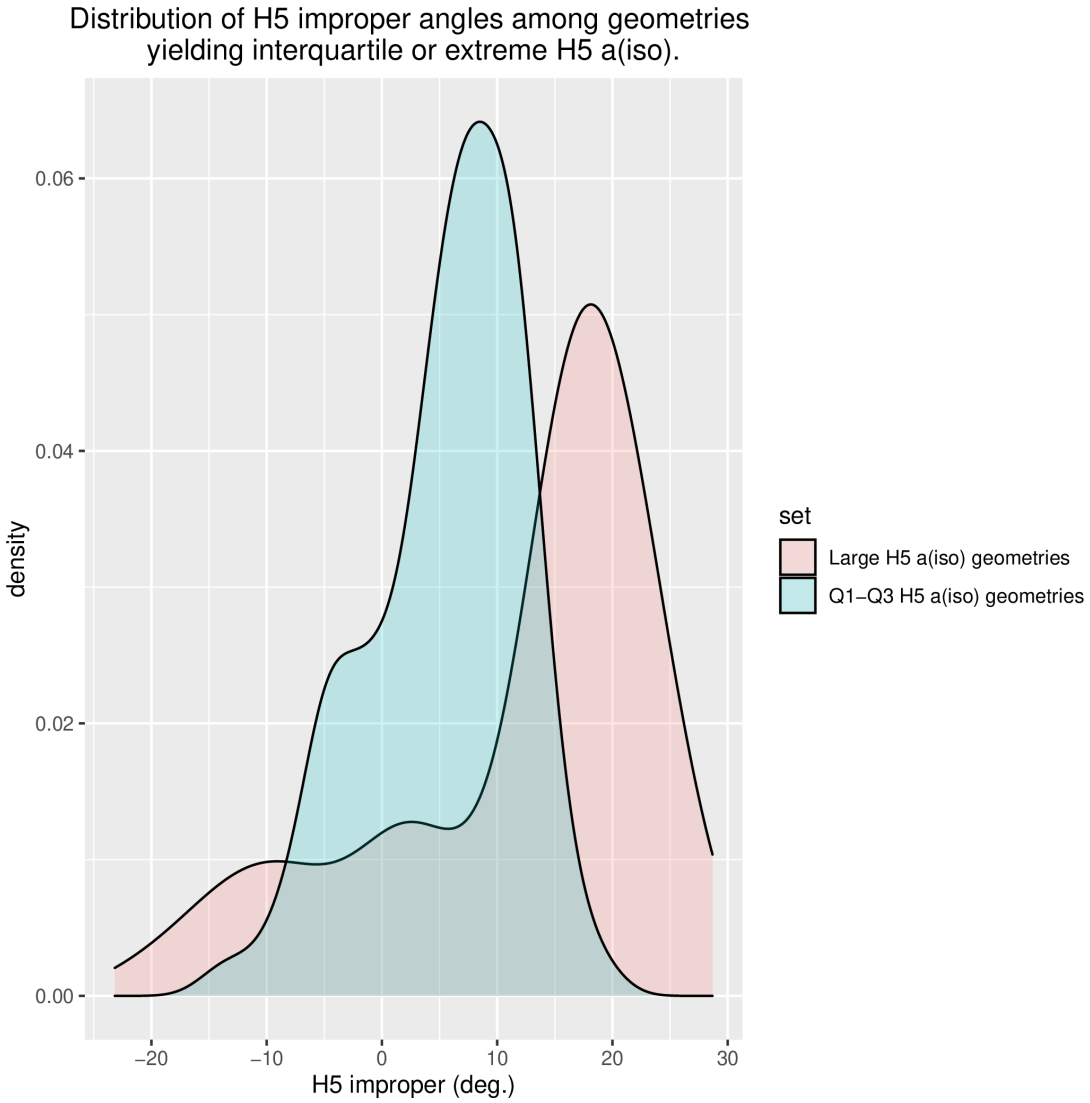

Figure B.10: Density plots of H5 improper angle (out-of-planeness) for geometries yielding respectively interquartile (Q1-Q3, in blue) or large (>Q3, in red) a_{iso} values of H5.

B.1.17 Statistical uncertainties on a_{iso} and ΔA in $MD_{cluster}$ and $MD_{QM/MM}$ datasets.

Atom	MD_{vac}: N_{tot} = 400					
	Lowest N_{eff}	$U(A_{yy})$	$U(A_{xx})$	$U(A_{zz})$	$U(a_{iso})$	$U(\Delta A)$
N5	400	0.067	0.069	0.339	0.158	0.068
N10	332	0.105	0.107	0.211	0.141	0.075
H1'a	270	0.105	0.103	0.131	0.113	0.051
H1'b	293	0.179	0.155	0.188	0.174	0.121
H8α	400	0.183	0.182	0.201	0.189	0.142
H7α	400	0.061	0.062	0.070	0.060	0.014
H6	400	0.124	0.182	0.067	0.124	0.059

(a) $FAD^{\bullet -}$ MD_{vac}

Atom	MD_{vac}: N_{tot} = 400					
	Lowest N_{eff}	$U(A_{yy})$	$U(A_{xx})$	$U(A_{zz})$	$U(a_{iso})$	$U(\Delta A)$
N5	368	0.397	0.397	0.356	0.383	0.587
N10	400	0.074	0.074	0.261	0.136	0.058
H1'a	322	0.181	0.152	0.178	0.170	0.116
H1'b	27	1.502	0.423	1.659	1.195	5.493
H8α	400	0.122	0.119	0.135	0.125	0.063
H7α	400	0.051	0.051	0.052	0.051	0.010
H6	400	0.081	0.075	0.063	0.073	0.021
H5	400	0.717	0.817	0.723	0.752	2.263

(b) $FADH^{\bullet}$ MD_{vac}

Atom	$MD_{cluster}$: N_{tot} = 386					
	Lowest N_{eff}	$U(A_{yy})$	$U(A_{xx})$	$U(A_{zz})$	$U(a_{iso})$	$U(\Delta A)$
N5	386	0.069	0.071	0.319	0.153	0.066
N10	223	0.114	0.116	0.314	0.181	0.114
H1'a	258	0.150	0.149	0.164	0.154	0.095
H1'b	386	0.172	0.172	0.179	0.175	0.122
H8α	230	0.255	0.253	0.266	0.258	0.266
H7α	386	0.079	0.080	0.071	0.077	0.024
H6	386	0.130	0.165	0.072	0.123	0.057

(a) $FAD^{\bullet -}$ $MD_{cluster}$

Atom	$MD_{cluster}$: N_{tot} = 389					
	Lowest N_{eff}	$U(A_{yy})$	$U(A_{xx})$	$U(A_{zz})$	$U(a_{iso})$	$U(\Delta A)$
N5	57	0.511	0.512	1.346	0.789	2.183
N10	50	0.076	0.075	0.976	0.376	0.204
H1'a	217	0.198	0.187	0.252	0.212	0.179
H1'b	24	1.918	2.074	2.190	2.061	16.970
H8α	172	0.213	0.206	0.251	0.224	0.199
H7α	201	0.116	0.121	0.110	0.116	0.054
H6	320	0.089	0.093	0.064	0.082	0.027
H5	389	0.705	0.837	0.704	0.749	2.240

(b) $FADH^{\bullet}$ $MD_{cluster}$

Atom	$MD_{QM/MM}$: N_{tot} = 396					
	Lowest N_{eff}	$U(A_{yy})$	$U(A_{xx})$	$U(A_{zz})$	$U(a_{iso})$	$U(\Delta A)$
N5	326	0.074	0.078	0.326	0.159	0.074
N10	290	0.109	0.111	0.259	0.160	0.092
H1'a	280	0.125	0.122	0.154	0.134	0.071
H1'b	339	0.189	0.189	0.181	0.186	0.139
H8α	396	0.183	0.181	0.199	0.188	0.141
H7α	396	0.072	0.073	0.065	0.070	0.020
H6	396	0.129	0.169	0.072	0.123	0.058

(a) $FAD^{\bullet -}$ $MD_{QM/MM}$

Atom	$MD_{QM/MM}$: N_{tot} = 369					
	Lowest N_{eff}	$U(A_{yy})$	$U(A_{xx})$	$U(A_{zz})$	$U(a_{iso})$	$U(\Delta A)$
N5	369	0.371	0.372	0.463	0.402	0.643
N10	199	0.074	0.081	0.429	0.195	0.097
H1'a	369	0.176	0.167	0.179	0.174	0.121
H1'b	22	1.742	1.899	1.888	1.843	13.584
H8α	369	0.138	0.134	0.152	0.141	0.080
H7α	307	0.086	0.088	0.068	0.081	0.026
H6	369	0.088	0.083	0.064	0.078	0.024
H5	369	0.712	0.848	0.704	0.755	2.276

(b) $FADH^{\bullet}$ $MD_{QM/MM}$

Table B.11: Statistical uncertainties, in MHz, on the average values of a_{iso} and ΔA for every atom of interest on the flavin, from the MD_{vac}, $MD_{cluster}$ and $MD_{QM/MM}$ datasets. For each table, N_{tot} is the number of data points, *i.e* the number of structures for which the HFC calculation converged successfully. "Lowest N_{eff}" is, for each atom, the smallest N_{eff} among the samples of A_{yy}, A_{xx} and A_{zz} values. This quantity is reported because the uncertainties on a_{iso} and ΔA, are calculated from those on the the tensors' eigenvalues $A_{ii\in\{x,y,z\}}$.

B.1.18 Average values of the full HFC tensor.

All values reported below are in MHz.

B.1.18.1 $FAD^{\bullet -}$ out of cluster (MD_{vac}).

$$N5 = \begin{pmatrix} -1.904 & 0.038 & -1.140 \\ 0.044 & -1.665 & -2.467 \\ -1.141 & -2.467 & 52.707 \end{pmatrix} \qquad N10 = \begin{pmatrix} 0.976 & -0.073 & 2.398 \\ -0.077 & 0.398 & -0.839 \\ 2.396 & -0.839 & 16.421 \end{pmatrix}$$

$$Hb2 = \begin{pmatrix} 6.965 & -0.532 & -1.236 \\ -0.532 & 4.434 & 0.302 \\ -1.237 & 0.302 & 4.297 \end{pmatrix} \qquad Hb1 = \begin{pmatrix} 4.470 & 0.915 & -1.112 \\ 0.913 & 2.050 & -0.322 \\ -1.113 & -0.323 & 1.742 \end{pmatrix}$$

$$\mathrm{H6} = \begin{pmatrix} -4.931 & -1.282 & 0.217 \\ -1.281 & -11.790 & -0.269 \\ 0.217 & -0.269 & -11.007 \end{pmatrix} \qquad \mathrm{H7}\alpha = \begin{pmatrix} -3.598 & -0.533 & -0.001 \\ -0.533 & -2.712 & 0.039 \\ -0.001 & 0.039 & -4.073 \end{pmatrix}$$

$$\mathrm{H8}\alpha = \begin{pmatrix} 9.890 & 0.835 & 0.087 \\ 0.835 & 11.010 & 0.158 \\ 0.087 & 0.158 & 9.453 \end{pmatrix}$$

B.1.18.2 $FAD^{\bullet -}$ in cluster ($MD_{cluster}$).

$$\mathrm{N5} = \begin{pmatrix} -1.744 & 0.054 & -1.406 \\ 0.059 & -1.555 & -2.688 \\ -1.407 & -2.688 & 55.522 \end{pmatrix} \qquad \mathrm{N10} = \begin{pmatrix} 1.133 & -0.098 & 2.528 \\ -0.102 & 0.557 & -0.978 \\ 2.527 & -0.978 & 18.794 \end{pmatrix}$$

$$\mathrm{Hb1} = \begin{pmatrix} 5.410 & 0.996 & -1.160 \\ 0.994 & 2.809 & -0.345 \\ -1.162 & -0.346 & 2.520 \end{pmatrix} \qquad \mathrm{Hb2} = \begin{pmatrix} 7.760 & -0.671 & -1.277 \\ -0.671 & 5.192 & 0.384 \\ -1.278 & 0.385 & 5.024 \end{pmatrix}$$

$$\mathrm{H6} = \begin{pmatrix} -4.180 & -1.606 & 0.146 \\ -1.606 & -9.984 & -0.227 \\ 0.146 & -0.228 & -10.028 \end{pmatrix} \qquad \mathrm{H7}\alpha = \begin{pmatrix} -3.404 & -0.558 & 0.001 \\ -0.558 & -2.530 & 0.036 \\ 0.001 & 0.036 & -3.886 \end{pmatrix}$$

$$\mathrm{H8}\alpha = \begin{pmatrix} 10.132 & 0.754 & 0.076 \\ 0.754 & 11.155 & 0.139 \\ 0.076 & 0.139 & 9.738 \end{pmatrix}$$

B.1.18.3 $FAD^{\bullet -}$ in QM/MM ($MD_{QM/MM}$).

$$\mathrm{N5} = \begin{pmatrix} -1.813 & -0.001 & -1.687 \\ 0.004 & -1.731 & -0.375 \\ -1.689 & -0.375 & 53.680 \end{pmatrix} \qquad \mathrm{N10} = \begin{pmatrix} 1.188 & 0.019 & 2.496 \\ 0.016 & 0.591 & -0.205 \\ 2.495 & -0.205 & 18.868 \end{pmatrix}$$

$$\mathrm{Hb1} = \begin{pmatrix} 5.168 & 0.920 & -1.159 \\ 0.918 & 2.642 & -0.342 \\ -1.160 & -0.342 & 2.389 \end{pmatrix} \qquad \mathrm{Hb2} = \begin{pmatrix} 8.030 & -0.677 & -1.211 \\ -0.676 & 5.551 & 0.355 \\ -1.212 & 0.356 & 5.326 \end{pmatrix}$$

$$\mathrm{H6} = \begin{pmatrix} -4.420 & -1.419 & 0.218 \\ -1.418 & -10.578 & -0.235 \\ 0.219 & -0.235 & -10.321 \end{pmatrix} \qquad \mathrm{H7}\alpha = \begin{pmatrix} -3.362 & -0.554 & 0.024 \\ -0.554 & -2.503 & -0.020 \\ 0.024 & -0.020 & -3.849 \end{pmatrix}$$

$$\mathrm{H8}\alpha = \begin{pmatrix} 9.616 & 0.778 & 0.053 \\ 0.778 & 10.707 & 0.091 \\ 0.053 & 0.091 & 9.218 \end{pmatrix}$$

B.1.18.4 FADH• out of cluster (MD_{vac}).

$$N5 = \begin{pmatrix} 2.162 & -0.160 & 2.250 \\ -0.163 & 1.885 & -0.812 \\ 2.250 & -0.812 & 46.440 \end{pmatrix} \qquad N10 = \begin{pmatrix} 1.965 & 0.083 & -3.130 \\ 0.080 & 0.864 & -0.032 \\ -3.129 & -0.032 & 19.667 \end{pmatrix}$$

$$Hb2 = \begin{pmatrix} 16.208 & 0.046 & -0.797 \\ 0.045 & 12.979 & 0.136 \\ -0.797 & 0.136 & 12.819 \end{pmatrix} \qquad Hb1 = \begin{pmatrix} 3.800 & 1.258 & 0.457 \\ 1.256 & 1.767 & 0.226 \\ 0.457 & 0.226 & 1.175 \end{pmatrix}$$

$$H5 = \begin{pmatrix} 2.867 & -2.024 & 0.135 \\ -2.016 & -35.803 & -0.136 \\ 0.137 & -0.136 & -22.836 \end{pmatrix} \qquad H6 = \begin{pmatrix} -2.184 & -1.928 & 0.003 \\ -1.929 & -3.184 & -0.092 \\ 0.003 & -0.092 & -5.384 \end{pmatrix}$$

$$H7\alpha = \begin{pmatrix} -1.060 & -0.405 & 0.046 \\ -0.405 & -0.288 & -0.127 \\ 0.046 & -0.127 & -1.354 \end{pmatrix} \qquad H8\alpha = \begin{pmatrix} 5.515 & 0.522 & -0.106 \\ 0.522 & 6.205 & -0.191 \\ -0.106 & -0.191 & 5.247 \end{pmatrix}$$

B.1.18.5 FADH• in cluster ($MD_{cluster}$).

$$N5 = \begin{pmatrix} 2.154 & -0.125 & 2.656 \\ -0.127 & 1.839 & -0.842 \\ 2.657 & -0.842 & 47.393 \end{pmatrix} \qquad N10 = \begin{pmatrix} 2.080 & 0.053 & -3.477 \\ 0.050 & 0.889 & 0.016 \\ -3.476 & 0.016 & 20.597 \end{pmatrix}$$

$$Hb1 = \begin{pmatrix} 4.062 & 1.245 & 0.502 \\ 1.243 & 1.898 & 0.236 \\ 0.503 & 0.237 & 1.353 \end{pmatrix} \qquad Hb2 = \begin{pmatrix} 16.990 & -0.067 & -0.801 \\ -0.067 & 13.653 & 0.142 \\ -0.801 & 0.142 & 13.576 \end{pmatrix}$$

$$H5 = \begin{pmatrix} 2.738 & -1.780 & -0.173 \\ -1.774 & -36.707 & -0.110 \\ -0.171 & -0.111 & -23.508 \end{pmatrix} \qquad H6 = \begin{pmatrix} -1.970 & -1.969 & 0.036 \\ -1.969 & -2.769 & -0.124 \\ 0.036 & -0.125 & -5.118 \end{pmatrix}$$

$$H7\alpha = \begin{pmatrix} -0.818 & -0.454 & 0.055 \\ -0.454 & -0.073 & -0.134 \\ 0.055 & -0.134 & -1.160 \end{pmatrix} \qquad H8\alpha = \begin{pmatrix} 6.412 & 0.525 & -0.112 \\ 0.525 & 7.086 & -0.201 \\ -0.112 & -0.201 & 6.135 \end{pmatrix}$$

B.1.18.6 FADH• in QM/MM ($MD_{QM/MM}$).

$$N5 = \begin{pmatrix} 2.091 & -0.133 & 2.724 \\ -0.134 & 1.787 & -0.880 \\ 2.725 & -0.881 & 47.580 \end{pmatrix} \qquad N10 = \begin{pmatrix} 1.965 & 0.059 & -3.344 \\ 0.056 & 0.798 & -0.016 \\ -3.343 & -0.016 & 19.941 \end{pmatrix}$$

$$\text{Hb2} = \begin{pmatrix} 16.053 & -0.031 & -0.757 \\ -0.031 & 12.738 & 0.114 \\ -0.757 & 0.114 & 12.638 \end{pmatrix} \qquad \text{Hb1} = \begin{pmatrix} 4.025 & 1.229 & 0.504 \\ 1.227 & 1.861 & 0.235 \\ 0.505 & 0.235 & 1.353 \end{pmatrix}$$

$$\text{H5} = \begin{pmatrix} 2.659 & -1.843 & -0.271 \\ -1.838 & -36.927 & -0.124 \\ -0.269 & -0.124 & -23.830 \end{pmatrix} \qquad \text{H6} = \begin{pmatrix} -2.160 & -1.938 & 0.040 \\ -1.939 & -3.101 & -0.092 \\ 0.040 & -0.092 & -5.323 \end{pmatrix}$$

$$\text{H7}\alpha = \begin{pmatrix} -1.268 & -0.436 & 0.054 \\ -0.436 & -0.512 & -0.131 \\ 0.054 & -0.131 & -1.586 \end{pmatrix}$$

$$\text{H8}\alpha = \begin{pmatrix} 5.911 & 0.522 & -0.110 \\ 0.522 & 6.586 & -0.196 \\ -0.110 & -0.197 & 5.644 \end{pmatrix}$$

B.1.19 Standard deviations of the full HFC tensor.

All values reported below are in MHz.

B.1.19.1 $FAD^{\bullet -}$ out of cluster (MD_{vac}).

$$\text{N5} = \begin{pmatrix} 0.842 & 0.304 & 4.200 \\ 0.304 & 0.729 & 2.931 \\ 4.201 & 2.932 & 3.442 \end{pmatrix} \qquad \text{N10} = \begin{pmatrix} 1.287 & 0.172 & 1.250 \\ 0.172 & 1.108 & 0.995 \\ 1.250 & 0.995 & 1.874 \end{pmatrix}$$

$$\text{Hb2} = \begin{pmatrix} 1.565 & 0.176 & 0.259 \\ 0.176 & 1.546 & 0.104 \\ 0.259 & 0.104 & 1.679 \end{pmatrix} \qquad \text{Hb1} = \begin{pmatrix} 1.151 & 0.165 & 0.294 \\ 0.165 & 1.031 & 0.152 \\ 0.294 & 0.152 & 1.049 \end{pmatrix}$$

$$\text{H6} = \begin{pmatrix} 0.572 & 0.509 & 0.605 \\ 0.509 & 2.037 & 0.413 \\ 0.605 & 0.413 & 1.189 \end{pmatrix} \qquad \text{H7}\alpha = \begin{pmatrix} 2.213 & 0.163 & 0.160 \\ 0.162 & 2.380 & 0.264 \\ 0.160 & 0.264 & 2.264 \end{pmatrix}$$

$$\text{H8}\alpha = \begin{pmatrix} 7.028 & 0.335 & 0.246 \\ 0.335 & 7.380 & 0.495 \\ 0.246 & 0.496 & 7.200 \end{pmatrix}$$

B.1.19.2 $FAD^{\bullet -}$ in cluster ($MD_{cluster}$).

$$\text{N5} = \begin{pmatrix} 0.852 & 0.322 & 4.339 \\ 0.322 & 0.727 & 3.076 \\ 4.340 & 3.077 & 3.220 \end{pmatrix} \qquad \text{N10} = \begin{pmatrix} 1.355 & 0.188 & 1.391 \\ 0.188 & 1.175 & 1.152 \\ 1.391 & 1.152 & 2.313 \end{pmatrix}$$

$$\text{Hb2} = \begin{pmatrix} 1.728 & 0.202 & 0.269 \\ 0.202 & 1.698 & 0.122 \\ 0.270 & 0.122 & 1.828 \end{pmatrix} \qquad \text{Hb1} = \begin{pmatrix} 1.371 & 0.183 & 0.301 \\ 0.183 & 1.259 & 0.155 \\ 0.301 & 0.155 & 1.279 \end{pmatrix}$$

$$\text{H6} = \begin{pmatrix} 0.573 & 0.436 & 0.572 \\ 0.436 & 1.939 & 0.377 \\ 0.572 & 0.378 & 1.175 \end{pmatrix} \qquad \text{H7}\alpha = \begin{pmatrix} 2.113 & 0.156 & 0.158 \\ 0.156 & 2.239 & 0.249 \\ 0.158 & 0.249 & 2.177 \end{pmatrix}$$

$$\text{H8}\alpha = \begin{pmatrix} 7.234 & 0.327 & 0.262 \\ 0.327 & 7.607 & 0.507 \\ 0.262 & 0.507 & 7.493 \end{pmatrix}$$

B.1.19.3 $FAD^{\bullet -}$ in QM/MM ($MD_{QM/MM}$).

$$\text{N5} = \begin{pmatrix} 0.858 & 0.250 & 4.257 \\ 0.251 & 0.714 & 2.944 \\ 4.258 & 2.944 & 3.302 \end{pmatrix} \qquad \text{N10} = \begin{pmatrix} 1.300 & 0.174 & 1.376 \\ 0.174 & 1.127 & 1.141 \\ 1.376 & 1.141 & 2.182 \end{pmatrix}$$

$$\text{Hb2} = \begin{pmatrix} 1.763 & 0.188 & 0.259 \\ 0.188 & 1.753 & 0.119 \\ 0.260 & 0.119 & 1.875 \end{pmatrix} \qquad \text{Hb1} = \begin{pmatrix} 1.341 & 0.171 & 0.293 \\ 0.171 & 1.238 & 0.142 \\ 0.293 & 0.142 & 1.254 \end{pmatrix}$$

$$\text{H6} = \begin{pmatrix} 0.602 & 0.463 & 0.567 \\ 0.463 & 1.968 & 0.378 \\ 0.567 & 0.378 & 1.183 \end{pmatrix} \qquad \text{H7}\alpha = \begin{pmatrix} 0.700 & 0.078 & 0.075 \\ 0.078 & 0.693 & 0.122 \\ 0.075 & 0.122 & 0.733 \end{pmatrix}$$

$$\text{H8}\alpha = \begin{pmatrix} 1.898 & 0.102 & 0.097 \\ 0.102 & 1.944 & 0.169 \\ 0.097 & 0.169 & 1.867 \end{pmatrix}$$

B.1.19.4 $FADH^{\bullet}$ out of cluster (MD_{vac}).

$$\text{N5} = \begin{pmatrix} 4.007 & 0.304 & 4.443 \\ 0.304 & 4.077 & 2.379 \\ 4.443 & 2.379 & 3.664 \end{pmatrix} \qquad \text{N10} = \begin{pmatrix} 0.919 & 0.260 & 2.722 \\ 0.260 & 0.763 & 1.168 \\ 2.721 & 1.169 & 2.646 \end{pmatrix}$$

$$\text{Hb2} = \begin{pmatrix} 4.419 & 0.377 & 0.328 \\ 0.377 & 4.154 & 0.160 \\ 0.328 & 0.161 & 4.347 \end{pmatrix} \qquad \text{Hb1} = \begin{pmatrix} 1.596 & 0.172 & 0.695 \\ 0.172 & 1.645 & 0.288 \\ 0.696 & 0.288 & 1.628 \end{pmatrix}$$

$$\text{H5} = \begin{pmatrix} 7.054 & 2.513 & 3.258 \\ 2.514 & 8.336 & 0.823 \\ 3.258 & 0.822 & 7.679 \end{pmatrix} \qquad \text{H6} = \begin{pmatrix} 0.379 & 0.171 & 0.309 \\ 0.171 & 1.162 & 0.306 \\ 0.309 & 0.306 & 0.736 \end{pmatrix}$$

$$\text{H7}\alpha = \begin{pmatrix} 0.828 & 0.086 & 0.100 \\ 0.086 & 0.868 & 0.209 \\ 0.100 & 0.209 & 0.829 \end{pmatrix} \qquad \text{H8}\alpha = \begin{pmatrix} 4.063 & 0.169 & 0.182 \\ 0.170 & 4.243 & 0.325 \\ 0.182 & 0.325 & 4.279 \end{pmatrix}$$

B.1.19.5 FADH• in cluster ($MD_{cluster}$).

$$\text{N5} = \begin{pmatrix} 3.701 & 0.316 & 4.511 \\ 0.316 & 3.784 & 2.427 \\ 4.510 & 2.427 & 5.300 \end{pmatrix} \qquad \text{N10} = \begin{pmatrix} 0.974 & 0.274 & 2.885 \\ 0.274 & 0.764 & 1.198 \\ 2.884 & 1.198 & 3.296 \end{pmatrix}$$

$$\text{Hb2} = \begin{pmatrix} 5.505 & 0.395 & 0.313 \\ 0.395 & 5.023 & 0.161 \\ 0.313 & 0.161 & 5.221 \end{pmatrix} \qquad \text{Hb1} = \begin{pmatrix} 1.790 & 0.230 & 0.709 \\ 0.230 & 1.811 & 0.280 \\ 0.709 & 0.281 & 1.802 \end{pmatrix}$$

$$\text{H5} = \begin{pmatrix} 6.843 & 2.578 & 3.253 \\ 2.579 & 8.407 & 0.808 \\ 3.254 & 0.808 & 7.381 \end{pmatrix} \qquad \text{H6} = \begin{pmatrix} 0.399 & 0.239 & 0.308 \\ 0.239 & 1.176 & 0.300 \\ 0.308 & 0.300 & 0.829 \end{pmatrix}$$

$$\text{H7}\alpha = \begin{pmatrix} 1.066 & 0.116 & 0.115 \\ 0.116 & 1.069 & 0.220 \\ 0.115 & 0.220 & 1.077 \end{pmatrix} \qquad \text{H8}\alpha = \begin{pmatrix} 4.715 & 0.193 & 0.213 \\ 0.193 & 4.906 & 0.356 \\ 0.213 & 0.356 & 4.984 \end{pmatrix}$$

B.1.19.6 FADH• in QM/MM ($MD_{QM/MM}$).

$$\text{N5} = \begin{pmatrix} 3.561 & 0.315 & 4.490 \\ 0.315 & 3.646 & 2.424 \\ 4.490 & 2.424 & 4.665 \end{pmatrix} \qquad \text{N10} = \begin{pmatrix} 0.911 & 0.259 & 2.741 \\ 0.259 & 0.737 & 1.140 \\ 2.740 & 1.140 & 2.994 \end{pmatrix}$$

$$\text{Hb2} = \begin{pmatrix} 4.748 & 0.392 & 0.321 \\ 0.392 & 4.387 & 0.158 \\ 0.321 & 0.159 & 4.558 \end{pmatrix} \qquad \text{Hb1} = \begin{pmatrix} 1.676 & 0.204 & 0.692 \\ 0.204 & 1.717 & 0.271 \\ 0.693 & 0.271 & 1.708 \end{pmatrix}$$

$$\text{H5} = \begin{pmatrix} 6.692 & 2.570 & 3.228 \\ 2.571 & 8.286 & 0.796 \\ 3.229 & 0.795 & 7.210 \end{pmatrix} \qquad \text{H6} = \begin{pmatrix} 0.391 & 0.212 & 0.312 \\ 0.212 & 1.130 & 0.298 \\ 0.312 & 0.298 & 0.799 \end{pmatrix}$$

$$\text{H7}\alpha = \begin{pmatrix} 0.764 & 0.085 & 0.055 \\ 0.085 & 0.734 & 0.105 \\ 0.055 & 0.105 & 0.775 \end{pmatrix} \qquad \text{H8}\alpha = \begin{pmatrix} 1.377 & 0.081 & 0.090 \\ 0.081 & 1.415 & 0.145 \\ 0.090 & 0.145 & 1.355 \end{pmatrix}$$

APPENDIX C

APPENDIX C

This appendix contains additional data not reported in full in Chapter 4. Figures C.1 through C.4 report a superimposed view of full-protein backbone RMSD and per-residue RMSF, allowing to correlate overall flexibility changes with fluctuations in a specific region.

Figures C.5 and C.6 report the occupancy by a $O_2^{\bullet -}$ radical, throughout 500-ns MD simulations from the FD-SUP trajectory set, of various binding sites composed of a combination of arginine residues. A single numeric ID is associated to each combination of arginines binding the same $O_2^{\bullet -}$, attributed according to the following rule: R365 (near site 1) has ID = 1, R409 (site 4) has ID = 2, R415 (site 2) has ID = 4, and R419 (site 2) has ID = 8. If a $O_2^{\bullet -}$ is held by both R365 and R409 simultaneously, *i.e.* stays within 3.0 Å of both, this configuration has ID = 1 + 2 = 3. The same logic applies to 3-arginine binding, although this configuration never appeared in practice.

Figure C.7 reports characteristic binding lifetimes for each of the 5 $O_2^{\bullet -}$ binding sites (labelled site 1 through 5), computed from the binding times in the T-SUP trajectory set.

C.0.1 *cl*Cry RMSD/RMSF

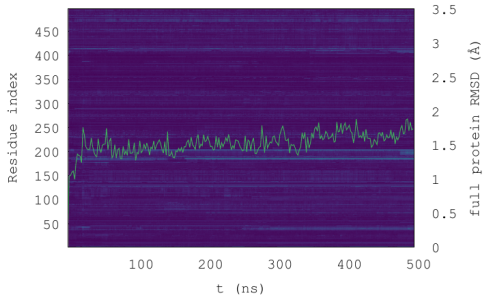

(a) Traj. 1

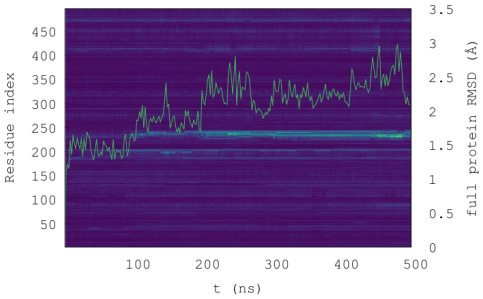

(b) Traj. 2

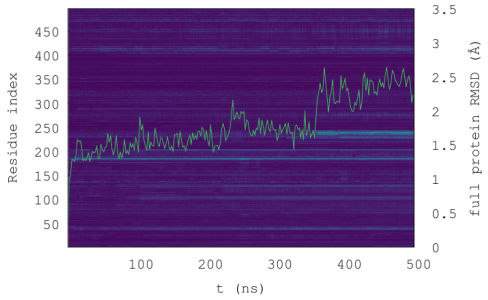

(c) Traj. 3

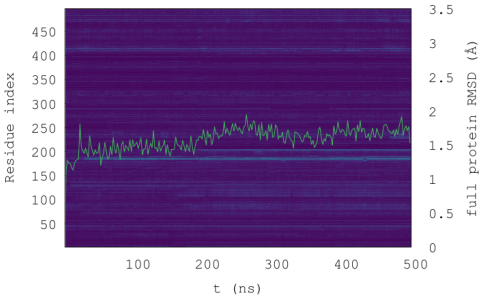

(d) Traj. 4

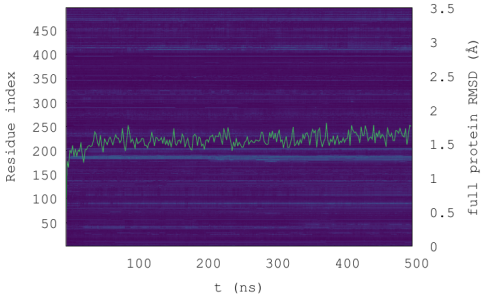

(e) Traj. 5

Figure C.1: (Part 1 of 2) Per-residue RMSD of the backbone heavy atoms (AMBER names: N, CA, C, O) along each of the 10 500-ns MD trajectories of *cl*Cry with 21 $O_2^{\bullet -}$ radicals. A lighter spot at coordinates (x,y) denote a large RMSD for residue y at time x. The average RMSD for the full protein, as shown in Fig. 4.3, is superimposed. All axes scaling and colourscales are harmonised, allowing a direct visual comparison across subfigures.

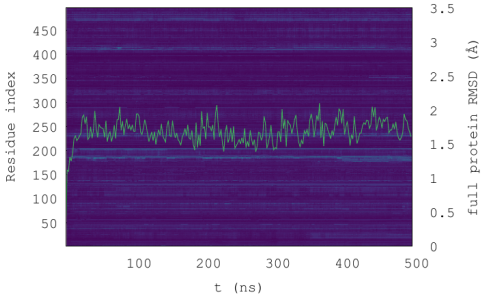

(a) Traj. 6

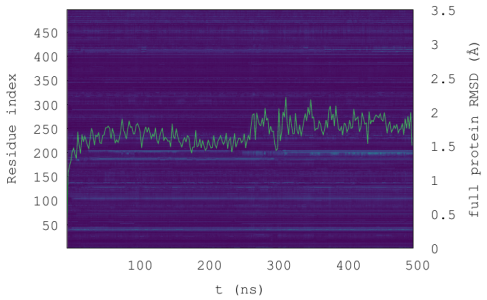

(b) Traj. 7

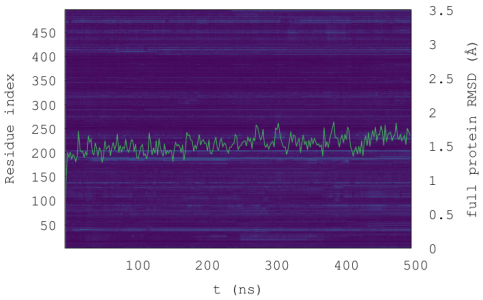

(c) Traj. 8

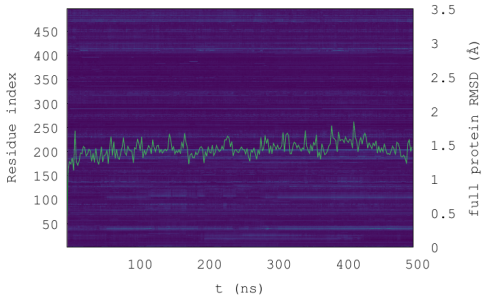

(d) Traj. 9

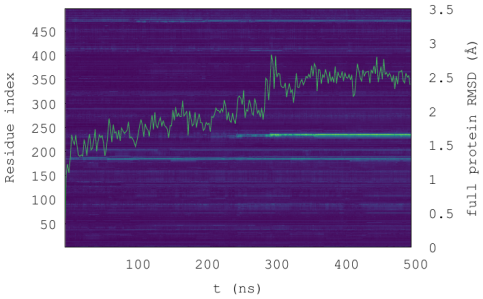

(e) Traj. 10

Figure C.2: (Part 2 of 2) Per-residue RMSD of the backbone heavy atoms (AMBER names: N, CA, C, O) along each of the 10 500-ns MD trajectories of *cl*Cry with 21 $O_2^{\bullet -}$ radicals. A lighter spot at coordinates (x,y) denote a large RMSD for residue y at time x. The average RMSD for the full protein, as shown in Fig. 4.3, is superimposed. All axes scaling and colourscales are harmonised, allowing a direct visual comparison across subfigures.

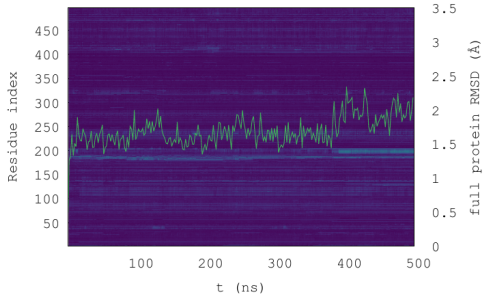

(a) Traj. 1

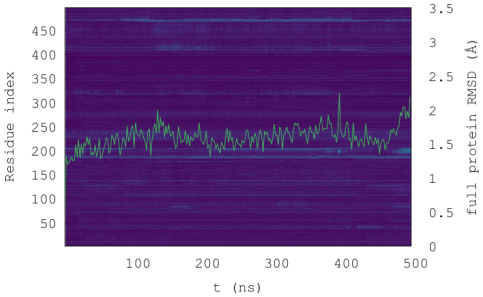

(b) Traj. 2

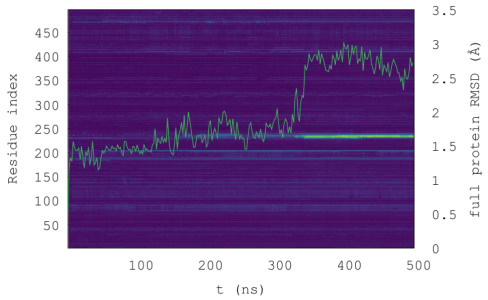

(c) Traj. 3

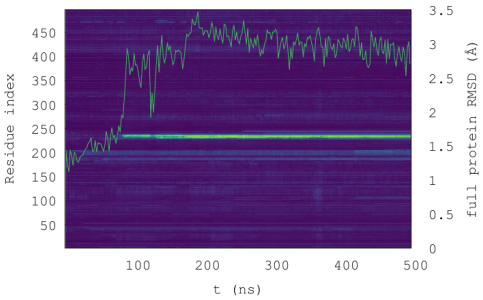

(d) Traj. 4

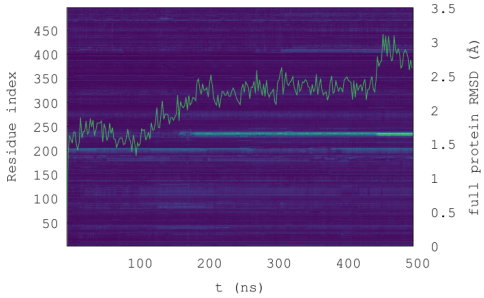

(e) Traj. 5

Figure C.3: (Part 1 of 2) Per-residue RMSD of the backbone heavy atoms (AMBER names: N, CA, C, O) along each of the 10 500-ns MD trajectories of *cl*Cry with 21 Cl^{-} radicals. A lighter spot at coordinates (x,y) denote a large RMSD for residue y at time x. The average RMSD for the full protein, as shown in Fig. 4.3, is superimposed. All axes scaling and colourscales are harmonised, allowing a direct visual comparison across subfigures.

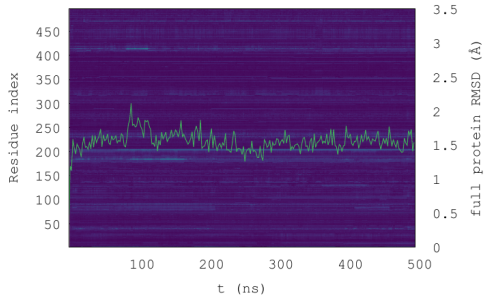

(a) Traj. 6

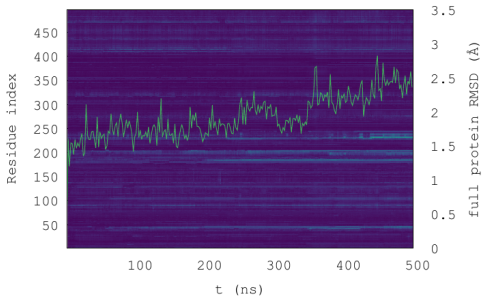

(b) Traj. 7

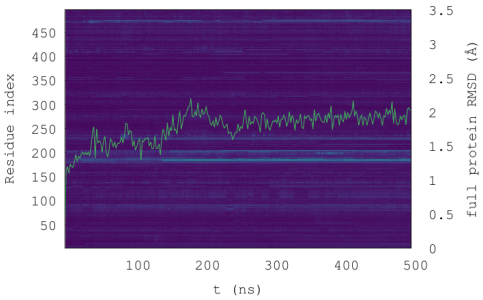

(c) Traj. 8

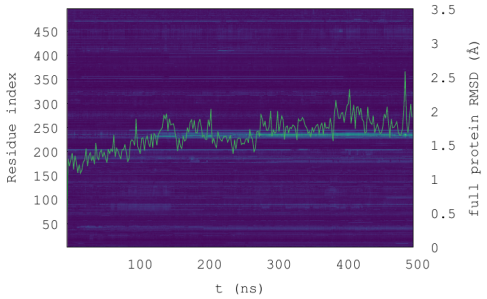

(d) Traj. 9

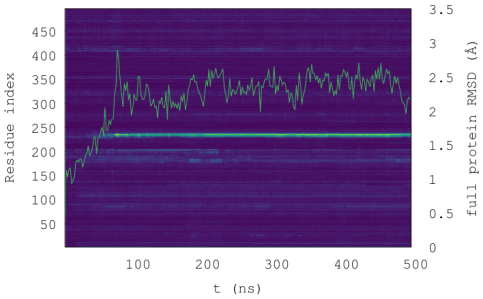

(e) Traj. 10

Figure C.4: (Part 2 of 2) Per-residue RMSD of the backbone heavy atoms (AMBER names: N, CA, C, O) along each of the 10 500-ns MD trajectories of *cl*Cry with 21 Cl^{-} radicals. A lighter spot at coordinates (x,y) denote a large RMSD for residue y at time x. The average RMSD for the full protein, as shown in Fig. 4.3, is superimposed. All axes scaling and colourscales are harmonised, allowing a direct visual comparison across subfigures.

C.0.2 ARG combinations

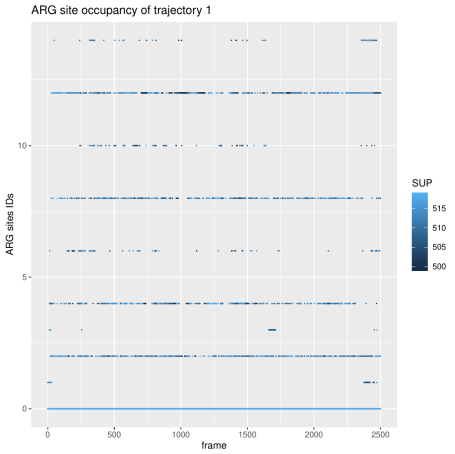

(a) Traj. 1

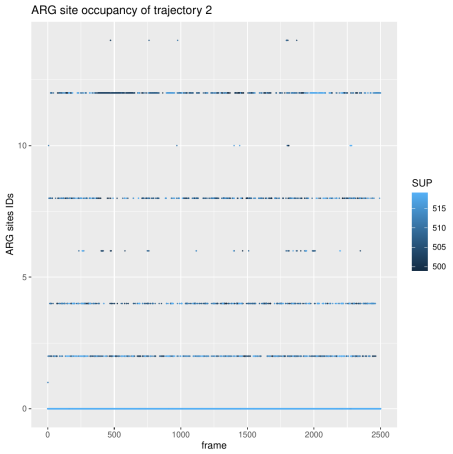

(b) Traj. 2

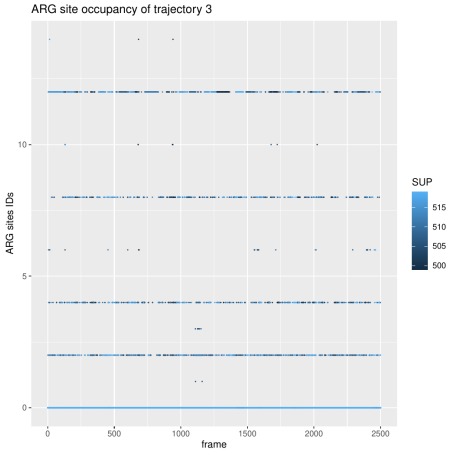

(c) Traj. 3

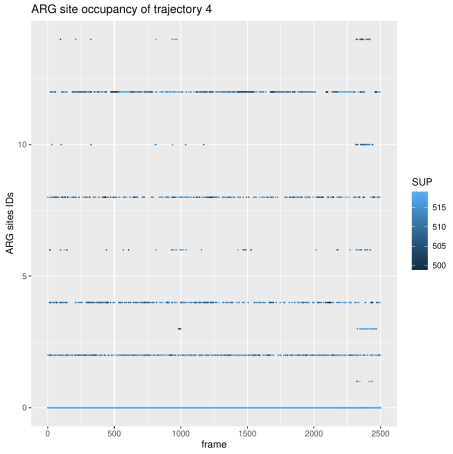

(d) Traj. 4

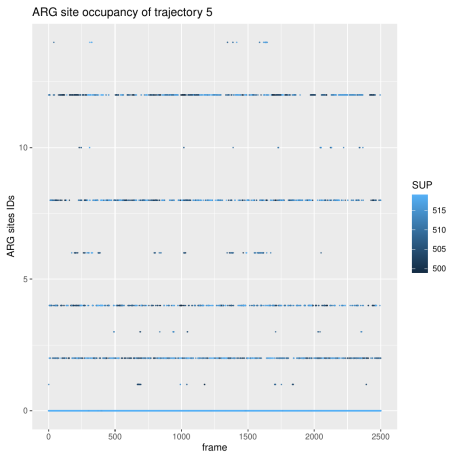

(e) Traj. 5

Figure C.5: Occupancy of the various binding sites consisting of the possible combinations of R365, R409, R415, and R419, for trajectories 1 through 5 of the FD-SUP dataset. To each combination corresponds a unique ID, according to a naming protocol given in the main text, in Chapter 4.

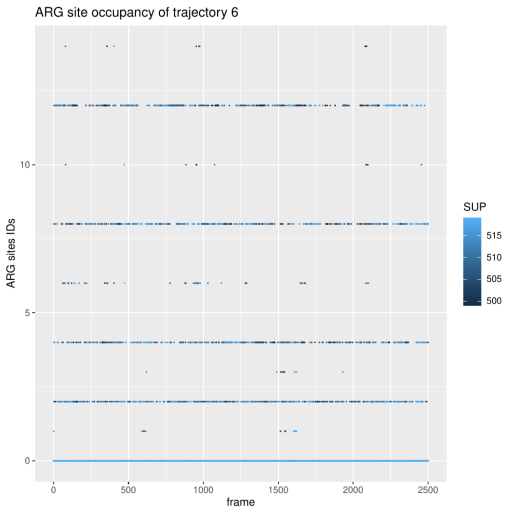

(a) Traj. 6

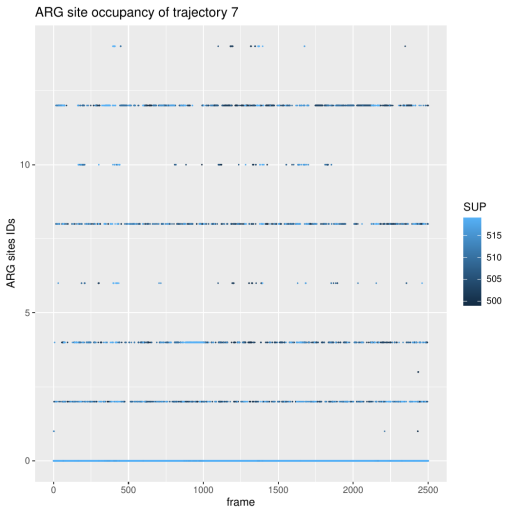

(b) Traj. 7

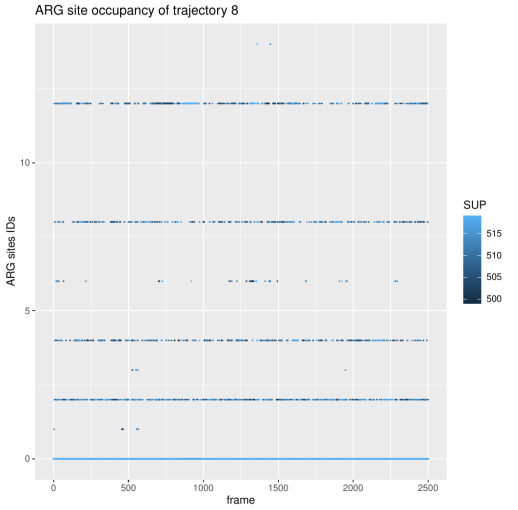

(c) Traj. 8

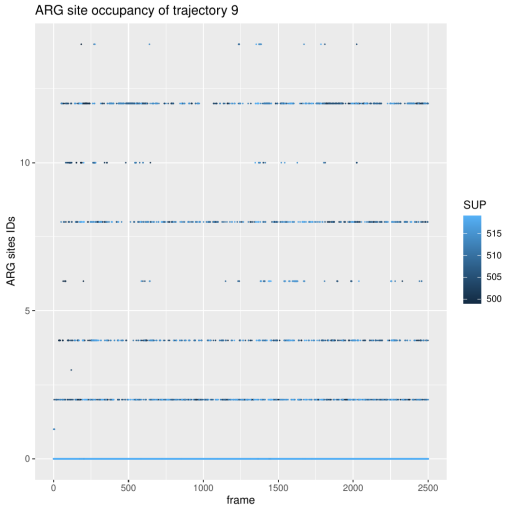

(d) Traj. 9

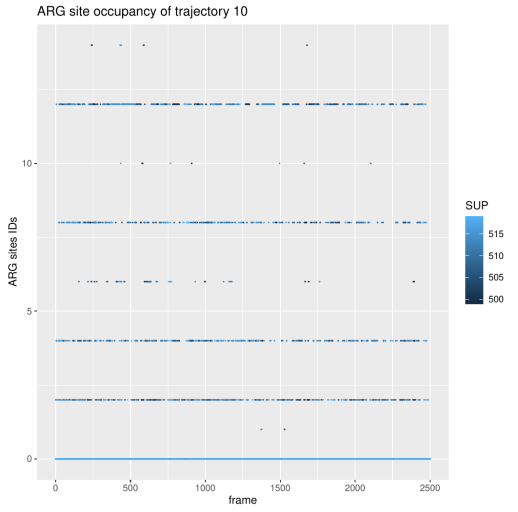

(e) Traj. 10

Figure C.6: Occupancy of the various binding sites consisting of the possible combinations of R365, R409, R415, and R419, for trajectories 6 through 10 of the FD-SUP dataset. To each combination corresponds a unique ID, according to a naming protocol given in the main text, in Chapter 4.

C.0.3 Site occupancy lifetime

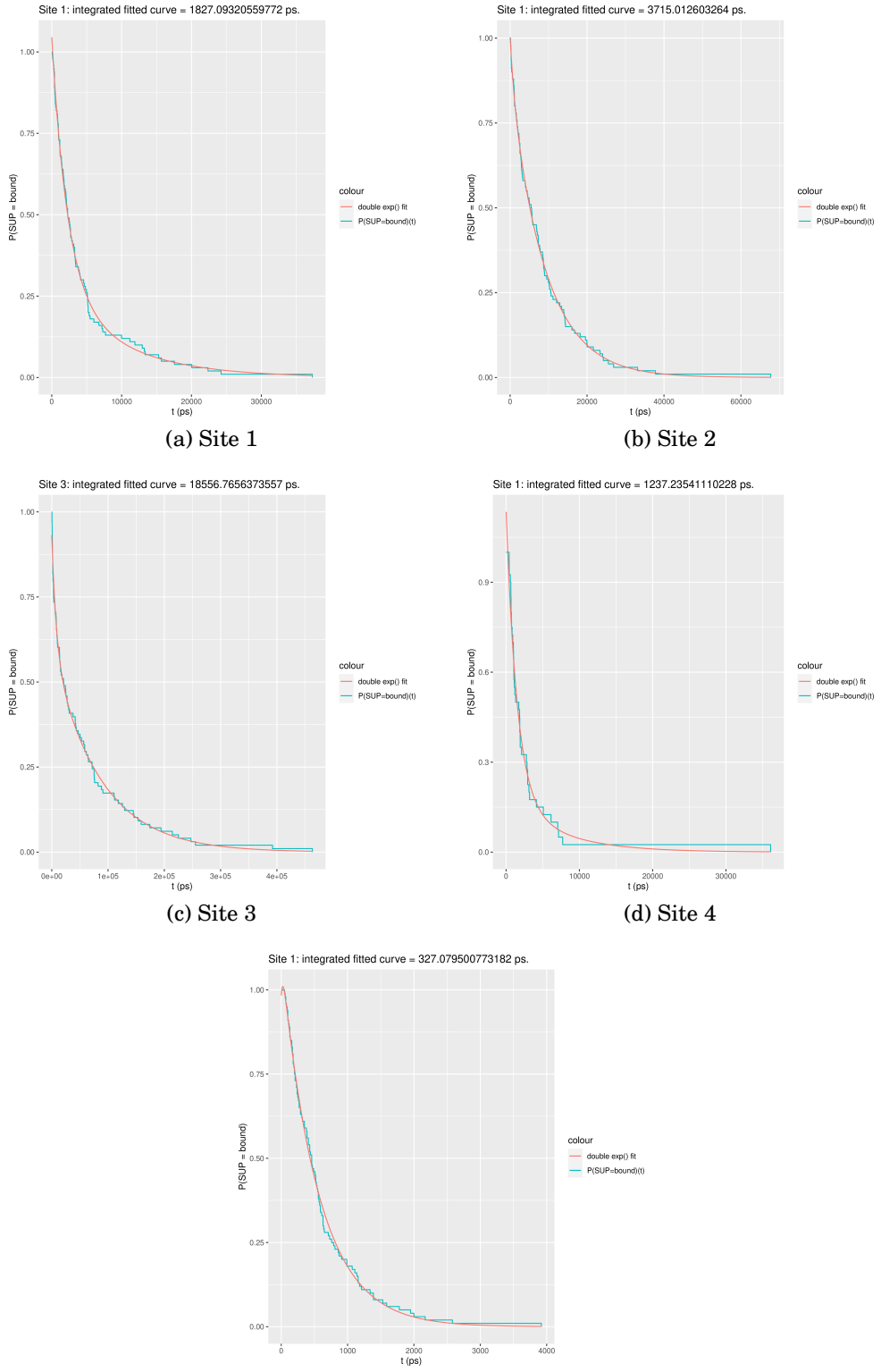

(a) Site 1

(b) Site 2

(c) Site 3

(d) Site 4

(e) Site 5

Figure C.7: Integrated occupancy lifetime of $O_2^{\bullet -}$ in site (a) 1 through (f) 5, computed from the lengths of all 100 trajectories per site (40 for site 4).

BIBLIOGRAPHY

[1] P. J. Hore and H. Mouritsen. The radical-pair mechanism of magnetoreception. *Annu. Rev. Biophys.*, 45:299–344, 2016.

[2] P. Mondal and M. Huix-Rotllant. Theoretical insights into the formation and stability of radical oxygen species in cryptochromes. *Phys. Chem. Chem. Phys.*, 21:8874, 2019.

[3] H. G. Hiscock, S. Worster, D. R. Kattnig, C. Steers, Y. Jin, D. E. Manolopoulos, H. Mouritsen, and P. J. Hore. The quantum needle of the avian magnetic compass. *PNAS*, 113:4634–4639, 2016.

[4] H. W. Henshaw. Migration of the pacific plover to and from the hawaiian islands. *The Auk*, 27, 1910.

[5] R. Wiltschko and W. Wiltschko. The magnetite-based receptors in the beak of birds and their role in avian navigation. *Journal of Comparative Physiology A: Neuroethology, Sensory, Neural, and Behavioral Physiology*, 199, 2013.

[6] R. Muheim, H. Schmaljohann, and T. Alerstam. Feasibility of sun and magnetic compass mechanisms in avian long-distance migration. *Movement Ecology*, 6, 2018.

[7] W. Wiltschko. Compasses used by birds. *Comparative Biochemistry and Physiology – Part A: Physiology*, 76, 1983.

[8] R. Wiltschko and W. Wiltschko. *Magnetic orientation in animals*, volume 33. Springer Berlin Heidelberg, Berlin, Heidelberg, 1995.

[9] S. Åkesson, J. Morin, R. Muheim, and U. Ottosson. Avian orientation at steep angles of inclination: Experiments with migratory white-crowned sparrows at the magnetic north pole. *Proceedings of the Royal Society B: Biological Sciences*, 268, 2001.

[10] W. Wiltschko and R. Wiltschko. Interrelation of magnetic compass and star orientation in night-migrating birds. *Journal of Comparative Physiology A*, 109, 1976.

[11] R. Wiltschko, M. Ahmad, C. Nießner, D. Gehring, and W. Wiltschko. Light-dependent magnetoreception in birds: the crucial step occurs in the dark. *J. R. Soc. Interface*, 13(118):20151010, May 2016.

[12] R. Muheim, J. Bäckman, and S. Åkesson. Magnetic compass orientation in european robins is dependent on both wavelength and intensity of light. *Journal of Experimental Biology*, 205, 2002.

[13] M Winklhofer, E. Dylda, P. Thalau, W. Wiltschko, and R. Wiltschko. Avian magnetic compass can be tuned to anomalously low magnetic intensities. *Proceedings of the Royal Society B: Biological Sciences*, 280, 2013.

[14] R. Wiltschko, P. Thalau, D. Gehring, C. Nießner, T. Ritz, and W. Wiltschko. Magnetoreception in birds: The effect of radio-frequency fields. *Journal of the Royal Society Interface*, 12, 2015.

[15] C. Nießner and M. Winklhofer. Radical-pair-based magnetoreception in birds: radio-frequency experiments and the role of cryptochrome. *Journal of Comparative Physiology A: Neuroethology, Sensory, Neural, and Behavioral Physiology*, 203, 2017.

[16] J. C. S. Lau, N. Wagner-Rundell, C. T. Rodgers, N. J. B. Green, and P. J. Hore. Effects of disorder and motion in a radical pair magnetoreceptor. *Journal of the Royal Society Interface*, 7, 2010.

[17] T. Ritz, S. Adem, and K. Schulten. A model for photoreceptor-based magnetoreception in birds. *Biophysical Journal*, 78:707–718, 2 2000.

[18] I. A. Solov'yov, T. Ritz, K. Schulten, and P. J. Hore. A chemical compass for bird navigation. *Quantum Effects in Biology*, 2014.

[19] J. B. Phillips and S. C. Borland. Behavioural evidence for use of a light-dependent magnetoreception mechanism by a vertebrate. *Nature*, 359, 1992.

[20] L. Fusani, C. Bertolucci, E. Frigato, and A. Foà. Cryptochrome expression in the eye of migratory birds depends on their migratory status. *Journal of Experimental Biology*, 217, 2014.

[21] S. El-Din El-Assal, C. Alonso-Blanco, A. J. M. Peeters, C. Wagemaker, J. L. Weller, and M. Koornneef. The role of cryptochrome 2 in flowering in arabidopsis. *Plant Physiology*, 133, 2003.

[22] T. Yoshii, M. Ahmad, and C. Helfrich-Förster. Cryptochrome mediates light-dependent magnetosensitivity of drosophila's circadian clock. *PLoS Biology*, 7, 2009.

[23] K. S. Hingorani and L. M. Gierasch. Comparing protein folding in vitro and in vivo: Foldability meets the fitness challenge. *Current Opinion in Structural Biology*, 24, 2014.

[24] S. Y. Wong, W. Yujing, H. Mouritsen, I. A. Solov'yov, and P. J. Hore. Cryptochrome magnetoreception: four tryptophans could be better than three. *J. R. Soc. Interface*, 184(18), November 2021.

[25] N. S. Babcock and D. R. Kattnig. Electron–electron dipolar interaction poses a challenge to the radical pair mechanism of magnetoreception. *J. Phys. Chem. Lett.*, 11:2414, 2020.

[26] R. H. Keens, S. Bedkihal, and D. R. Kattnig. Magnetosensitivity in dipolarly coupled three-spin systems. *Physical Review Letters*, 121, 2018.

[27] N. S. Babcock and D. R. Kattnig. Radical scavenging could answer the challenge posed by electron–electron dipolar interactions in the cryptochrome compass model. *JACS Au*, 1:2033, 2021.

[28] P. Müller and M. Ahmad. Light-activated cryptochrome reacts with molecular oxygen to form a flavin–superoxide radical pair consistent with magnetoreception. *J. Biol. Chem.*, 286:21033, 2011.

[29] D. R. Kattnig and P. J. Hore. The sensitivity of a radical pair compass magnetoreceptor can be significantly amplified by radical scavengers. *Scientific Reports*, 7:11640, 12 2017.

[30] B. D. Zoltowski. Chemical and structural analysis of a photoactive vertebrate cryptochrome from pigeon. *Proc. Natl. Acad. Sci. U. S. A.*, 116:19449, 2019.

[31] S. Oldemeyer. Essential role of an unusually long-lived tyrosyl radical in the response to red light of the animal-like cryptochrome acry. *J. Biol. Chem.*, 291:14062, 2016.

[32] B. Giovani, M. Byrdin, M. Ahmad, and K. Brettel. Light-induced electron transfer in a cryptochrome blue-light photoreceptor. *Nature Structural Biology*, 10, 2003.

[33] P. Faller. Rapid formation of the stable tyrosyl radical in photosystem ii. *Proc. Natl. Acad. Sci. U. S. A.*, 98:14368, 2001.

[34] F. Schuhmann, D. R. Kattnig, and I. A. Solov'yov. Exploring post-activation conformational changes in pigeon cryptochrome 4. *J. Phys. Chem. B*, 125:9652, 2021.

[35] K. S. Chae, I. T. Oh, S. H. Lee, and S. C. Kim. Blue light-dependent human magnetoreception in geomagnetic food orientation. *PLoS ONE*, 14, 2019.

[36] J. Helm and W. T. Strunz. Quantum decoherence of two qubits. *Physical Review A - Atomic, Molecular, and Optical Physics*, 80, 2009.

[37] J. Deviers, F. Cailliez, A. de la Lande, and D. R. Kattnig. Anisotropic magnetic field effects in the re-oxidation of cryptochrome in the presence of scavenger radicals. *The Journal of Chemical Physics*, 156:025101, 1 2022.

[38] J. Deviers, F. Cailliez, B. Z. Gutiérrez, D. R. Kattnig, and A. de la Lande. Ab initio derivation of flavin hyperfine interactions for the protein magnetosensor cryptochrome. *Physical Chemistry Chemical Physics*, 24, 2022.

[39] C. V. Mora, M. Davison, J. M. Wild, and M. M. Walker. Magnetoreception and its trigeminal mediation in the homing pigeon. *Nature*, 432, 2004.

[40] G. C. Nordmann, T. Hochstoeger, and D. A. Keays. Magnetoreception—a sense without a receptor. *PLOS Biology*, 15, 2017.

[41] D. Kishkinev, N. Chernetsov, D. Heyers, and H. Mouritsen. Migratory reed warblers need intact trigeminal nerves to correct for a 1,000 km eastward displacement. *PLoS ONE*, 8, 2013.

[42] K. Schulten, C. E. Swenberg, and A. Weller. A biomagnetic sensory mechanism based on magnetic field modulated coherent electron spin motion. *Zeitschrift für Physikalische Chemie*, 111:1–5, 1 1978.

[43] W. Wiltschko, U. Munro, H. Ford, and R. Wiltschko. Red light disrupts magnetic orientation of migratory birds. *Nature*, 364, 1993.

[44] D. Heyers, M. Manns, H. Luksch, O. Güntürkün, and H. Mouritsen. A visual pathway links brain structures active during magnetic compass orientation in migratory birds. *PLoS ONE*, 2, 2007.

[45] M. Zapka, D. Heyers, C. M. Hein, S. Engels, N. L. Schneider, J. Hans, S. Weiler, D. Dreyer, D. Kishkinev, J. M. Wild, and H. Mouritsen. Visual but not trigeminal mediation of magnetic compass information in a migratory bird. *Nature*, 461, 2009.

[46] H. Mouritsen, G. Feenders, M. Liedvogel, K. Wada, and E. D. Jarvis. Night-vision brain area in migratory songbirds. *Proceedings of the National Academy of Sciences of the United States of America*, 102, 2005.

[47] D. R. Kattnig, I. A. Solov'Yov, and P. J. Hore. Electron spin relaxation in cryptochrome-based magnetoreception. *Physical Chemistry Chemical Physics*, 18, 2016.

[48] D. Kobylkov. Electromagnetic 0.1–100 khz noise does not disrupt orientation in a night-migrating songbird implying a spin coherence lifetime of less than 10 µs. *J. R. Soc., Interface*, 16:20190716, 2019.

[49] C. R. Timmel, U. Till, B. Brocklehurst, K. A. McLauchlan, and P. J. Hore. Effects of weak magnetic fields on free radical recombination reactions. *Molecular Physics*, 95, 1998.

[50] C. T. Rodgers and P. J. Hore. Chemical magnetoreception in birds: The radical pair mechanism. *Proceedings of the National Academy of Sciences of the United States of America*, 106, 2009.

[51] P. Müller, J. Yamamoto, R. Martin, S. Iwai, and K. Brettel. Discovery and functional analysis of a 4th electron-transferring tryptophan conserved exclusively in animal cryptochromes and (6-4) photolyases. *Chemical Communications*, 51, 2015.

[52] F. Cailliez, P. Müller, T. Firmino, P. Pernot, and A. De La Lande. Energetics of photoinduced charge migration within the tryptophan tetrad of an animal (6-4) photolyase. *Journal of the American Chemical Society*, 138, 2016.

[53] J. Xu, L. E. Jarocha, T. Zollitsch, M. Konowalczyk, K. B. Henbest, S. Richert, M. J. Golesworthy, J. Schmidt, V. Déjean, D. J. C. Sowood, M. Bassetto, J. Luo, J. Jessica R. Walton, J. Fleming, Y. Wei, T. L. Pitcher, G. Moise, M. Herrmann, H. Yin, H. Wu, R. Bartölke, S. J. Käsehagen, S. Simon Horst, G. Dautaj, P. D. F. Murton, A. S. Gehrckens, Y. Chelliah, J. S. Takahashi, K.-W. Koch, S. Weber, I. A. Solov'yov, C. Xie, S. R. Mackenzie, C. R. Timmel, H. Mouritsen, and P. J. Hore. Magnetic sensitivity of cryptochrome 4 from a migratory songbird. *Nature*, 594:535, 2021.

[54] H. B. Gray and J. R. Winkler. Electron tunneling through proteins. *Quarterly Reviews of Biophysics*, 36, 2003.

[55] O. Efimova and P. J. Hore. Role of exchange and dipolar interactions in the radical pair model of the avian magnetic compass. *Biophysical Journal*, 94, 2008.

[56] D. Nohr. Determination of radical–radical distances in light-active proteins and their implication for biological magnetoreception. *Angew. Chem., Int. Ed.*, 56:8550, 2017.

[57] P. J. Hore and S. Bouguet-Bonnet. Nuclear magnetic resonance . second edition. by peter hore. oxford university press, 2015. pp. 120. isbn 9780198703419. *Journal of Applied Crystallography*, 50, 2017.

[58] J. Cai, G. G. Guerreschi, and H. J. Briegel. Quantum control and entanglement in a chemical compass. *Physical Review Letters*, 104, 2010.

[59] E. M. Gauger, E. Rieper, J. J. L. Morton, S. C. Benjamin, and V. Vedral. Sustained quantum coherence and entanglement in the avian compass. *Physical Review Letters*, 106, 2011.

[60] J. R. Woodward, T. J. Foster, A. T. Salaoru, and C. B. Vink. Direct observation of f-pair magnetic field effects and time-dependence of radical pair composition using rapidly switched magnetic fields and time-resolved infrared methods. *Physical Chemistry Chemical Physics*, 10, 2008.

[61] D. R. Kattnig. F-cluster: Reaction-induced spin correlation in multi-radical systems. *Journal of Chemical Physics*, 154, 2021.

[62] G. Grüning, S. Y. Wong, L. Gerhards, F. Schuhmann, D. R. Kattnig, P. J. Hore, and I. A. Solov'yov. Effects of dynamical degrees of freedom on magnetic compass sensitivity: A comparison of plant and avian cryptochromes. *Journal of the American Chemical Society*, 144(50):22902–22914, 2022. PMID: 36459632.

[63] C. Atkins, K. Bajpai, J. Rumball, and D. R. Kattnig. On the optimal relative orientation of radicals in the cryptochrome magnetic compass. *J. Chem. Phys.*, 151:065103, 2019.

[64] M. Ahmad. Cryptochrome mediated magnetic sensitivity in arabidopsis occurs independently of light-induced electron transfer to the flavin. *Photochem. Photobiol. Sci.*, 19:341, 2020.

[65] M. Pooam. Magnetic sensitivity mediated by the arabidopsis blue-light receptor cryptochrome occurs during flavin reoxidation in the dark. *Planta*, 249:319, 2019.

[66] C. Nießner, S. Denzau, L. Peichl, W. Wiltschko, and R. Wiltschko. Magnetoreception in birds: I. Immunohistochemical studies concerning the cryptochrome cycle. *J. Exp. Biol.*, 217(23):4221–4224, December 2014.

[67] C. Nießner, S. Denzau, L. Peichl, W. Wiltschko, and R. Wiltschko. Magnetoreception: activation of avian cryptochrome 1a in various light conditions. *J. Comp. Physiol. A*, 204(12):977–984, December 2018.

[68] P. Bolte, A. Einwich, P. K. Seth, R. Chetverikova, D. Heyers, I. Wojahn, U. Janssen-Bienhold, R. Feederle, P. Hore, K. Dedek, and H. Mouritsen. Cryptochrome 1a localisation in light- and dark-adapted retinae of several migratory and non-migratory bird species: no signs of light-dependent activation. *Ethology Ecology & Evolution*, 33(3):248–272, 2021.

[69] T. C. Player and P. J. Hore. Viability of superoxide-containing radical pairs as magnetoreceptors. *J. Chem. Phys.*, 151:225101, 2019.

[70] R. Kutta, N. Archipowa, and L. Johannissen. Vertebrate cryptochromes are vestigial flavoproteins. *Sci. Rep.*, page 44906, 2017.

[71] J. C. S. Lau, C. T. Rodgers, and P. J. Hore. Compass magnetoreception in birds arising from photo-induced radical pairs in rotationally disordered cryptochromes. *Journal of The Royal Society Interface*, 9:3329–3337, 12 2012.

[72] P. J. Hore, A. E. Lee, J. C. S. Lau, H. J. Hogben, T. Biskup, and D. R. Kattnig. Alternative radical pairs for cryptochrome-based magnetoreception. *J. R. Soc. Interface*, 11:20131063, 2014.

[73] D. R. Kattnig, E. W. Evans, V. Déjean, C. A. Dodson, M. I. Wallace, S. R. Mackenzie, C. R. Timmel, and P. J. Hore. Chemical amplification of magnetic field effects relevant to avian magnetoreception. *Nature Chemistry*, 8, 2016.

[74] Hans G. Wallraff. Social interrelations involved in migratory orientation of birds: Possible contribution of field studies. *Oikos*, 30(2):401–404, 1978.

[75] W. W. Cochran, H. Mouritsen, and M. Wikelski. Migrating songbirds recalibrate their magnetic compass daily from twilight cues. *Science*, 304, 2004.

[76] H. G. Hiscock, T. W. Hiscock, D. R. Kattnig, T. Scrivener, A. M. Lewis, D. E. Manolopoulos, and P. J. Hore. Navigating at night: fundamental limits on the sensitivity of radical pair magnetoreception under dim light. *Quarterly reviews of biophysics*, 52, 2019.

[77] K. Maeda, K. B. Henbest, F. Cintolesi, I. Kuprov, C. T. Rodgers, P. A. Liddell, D. Gust, C. R. Timmel, and P. J. Hore. Chemical compass model of avian magnetoreception. *Nature*, 453, 2008.

[78] Hadi Zadeh-Haghighi and Christoph Simon. Magnetic field effects in biology from the perspective of the radical pair mechanism. *Journal of The Royal Society Interface*, 19, 08 2022.

[79] G. Bleifuss, M. Kolberg, S. Pötsch, W. Hofbauer, R. Bittl, W. Lubitz, A. Gräslund, G. Lassmann, and F. Lendzian. Tryptophan and tyrosine radicals in ribonucleotide reductase: A comparative high-field epr study at 94 ghz. *Biochemistry*, 40, 2001.

[80] M. Liedvogel, K. Maeda, K. Henbest, E. Schleicher, T. Simon, C. T. Timmel, P. J. Hore, and H. Mouritsen. Chemical magnetoreception: Bird cryptochrome 1a is excited by blue light and forms long-lived radical-pairs. *PLoS ONE*, 2, 2007.

[81] D. Nohr, S. Franz, R. Rodriguez, B. Paulus, L.-O. Essen, S. Weber, and E. Schleicher. Extended electron-transfer in animal cryptochromes mediated by a tetrad of aromatic amino acids. *Biophysical Journal*, 111:301–311, 7 2016.

[82] D. R. Kattnig. Radical-pair-based magnetoreception amplified by radical scavenging: resilience to spin relaxation. *The Journal of Physical Chemistry B*, 121:10215–10227, 11 2017.

[83] R. H. Keens, C. Sampson, and D. R. Kattnig. How symmetry-breaking can amplify the magnetosensitivity of dipolarly coupled n-radical systems. *J. Chem. Phys.*, 154:094101, 2021.

[84] J. A. Maier, C. Martinez, K. Kasavajhala, L Wickstrom, K. E. Hauser, and C. Simmerling. ff14sb: Improving the accuracy of protein side chain and backbone parameters from ff99sb. *Journal of Chemical Theory and Computation*, 11:3696–3713, 8 2015.

[85] B. R. Brooks, C. L. Brooks, A. D. Mackerell, L. Nilsson, R. J. Petrella, B. Roux, Y. Won, G. Archontis, C. Bartels, S. Boresch, A. Caflisch, L. Caves, Q. Cui, A. R. Dinner, M. Feig, S. Fischer, J. Gao, M. Hodoscek, W. Im, K. Kuczera, T. Lazaridis, J. Ma, V. Ovchinnikov, E. Paci, R. W. Pastor, C. B. Post, J. Z. Pu, M. Schaefer, B. Tidor, R. M. Venable, H. L. Woodcock, X. Wu, W. Yang, D. M. York, and M. Karplus. Charmm: The biomolecular simulation program. *Journal of Computational Chemistry*, 30, 2009.

[86] I. G. Karogodina, T. Y.and Dranov, S. V. Sergeeva, D. V. Stass, and U. E. Steiner. Kinetic magnetic-field effect involving the small biologically relevant inorganic radicals no and o2·-. *ChemPhysChem*, 12:1714, 2011.

[87] D. Laage, G. Stirnemann, F. Sterpone, and J. T. Hynes. Water jump reorientation: From theoretical prediction to experimental observation. *Accounts of Chemical Research*, 45, 2012.

[88] R. G. Parr and W. Yang. Density-functional theory of atoms and molecules. r.g. parr and w. yang, oxford university press, new york, oxford. *Oxford University Press*, 1989.

[89] J. P. Perdew, K. Burke, and M. Ernzerhof. Generalized gradient approximation made simple. *Phys. Rev. Lett.*, 77(18):3865, October 1996.

[90] C. Adamo, M. Ernzerhof, and G. E. Scuseria. The meta-gga functional: Thermochemistry with a kinetic energy density dependent exchange-correlation functional. *Journal of Chemical Physics*, 112, 2000.

[91] A. D. Becke. Density-functional thermochemistry. Iii. The role of exact exchange. *J. Chem. Phys.*, 98(7):5648, April 1993.

[92] H. Iikura, T. Tsuneda, T. Yanai, and K. Hirao. A long-range correction scheme for generalized-gradient-approximation exchange functionals. *Journal of Chemical Physics*, 115, 2001.

[93] J. Toulouse, F. Colonna, and A. Savin. Long-range - short-range separation of the electron-electron interaction in density-functional theory. *Physical Review A - Atomic, Molecular, and Optical Physics*, 70, 2004.

[94] L. Hermosilla, P. Calle, J. M. García De La Vega, and C. Sieiro. Density functional theory predictions of isotropic hyperfine coupling constants. *Journal of Physical Chemistry A*, 109, 2005.

[95] L. Hermosilla, J. M. García De La Vega, C. Sieiro, and P. Calle. Dft calculations of isotropic hyperfine coupling constants of nitrogen aromatic radicals: The challenge of nitroxide radicals. *Journal of Chemical Theory and Computation*, 7, 2011.

[96] J. Shaw. Magnetic particle-mediated magnetoreception. *J. R. Soc., Interface*, 12:20150499, 2015.

[97] I. K. Kominis. The radical-pair mechanism as a paradigm for the emerging science of quantum biology. *Mod. Phys. Lett. B*, 29:1530013, 2015.

[98] Y. Kim. Quantum biology: An update and perspective. *Quantum Rep.*, 3:80, 2021.

[99] K. Maeda. Magnetically sensitive light-induced reactions in cryptochrome are consistent with its proposed role as a magnetoreceptor. *Proc. Natl. Acad. Sci. U. S. A.*, 109:4774, 2012.

[100] T. Ritz. Magnetic compass of birds is based on a molecule with optimal directional sensitivity. *Biophys. J.*, 96:3451, 2009.

[101] I. A. Solov'yov and K. Schulten. Magnetoreception through cryptochrome may involve superoxide. *Biophys. J.*, 96:4804, 2009.

[102] H. J. Hogben, O. Efimova, N. Wagner-Rundell, C. R. Timmel, and P. J. Hore. Possible involvement of superoxide and dioxygen with cryptochrome in avian magnetoreception: Origin of zeeman resonances observed by in vivo epr spectroscopy. *Chem. Phys. Lett.*, 480:118, 2009.

[103] M. Procopio and T. Ritz. The reference-probe model for a robust and optimal radical-pair-based magnetic compass sensor. *J. Chem. Phys.*, 152:065104, 2020.

[104] A. T. Vaidya. Flavin reduction activates drosophila cryptochrome. *Proc. Natl. Acad. Sci. U. S. A.*, 110:20455, 2013.

[105] B. D. Zoltowski. Structure of full-length drosophila cryptochrome. *Nature*, 480:396, 2011.

[106] R. Haberkorn. Density matrix description of spin-selective radical pair reactions. *Mol. Phys.*, 32:1491, 1976.

[107] J. Cai and M. B. Plenio. Chemical compass model for avian magnetoreception as a quantum coherent device. *Phys. Rev. Lett.*, 111:230503, 2013.

[108] T. P. Fay, L. P. Lindoy, and D. E. Manolopoulos. Spin-selective electron transfer reactions of radical pairs: Beyond the haberkorn master equation. *J. Chem. Phys.*, 149:064107, 2018.

[109] B. Adams, I. Sinayskiy, and F. Petruccione. An open quantum system approach to the radical pair mechanism. *Sci. Rep.*, 8:15719, 2018.

[110] M. K. Kuimova, G. Yahioglu, J. A. Levitt, and K. Suhling. Molecular rotor measures viscosity of live cells via fluorescence lifetime imaging. *J. Am. Chem. Soc.*, 130:6672, 2008.

[111] D. R. Kattnig, C. Nielsen, and I. A. Solov'yov. Molecular dynamics simulations disclose early stages of the photo-activation of cryptochrome 4. *New J. Phys.*, 20:083018, 2018.

[112] C. Levy. Updated structure of drosophila cryptochrome. *Nature*, 495:E3, 2013.

[113] J. B. Pedersen, C. Nielsen, and I. A. Solov'yov. Multiscale description of avian migration: From chemical compass to behaviour modeling. *Sci. Rep.*, 6:36709, 2016.

[114] C. C. Page, C. C. Moser, X. Chen, and P. L. Dutton. Natural engineering principles of electron tunnelling in biological oxidation–reduction. *Nature*, 402:47, 1999.

[115] J. R. Winkler and H. B. Gray. Long-range electron tunneling. *J. Am. Chem. Soc.*, 136:2930, 2014.

[116] D. S. Bendall. *Protein Electron Transfer, 1st ed.* Garland Science, 1996.

[117] F. Cailliez, P. Müller, M. Gallois, and A. de la Lande. Atp binding and aspartate protonation enhance photoinduced electron transfer in plant cryptochrome. *J. Am. Chem. Soc.*, 136:12974, 2014.

[118] A. T. Dellis and I. K. Kominis. The quantum zeno effect immunizes the avian compass against the deleterious effects of exchange and dipolar interactions. *Biosystems*, 107:153, 2012.

[119] A. de la Lande, J. Řezáč, B. Lévy, B. C. Sanders, and D. R. Salahub. Transmission coefficients for chemical reactions with multiple states: Role of quantum decoherence. *J. Am. Chem. Soc.*, 133:3883, 2011.

[120] D. R. Kattnig, J. K. Sowa, I. A. Solov'yov, and P. J. Hore. Electron spin relaxation can enhance the performance of a cryptochrome-based magnetic compass sensor. *New J. Phys.*, 18:063007, 2016.

[121] C. C. Winterbourn, H. N. Parsons-Mair, S. Gebicki, J. M. Gebicki, and M. J. Davies. Requirements for superoxide-dependent tyrosine hydroperoxide formation in peptides. *Biochem. J.*, 381:241, 2004.

[122] M. Procopio and T. Ritz. Inhomogeneous ensembles of radical pairs in chemical compasses. *Sci. Rep.*, 6:35443, 2016.

[123] C. Nielsen, D. R. Kattnig, E. Sjulstok, P. J. Hore, and I. A. Solov'yov. Ascorbic acid may not be involved in cryptochrome-based magnetoreception. *J. R. Soc., Interface*, 14:20170657, 2017.

[124] R. J. Usselman. The quantum biology of reactive oxygen species partitioning impacts cellular bioenergetics. *Sci. Rep.*, 6:38543, 2016.

[125] R. J. Usselman, I. Hill, D. J. Singel, and C. F. Martino. Spin biochemistry modulates reactive oxygen species (ros) production by radio frequency magnetic fields. *PLoS One*, 9:e93065, 2014.

[126] R. M. Sherrard. Low-intensity electromagnetic fields induce human cryptochrome to modulate intracellular reactive oxygen species. *PLoS Biol.*, 16:e2006229, 2018.

[127] J. Smith, H. Zadeh Haghighi, D. Salahub, and C. Simon. Radical pairs may play a role in xenon-induced general anesthesia. *Sci. Rep.*, 11:6287, 2021.

[128] H. Zadeh-Haghighi and C. Simon. Entangled radicals may explain lithium effects on hyperactivity. *Sci. Rep.*, 11:12121, 2021.

[129] B. Zhang. Long-term exposure to a hypomagnetic field attenuates adult hippocampal neurogenesis and cognition. *Nat. Commun.*, 12:1174, 2021.

[130] S. Ghodbane, A. Lahbib, M. Sakly, and H. Abdelmelek. Bioeffects of static magnetic fields: Oxidative stress, genotoxic effects, and cancer studies. *BioMed Res. Int.*, 2013:602987, 2013.

[131] Y. Ding, A. S. Kiryutin, A. V. Yurkovskaya, D. V. Sosnovsky, R. Z. Sagdeev, S. Bannister, T. Kottke, R. K. Kar, I. Schapiro, K. L. Ivanov, and J. Matysik. Nuclear spin-hyperpolarization generated in a flavoprotein under illumination: experimental field-dependence and theoretical level crossing analysis. *Scientific Reports*, 9(1):18436, 12 2019.

[132] N. Pompe, J. Chen, B. Illarionov, S. Panter, M. Fischer, A. Bacher, and S. Weber. Methyl groups matter: Photo-CIDNP characterizations of the semiquinone radicals of FMN and demethylated FMN analogs. *The Journal of Chemical Physics*, 151(23):235103, 12 2019.

[133] E. Pauwels, R. Declerck, T. Verstraelen, B. De Sterck, C. W. M. Kay, V. V. Speybroeck, and M. Waroquier. Influence of protein environment on the electron paramagnetic resonance properties of flavoprotein radicals: A QM/MM study. *J. Phys. Chem. B*, 114(49):16655–16665, 2010.

[134] J. I. Martínez, S. Frago, I. Lans, P. J. Alonso, I. García-Rubio, and M. Medina. Spin densities in flavin analogs within a flavoprotein. *Biophys. J.*, 110(3):561–571, February 2016.

[135] R. Wiltschko, C. Nießner, and W. Wiltschko. The magnetic compass of birds: the role of cryptochrome. *Front. Physiol.*, 12:667000, May 2021.

[136] S. Y. Wong, A. Frederiksen, M. Hanić, F. Schuhmann, G. Grüning, P. J. Hore, and I. A. Solov'yov. Navigation of migratory songbirds: a quantum magnetic compass sensor. *Neuroforum*, 27(3):141–150, August 2021.

[137] A. Sancar. Structure and function of dna photolyase and cryptochrome blue-light photoreceptors. *Chem. Rev.*, 103(6):2203–2237, 2003.

[138] P. Müller and M. Ahmad. Light-activated cryptochrome reacts with molecular oxygen to form a flavin–superoxide radical pair consistent with magnetoreception. *J. Biol. Chem.*, 286(24):21033–21040, June 2011.

[139] D. E. Manolopoulos and P. J. Hore. An improved semiclassical theory of radical pair recombination reactions. *J. Chem. Phys.*, 139(12):124106, 2013.

[140] R. K. Kar, A.-F. Miller, and M.-A. Mroginski. Understanding flavin electronic structure and spectra. *WIREs Comput. Mol. Sci.*, page e1541, 2021.

[141] J. I. Martínez, P. J. Alonso, and M. Medina. The electronic structure of the neutral isoalloxazine semiquinone within Anabaena flavodoxin: New insights from HYSCORE experiments. *J. Magn. Reson.*, 218:153–162, May 2012.

[142] M. Medina, A. Vrielink, and R. Cammack. ESR and electron nuclear double resonance characterization of the cholesterol oxidase from Brevibacterium sterolicum in its semiquinone state. *Eur. J. Biochem.*, 222:941–947, 1994.

[143] M. Medina, C. Gomez-Moreno, and R. Cammack. Electron spin resonance and electron nuclear double resonance studies of flavoproteins involved in the photosynthetic electron transport in the cyanobacterium Anabaena sp. Pcc 7119. *Eur. J. Biochem*, 227:529–536, 1995.

[144] S. Weber, G. Richter, E. Schleicher, A. Bacher, K. Möbius, and C. W.M. Kay. Substrate binding to DNA photolyase studied by electron paramagnetic resonance spectroscopy. *Biophys. J.*, 81(2):1195–1204, August 2001.

[145] E. Schleicher, K. Hitomi, C. W.M. Kay, E. D. Getzoff, T. Todo, and S. Weber. Electron nuclear double resonance differentiates complementary roles for active site histidines in (6-4) photolyase. *J. Biol. Chem.*, 282(7):4738–4747, February 2007.

[146] E. Schleicher, R. Wenzel, M. Ahmad, A. Batschauer, L.-O. Essen, K. Hitomi, E. D. Getzoff, R. Bittl, S. Weber, and A. Okafuji. The electronic state of flavoproteins: investigations with proton electron–nuclear double resonance. *Appl. Magn. Reson.*, 37(1-4):339–352, January 2010.

[147] J. I. García, M. Medina, J. Sancho, P. J. Alonso, C. Gómez-Moreno, J. A. Mayoral, and J. I. Martínez. Theoretical analysis of the electron spin density distribution of the flavin semiquinone isoalloxazine ring within model protein environments. *J. Phys. Chem. A*, 106(18):4729–4735, 2002.

[148] S. Weber, K. Mo, G. Richter, and C. W. M. Kay. The electronic structure of the flavin cofactor in DNA photolyase. *JACS*, 123(16):3790–3798, 2001.

[149] D. Nohr, R. Rodriguez, S. Weber, and E. Schleicher. How can epr spectroscopy help to unravel molecular mechanisms of flavin-dependent photoreceptors? *Front. Mol. Biosci.*, 2:49, 2015.

[150] D. Nohr, S. Weber, and E. Schleicher. Epr spectroscopy on flavin radicals in flavoproteins. In Bruce A. Palfey, editor, *New Approaches for Flavin Catalysis*, volume 620 of *Methods in Enzymology*, chapter 10, pages 251–275. Academic Press, 2019.

[151] B. I. Dunlap, J. W. D. Connolly, and J. R. Sabin. On first-row diatomic molecules and local density models. *The Journal of Chemical Physics*, 71(12):4993, 1979.

[152] J. W. Mintmire and B. I. Dunlap. Fitting the Coulomb potential variationally in linear-combination-of-atomic-orbitals density-functional calculations. *Physical Review A*, 25(1):88–95, 1 1982.

[153] J. W. Mintmire, J. R. Sabin, and S. B. Trickey. Local-density-functional methods in two-dimensionally periodic systems. Hydrogen and beryllium monolayers. *Physical Review B*, 26(4):1743–1753, 8 1982.

[154] H. Sambe and R. H. Felton. A new computational approach to Slater's SCF–X α equation. *The Journal of Chemical Physics*, 62(3):1122–1126, 2 1975.

[155] E. Krieger and G. Vriend. YASARA View - molecular graphics for all devices - from smartphones to workstations. *Bioinformatics*, 30(20):2981–2982, October 2014.

[156] E. Krieger, J. E. Nielsen, C. A.E.M. Spronk, and G. Vriend. Fast empirical pKa prediction by Ewald summation. *J. Mol. Graph. Model.*, 25(4):481–486, December 2006.

[157] L. Wang, L. Li, and E. Alexov. pKa predictions for proteins, RNAs, and DNAs with the Gaussian dielectric function using DelPhi pKa. *Proteins: Struct., Funct., Bioinf.*, 83(12):2186–2197, December 2015.

[158] L. Wang, M. Zhang, and E. Alexov. DelPhiPKa web server: predicting pKa of proteins, RNAs and DNAs. *Bioinformatics*, 32(4):614–615, February 2016.

[159] S. Pahari, L. Sun, S. Basu, and E. Alexov. DelPhiPKa: Including salt in the calculations and enabling polar residues to titrate. *Proteins: Struct., Funct., Bioinf.*, 86(12):1277–1283, December 2018.

[160] T. J. Dolinsky, P. Czodrowski, H. Li, J. E. Nielsen, J. H. Jensen, G. Klebe, and N. A. Baker. PDB2PQR: expanding and upgrading automated preparation of biomolecular structures for molecular simulations. *Nucleic Acids Res.*, 35(Web Server):522–525, May 2007.

[161] T. J. Dolinsky, J. E. Nielsen, J. A. McCammon, and N. A. Baker. PDB2PQR: an automated pipeline for the setup of Poisson-Boltzmann electrostatics calculations. *Nucleic Acids Res.*, 32(Web Server):665–667, July 2004.

[162] K. Sadeghian, M. Bocola, T. Merz, and M. Schütz. Theoretical Study on the Repair Mechanism of the (6-4) Photolesion by the (6-4) Photolyase. *Journal of the American Chemical Society*, 132(45):16285–16295, 11 2010.

[163] G. Lüdemann, I. A. Solov'yov, T. Kubař, and M. Elstner. Solvent Driving Force Ensures Fast Formation of a Persistent and Well-Separated Radical Pair in Plant

Cryptochrome. *Journal of the American Chemical Society*, 137(3):1147–1156, 1 2015.

[164] S. Fox, H. G. Wallnoefer, T. Fox, C. S. Tautermann, and C.-K. Skylaris. First principles-based calculations of free energy of binding: application to ligand binding in a self-assembling superstructure. *J. Chem. Theory Comput.*, 7(4):1102–1108, 2011.

[165] J.-P. Ryckaert, G. Ciccotti, and H. J. C. Berendsen. Numerical integration of the cartesian equations of motion of a system with constraints: molecular dynamics of n-alkanes. *Journal of Computational Physics*, 23(3):327–341, 3 1977.

[166] S. Miyamoto and P. A. Kollman. Settle: An analytical version of the SHAKE and RATTLE algorithm for rigid water models. *Journal of Computational Chemistry*, 13(8):952–962, 10 1992.

[167] A. M. Koster, G. Geudtner, A. Alvarez-Ibarra, P. Calaminici, M. E. Casida, J. Carmona-Espindola, V. D. Dominguez, R. Flores-Moreno, G. U. Gamboa, A. Goursot, T. Heine, A. Ipatov, A. de la Lande, F. Janetzko, J. M. del Campo, D. Mejia-Rodriguez, J. U. Reveles, J. Vasquez-Perez, A. Vela, B. Zuniga-Gutierrez, and D. R. Salahub. deMon2k, Version 6, 2018.

[168] D. Mejía-Rodríguez and A. M. Köster. Robust and efficient variational fitting of Fock exchange. *The Journal of Chemical Physics*, 141(12):124114, 9 2014.

[169] P. J. Stephens, F. J. Devlin, C. F. Chabalowski, and M. J. Frisch. Ab initio calculation of vibrational absorption and circular dichroism spectra using density functional force fields. *J. Phys. Chem.*, 98(45):11623–11627, November 1994.

[170] C. Lee, W. Yang, and R. G. Parr. Development of the Colle-Salvetti correlation-energy formula into a functional of the electron density. *Phys. Rev. B*, 37(2):785, January 1988.

[171] R. Improta and V. Barone. Interplay of electronic, environmental, and vibrational effects in determining the hyperfine coupling constants of organic free radicals. *Chem. Rev.*, 104(3):1231–1254, March 2004.

[172] M. Krack and A. M. Köster. An adaptive numerical integrator for molecular integrals. *J. Chem. Phys.*, 108(8):3226, February 1998.

[173] A. de la Lande, A. Alvarez-Ibarra, K. Hasnaoui, F. Cailliez, X. Wu, T. Minerva, J. Cuny, P. Calaminici, L. López-Sosa, G. Geudtner, I. Navizet, C. Garcia Iriepa, D. R. Salahub, and A. M. Köster. Molecular Simulations with in-deMon2k QM/MM, a Tutorial-Review. *Molecules*, 24(9):1653, 4 2019.

[174] RStudio Team. *RStudio: Integrated Development Environment for R*. RStudio, PBC., Boston, MA, 2020.

[175] M. Plummer, N. Best, K. Cowles, and K. Vines. Coda: Convergence diagnosis and output analysis for mcmc. *R News*, 6(1):7–11, 2006.

[176] D. R. Roe and T. E. Cheatham. PTRAJ and CPPTRAJ: Software for Processing and Analysis of Molecular Dynamics Trajectory Data. *Journal of Chemical Theory and Computation*, 9(7):3084–3095, 7 2013.

[177] V. Barone. *Structure, magnetic properties and reactivities of open-shell species from density functional and self-consistent hybrid methods*, volume 1. World Scientific, 1995.

[178] L. Hermosilla, P. Calle, and J. M. García de la Vega. Modeling EPR parameters of nitrogen containing conjugated radical cations. *RSC Adv.*, 5(77):62551–62562, 2015.

[179] V. Barone, P. Cimino, and E. Stendardo. Development and validation of the B3LYP/N07D computational model for structural parameter and magnetic tensors of large free radicals. *J. Chem. Theory Comput.*, 4(5):751–764, May 2008.

[180] P. Jakobsen and F. Jensen. Probing basis set requirements for calculating hyperfine coupling constants. *J. Chem. Phys.*, 151(17):17407, November 2019.

[181] F Neese. The orca program system. *WIREs Computational Molecular Science*, 2:73–78, 1 2012.

[182] S. Grimme, J. G. Brandenburg, C. Bannwarth, and A. Hansen. Consistent structures and interactions by density functional theory with small atomic orbital basis sets. *The Journal of Chemical Physics*, 143:054107, 8 2015.

[183] K. S. Conrad, C. C. Manahan, and B. R. Crane. Photochemistry of flavoprotein light sensors. *Nature Chemical Biology*, 10(10):801–809, 10 2014.

[184] B. Kopka, K. Magerl, A. Savitsky, M. D. Davari, K. Röllen, M. Bocola, B. Dick, U. Schwaneberg, K.-E. Jaeger, and U. Krauss. Electron transfer pathways in a light, oxygen, voltage (LOV) protein devoid of the photoactive cysteine. *Scientific Reports*, 7(1):13346, 12 2017.

[185] E. Cadenas, A. Boveris, C. I. Ragan, and A. O. M. Stoppani. Production of superoxide radicals and hydrogen peroxide by nadh-ubiquinone reductase and ubiquinol-cytochrome c reductase from beef-heart mitochondria. *Archives of Biochemistry and Biophysics*, 180, 1977.

[186] R. B. Johnston, B. B. Keele, H. P. Misra, J. E. Lehmeyer, L. S. Webb, L. R. Baehner, and K. V. RaJagopalan. The role of superoxide anion generation in phagocytic bactericidal activity. studies with normal and chronic granulomatous disease leukocytes. *Journal of Clinical Investigation*, 55, 1975.

[187] I. B. Afanas'ev. On mechanism of superoxide signaling under physiological and pathophysiological conditions. *Medical Hypotheses*, 64, 2005.

[188] T. M. Buetler, A. Krauskopf, and U. T. Ruegg. Role of superoxide as a signaling molecule. *News in Physiological Sciences*, 19, 2004.

[189] T. Finkel. Signal transduction by reactive oxygen species. *Journal of Cell Biology*, 194, 2011.

[190] T. C. Bruice. Oxygen-flavin chemistry. *Israel Journal of Chemistry*, 24, 1984.

[191] M. B. Shine, K. N. Guruprasad, and A. Anand. Effect of stationary magnetic field strengths of 150 and 200mt on reactive oxygen species production in soybean. *Bioelectromagnetics*, 33, 2012.

[192] I. A. Paponov, J. Fliegmann, R. Narayana, and M. E. Maffei. Differential root and shoot magnetoresponses in arabidopsis thaliana. *Scientific Reports*, 11, 2021.

[193] A. B. Fisher. Redox signaling across cell membranes. *Antioxidants and Redox Signaling*, 11, 2009.

[194] B. J. Hawkins, M. Madesh, C. J. Kirkpatrick, and A. B. Fisher. Superoxide flux in endothelial cells via the chloride channel-3 mediates intracellular signaling. *Molecular Biology of the Cell*, 18, 2007.

[195] H. P. Indo, H. C. Yen, I. Nakanishi, K. I. Matsumoto, M. Tamura, Y. Nagano, H. Matsui, O. Gusev, R. Cornette, T. Okuda, Y. Minamiyama, H. Ichikawa, S. Suenaga, M. Oki, T. Sato, T. Ozawa, D. K. St Clair, and H. J. Majima. A mitochondrial superoxide theory for oxidative stress diseases and aging. *Journal of Clinical Biochemistry and Nutrition*, 56, 2015.

[196] C. Muscoli, S. Cuzzocrea, D. P. Riley, J. L. Zweier, C. Thiemermann, Z. Q. Wang, and D. Salvemini. On the selectivity of superoxide dismutase mimetics and its importance in pharmacological studies. *British Journal of Pharmacology*, 140, 2003.

[197] T. B. Salmon, B. A. Evert, B. Song, and P. W. Doetsch. Biological consequences of oxidative stress-induced dna damage in saccharomyces cerevisiae. *Nucleic Acids Research*, 32, 2004.

[198] M. Comporti. Lipid peroxidation. biopathological significance. *Molecular Aspects of Medicine*, 14, 1993.

[199] J. I. Kourie. Interaction of reactive oxygen species with ion transport mechanisms. *American Journal of Physiology - Cell Physiology*, 275, 1998.

[200] O. M. Ighodaro and O. A. Akinloye. First line defence antioxidants-superoxide dismutase (sod), catalase (cat) and glutathione peroxidase (gpx): Their fundamental role in the entire antioxidant defence grid. *Alexandria Journal of Medicine*, 54, 2018.

[201] A. Nandi and I. B. Chatterjee. Scavenging of superoxide radical by ascorbic acid. *Journal of Biosciences*, 11, 1987.

[202] C. C. Winterbourn. Revisiting the reactions of superoxide with glutathione and other thiols. *Archives of Biochemistry and Biophysics*, 595, 2016.

[203] K. M. Salerno, J. Domenico, N. Q. Le, C. D. Stiles, I. A. Solov'yov, and C. F. Martino. Long-time oxygen localization in electron transfer flavoprotein. *Journal of Chemical Information and Modeling*, 62(17):4191–4199, 2022. PMID: 35998902.

[204] C. L. Fisher, D. E. Cabelli, J. A. Tainer, R. A. Hallewell, and E. D. Getzoff. The role of arginine 143 in the electrostatics and mechanism of cu, zn superoxide dismutase: Computational and experimental evaluation by mutational analysis. *Proteins: Structure, Function, and Bioinformatics*, 19, 1994.

[205] V. Sedláček and I Kučera. Arginine-95 is important for recruiting superoxide to the active site of the ferb flavoenzyme of paracoccus denitrificans. *FEBS Letters*, 593, 2019.

[206] C. L. Fisher, D. E. Cabelli, R. A. Hallewell, P. Beroza, T. P. Lo, E. D. Getzoff, and J. A. Tainer. Computational, pulse-radiolytic, and structural investigations of lysine-136 and its role in the electrostatic triad of human cu,zn superoxide dismutase. *Proteins: Structure, Function and Genetics*, 29, 1997.

[207] M. W. Adams, F. E. Jenney, M. D. Clay, and M. K. Johnson. Superoxide reductase: Fact or fiction? *Journal of Biological Inorganic Chemistry*, 7, 2002.

[208] M. Lombard, C. Houée-Levin, D. Touati, M. Fontecave, and V. Nivière. Superoxide reductase from desulfoarculus baarsii: Reaction mechanism and role of glutamate 47 and lysine 48 in catalysis. *Biochemistry*, 40, 2001.

[209] P. Husen, C. Nielsen, C. F. Martino, and I. A. Solov'Yov. Molecular oxygen binding in the mitochondrial electron transfer flavoprotein. *Journal of Chemical Information and Modeling*, 59, 2019.

[210] D.A Case, I. Y. Ben-Shalom, S. R. Brozell, D. S. Cerutti, T. E. Cheatham, V. W. D. Cruzeiro, T. A. Darden, R. E. Duke, D. Ghoreishi, M. K. Gilson, H. Gohlke, A. W. Götz, D. Greene, R. Harris, N. Homeyer, Y. Huang, S. Izadi, A. Kovalenko, T. Kurtzman, T. S. Lee, S. Le Grand, P. Li, C. Lin, J. Liu, T. Luchko, R. Luo, D. J. Mermelstein, K. M. Merz, Y. Miao, G. Monard, C. Nguyen, H. Nguyen, I. Omelyan, A. Onufriev, F. Pan, R. Qi, D. R. Roe, A. Roitberg, C. Sagui, S. Schott-Verdugo, J. Shen, C. L. Simmerling, J. Smith, R. Salomon-Ferrer, J Swails, R. C. Walker, J. Wang, H. Wei, R. M. Wolf, X. Wu, L. Xiao, D. M. York, and P. A. Kollman. Amber 2018. 2018.

[211] R. Salomon-Ferrer, D. A. Case, and R. C. Walker. An overview of the amber biomolecular simulation package. *Wiley Interdisciplinary Reviews: Computational Molecular Science*, 3:198–210, 3 2013.

[212] A. W. Götz, M. J. Williamson, D. Xu, D. Poole, S. Le Grand, and R. C. Walker. Routine microsecond molecular dynamics simulations with amber on gpus. 1. generalized born. *Journal of Chemical Theory and Computation*, 8:1542–1555, 5 2012.

[213] R. Salomon-Ferrer, A. W. Götz, D. Poole, S. Le Grand, and R. C. Walker. Routine microsecond molecular dynamics simulations with amber on gpus. 2. explicit solvent particle mesh ewald. *Journal of Chemical Theory and Computation*, 9:3878–3888, 9 2013.

[214] M. A. Bittencourt, F. Falkenburger, M. Marino-Neto, and J. Marino-Neto. Stress-induced core temperature changes in pigeons (columba livia). *Physiology & Behavior*, 139:449–458, 2 2015.

[215] J. A. Izaguirre, D. P. Catarello, J. M. Wozniak, and R. D. Skeel. Langevin stabilization of molecular dynamics. *The Journal of Chemical Physics*, 114:2090–2098, 2 2001.

[216] H. J. C. Berendsen, J. P. M. Postma, W. F. van Gunsteren, A. DiNola, and J. R. Haak. Molecular dynamics with coupling to an external bath. *The Journal of Chemical Physics*, 81:3684–3690, 10 1984.

[217] U. Essmann, L. Perera, M. L. Berkowitz, T. Darden, H. Lee, and L. G. Pedersen. A smooth particle mesh ewald method. *The Journal of Chemical Physics*, 103:8577–8593, 11 1995.

[218] L. Martínez, R. Andrade, E. G. Birgin, and J. M. Martínez. Packmol: A package for building initial configurations for molecular dynamics simulations. *Journal of Computational Chemistry*, 30:2157–2164, 10 2009.

[219] M. Hayyan, M. A. Hashim, and I. M. Alnashef. Superoxide ion: Generation and chemical implications. *Chemical Reviews*, 116, 2016.

[220] C. M. C. Andrés, J. M. Pérez de la Lastra, C. Andrés Juan, F. J. Plou, and E. Pèrez-Lebeña. Superoxide anion chemistry;its role at the core of the innate immunity. *International Journal of Molecular Sciences*, 24(3), 2023.

[221] S. F. Boys and F. Bernardi. The calculation of small molecular interactions by the differences of separate total energies. some procedures with reduced errors. *Molecular Physics*, 19, 1970.

[222] S. Simon, M. Duran, and J. J. Dannenberg. How does basis set superposition error change the potential surfaces for hydrogen-bonded dimers? *Journal of Chemical Physics*, 105, 1996.

[223] I. S. Joung and T. E. Cheatham. Determination of alkali and halide monovalent ion parameters for use in explicitly solvated biomolecular simulations. *Journal of Physical Chemistry B*, 112, 2008.

[224] V. Lounnas, B. E. Pettitt, and G. N. Phillips. A global model of the protein-solvent interface. *Biophysical Journal*, 66, 1994.

[225] Andrea Brugnara, Filip Topić, Kari Rissanen, Aurélien De La Lande, Benoit Colasson, and Olivia Reinaud. Selective recognition of fluoride anion in water by a copper(ii) center embedded in a hydrophobic cavity. *Chemical Science*, 5, 2014.

[226] B. Mennucci, J. Tomasi, R. Cammi, J. R. Cheeseman, M. J. Frisch, F. J. Devlin, S. Gabriel, and P. J. Stephens. Polarizable continuum model (pcm) calculations of solvent effects on optical rotations of chiral molecules. *Journal of Physical Chemistry A*, 106, 2002.

[227] M. D. Tissandier, K. A. Cowen, W. Y. Feng, E. Gundlach, M. H. Cohen, A. D. Earhart, J. V. Coe, and T. R. Tuttle. The proton's absolute aqueous enthalpy and gibbs free energy of solvation from cluster-ion solvation data. *Journal of Physical Chemistry A*, 102, 1998.

[228] J. W. Ponder, C. Wu, P. Ren, V. S. Pande, J. D. Chodera, M. J. Schnieders, I. Haque, D. L. Mobley, D. S. Lambrecht, R. A. Distasio, M. Head-Gordon, G. N. I. Clark, M. E. Johnson, and T. Head-Gordon. Current status of the amoeba polarizable force field. *Journal of Physical Chemistry B*, 114, 2010.

[229] A. Okafuji, A. Schnegg, E. Schleicher, K. Möbius, and S. Weber. G-tensors of the flavin adenine dinucleotide radicals in glucose oxidase: a comparative multifrequency electron paramagnetic resonance and electron-nuclear double resonance study. *J. Phys. Chem. B*, 112(11):3568–3574, March 2008.